University of Southampton

Simultaneous Space Charge and Current Measurements in Polyethylene Insulation under HVDC Conditions

By

Wai Shyan Lau
BEng (Hons)

A thesis submitted for the Degree of
Doctor of Philosophy

School of Electronics and Computer Science
Faculty of Engineering, Science and Mathematics

August 2003

UNIVERSITY OF SOUTHAMPTON

ABSTRACT

FACULTY OF ENGINEERING, SCIENCE AND MATHEMATICS
SCHOOL OF ELECTRONICS AND COMPUTER SCIENCE

Doctor of Philosophy

SIMULTANEOUS SPACE CHARGE AND CURRENT MEASUREMENTS IN POLYETHYLENE INSULATION UNDER HVDC CONDITIONS

by Wai Shyan Lau

The increasing worldwide usage of extruded polymeric high voltage (HV) cable demands for a more reliable cable insulation with lower rate of unpredicted premature failures. These premature failures have been accredited to a combination of causes, including insulation flaws and trapped space charges. Accumulation of space charge in the cable polymeric insulation occurs only to very limited extent under alternating current (AC) electric stress, significant charge densities can be generated during direct current (DC) testing of AC cables before installation, leading to premature failure when AC stress is applied subsequently. Therefore, the need to investigate and understand space charge formation is ever more crucial in hoping conceivable solutions of eliminating or at least reducing space charge accumulation to be established.

This thesis reports on the construction of an improved Pulsed Electro-acoustic (PEA) fully automated measurement system. This system is capable of not only measuring space charge but also current simultaneously on thin plaque specimens under a controlled temperature environment. This additional valuable piece of information enhances comprehension on their relationship. They complement each other to give details about charge carrier generation, transportation and accumulation processes.

Additive-free low density polyethylene (LDPE) is the basic element of crosslinked polyethylene (XLPE); it was chosen for initial testing to eliminate the contribution of the impurities (by-products created in XLPE due to the usage of crosslinking agent). Electrode materials and measurement temperature had been confirmed to affect space charge and current performance intensely.

Measurements were also carried out on XLPE (degassed and undegassed) at different temperatures to study the differences as compared to LDPE. It is believed that the by-products (acetophenone, α-methylstyrene, cumyl-alcohol etc.) in undegassed XLPE have played an important role in creating consecutive fast moving charge packet activity (using solid aluminium cathode and semicon anode) where this happened neither in degassed XLPE nor LDPE.

Further tests were carried out using LDPE soaked in chemicals, namely acetophenone, α-methylstyrene and cumyl-alcohol that are found in undegassed XLPE to examine the contribution of each chemical on charge and current responses. All these by-products had proven to increase the conductivity of the charge carriers. Their presence have enhanced either one or both signs of charge carriers being injected from the electrodes.

Content

List of Figures

List of Tables

Acknowledgements

The completion of this PhD project has not been without obstacles and help from many people. My heartfelt thanks goes to Dr. George Chen for his guidance, advice, encouragement and supervision throughout the PhD course, without which the completion of this thesis would be impossible. I would also like to express my gratitude to late Professor A. E. Davies for giving me the opportunity to pursue this PhD degree in University of Southampton. I am honoured to be seen through the award of Master of Philosophy transfer to PhD by Professor Davies. My appreciation also goes to all my colleagues working in the Tony Davies High Voltage Laboratory, especially to late Mr. Roland Caldecutt who helped to construct and carried out endless modifications to the physical system of my experimental rig. Not forgetting Mr Neil Palmer, Mr. Brian Rodgers and Mr. Richard Howell providing assistance in technical work.

I dedicate this thesis to my beloved Dad, Kin Fong Lau, who had passed away at the beginning of my PhD course. I thank my mum, Pek Lan, my two elder brothers, James and Ken, also sister-in-law Jocelyn for their support and encouragement at difficult times. I am most grateful to my fiancé Chun Kong Wong for understanding and appreciating the importance of this PhD course to me and had to spend most of our time apart during my stay in UK.

Symbols

A	Richardson-Dushman constant
Al	Aluminium
C, C	Capacitor
d, x	Thickness
e	Electron charge
E, E	Electric field
E_a	Activation energy
E_c	The bottom of conduction band
E_f	Fermi level
E_g	The insulation energy gap
E_{tde}	Deep electron trap
E_{tdh}	Deep hole trap
E_{tse}	Shallow electron trap
E_{tsh}	Shallow hole trap
E_v	The top of valence band
f^*	Hopping frequency
h	Planck's constant
$H(f)$	The transfer function of the whole PEA system in frequency domain
h(t)	The unit impulse response of a system
$\hbar$	h/2π
I, i	Current
J, J	Current density
k	Wave number of the acoustic pressure wave
k_B	Boltzmann constant
kV	Kilo-volts
ℓ	Hopping distance
n	Power index
N	Defects per unit volume
$PW(f)$	Acoustic pressure signal for the whole system in frequency domain
$PW_1(f)$	Acoustic pressure signal for the first peak in frequency domain

pw(t)	Acoustic pressure signal for the whole system in time domain
pw_1(t)	Acoustic pressure signal for the first peak in time domain
R	The reflection coefficient depending on the actual barrier shape
R	Resistor
S	Area
Sc	Semicon
T	Temperature
t, t	Time
t_r	Transit time
υ	vibrational frequency
V	Apply voltage
V_C	Voltage drop across a capacitor
$V(f)$	The output from an amplifier in frequency domain
$V_1(f)$	The first peak output from an amplifier in frequency domain
V_R	Voltage drop across a resistor
$v(t)$	The whole PEA system output from an amplifier in time domain
$v_1(t)$	The first peak output from an amplifier in time domain
w	Angular frequency
α	Attenuation factor
β	Dispersion factor
χ	Electron affinity of the dielectric
ε_o	Permittivity of free space
ε_r	Relative permittivity of dielectric
ϕ_{boi}	The potential barrier height in the bulk of the insulation
ϕ_i	Work function of dielectric
ϕ_{int}	The potential barrier height at electrode-dielectric interface
ϕ_m	Work function of electrode
ϕ_o	Barrier height
ϕ_t	Barrier height from trap to enter conduction band
λ_a	The accumulation region
λ_d	The depletion region

μ	Mobility
ρ	Charge density
θ	Proportion of trap to free charge carrier
σ	Conductivity
σ_1	Surface induced charge

Abbreviations

AC	Alternating current
ASTM	The American Society for Testing and Materials
DC	Direct current
DCP	Dicumyl peroxide
EPR	Ethylene propylene rubber
GPIB	General purpose interface board
HDPE	High-density polyethylene
HV	High voltage
HVDC	High voltage direct current
LDPE	Low-density polyethylene
LIPP	Laser induced pressure pulse
MDPE	Medium density polyethylene
PE	Polyethylene
PEA	Pulsed Electro-acoustic
PG	Pulse generator
PIPWP	Piezoelectric induced pressure wave propagation
PVC	Polyvinyl chloride
PVDF	Polyvinylidene fluoride
SCLC	Space charge limited conduction
VHDPE	Very high density polyethylene
VLDPE	Very low density polyethylene
XLPE	Crosslinked polyethylene

Chapter 1

Introduction and Project Overview

1.1 Introduction

Overhead lines and underground high voltage (HV) cables are the principal elements of an electrical network grid. Electrical energy can be transmitted equally well by both overhead lines and underground cables. Nevertheless, owing to the distinct physical properties of underground cables and overhead lines, there are numerous disadvantages in their technical and functional features that must be considered together with the other elements of the network grid. Below are compared the pros and cons of overhead lines and underground cables: -

(a) Natural atmospheric air is the insulation material for overhead lines; assurance of sufficient spacing between the conductors must be given. Solid dielectrics are used in underground cables with high dielectric strength and permit relatively thin layers of insulation. The demand for higher operating voltage led to greater difficulties in insulation design. The superiority of the HV cables lies in the fact that high potential difference can be withstood at low spacing. Consequently, the dielectric is stressed electrically, thermally and also mechanically.

(b) Due to the fact that overhead lines are exposed to the environment, disturbances such as arcing faults caused by lightning strikes occur more frequently compared to cables. However, these disturbances cause no permanent damage that would result in failure of the overhead lines. On the other hand, disturbance to cables usually caused by building work can cause permanent harm although not as common. Disconnection and subsequent repair are unavoidable because cable insulation is destroyed at the fault location and cannot regenerate itself like the air for an overhead line. The repair time and cost for underground cable is also considerably dearer compared to overhead lines.

(c) The lengths in which cables can be supplied are restrained for reasons of fabrication and transportation. As a result, relatively high cost occurs for the fittings of joints and, if necessary, associate building works for joints. The cost of laying the cables is also considerably higher than the construction of an overhead line.

(d) The main advantages of underground cables are aesthetic and environmental privileges. This is ever important especially in densely populated areas. Underground cables are also used where the installation of overhead lines would not be possible, such as the vicinity of airports and across wide waterways.

There are many instances where only overhead lines make more sense on technical grounds, for example in the case of long distances. In other cases, the use of underground cable is forced by external circumstances, for example in conurbation and large cities or in cases of difficult construction conditions. Environmental protection and compatibility alongside with technical and economic attentions are increasingly important when planning for a new transmission system. Underground transmission and distribution will become progressively more important worldwide due to the following facts: -

(a) The high intensity of energy consumption by major conurbations in industrialized countries due to the escalating population and the demands of local public transport, in which only underground cable is achievable for this demand.

(b) Intensifying environmental awareness of the public hinders the erection of any new overhead transmission system. The many demands for the substitution of overhead lines also increases the demand for cables.

(c) Extra demand for the cable arises from the fact that segments of the existing network is approaching the end of their predicted life span. They have to be replaced due to their technical and ecological condition, especially for oil-filled paper insulation cables as they can suffer from oil losses due to leakage.

1.2 Establishment of underground cables

The establishment of HV cables started off with the introduction of the multi-layer dielectric using lapped paper tapes by Ferranti [1] in 1890. Progressively, impregnation of the paper dielectric with low viscosity insulating oil under permanent pressure was launch based on "Oil-filled Cable" principle by Emanueli [2] in 1917.

HV cable with extruded dielectric was set forth by the extrusion of single layer insulation using thermoplastic polyethylene (PE) in 1947. Successively, crosslinked polyethylene (XLPE) was used due to its ability to withstand higher operating temperatures. The two major groups of dielectrics commonly used for high voltage cables are namely, impregnated paper and extruded polymeric materials. Paper used for insulation of cable is chosen from softwoods. Based on the rated voltage of the cable, the dielectric may consist of a few tens up to several hundreds of narrow strips lapped spirally over each other, the butt gaps of these being axially displaced from layer to layer. The occurrences of air spaces in the axial gaps and between the individual machine spun paper layers are ineludible (necessary in the case of the gaps to allow the cable to be bent). In order to adequately prohibit pre-discharges in the electrical field within these spaces, the air must be removed and filled by an electrically stable medium. The materials ideal for this must be able to flow in order to be able to infiltrate the gaps and air spaces completely during manufacturing stages.

There will be a gradual worldwide swing away from paper to extruded polymeric materials. This is brought about by the high processing cost of paper and impregnating medium to form a voltage-resistant impregnated multi-layer dielectric, which involves time-intensive procedures. Polymeric cable is implemented by extrusion of solid dielectric over the conductor in a continuous fully automatic operation that, in addition, needed no impregnated medium. Another factor is it has become increasingly difficult to secure at a reasonable cost for the joining and termination of traditional paper insulated cable, this is especially obvious in the less developed countries. The simpler concept and reduced number of skills involved with the installation of polymeric cable have also contributed to a significant influence on the swing away from paper insulated cables [3, 4].

1.3 Causes of cable failure

Investigations on cable samples have shown that noticeable field distortion reduces the breakdown strength of the insulation, leading to premature failure of the cable. The root to this includes inhomogenities in the dielectric and the formation of space charge. The influence of inhomogenities on the field distribution and possibly resulting danger for the long term behaviour of the insulation are determined by the type of impurity. The three main types of impurity are inclusions (conducting and insulating), voids in the dielectric and protrusion into the semiconductive layer boundary surfaces, see figure 1. This can strongly and locally enhance the electric field. Such an increase can create electrical ageing, which may be responsible for degradation and breakdown of the material.

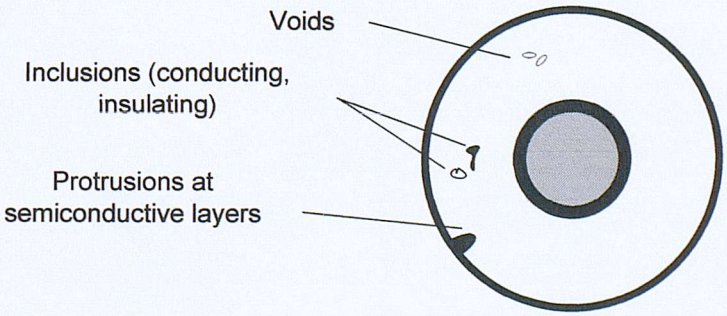

Figure1.1. Impurities in polymeric cable

Space charge is a collection of charge carriers in the insulation. At room temperature space charge can enter insulation within a very short time at high electrical stress and then take many hours to decay after the applied stress is removed. It creates an additional electrical source field that is superimposed on the geometrically determined field pattern and thus changes the resultant stress in the dielectric. Local high stress can lead to the formation of electrical trees. Space charge effects have now been recognised as one of the major components of the electrical aging process in polymers [5].

For the past two decades, an enormous number of investigators have been working to explore the causes, behaviour and possible ways of controlling the space charge accumulation such that a homogeneous field distribution results or by reducing the amount of accumulated space charge [6, 7]. Only by understanding all these factors can one design a HV polymeric cable with a lower chance of failure under operating conditions. In order to comprehend the nature of space charges, many non-destructive measurement techniques have been devised for identifying space charges in polymeric material. The most commonly used technique is the Pulsed Electro-acoustic (PEA) method. The construction of PEA set-up is simple, uses few materials and high resolution can be achieved.

1.4 Project overview

For the past two decades, the non-destructive PEA technique has been used by many to conduct a vast volume of investigations to obtain in depth knowledge about the formation of space charge. The conventional PEA set-up only provides charge behaviour information for that specimen under test. It would be an advantage to be able to know the corresponding current trend with reference to the charge measurement. With this additional parameter known, it will enable us to have a better insight about their relationship contributing to the breakdown of a cable. This has been realised by others by having to perform two separate tests on the same batch of specimens, one to measure current density only while the other measures the charge density profile [8]. However, this might introduce experimental errors caused by the difference of contact (or surface) conditions such as contact pressure, surface states

and chemical structures in preparing and treating specimen [9, 10], which may also affect the activation energy for carrier injection and the type of contact [11]. An alternative attempt was to have a high-speed switch to toggle between charge and current measurement [12]. But this also has the disadvantages of having to consider the maximum power, which can be dissipated within the switch and a drive circuit for the switch to prevent spurious triggering that would eventually damage the switch.

One of the objectives of this research project involves building an improved version of the PEA system. This improved PEA system allows the detection of charge and current measurement concurrently at a few seconds interval in a temperature-controlled environment. The experimental work in this thesis was carried out on additive-free low-density polyethylene (LDPE) and crosslinked polyethylene (XLPE), which is now the paramount technology for underground electric power distribution. The basic structure of XLPE is composed of three parts, (a) a non-crosslinked part, usually LDPE, (b) a crosslinked part (crosslinking agent), e.g., dicumyl peroxide and (c) impurities that consist of residual by-products formed by crosslinking reaction, also additives added to modify electrical breakdown level and moisture level. Every part has a distinct effect on space charge formation. LDPE was chosen because of its simple chemical structure and also to remove the influence of the impurity content. The elimination of the influence of the impurity content will enable us to explore the sole behaviour of the basic element of the XLPE structure under different test conditions without having speculation on the various factors that might have caused the resulting response.

The thesis is divided into 9 chapters. The first chapter gives a brief history about overhead and underground transmission. Followed by the evolution of underground cables, causes of cable failure and also the project overview. Chapter 2 deals with the polymeric materials that are use in cables. Fundamental concepts about space charge formation, transportation and accumulation are also presented.

Many non-destructive techniques have been invented to scrutinise space charge behaviour. Chapter 3 reviews principles of the different available measuring

techniques which include the Laser Induced Pressure Pulse (LIPP) technique, Piezoelectric Induced Pressure Wave Propagation (PIPWP) technique and Pulsed Electro-acoustic (PEA) technique. It has also included detail construction process of the improved PEA system, which discusses the problems encountered and solutions to them. Furthermore, essential PEA signal processing techniques like deconvolution, attenuation-dispersion compensation and charge density calibration are introduced.

Chapter 4 talks about the connection between space charge and current measurement. The space charge carrier behaviour in relation to the measured current was explained using an energy band diagram and actual experimental result. The importance of temperature influences on current measurement is also determined. Conduction current relies on two crucial factors, (a) the amount of mobile charge available for conduction and (b) its mobility. Since these two elements are temperature dependent, any increase of these two values (caused by higher temperature) will result in an escalation of the measured current.

Chapter 5 reports on the test results and analysis on additive-free LDPE under various different testing conditions that would affect the conduction characteristics. These include electrode material configurations, applied electric stresses and various measurement temperatures. Chapter 6 evaluates the performance of XLPE (degassed and undegassed) under two different measurement temperatures and electrode material configurations. Chapter 7 demonstrates the conduction behaviour of additive-free LDPE soaked in three separate by-products which are present in undegassed XLPE, namely acetophenone, α-methylstyrene and cumyl-alcohol. This is to demonstrate the contribution of each type of chemical on the conduction processes.

Chapter 8 makes a comparison of the experimental results as discussed in chapter 5 to 7. Chapter 9 concludes the overall research work done and possible improvements and recommendations for future direction.

Chapter 2

Polymeric Materials and Space Charge Properties

2.1 Introduction

Synthetic polymers have superseded natural materials such as paper, mineral oil and natural rubber for the insulation of cables. Development of new polymeric materials for HV cable insulation should consider the survey of suitable additives to the polymer. With the massive varieties of polymers available, mixture of chemical composition enable specific mechanical, electrical and thermal properties to be obtained [6, 13].

In this chapter, the evolution of polymeric materials used for underground cable is outlined. The generation and accumulation of charge in polymeric materials and eventual electrical breakdown, depend greatly on a number of material limiting factors such as crosslinking and additives. A pithy review on electrical conduction, space charge generation, transportation and accumulation in polymeric materials provides essential understanding for discussion of the experimental results in later chapters.

2.2 Polymeric materials use in cables

2.2.1 Polymeric materials

Polymeric materials denote polymers, which are either plastics or rubbers. Plastics can be further broken down into thermoplastics and thermosets. In thermoplastic materials, their molecules are separated, permitting them to slide against one another virtually unhindered, thus when it is heated and/or subjected to pressure they can soften and flow. This process is reversible and upon cooling the material solidifies. Classical examples are polyvinyl chloride (PVC) and polyethylene (PE). The arrangement of thermoplastic molecules is shown in figure 2.1.

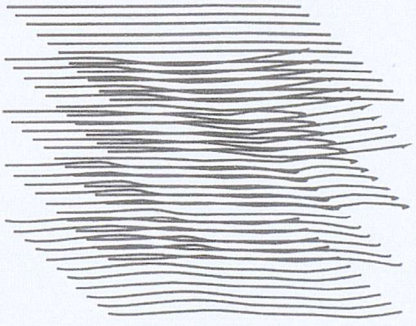

Figure 2.1. Thermoplastic molecules. Taken from E. F. Peschke et al [14].

Molecules in thermoset materials are joined together, crosslinked at one or more places along the molecular chain and formed a rigid structure, which will neither soften nor flow. Typical examples are ethylene propylene rubber (EPR) and crosslinked polyethylene (XLPE). Many thermoplastics may be transformed to thermosets by performing "crosslinking" treatment, whereby crosslinking agent is added. Figure 2.2 shows the arrangement of the thermoset molecules.

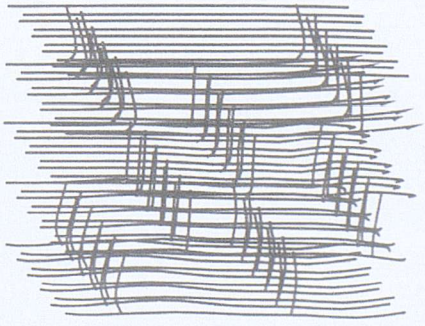

Figure 2.2. Thermoset molecules. Taken from E. F. Peschke et al [14].

2.2.2 Types of polymeric material use in cables

A. Thermoplastic Polyvinyl Chloride (PVC) [15, 16]

Rubber insulation was rapidly replaced by PVC in the 1940s. The advantages of PVC insulated cables are lighter weight compared to the paper/oil insulated cables and is much easier to handle. They are little affected by moisture and do not require a metal sheath, which leads to simple jointing and terminating. However, the amount of softening at raised temperature (a sustained maximum temperature of 70°C) due to its thermoplastic nature can result in deformation of the insulation due to conductor thrust at bends. PVC cables need adequate protection against overload or alternatively a reduced rating to be assigned to them and it also suffers from high dielectric loss. As a result, apart from house service cables, PVC has not been used for public supply.

B. Thermoplastic Polyethylene (PE) [17, 18]

Polyethylene was used as an insulator as early as 1943. Its high intrinsic electrical strength and low dielectric loss angle, together with its good resistance to chemicals, ease of processing and low cost make it an ideal candidate for use in the manufacturing of power cables. The main disadvantage proves to be the relatively low melting point (105°C – 115°C), which means that the sustained current rating, overloaded and short circuit temperature (maximum sustained temperature is ~70°C) are limited.

It is available in a variety of grades, differing in molecular weight and density. These varieties come about by the use of different methods of polymerisation. A classification dividing polyethylene resins into five ranges of density is generally used by the American Society for Testing and Materials (ASTM). They include very high density polyethylene (VHDPE), high density polyethylene (HDPE), medium density polyethylene (MDPE), low density polyethylene (LDPE) and very low density polyethylene (VLDPE). These ranges are shown in Table 2.1.

Density	g/cm^3	ASTM D1248
Very Low (VLDPE)	<0.910	-
Low (LDPE)	0.910 – 0.925	Type I
Medium (MDPE)	0.926 – 0.940	Type II
High (HDPE)	0.941 – 0.959	Type III
Very High (VHDPE)	0.959 & >	Type IV

Table 2.1. The density ranges of polyethylene [18].

C. Thermoset Ethylene Propylene Rubber (EPR) [19-21]

EPR was first use as insulant during early 1960s and is always used in crosslinked form. It has a main advantage for continuous operation at 90°C. EPR also has excellent resistance to ozone and electrical discharges but the high loss angle and poorer thermal resistivity make it a poor competitor against XLPE at higher voltages. Generally the use of EPR has been confined to applications where greater flexibility is needed. EPR is also more expensive than XLPE and it seems likely that applications for it will be limited to a voltage not greater than 30 kilovolts (kV), especially where flexibility of the core is an important factor, e.g., mining industry.

D. Thermoset Crosslinked Polyethylene (XLPE) [18, 22-24]

Despite its excellent electrical properties, an upper operational temperature of about 70°C has limited the use of polyethylene because of its thermoplasticity. By converting the thermoplastic polyethylene into crosslinked thermoset, the melting point is greatly increased and the material is well able to surpass the thermal capabilities of a paper insulated cable. The maximum sustained operating temperature for XLPE is 90°C. Crosslinking can be achieved either by radiation or chemical means. More about the crosslinking methods and residual byproducts created by crosslinking reaction will be discussed in chapter 6.

2.3 Electrical conduction and space charge related features

Although most polymers are excellent electrical insulators charge carriers do exist within these materials and are mobile under the influence of suitably high stresses. These charge carriers originate either from the electrode or within the bulk of the polymer and might be retained in the material for a long period of time.

The supply of charge from the electrodes involves transfer of electrons and holes across the electrode-dielectric interface. These processes greatly depend on the conditions at the interfaces, which include electrode material, surface state, impurities etc.[25, 26]. For charge accumulation in the bulk, the injected charge must become trapped in the dielectric and thus rely on the availability and nature of the traps. The residence time of a charge carrier in a trap will be dependent on the depth of the trap, i.e. the energy required to activate the carrier free of the trap, the temperature and the electric field. The generation of space charge within the bulk of the polymer is usually associated with ionisation of chemical species in the polymer. These may be chemical products introduced during the manufacturing process such as crosslinking reaction, antioxidant and other impurities.

2.3.1 Electrode-dielectric interfaces

Conduction in polymeric material is made possible with the help of electrodes. The electrical conduction properties are not only determined by the material itself but also the electrode-dielectric interface. Once in contact, charge is exchanged between the electrode and dielectric until equilibrium is reached. This is a process whereby the change in position of the dielectric Fermi level reduces the energy difference between the electrode and dielectric Fermi levels. This will cease only when the two Fermi levels coalesce to form a discrete mono-energetic system Fermi level. The discrete mono-energetic system Fermi level determines the height of the interface barrier ϕ_{int}, whereby:

$$\phi_{int} = \phi m - \chi \tag{2.1}$$

where ϕ_{int} = potential barrier height at electrode–dielectric interface,

ϕ_m = work function of electrode and

χ = electron affinity of the dielectric.

Figure 2.3(a) and (b) show the energy band diagram of a dielectric and metal respectively. Note that in metal there is no energy gap so the conduction and valence bands are touching and the Fermi level lies between the two bands.

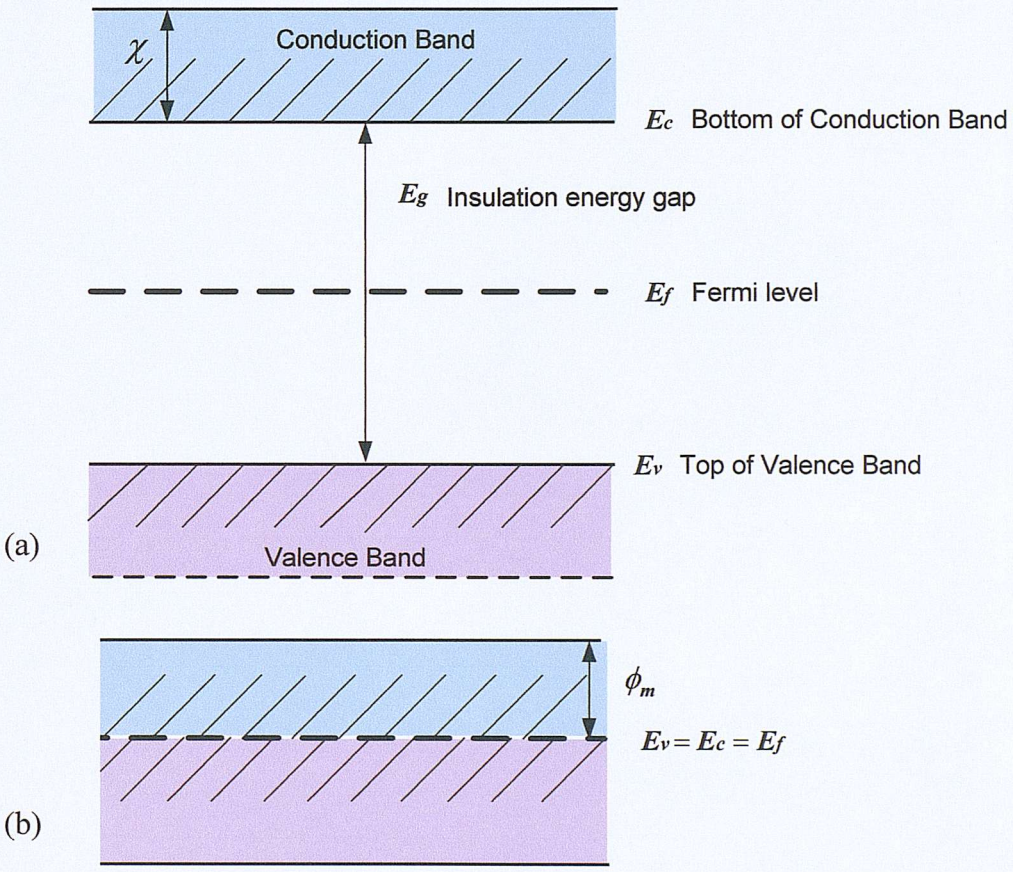

Figure 2.3 (a) and (b). Energy band diagram of a dielectric and metal respectively.

There are 3 types of electrode-dielectric interface depending on the work function of the electrode and dielectric:

A. Ohmic contact [27]

Ohmic contact will occur at an electrode-dielectric interface if the electrode work function ϕ_m is smaller than the dielectric work function, ϕ_i. Upon contact, thermal

equilibrium requirement must be fulfilled; therefore electrons are injected from the electrode into the conduction band of the dielectric until a mono-energetic Fermi level is achieved. This process gives rise to a space charge region and hence a space charge induced field in the dielectric. This field causes the bottom of the conduction band to come upwards away from the interface. This injected charge region will extend back into the bulk of the dielectric to a distance λ_a, equal to the distance of band bending, known as accumulation region, referred to energy band diagram in figure 2.4.

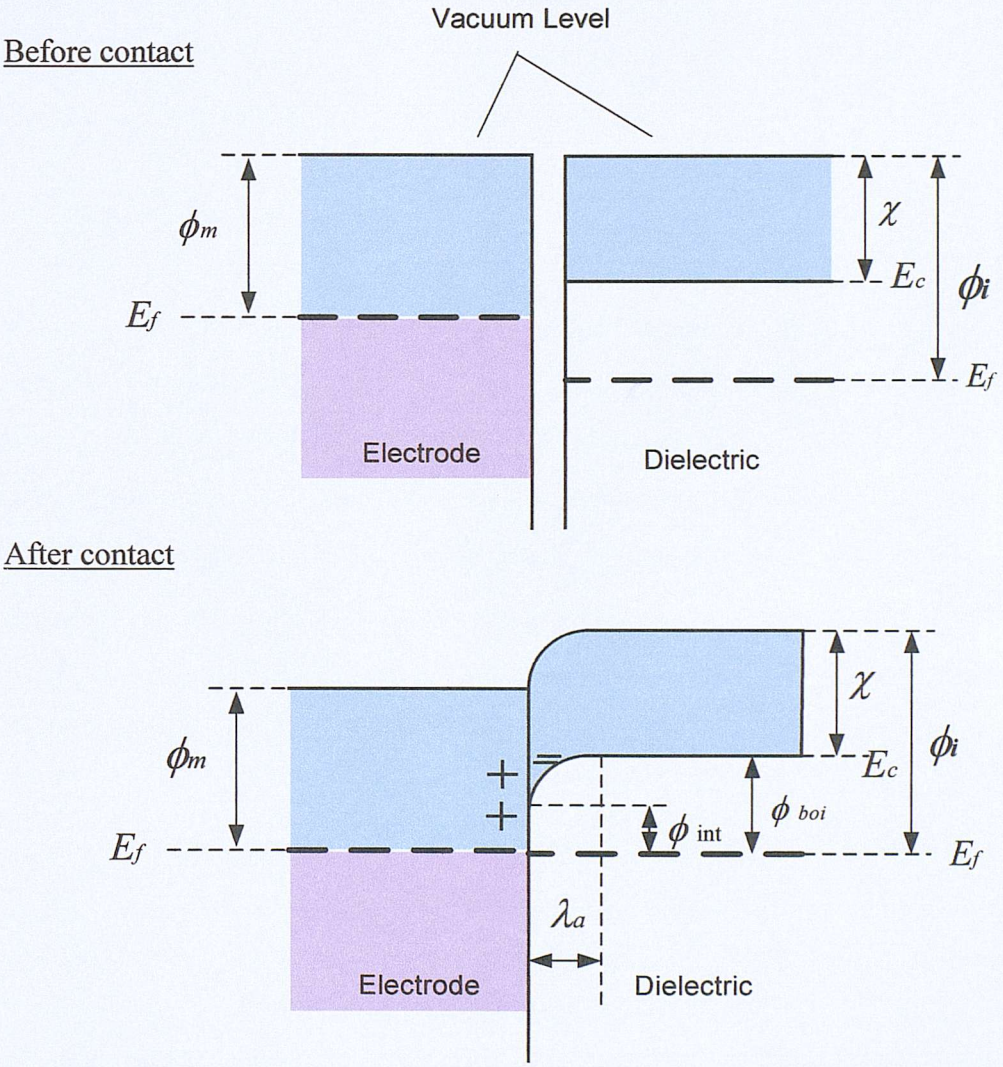

where ϕ_{boi} = potential barrier height in the bulk of the insulation and

λ_a = accumulation region

Figure 2.4. Energy band diagram of an ohmic contact.

Equation 2.1 only holds for the point of contact, where the actual barrier height of the interface, 'ϕ_{int}', is at minimum. Moving out from the space charge accumulation region, the barrier height increases up to the point where it becomes equal to the difference between the work function of the dielectric and its electron affinity, shown as 'ϕ_{boi}'. Thus, ohmic contact has reduced the barrier height at the interface, making charge injection into the dielectric easier.

The ohmic contact acts as a reservoir of charge capable of supplying electrons to the dielectric, as required by bias condition. The conduction process through the system is limited by the rate of which the electrons can flow through the bulk of dielectric, hence the process is bulk-limited.

B. Blocking contact [27]

Blocking contact occurs when the electrode work function is greater than the dielectric work function. In this case, electrons flow from the dielectric into the electrode to establish thermal equilibrium condition. This give rise to a positive space charge region created in the dielectric. As mentioned earlier, equation 2.1 only holds true for the point of contact. In this case, the barrier height of interface 'ϕ_{int}' is at maximum. Moving away from the space charge depletion region, λ_d, the barrier height decreases down to a height equal to the difference between the work function of the dielectric and its electron affinity, shown as 'ϕ_{boi}'.

From the energy band diagram figure 2.5, the rate of flow of electrons through the system will be restricted by the rate of which they flow over the interfacial barrier; here the conduction process is electrode limited. Practically, the depletion region in realisable dielectric will be quite low due to the low number of free electrons available for donation to the electrode. In which case, the conduction band of the dielectric will slope imperceptibly down, away from the interface and contact can effectively be considered as a neutral type contact.

Before contact

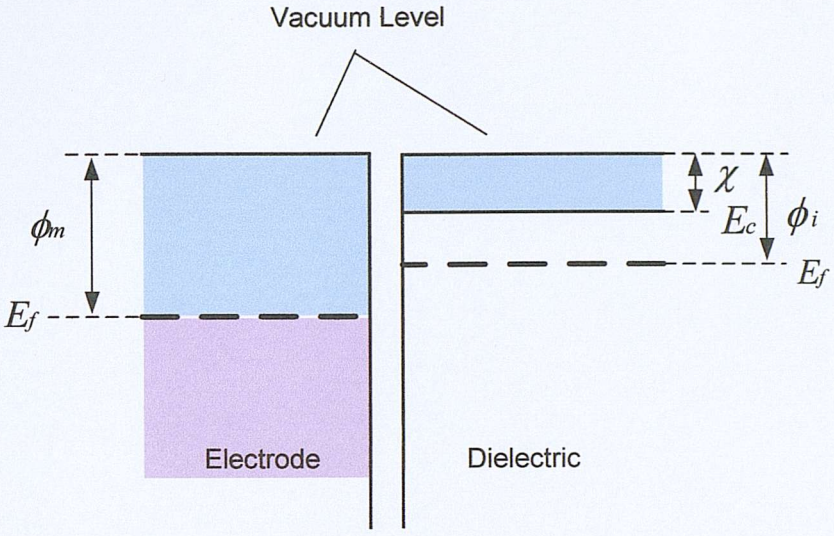

After contact

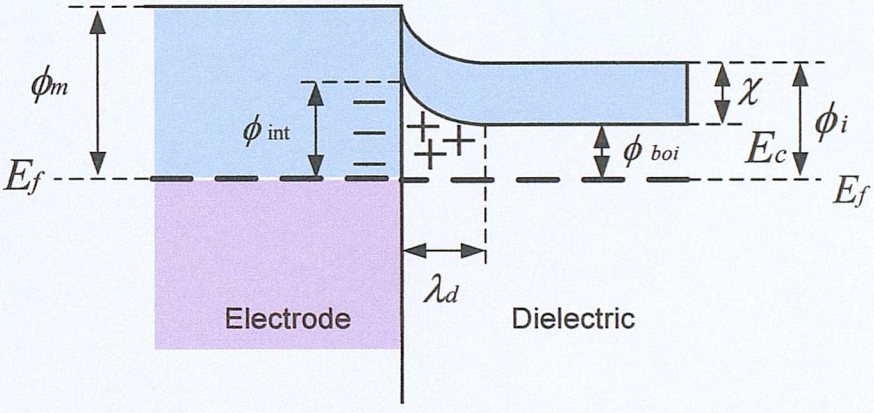

where λ_d = depletion region.

Figure 2.5. Energy band diagram of a blocking contact.

C. Neutral contact [27]

This happens when electrode work function is equal to dielectric work function naturally without the necessity of charge travelling between electrode and dielectric. Therefore, no band bending is present, see figure 2.6.

Before contact

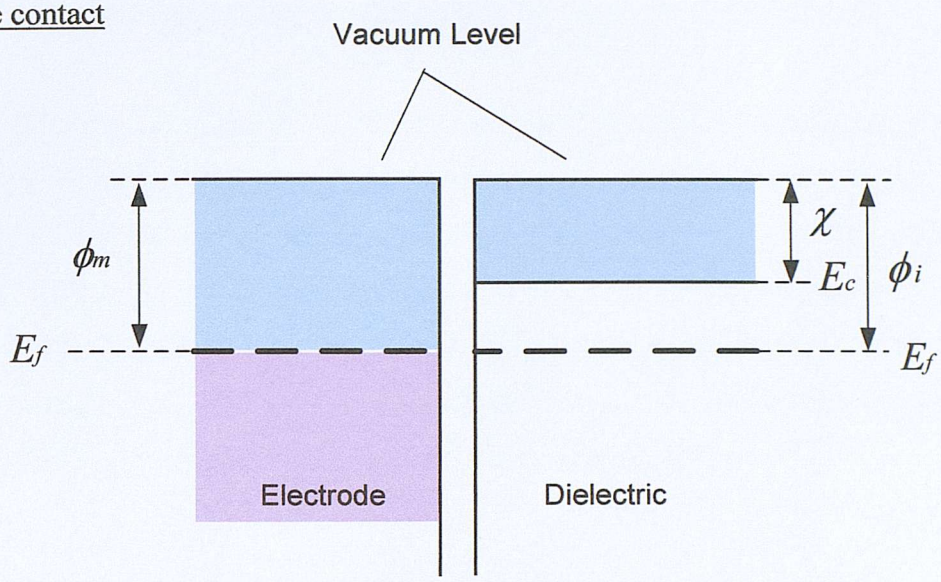

After contact

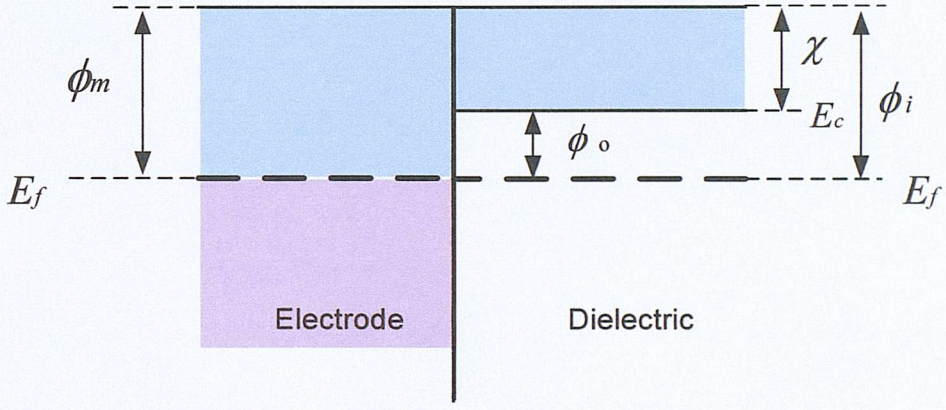

where ϕ_o = barrier height.

Figure 2.6. Energy band diagram of a neutral contact.

D. Surface states [27]

It has been assumed the barrier height at the electrode-dielectric interface to be defined by equation 2.1. If surface states exist on the dielectric surface and they are high in number, the interfacial barrier height is virtually independent of the electrode material. They owe their existence in part to the sudden departure from periodicity of the potential at the surface or simply to the manner in which the film is prepared. Thus it is normally not possible to determine in priori if surface states will exhibit a dominant role in the determination of the interfacial barrier height.

2.3.2 Electrode-polyethylene interface under an applied electric field

Figure 2.7(a) to (e) show the modification of the potential barrier at an electrode-polyethylene ohmic contact interface under an applied electric field. Figure 2.7(d) shows the potential energy due to an uniform applied field, E, to the dielectric. This electric field encourages the movement of the negative charge away from the electrode into the bulk of the dielectric. In the direction of the field, the barrier height will be lowered, as can be seen from figure 2.7(e). This will reduce the blocking action of this injected charge, allowing further charge injection.

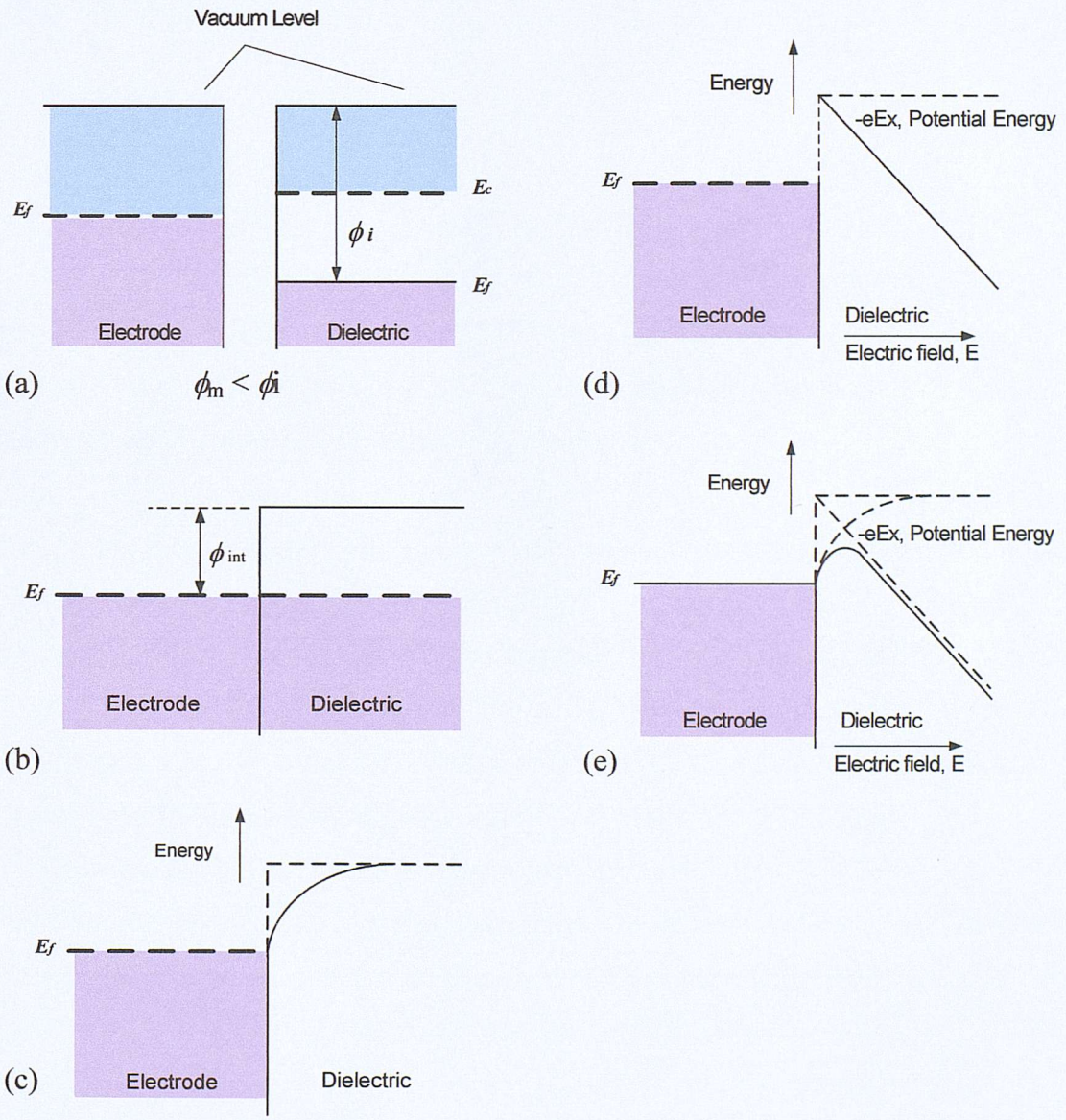

Figure 2.7(a) to (e). Modification of the potential barrier at an electrode-polyethylene ohmic interface by an applied electric field.

2.3.3 Homocharge and heterocharge

The uniform electric field may be expressed mathematically as

$$\frac{dE}{dx} = \frac{d^2V}{dx^2} = 0 \tag{2.2}$$

where E is the electric field and V is the applied voltage. If however, an additional charge density ρ C/m^3 is present in the element of width dx, the electric field is no longer constant between x and $(x+dx)$. Gauss' theorem defines the change in field, for a material of relative permittivity ε_r as

$$\frac{dE}{dx} = -\frac{\rho}{\varepsilon_0 \varepsilon_r} = \frac{d^2V}{dx^2} \tag{2.3}$$

which is known as the Poisson's equation. So that the change in the field is directly proportional to the density of the additional space charge. The space charge can be of either sign and hence either increase or decrease the electric field, but within a system with a fixed applied voltage, we can expect both an increase and a decrease in the field with the average field remaining constant.

There are two possible types of accumulated space charge within the bulk of a polymeric material, namely "homocharges" and "heterocharges". As shown in figure 2.8, the average uniform applied field, E, is given by V/d (d is the thickness) when no charge is present in the dielectric. Suppose that homocharges are injected from both electrodes; the electric field at the interface of the electrodes is lower than the average field E, while the field in the bulk becomes higher. Homocharges are initiated by charge injection at the electrodes and hence dependent upon the electrode-dielectric surface contact, temperature, applied field and the polarity. Polarity is a factor to consider for the reason that some metal may inject carrier of only one sign (either positive or negative), while others will support bipolar injection.

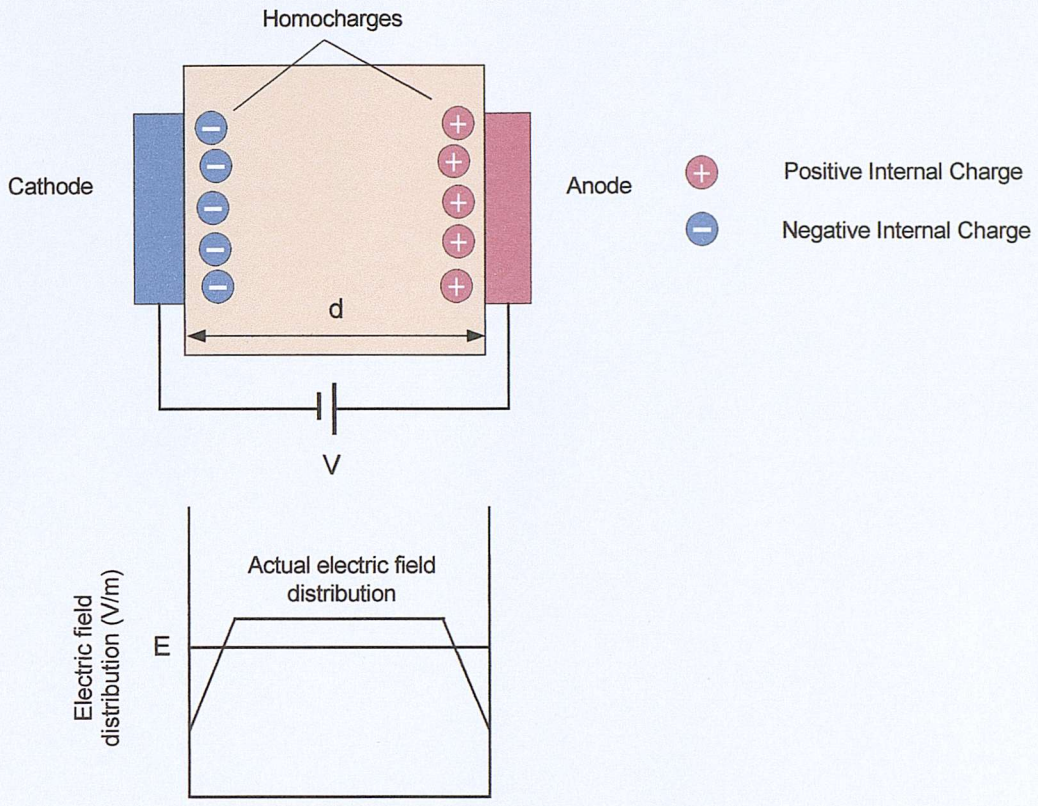

Figure 2.8. Electric field distribution of a dielectric with homocharges.

Given ample time, the injected carriers will be transported across the dielectric under DC electric stress, where they might recombine with injected charge of the opposite polarity or be extracted. Replenishment of homocharge density will then occur by means of repetitive charge injection from the electrode. The resultant space charge distribution will rely upon the relative magnitude of the injection efficiency, trapping time, recombination efficiency and transit time. When transit and recombination time are higher compared to the injection time, space charge may constantly build up in the bulk of the material and the dielectric will only approach the equilibrium condition very slowly. It may even be possible that no equilibrium state can be achieved and insulation will fail after some time.

Heterocharges shown in figure 2.9 may appear in a dielectric when one of the electrodes partially blocks the extraction of mobile charge injected by the other. Heterocharges can also occur when ionic carriers are supplied through the process of ionisation from impurities in the bulk where additives (antioxidants, antistatic agent

etc.) and by-products from the crosslinking reaction (acetophenone etc.) are the predominant sources of heterocharges.

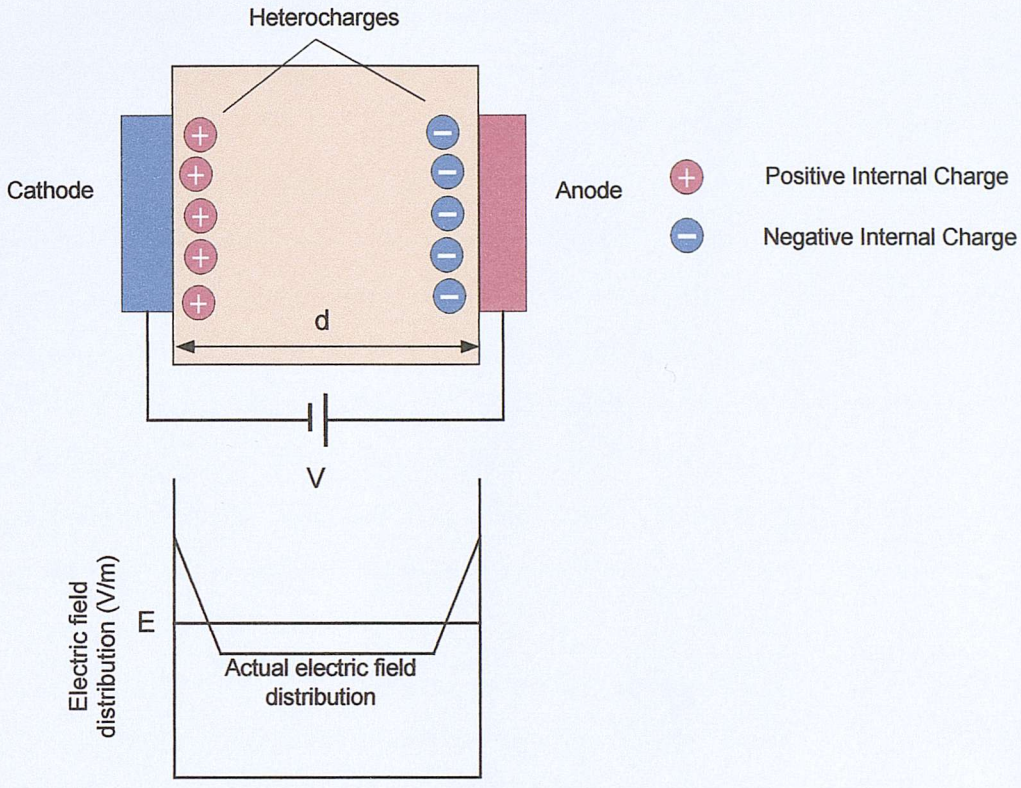

Figure 2.9. Electric field distribution of a dielectric with heterocharges.

2.3.4 Role of electrode material

An electrode is essential to assure the application of electric stress in measurement of electrical properties. Various electrodes such as vacuum evaporated metals and conductive paste are used. However, these electrodes are not seen in power cables, a semiconductive layer called 'strand shield' exists between the metal conductor and the insulation layer. Therefore, the use of a semiconductive electrode [28-30] made of the semiconductive compound used for the strand shield may be necessary to simulate the cable situation best.

Different electrical behaviour depending on the type of electrode is frequently observed. For instance, several researchers have reported that semiconductive electrode enhances carrier injection into polymeric insulation [31-33]. F. Chapeau et

al [34] have found that homocharges are developed in polyethylene with a vacuum evaporated metal electrode whereas heterocharges are accumulated with a conductive silicon grease electrode. T. Ditchi et al [35] have also reported that the composition of the semiconductive compound used as an electrode may be critical in determining the internal charge distribution in XLPE. Furthermore, K. S. Suh et al [32] revealed that with various contacts, such as aluminium, silicon oil and semiconductive film, aluminium shows the lowest current density, silicon oil the highest and semiconducitve film lies in between. They had also carried out tests to show the difference in potential barrier between the three materials consisting of aluminium, semiconductive film and silicon oil. These tests suggested that conduction is the result of injection of excess carriers from an ohmic contact into material depending on the level of potential barrier (higher the energy level, the more difficult for carrier injection and penetration into the bulk). The concentration of carriers builds up near the injecting contact leading to the reduction in current.

The above few examples of the many cases presented [36-38] clearly demonstrate that the electrode materials have significant effect on the charge carrier injection behaviour. This will subsequently affect charge trapping and transportation in the material.

2.3.5 Role of impurities in dielectric

Many researchers have reported that residual by-products formed by the crosslinking reaction encourage the formation of heterocharges. T. Mizutani [36] discovered that large amount of by-products and/or low applied fields resulted in hetero space charge in XLPE. N. Hozumi et al [39] demonstrated that the presence of acetophenone does not directly lead to heterocharge formation but heat treatment at 150°C in the presence of acetophenone can cause the formation of heterocharge when a DC voltage is applied. K. S. Suh et al [32] has also proven that when by-products were removed by vacuum degassing, heterocharge was also diminished. As for antioxidants [40] it had been made known that they have the effect of prohibiting the formation of heterocharges and T. Mizutani et al [41] disclosed that they tend to enhance the carrier injection and/or transport which tallies with what K. S. Suh et al

[40] had registered. The effect of water absorption on the formation of space charge has been carried out by S. Fujita et al [42] in Polyimide, it has been shown that as immersion time of specimen in distilled water increases, the charge moved more easily into the specimen on the application of the bias voltage.

All the above indicated that the impurities created either by crosslinking reaction or added additives had actively participated in space charge formation.

2.3.6 Trapping and detrapping

At the electrode-dielectric interface, the energy band diagram is complicated by the presence of physical, chemical and electrical defects such as: surface roughness, imperfect contact, chemical impurities including oxidation and moisture, dangling bonds, local polarisation resulting in band bending and trap states. The effect of the above is to create trapping states on the surface of the polymer.

In general, there are a great number of trapping levels in the forbidden energy gap in a dielectric. These trapping levels consist of many localised states, which may act as traps or recombination centres. Some traps will capture only negative charges while some will capture only positive charge. Others, however, will be able to trap either polarity of charges and may act as recombination centres. They are mainly due to imperfections caused either by structural defects or impurities or both.

On the basis of the energy levels of traps, the traps can be classified into shallow traps and deep traps [11]. The so-called shallow traps refer to the traps whose energy levels E_{tse} are located above the discrete mono-energetic system Fermi level E_f for electron traps and refer to the traps whose energy level E_{tsh} are located below the discrete mono-energetic system Fermi level E_f for hole traps. Conversely, if E_{tde} is below E_f or E_{tdh} above E_f, these traps are called deep traps. The defined shallow and deep traps energy levels here are generally applicable to semiconductors. Figure 2.10 (a) and (b) show schematically these two cases.

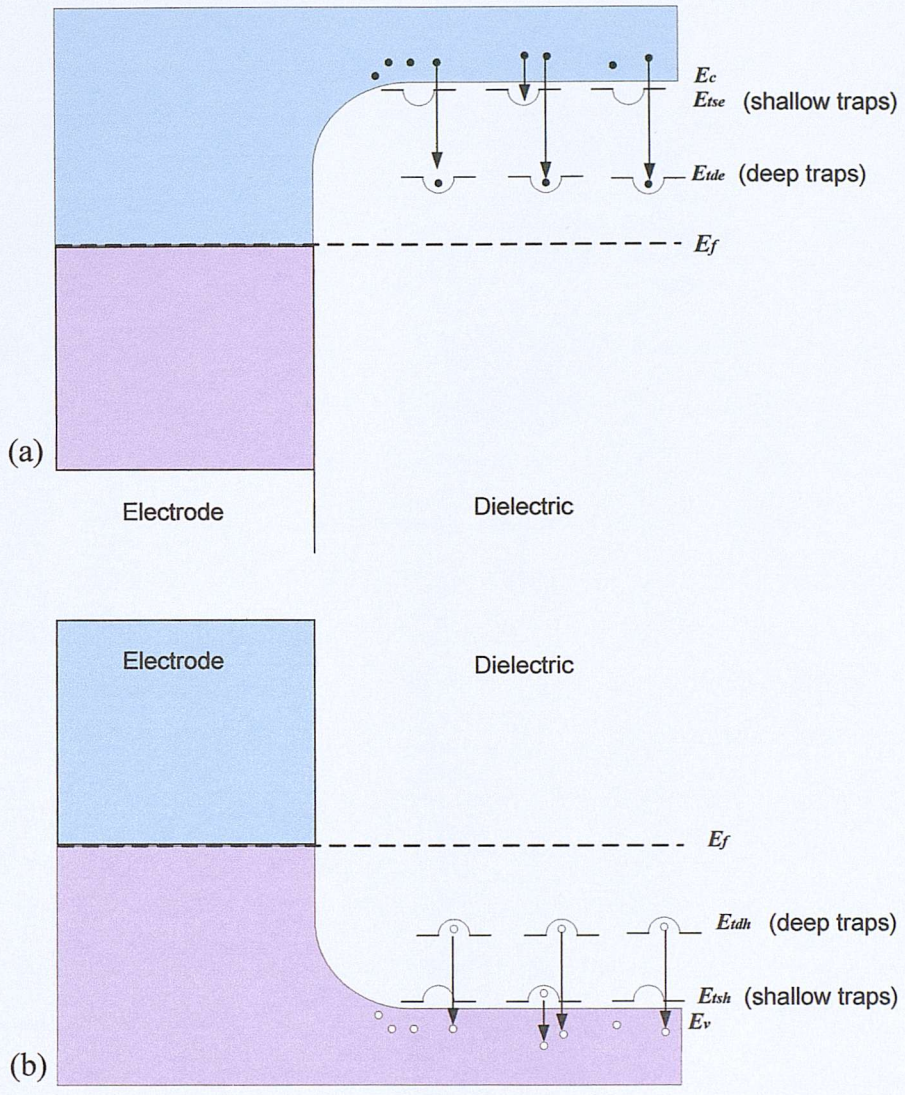

Figure 2.10. Schematic energy level diagram for (a) ohmic contact with shallow and deep electron traps, and (b) ohmic contact with shallow and deep hole traps.

Thermally stimulated current (TSC) [43, 44] is a typical application used to prove the trapping and detrapping process in dielectrics. The trap depth of polyethylene can be classified into:

(a) Shallow trap is located in the region of 0.1eV to 0.3eV below conduction band, having a concentration of 10^{24} traps/m^3[45].

(b) Deep trap is located in the region of 0.8eV to 1.7eV below the conduction band, having a concentration of 10^{20} traps/m^3[45].

The accumulation of space charge depends on the availability and nature of the traps. In fact, the process of space charge accumulation is the result of a competition between trapping and detrapping rate.

2.4 Electrical conduction mechanisms in polymers

Generally, electrical conduction occurs through the movement of either electrons, holes or ions. In addition, conduction strongly depends on carrier concentration and the injection of charge from the electrodes. Usually, assumption is made that at steady state, the current is controlled by either electrode or bulk processes. The different mechanisms may be active at the same time, but usually one mechanism is dominating. The following will discuss the various electrical conduction mechanisms. When a high electric stress is applied to a piece of polymeric material, charge movement commences. These charges can originate either from the electrodes or within the bulk of the material. There are a few aspects to look into regarding charge generation and transportation, it includes: -

(a) The penetration and extraction of electrons or holes at the electrode-dielectric interface. These processes very much rely on the types of interface. In other words, the work function of the materials and the surface defect of the dielectric. Basically, there are two such processes, Schottky and Tunnelling.

(b) The process whereby electric field assisted dissociation of chemical content such as by-products produced by the crosslinking agent, additives and other impurities in the bulk of polymer material, i.e., ionisation.

(c) Charge migration within the bulk polymeric material, e.g., hopping process.

2.4.1 Electrode-limited processes

The energy-band diagram of a blocking contact shows that the work function of the electrode is greater than the dielectric. Thus the rate of flow of electrons will be limited by the rate at which they flow over the interfacial barrier; hence the conduction process is electrode-limited. If the dielectric is sufficiently thin, the predominant contribution to the current is derived from electron tunnelling through

the dielectric potential barrier. For thicker films and deeper traps the current will be due to electrons thermally excited over the potential barrier.

A. Schottky injection [46]

Considering the potential barrier at the electrode-dielectric interface, Schottky injection mechanism arises from field assisted thermionic injection of electrons from an electrode into the conduction band of the dielectric. When the potential barrier is too thick to permit tunnelling to occur, the current flowing through the dielectric is limited by the rate at which electrons are thermally excited over the interfacial potential barrier into the dielectric conduction band. This type of electron emission from the metal is made possible by the applied field which lowers the barrier height and increases the probability of emission, see figure.2.11.

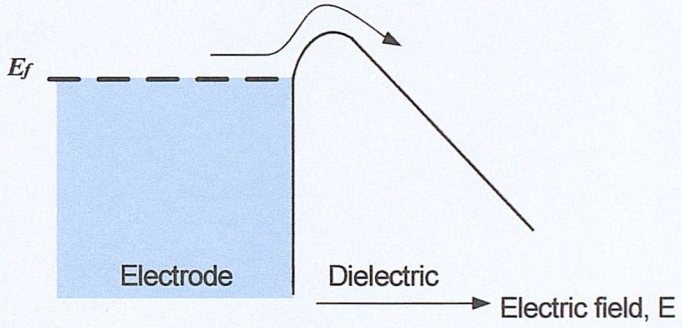

Figure 2.11. Diagram of Schottky electron-transfer mechanism separated by a potential energy barrier.

The expression for Schottky injection is:

$$J = A(1-R)T^2 \exp\left(-\frac{\phi_{int}}{k_B T}\right)\exp\left(\frac{\beta_{sc} E^{1/2}}{k_B T}\right) \qquad (2.4)$$

where $\beta_{sc} = \left(\frac{e^3}{4\pi\varepsilon_o\varepsilon_r}\right)^{1/2}$

J = current density,

e = electron charge,

A = Richardson-Dushman constant,

R = reflection coefficient depends on the actual barrier shape,

T = temperature,

ϕ_{int} = potential barrier height at the interface,

k_B = Boltzmann constant,

E = electric field

ε_o = permittivity of free space and

ε_r = relative dielectric permittivity.

B. Fowler-Nordheim injection [47]

Consider a conducting region touching a dielectric film, see figure 2.12. If the barrier is thin enough, electrons can flow through the barrier from the conducting region by quantum mechanical tunnelling. This tunnelling effect which is known as Fowler-Nordheim injection will only occur at very high fields in the dielectric (~10^9 V/m). The applied high voltage will reduce the barrier thickness to a sufficiently small value (<~10nm).

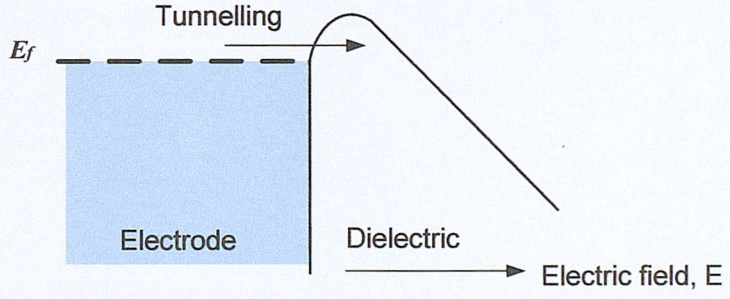

Figure 2.12. Diagram of Fowler-Nordheim electron-transfer mechanism separated by a potential energy barrier.

The Fowler-Nordhiem injection current density equation is given as:

$$J = \frac{e^3 E^2}{8\pi h \phi_{int}} exp\left\{-\frac{4}{3}\left(\frac{2m}{\hbar^2}\right)^{1/2} \frac{\phi_{int}^{3/2}}{eE}\right\} \qquad (2.5)$$

where h = Planck's constant,

m = longitudinal electron mass in an dielectric and

$\hbar$ = h/2π

2.4.2 Bulk-limited processes

When the conduction is limited by the rate at which electrons can flow through the bulk of the dielectric, rather than the rate that they are supplied by the electrode; the conduction process is bulk-limited. The conduction mechanisms in the bulk under the influence of high applied electric field include space charge limited current (SCLC) and Poole-Frenkel effect.

A. Space charge limited current (SCLC) [48, 49]

SCLC arises from the study of electrical conductivity from the injection and transport of extrinsically generated charge carriers in dielectrics. The current becomes limited by space charge injected from the electrode. The current flowing through the electrodes will then depend on the charge concentration, the type of charge, the injecting properties of the electrodes, the mobility of the charge carriers and the trapping characteristics of the dielectrics. Investigation concerning electrical conduction in dielectrics has found a relation of power law dependence between the current density J and electric field E.

Given

$$J = a E^n \tag{2.6}$$

where a is a constant and n the power index.

Applying log to both sides, equation 2.6 becomes

$$\log J = \log a + n \log E \tag{2.7}$$

Various conduction mechanisms are characterised by different values of n. In the case of n=1 (ohmic conduction) is usually the result of field independent values of the carrier concentration and mobility.

SCLC is derived from a mathematical model. This is derived given an electrode-dielectric system with an ohmic contact (work function of the injecting electrode is smaller than the material being injected) where it is possible to inject charge carriers in excess of those intrinsically present in the polymer. If the mobility

of the dielectric is low and may be unable to transport all the injected charge, in other words, the injecting rate is much greater than transportation, the concentration of carriers will build up near the injecting contact and neither the charge carrier density nor the electric field remain constant across the specimen therefore reduces the current.

In the case of trap-free material:

$$J = \frac{9}{8}\frac{\varepsilon_o \varepsilon_r \mu V^2}{d^3} \tag{2.8}$$

where μ = mobility,

V = applied voltage,

d = thickness and

in this case power index, n, is 2.

In the presence of traps

$$J = \frac{9}{8}\frac{\theta \varepsilon_o \varepsilon_r \mu V^2}{d^3} \tag{2.9}$$

where θ is the fraction of total charge which are free.

Figure 2.13 shows a graph of current density versus voltage for an ideal case of SCLC. From this log(J) versus log(V) plot, there are four relations between the voltage and current density, they are being explained as:

(1) $J \alpha V$ = ohmic conduction (n = 1)

(2) $J \alpha V^2$ = trap-limited SCLC (n = 2)

(3) $J \alpha V^{\infty}$ = all traps filled up (n = ∞)

(4) $J \alpha V^2$ = trap-free SCLC (n = 2)

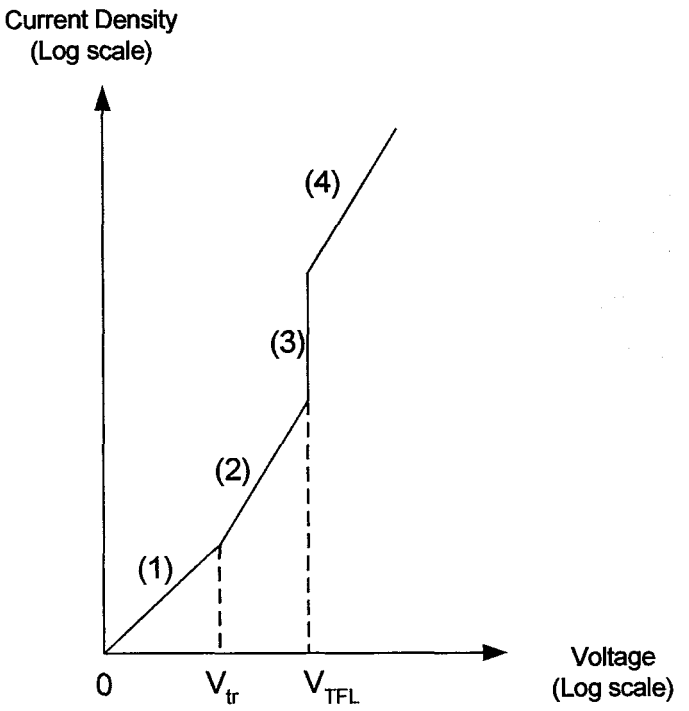

Figure 2.13. Graph of current density versus voltage for an ideal case of SCLC.

In practice, with large distributions in band structures and energy of traps, the trapped-filled limit (V_{TFL}) is not well defined and the distinction between trap limited SCLC and trap free SCLC therefore usually becomes blurred and the ideal relationship described is seldom observed in polymers.

According to the transient SCLC theory [48, 49], a current peak occurs when the injected charge front reaches the counter-electrode and the transit time t_r is given by

$$t_r = \frac{0.786\, d^2}{\mu V} \tag{2.10}$$

An example of the transient SCLC characteristic graph is shown in figure 2.14.

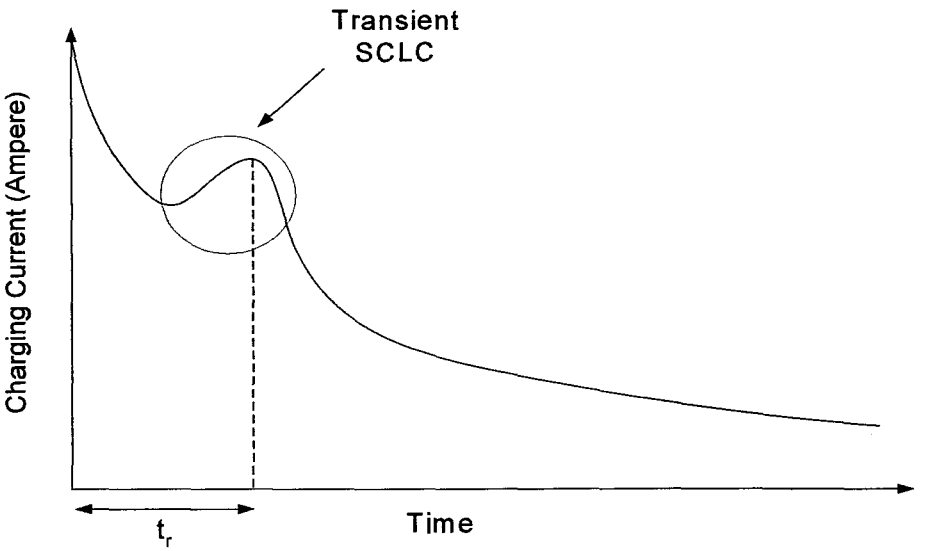

Figure 2.14. A typical transient SCLC characteristic graph.

B. Poole-Frenkel conduction [50]

This effect involves a mechanism, which is very similar to the previously described Schottky effect, except that is applied to the thermal excitation of electrons from traps into the conduction band of the dielectric as shown in figure 2.15.

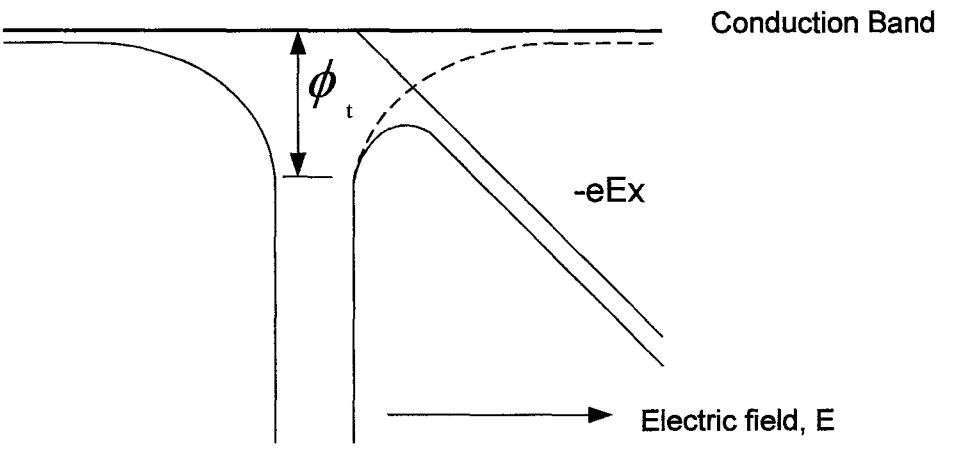

where ϕ_t = Barrier height to enter conduction band

Figure 2.15. The lowering of the potential-energy barrier due to an external electric field.

The Pool-Frenkel conductivity is field-dependent and of the form:

$$J = \sigma_o \exp\left(\frac{\beta_{PF} E^{1/2}}{2k_B T}\right) E \tag{2.11}$$

where $\beta_{PF} = \left(\frac{e^3}{\pi \varepsilon_o \varepsilon_r}\right)^{1/2}$ and

σ_o = a constant.

2.4.3 Hopping conduction [51]

In dielectrics conduction is most likely to be a thermally activated transfer between localised sites. Conduction via localised states implies discrete jumps across a potential barrier from one site to another; by thermally excitation, refers to figure 2.16. The relative importance of this mechanism depends on the shape of the barrier and the availability of thermal energy.

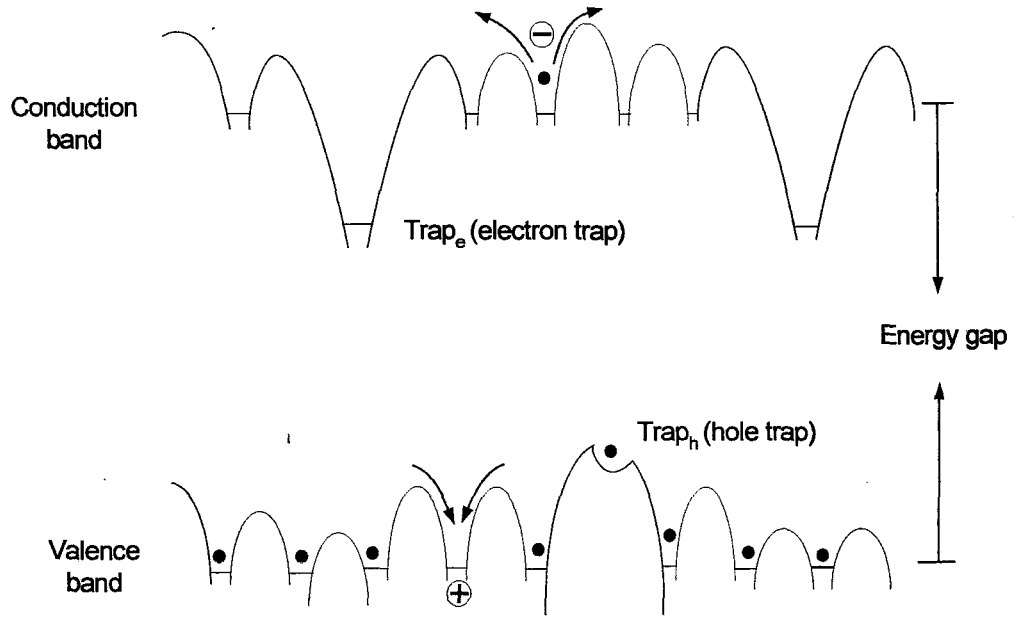

Figure 2.16. Diagram of charge-transfer mechanisms between adjacent sites separated by potential energy barriers.

The expression of current density, J, for hopping conduction is:

$$\boldsymbol{J = e\, n\, \ell\, f^{*}} \tag{2.12}$$

where $$f^{*} = \frac{1}{m}\frac{(k_B T)^3}{h^3 \nu^2} exp\left(-\frac{\phi_{int}}{k_B T}\right) exp\left(\frac{e\,E\,\ell}{2k_B T}\right)$$

n = charge per unit volume,

ℓ = hopping distance,

ϕ_{int} = potential barrier height at the interface,

f^* = hopping frequency and

υ = vibrational frequency in the two directions perpendicular to the direction of jump.

Chapter 3

Newly Improved PEA System and Other Space Charge Detection Techniques

3.1 Introduction

Polymers are used as electrical insulators because of their economic value. They usually display very high breakdown strengths (generally up to 10^9 V/m), wide range of mechanical toughness, pliancy of plastics, corrosion resistance and simplicity of manufacturing. The fabrication and usage of high voltage direct current (HVDC) cables with dielectrics cause the formation of space charges. Space charges are charge carriers (either positive or negative) formed either by injection at electrode-dielectric interface or ionisation of dissociable species in polymer. Under the influence of electric field, they might stay within or travel through the bulk. These charge formation processes may occur simultaneously and it is often difficult to verify which process is dictating. The consequence of such behaviour weakens the performance of the cable and lead to eventual breakdown [52]. Space charge formation very much depends on the condition of the conducting and insulating materials themselves, the condition of the interface between the conducting and

insulating materials and additives to the insulating materials. It also relies upon the applied field and temperature.

PE is one of the most commonly used insulation in high voltage power cables. A long history of space charge formation in polyethylene material had been reported. The space charge behaviour in PE seems rather complex. Changes in any combination of the test conditions, e.g. temperature, stress level, amount of impurities, type of impurities and moisture etc., might cause a change of result and therefore an entire different hypothesis can be deduced.

Even in a situation where the applied field is lower than the breakdown field of the material, charge migration and injection can lead to internal fields larger than the applied one. This creates destructive discharges in the material that affect the electrical performance and also shorten the lifespan of the cable. For PE power cable where crosslinking is achieved by radiation, one of the processes for cable production includes polyethylene irradiated with electron beams to improve their mechanical and thermal properties. Although precautions are taken to reduce accumulated charges, some of it still remains after processing. Thus, when these cables are put in operation, the remaining charges may distort the normal electric field distribution in the insulated materials and cause electrical breakdown.

3.2 Non-destructive space charge measurement techniques

The fact that polymers tend to accumulate space charge under HVDC stress, these charges distort the electric field distribution and may result in reducing electrical breakdown strength of the dielectric. Improved electrical breakdown strength may be obtained by controlling the space charge accumulation such that a homogenous field distribution results or by reducing the amount of accumulated charges.

In order to achieve this, it is vital to enhance the understanding of space charge formation by measuring the space charge distribution within the dielectric. Direct measurement of space charges distribution in dielectric is a better way of understanding the conduction process and analysing the evolution of various

phenomena involved. For this reason, many attempts have been made to perform non-destructive measurement of the dynamic electric charge distribution [53-56]. In the following sections, we will discuss about the Pulsed Electro-acoustic (PEA) technique and the Pressure Wave Propagation (PWP) technique. According to the generation principles of the acoustic wave, the PWP technique can be classified as Piezoelectric Induced Pressure Wave Propagation (PIPWP) method and Laser Induced Pressure Pulse (LIPP) method. In our case, PEA technique was chosen to carry out tests because of its simplicity in construction as it uses few materials and high resolution can be achieved.

3.2.1 Laser Induced Pressure Pulse (LIPP) technique

Figure 3.1 shows a schematic diagram of the LIPP measurement technique. A pressure pulse is generated by laser ablation when the impact of a short duration laser-light pulse irradiates the target. The propagation of this acoustic wave changes the amount of induced charges on the electrode creating a current in the external circuit which is monitored and treated to give the space charge distribution. For more details, refer to references [57, 58].

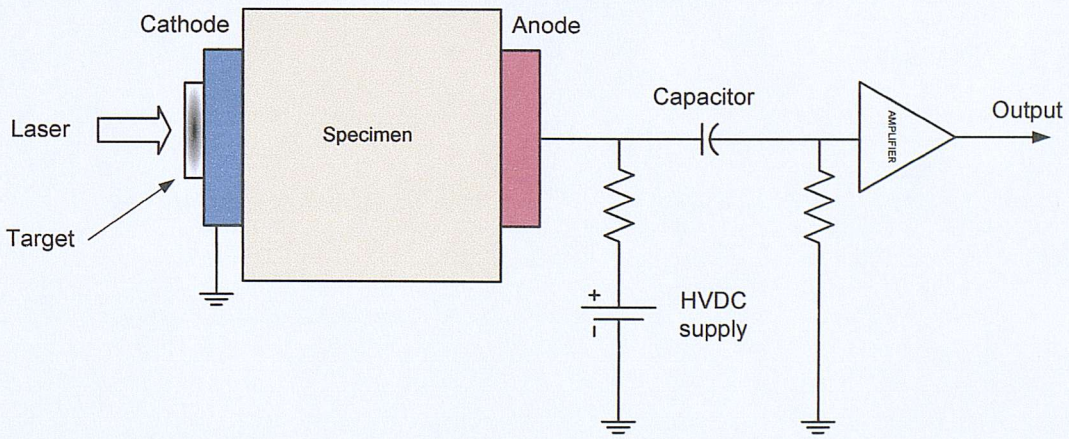

Figure 3.1. Schematic diagram of LIPP measurement technique.

3.2.2 Piezoelectric Induced Pressure Wave Propagation (PIPWP) technique

Figure 3.2 shows a schematic diagram of the PIPWP measurement technique. An electric pulse is applied to the transducer; it produces an acoustic wave which acts as a charge probe. The charge moves as the acoustic wave propagates through the specimen. This movement brings about a change of surface charge on the electrodes. The time signal of displacement current indicates the charge distribution in the specimen. By measuring the displacement current between the electrodes, the charge distribution can be obtained. Details can be found in references [59, 60].

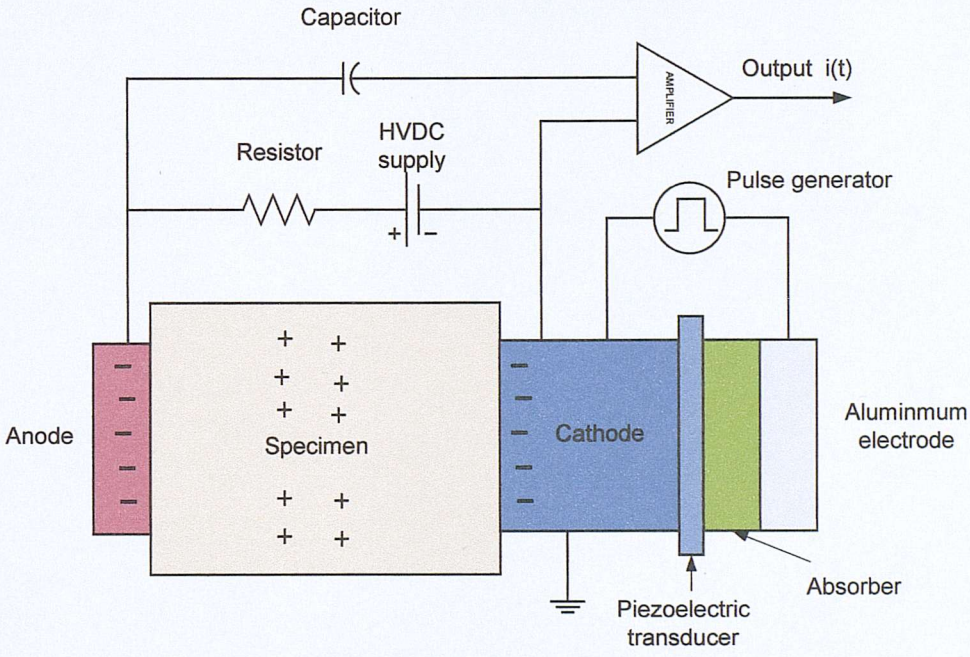

Figure 3.2. Schematic diagram of PIPWP measurement technique.

3.2.3 Pulsed Electro-acoustic (PEA) technique

The schematic diagram of a conventional PEA system is shown in figure 3.3. Figure 3.4 shows the schematic of the new improved PEA system, which allows the simultaneous current and charge measurement. To obtain a measurement an electric pulse of a few nano seconds width and few hundred volts amplitude pulse generator (PG) is connected across the specimen electrodes. The electric field pulse acts on space charges within the specimen to produce a mechanical stress with amplitude proportional to the local net charge density.

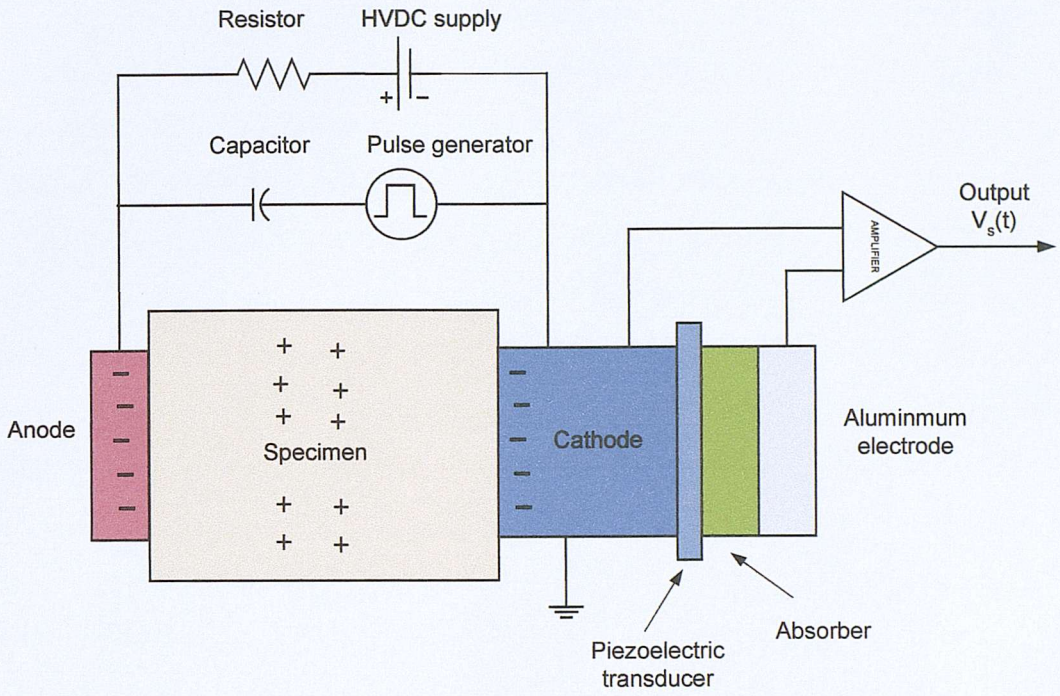

Figure 3.3. Schematic diagram of a conventional PEA measurement system.

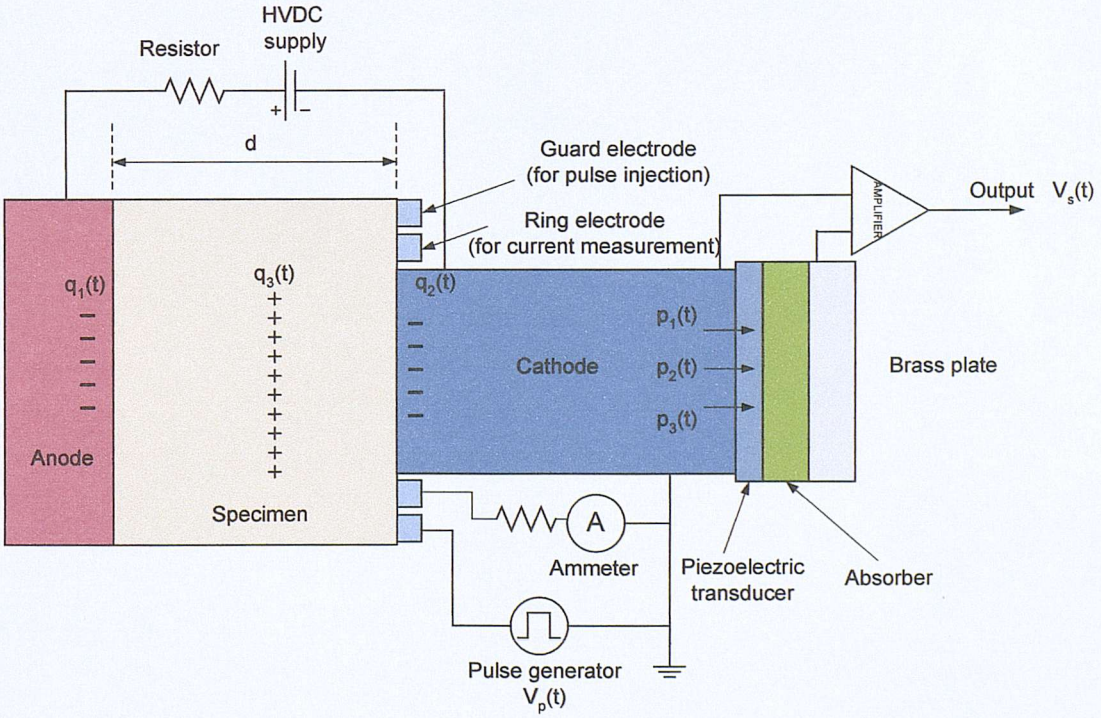

Figure 3.4. Schematic diagram of the newly improved PEA measurement system.

The basic principle of this technique can be explained using figure 3.5. Consider a plaque specimen of thickness d containing a layer of space charge q_3. The space charge q_3 induces image charge q_1 and q_2 on the anode and cathode respectively. In order to measure the space charge, an external voltage pulse $V_p(t)$ of short duration Δt is applied to the sample, producing an electric stress $e_p(t)$ across the sample. This applied pulse electric field $e_p(t)$ generates a perturbation force on each charge. This force causes charge q_1, q_2 and q_3 to move slightly. This movement launches acoustic waves p_1, p_2, and p_3, which propagate through the sample and cathode towards the piezoelectric transducer. The transducer detects the acoustic waves and transforms them into electrical signals, $V_{s1}(t)$, $V_{s2}(t)$ and $V_{s3}(t)$,which can then be read by an oscilloscope. The description given above is only a brief overview, for in-depth explanation refer to [61, 62].

The capacitance of the piezoelectric transducer together with impedance of the amplifier tends to attenuate low frequencies and this produces a typical high-pass filter response. The acoustic wave propagates through the sample will suffer losses due to the effect of attenuation and dispersion as most of the polymeric materials are of lossy and/or dispersive medium. Therefore, the collected electrical signals contained distorted space charge information. Deconvolution, attenuation and dispersion compensation and calibration techniques are needed to be applied to recover the real space charge data through digital signal processing. This will be discussed in section 3.5.

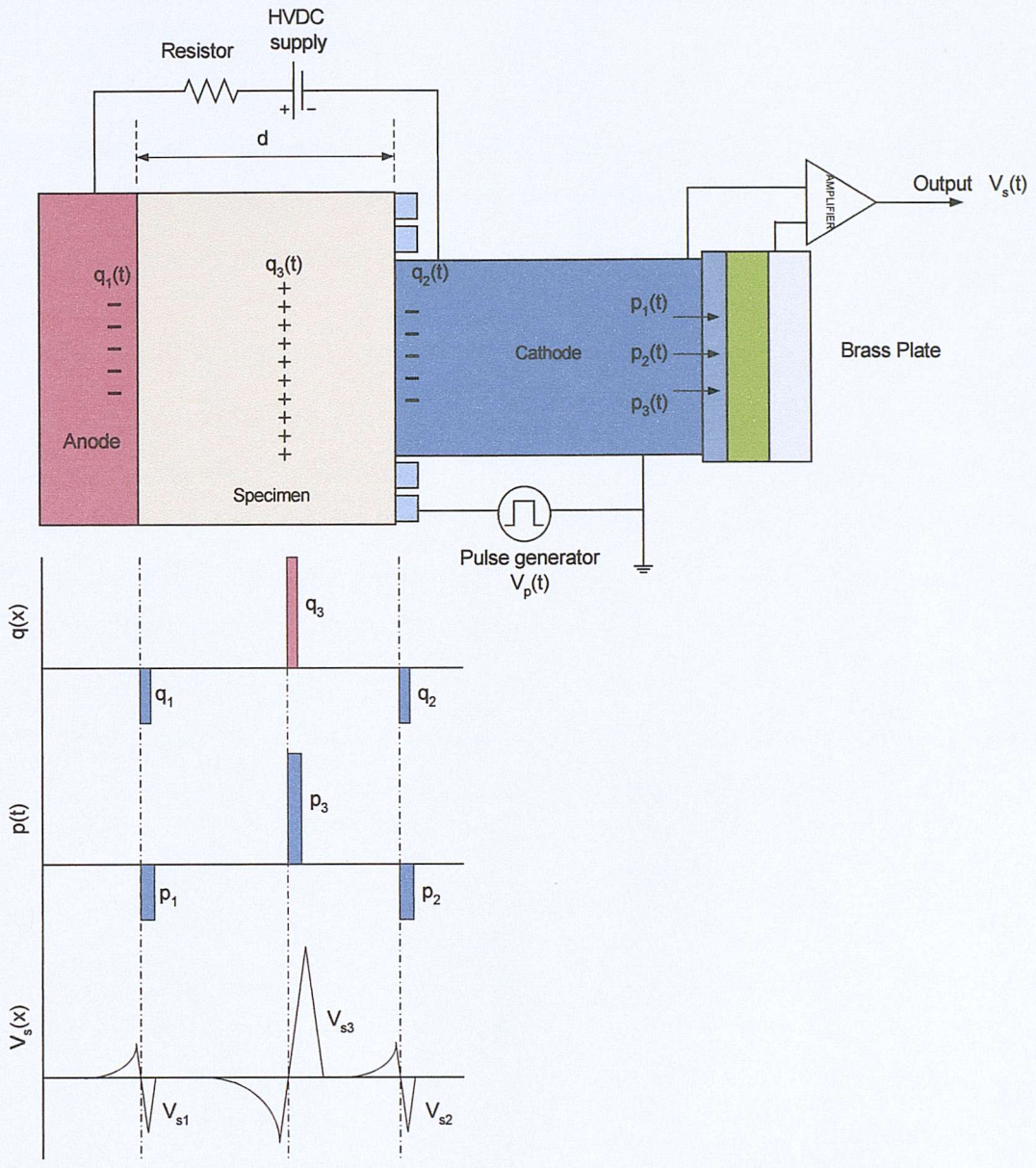

Figure 3.5. Basic principle of PEA measurement technique.

3.3 Newly improved PEA system

One of the main objectives of this research is to fabricate an improved PEA system that can detect not only charge profile but also current information simultaneously. With this piece of additional information, a better insight of conduction current in relation to the space charge distribution can be attained. The following sections will delve into the process of initial design, occurrence of unexpected complications, trouble-shooting the former, modifications and eventual setup.

3.3.1 Initial PEA system design

Figure 3.6(a) and (b) show different cross section views of our initial PEA system. The whole PEA system is mounted onto the door of an oven, this enables experiments to be carried out at a desired temperature.

A single connection is made between the top electrode (~90mm diameter) and high voltage supply through a 1MΩ charging resistor. A suitable value for the charging resistor can be any value range between 0.1MΩ to a few MΩ. The purpose of the charging resistor are to prevent pulse generated by the pulse generator from propagating along the high voltage lead and also to limit the current in case of specimen breakdown. Instead of having a HV capacitor as in the conventional PEA setup to isolate HV supply from the pulse generator network, in this case the specimen is acting as a capacitor. The top electrode is mounted within a tufnol-insulated shelter. Pressure is exerted onto the specimen through a spring-loaded top.

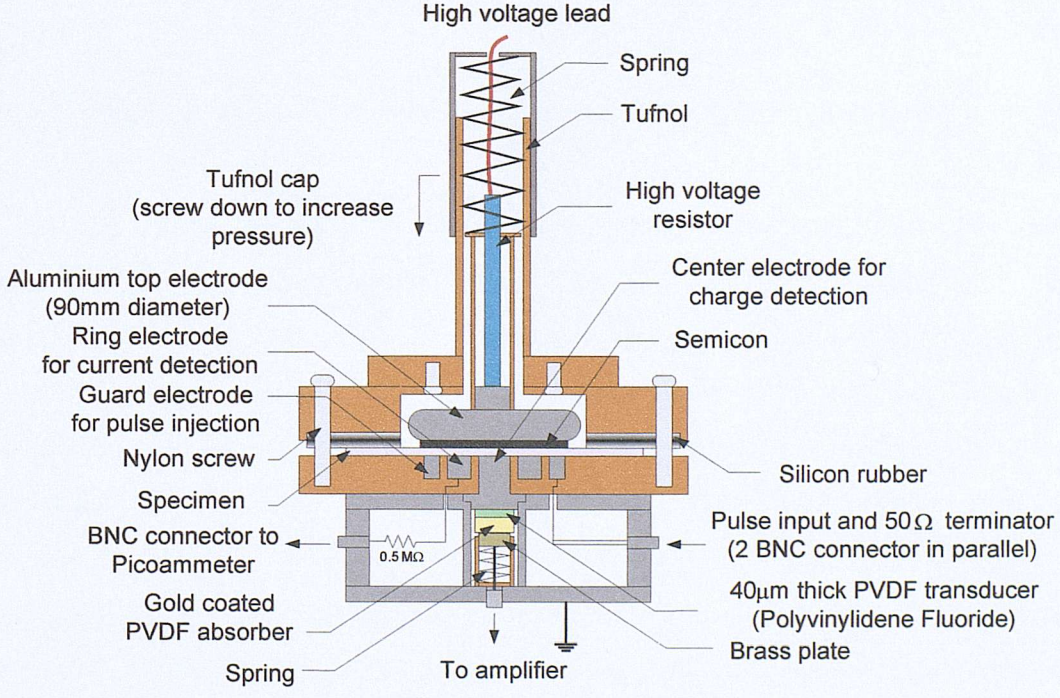

(a)

(b)

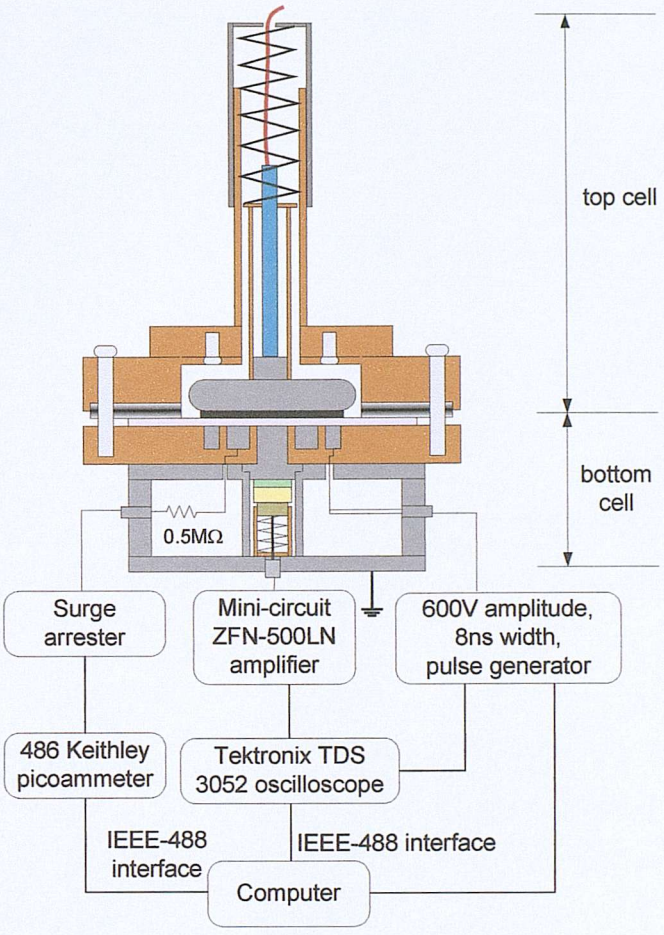

Figure 3.6 (a) and (b). Different cross section views of the initial PEA system design.

The main difference between a conventional PEA and this system is the electrically screened bottom cell made up of two concentric ring electrodes surrounding a central electrode. The outer ring also known as the guard ring is used as an electrode for pulse voltage application and to prevent the measurement of surface leakage current. The inner ring electrode is used for current detection, which is connected to a Keithley 486 Picoammeter via a 0.5MΩ limiting resistor and surge arrestor for current limiting purpose in case of specimen breakdown. This arrangement enables simultaneous measurement of charge and current on the same specimen. The amplitude of the electric pulse appearing across the top electrode and the bottom central electrode is given by:

$$V_c = \frac{C_{guard}}{C_{guard} + C_{specimen}} \times V_p \tag{3.1}$$

where V_c is the voltage drop across the specimen, C_{guard} is the capacitance formed by the guard electrode-specimen-top electrode, $C_{specimen}$ is the capacitance formed by the top electrode-specimen-bottom central electrode and V_p is the applied pulse voltage from the pulse generator. With $C_{guard} \approx C_{ring} \approx 10$ x $C_{specimen}$, effectively all the pulse voltage appears across the centre of the sample. C_{guard}, C_{ring}, and $C_{specimen}$ can be calculated using this equation:

$$C = \frac{\varepsilon_o \cdot \varepsilon_r \cdot S}{d} \tag{3.2}$$

where ε_o is the permittivity constant, ε_r is the relative permittivity of the material (2.3 for polyethylene), S is the area of the specimen and d is the thickness of the specimen.

The dimensions and arrangement of the guard, ring and centre electrodes of the designed system is shown in figure 3.7. Using equation 3.2 and making assumption that the specimen under test is about 100 μm thicknesses, therefore the calculated $C_{guard} \approx 227$pF, $C_{specimen} \approx 16$pF and $C_{ring} \approx 583$pF. The pulse generated by the pulse generator is about 600V magnitude and 8ns pulse width. Using equation 3.1, the calculated pulse voltage dropped across the specimen is about 560V. Figure 3.8 shows the partial equivalent electric circuit diagram of a specimen in the PEA system.

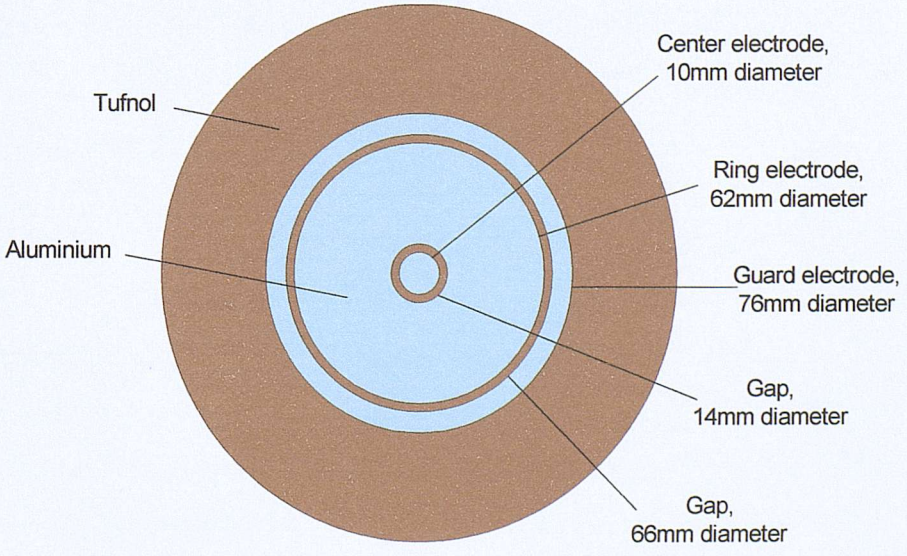

Figure 3.7. Dimensions of the centre, ring and guard electrodes of the PEA system.

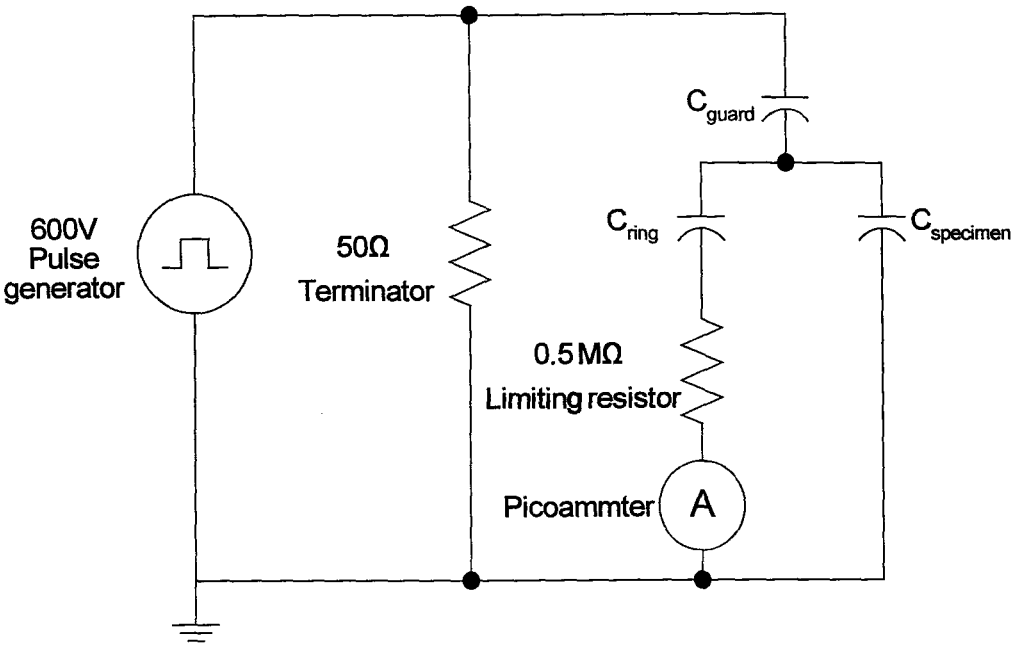

Figure 3.8. Partial equivalent electric circuit diagram of a specimen in the PEA system.

A Polyvinylidene Fluoride (PVDF) piezoelectric transducer is placed underneath the aluminium centre electrode. Another possible alternative to PVDF is Lithium Niobate piezoelectric transducer. The 40μm thick PVDF transducer used is reinforced by a PVDF acoustic absorber (to eliminate reflections of the acoustic waves) compressed together with a brass plate using a spring. This spring will ensure good contact even during thermal expansion when the whole cell is subjected to high temperature. The contacts between different parts must be flawless, without air pockets. It is necessary to use minimal silicon oil to bring the parts together and mirror-smooth surfaces of the metal parts.

A layer of semiconductive material is placed between the top electrode and specimen. This is to provide acoustic matching for the top electrode. The semiconductive layer used here is simulating the semiconductive layer used in cables between interface of conductor and insulation, also between insulation and metal sheath as a field-smoothing layer. There are two principals behind this, first of which is to equalize and reduce the electrical stress in the cable dielectric by preventing local field enhancement in non-homogeneous areas such as the individual wires of the conductor. The semiconductive layers eliminate the effect of the individual wires

on the field distribution, see figure 3.9. Secondly, to prevent the formation of gaps or voids between the voltage carrying-components of the cable (conductor, screen and metal sheath) and the insulation layer due to mechanical stress, e.g. bending of the cable or differential expansion of the various materials under varying thermal stress. A solid and permanent bond between the semiconductive layers and the insulation effectively prevents the occurrence of partial discharges, an essential feature in the case of polymer-insulated cables, which have no impregnating medium.

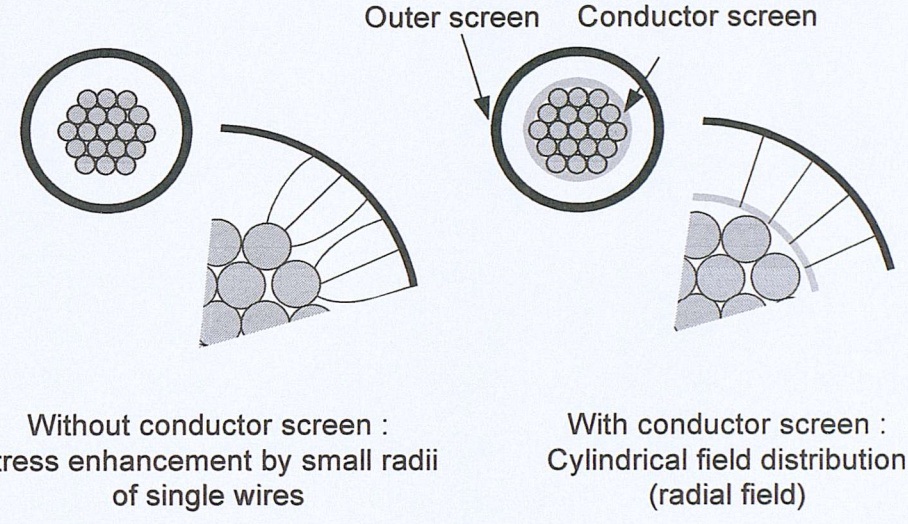

Figure 3.9. Principle of field equalization over a stranded conductor by using a semiconductive layer.

With the above-described PEA setup, an applied voltage of 1.6kV was applied to a 200μm thick LDPE specimen for a very short time to capture a measurement before any space charge formation is possible; the raw output signal (before any signal processing was performed) from the oscilloscope was obtained as shown in figure 3.10. It is a very noisy system with very significant noise level although it was captured after an averaging of 512 times to improve signal to noise ratio. Furthermore, it does not exhibit any of the characteristics of a conventional PEA setup such as the attenuation and dispersion factor between the first and second peak. There were ambiguous suspicions on the signal, which include (1) pulse passing through the specimen, (2) design of the top cell and (3) design of the bottom cell.

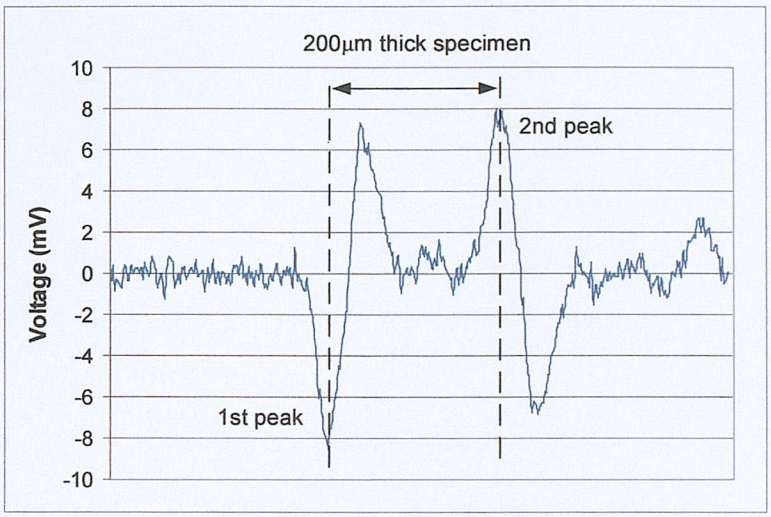

Figure 3.10. Output signal from the setup shown in figure 3.6(a) at 1.6kV.

So as to proceed systematically to analyse the rig, the system was splitted into parts, combined and tested with a conventional functioning PEA system. The aim was to make the system work like a conventional PEA and gradually work towards the desirable system. The next section shows tests carried out with different voltages and amplifiers, hence signals should not be compared in terms of magnitude but rather their characteristics.

3.3.2 Trouble-shooting charge measurement ability

A thorough and tedious procedure was commissioned to test and rectify the faults of the system. In order to clearly unfold the process, table 3.1 shows the summary of the steps taken; followed by detail systematic account of every step carried out. The type of specimen under tests is similar to those used in figure 3.10. All output signals presented here are prior to signal processing.

Step no.	Descriptions	Conclusions
1.	Conventional PEA system A.	System output signal is used as a reference
2.	Conventional PEA system A + newly improved PEA system B's pulse generator.	Show similar signal as to step no. 1. From this point onwards, system B's PG is employed for subsequent testing.
3.	Conventional PEA system A's top cell + newly improved PEA system B's modified bottom cell (replacing Tufnol, guard and ring electrode by an aluminium plate).	Severe oscillations throughout the specimen. Incorrect attenuation and dispersion factor.
4.	Arrangement similar to step 3, but with constant pressure evenly applied.	A clearer waveform, but oscillations in bulk prevailed. Applied pressure played an important part.
5.	Arrangement similar to step 4, but replaced system B's absorber by A	System B's absorber is in working order. System B's absorber will continue to be used from this step onwards.
6.	Arrangement similar to step 4, but replaced system B's 40μm thick PVDF transducer with a 9μm thick one.	Only single oscillation left in the bulk. Incorrect attenuation and dispersion factor. From now on, 9μm transducer is used.

Step no.	Descriptions	Conclusions
7.	Arrangement similar to step 6, but with further modification to system B's bottom cell (Replacing the two piece Aluminium bottom electrodes by one).	A similar response to step 1, therefore concluded that the only oscillation left in the bulk is unavoidable if more than one bottom electrode are to be used.
8.	Conventional PEA system A's top cell + newly improved PEA system B's original bottom cell (three concentric electrodes) and 9μm PVDF transducer.	A desirable response achieved. Attenuation and dispersion factor is correct.
9.	Arrangement similar to step 8, but replaced system A's top cell with modified system B's top cell where stronger pressure can be applied.	More oscillations were introduced, incorrect attenuation and dispersion factor. Problem might due to size of the top electrode.
10.	Modified system B's top and bottom electrode size.	A desirable response achieved. Deconvolution, attenuation and dispersion compensation and calibration is feasible.
11.	Further modification to system B's top cell to withstand long term constant pressure	A working PEA setup for charge measurement.

Table 3.1. Summary of steps taken for trouble-shooting charge measuring ability of the newly improved system.

Step 1

A cross section view of the existing conventional PEA system is shown in figure 3.11. An output from this system was recorded, see figure 3.12. Here, a clear low noise signal is obtained. The few features of a functioning PEA system raw output signal include (a) the overshoot nature of the signal caused by the conversion process of acoustic pressure wave to an electrical signal, (b) attenuation and dispersion trend exhibited by the 1st and 2nd peak, usually the magnitude and width of the 2nd peak is smaller (~60 to ~70%) and wider than the first peak. This signal is used as a reference for evaluation of the newly improved PEA system.

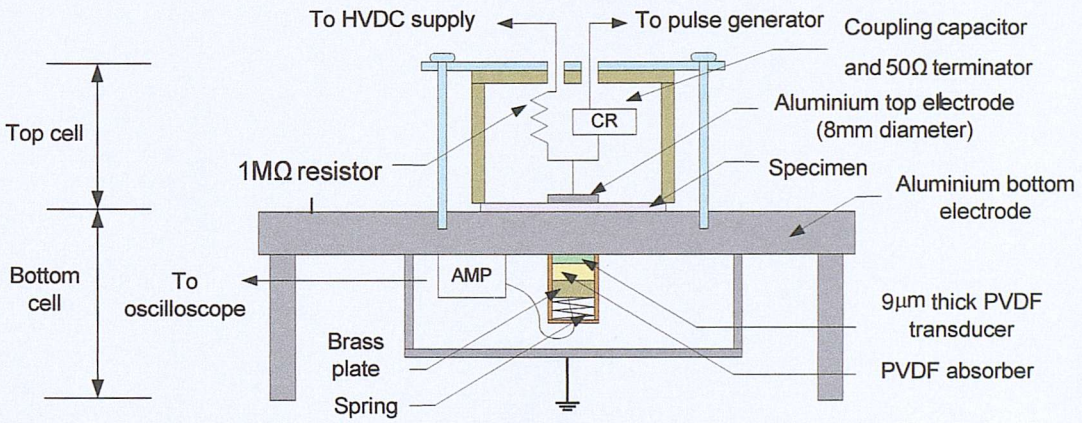

Figure 3.11. Cross section view of the conventional PEA setup.

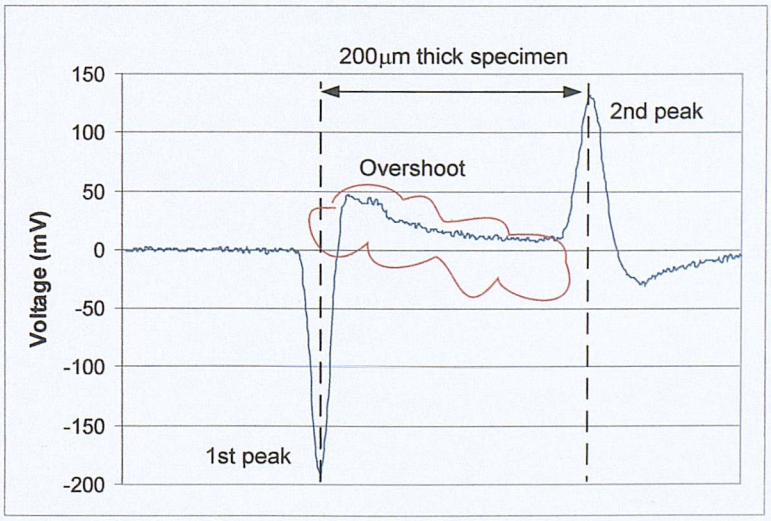

Figure 3.12. Output signal from the setup shown in figure 3.11 at 4kV.

The above system setup, figure 3.11, consists of its own pulse generator, high voltage supply etc. From now onwards, this system and its component will be named as A and the newly improved system and its components, figure 3.6, as B.

Step 2

The first aim was to eliminate the possible fault of the pulse generated by pulse generator B. Therefore system A's rig was setup with system B's PG and the response is shown in figure 3.13.

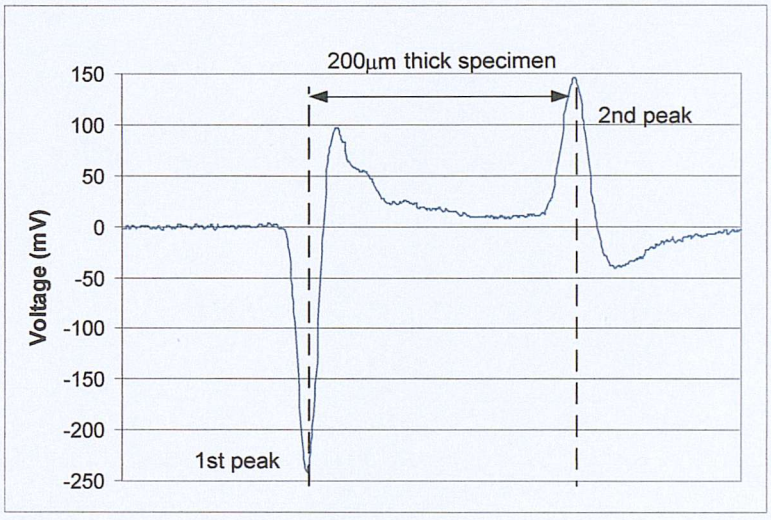

Figure 3.13. Output signal from the system A's rig with system B's PG at 4kV.

Signal displays a similar characteristic to figure 3.12. The conclusion drawn here was that the problem does not lie with the pulse passing through the specimen that was generated by system B's pulse generator. Therefore, system B's pulse generator is used for subsequent testing.

Step 3

The next step was to omit the flaw, which may arise from the design of the three separate bottom concentric electrodes of cell B. Details of the bottom cell B are magnified in figure 3.14. Modification was made by replacing the Tufnol insulating plate, guard and ring electrode with a piece of aluminium plate, refer to figure 3.15. Notice that the current measuring ability was removed; this is necessary to investigate if the separate concentric electrodes arrangement contributed to the undesirable response.

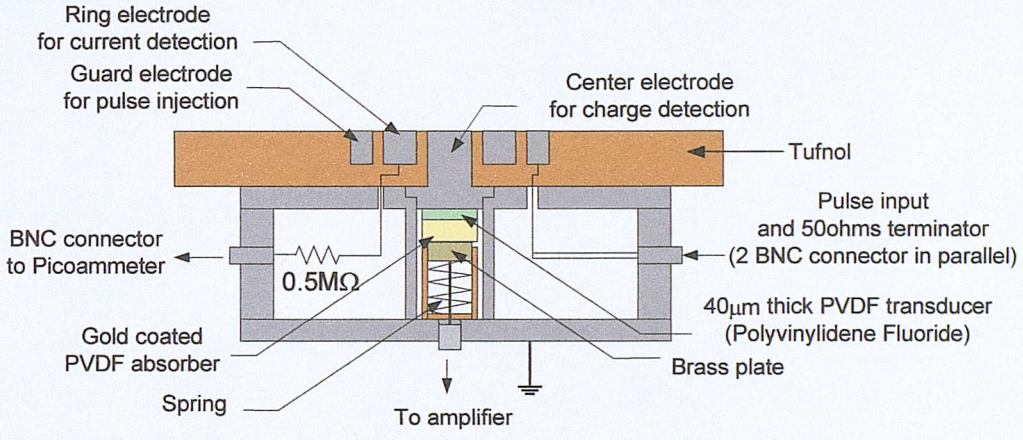

Figure 3.14. Magnified cross section view of the system B's bottom cell.

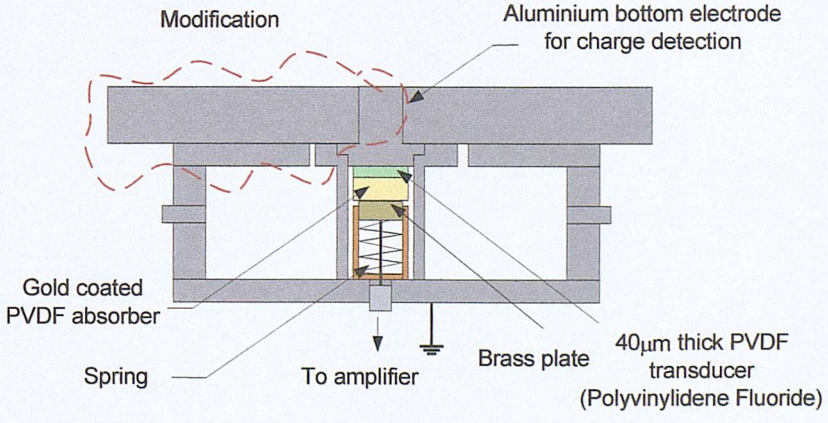

Figure 3.15. Cross section view of the modified system B's bottom cell.

Test was carried out with the system A's top cell and system B's modified bottom cell, see figure 3.16.

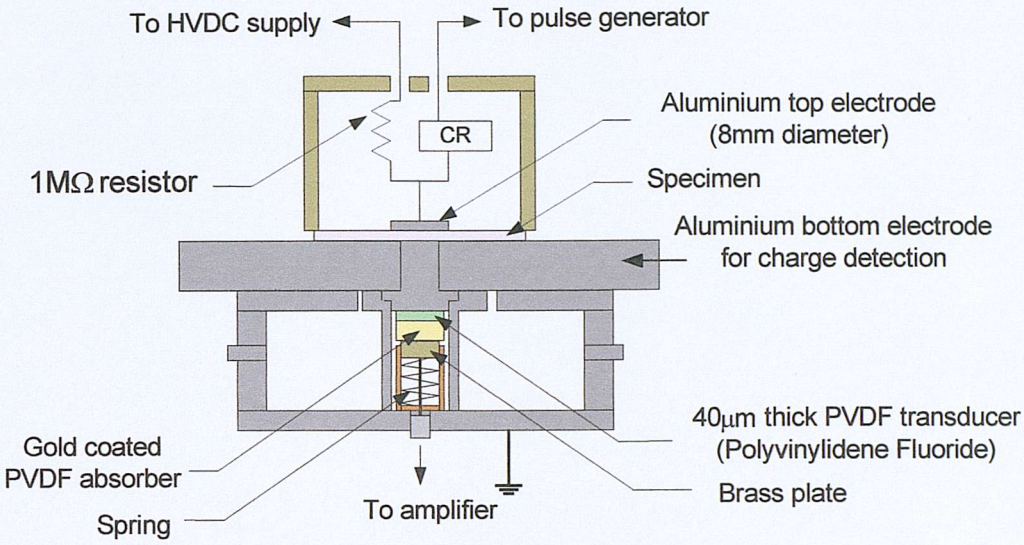

Figure 3.16. Cross section view of the system A's top cell with modified system B's bottom cell.

Much pressure was applied onto the specimen by pressing top cell A against bottom cell B and the response shown in figure 3.17 was obtained. Severe oscillations throughout the specimen were detected and illogical attenuation and dispersion factor between the 1st and 2nd peak.

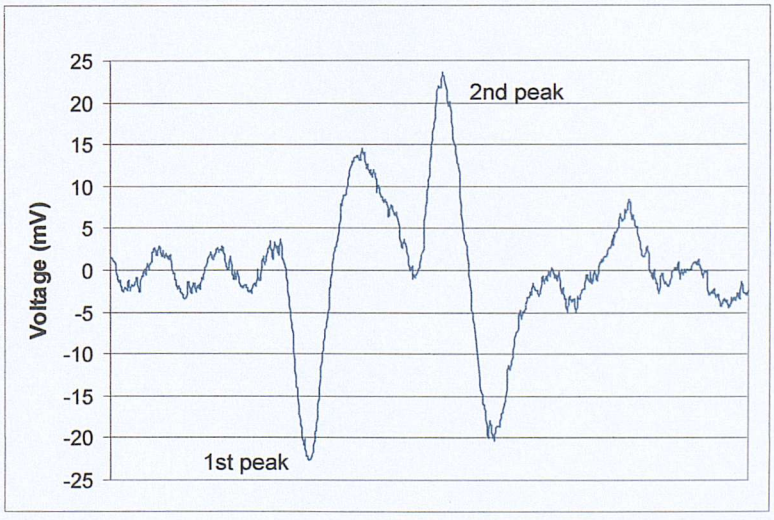

Figure 3.17. Output signal from the setup shown in figure 3.16 at 3.5kV.

Step 4

In addition, a constant pressure was evenly applied to the bottom cell B by sandwiching them between 2 metal plates as illustrated below, figure 3.18, output signal as shown in figure 3.19.

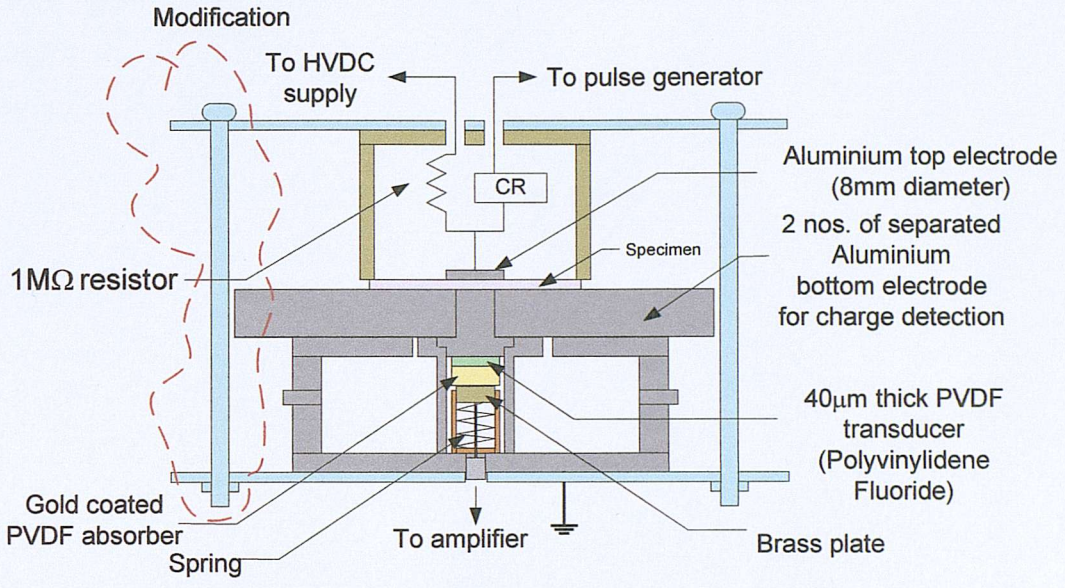

Figure 3.18. Cross section view of the system A's top cell and modified system B's bottom cell with a constant applied pressure.

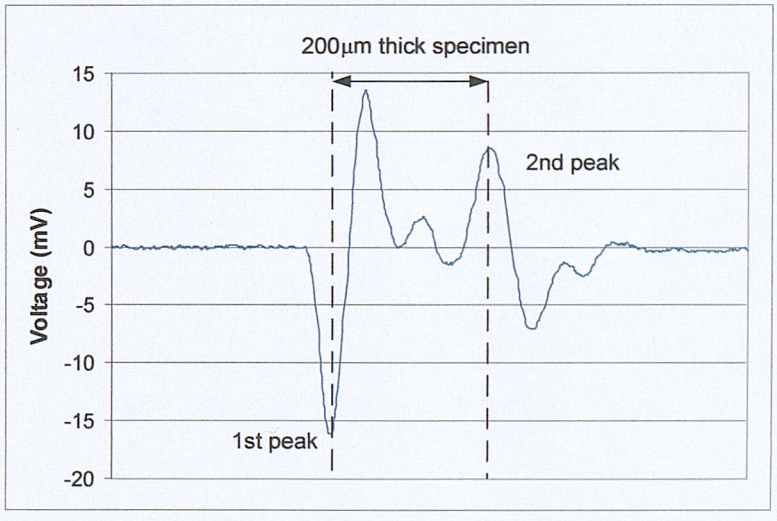

Figure 3.19. Output signal from the setup shown in figure 3.18 at 5kV.

A clearer waveform is observed despite oscillations in the bulk prevailed. This indicates that noisy waveform detected in figure 3.10 produced by our initial newly improved system B was probably caused by insufficient pressure being

exerted by the spring of top cell and noise is being generated between interfaces which eventually pickup by the transducer.

Step 5

Thereafter, the next immediate concern was the oscillations in the bulk of the specimen. By replacing PVDF absorber B with A, a result as shown in figure 3.20 is achieved.

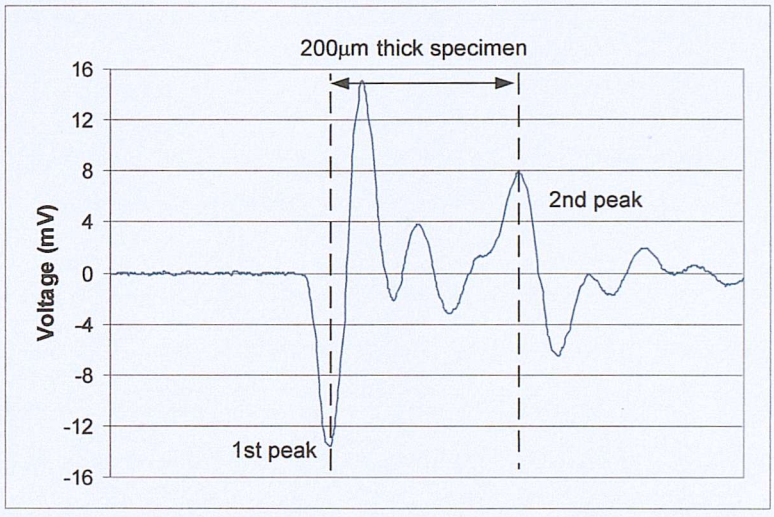

Figure 3.20. Output signal from the system A's top cell with modified system B's bottom cell and system A's PVDF absorber at 5kV.

Almost identical output is observed as with figure 3.19 and therefore the possibility of absorber defect was expelled.

Step 6

As the system A uses a 9μm thick transducer, therefore a 9μm transducer was used to replace B's 40μm thick transducer. The initial intention of using a 40μm thick transducer was hoping for a larger output signal. This change produces an outcome of figure 3.21.

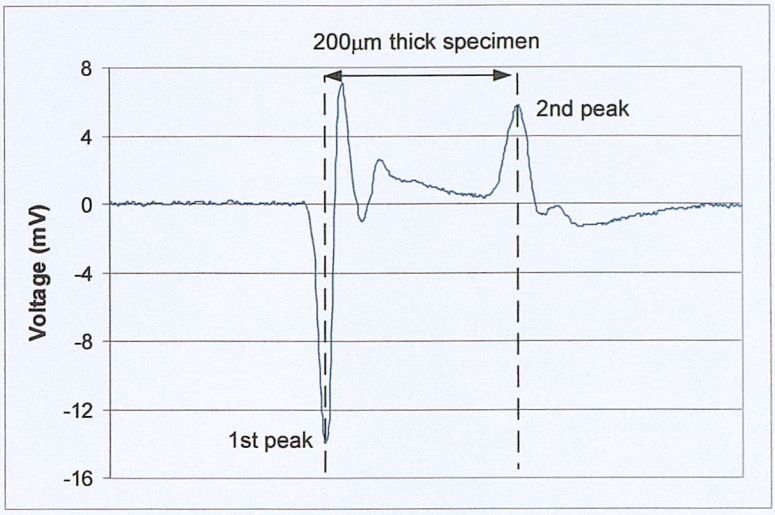

Figure 3.21. Output signal from the system A's top cell with modified system B's bottom cell using a 9μm thick PVDF transducer at 5kV.

The output shows most of the oscillations in the bulk had been removed; this indicates that the thickness of the transducer contributes to the oscillation of the system response. At this moment, there is no conclusion drawn to the oscillation phenomenon but it is believed that the only oscillation left is part of the system response characteristic, more investigation is needed. The thickness of transducer also plays an important part in the system resolution and sensitivity [63]. The transducer thickness effect on oscillation was proven by adding multiple layers of 9μm thick transducer to the system; see figure 3.22 for the effect. The thinnest PVDF transducer that was available at that time of testing was 9μm thick. The attenuation and dispersion factor of the 1st and 2nd peak in figure 3.21 remains incorrect as the 2nd peak's magnitude is exceedingly smaller (usually it is ~60 to 70%) than the 1st peak.

Figure 3.22. System response with different thickness of PVDF transducer at 5kV.

Step 7

Further test was carried out with setup as show in figure 3.18 but with a 9μm thick transducer and system B's bottom cell replaced by one solid piece of bottom electrode, see figure 3.23. Figure 3.24 shows the response of this setup.

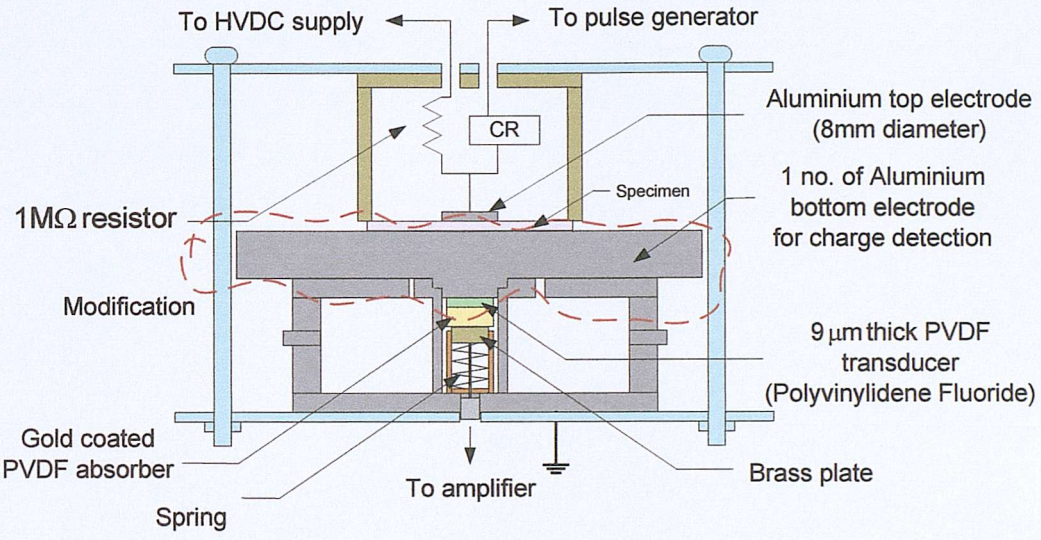

Figure 3.23. Cross section view of the system A's top cell with modified system B's bottom cell (one piece of aluminium bottom electrode).

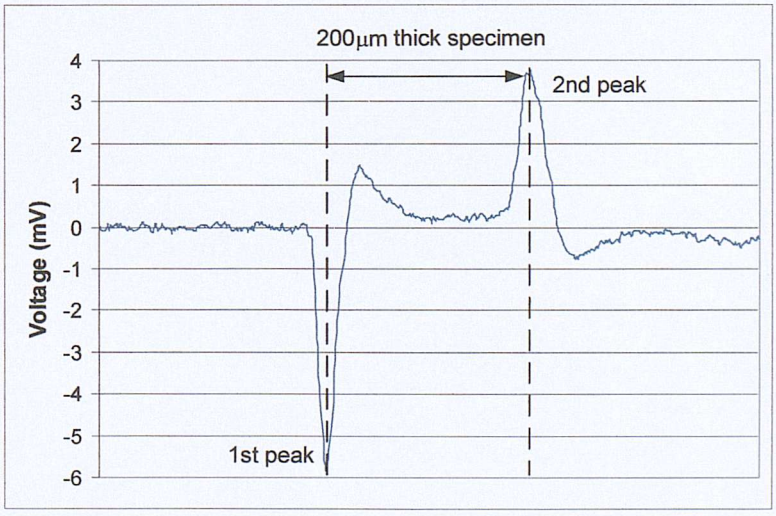

Figure 3.24. Output signal from the setup shown in figure 3.23 at 5kV.

System shown in figure 3.23 produced an output similar to the conventional PEA system shown in figure 3.11. This proves that the only oscillation shown in figure 3.21 is unavoidable if more than one electrode are used for the bottom cell. On

top of that, incorrect attenuation and dispersion factor might be due to the partial loss of signal through the gap of separate piece of aluminium electrode.

Step 8

Since the desirable waveform is achieved, attention is next turned to the separate bottom cell electrodes arrangement. The one-piece bottom electrode was replaced with the initial three separate concentric bottom electrodes, output as shown in figure 3.25. This result is acceptable as there will be oscillation emerged when more than one electrode are used for the bottom cell. The attenuation and dispersion factor between the 1st and 2nd peak is also correctly displayed.

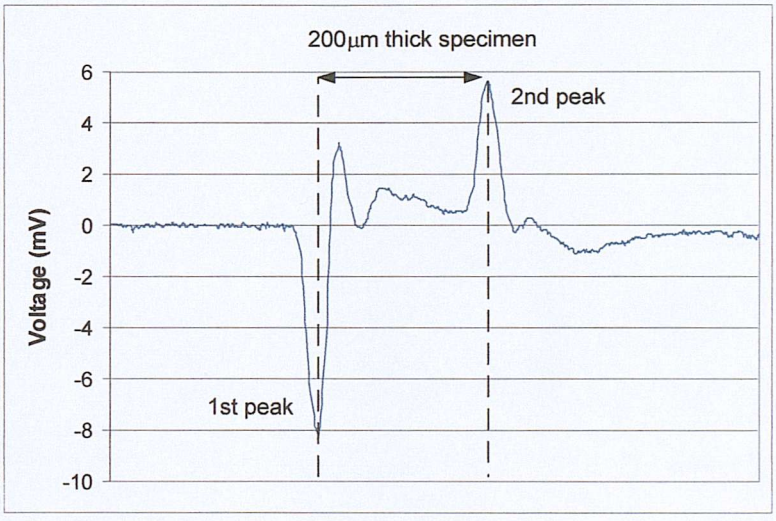

Figure 3.25. Output signal from the combination of system A's top cell with three separated concentric bottom electrodes at 5kV.

Step 9

Successively, system A's top electrode was replaced with modified system B's top cell (added pressure) see figure 3.26. Figure 3.27 shows the output of setup of figure 3.25. More oscillations were introduced.

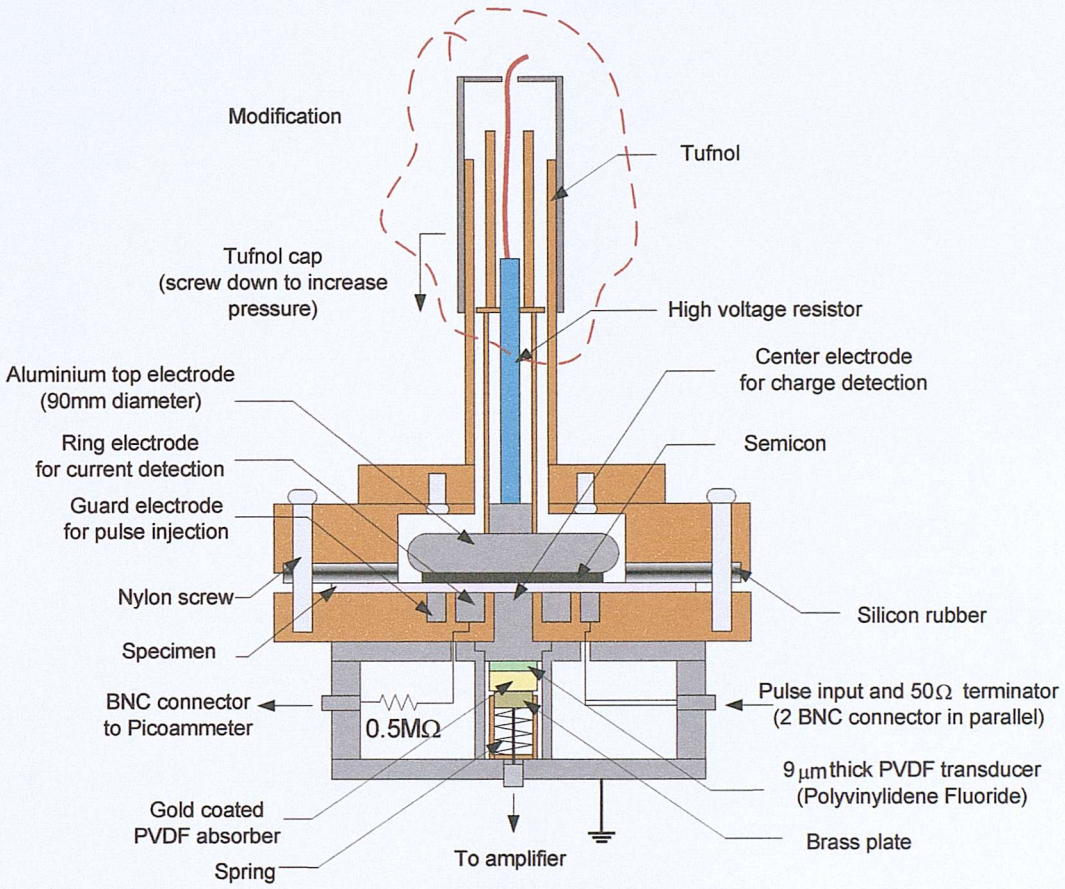

Figure 3.26. Cross section view of our PEA rig design with modified top cell.

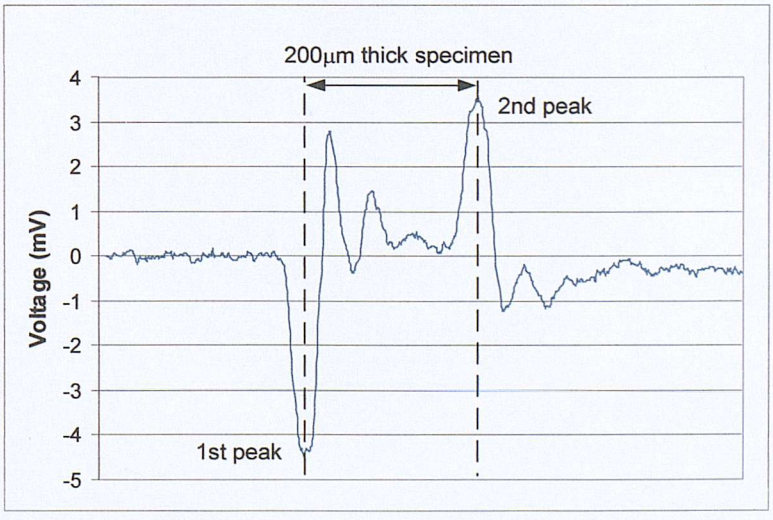

Figure 3.27. Output signal from the setup shown in figure 3.26 at 5kV.

Step 10

It was then suspected that it might have something to do with the size of the top electrode. Therefore, another test was performed using a piece of aluminium foil with surface area smaller than top electrode B but larger than top electrode A underneath system A's top electrode. Similar abnormal phenomenon is observed as in figure 3.27, this demonstrated that the size of top electrode was too large and therefore led to spurious field oscillations within the specimen following pulse application. J. M. Alison [12] also gave a similar conclusion that cell head greater than 60mm diameter might cause oscillation within the specimen. Therefore, modification was made to system B's top and bottom electrodes by reducing it to a diameter of 50mm. The dimensions of the guard, ring and centre electrodes of the designed system has to fulfill the condition $C_{guard} \approx C_{ring} \approx 10 \times C_{specimen}$ and the new bottom electrode is shown below in figure 3.28. Test was carried out using this new electrode dimension, see figure 3.29 for the output signal.

The proportion of attenuation and dispersion is correct although one significant oscillation is still present but as has been explained earlier, this is unavoidable when separate electrodes are used. It can be considered as part of the system response. With this response, deconvolution of the signal can be carried out for calibration.

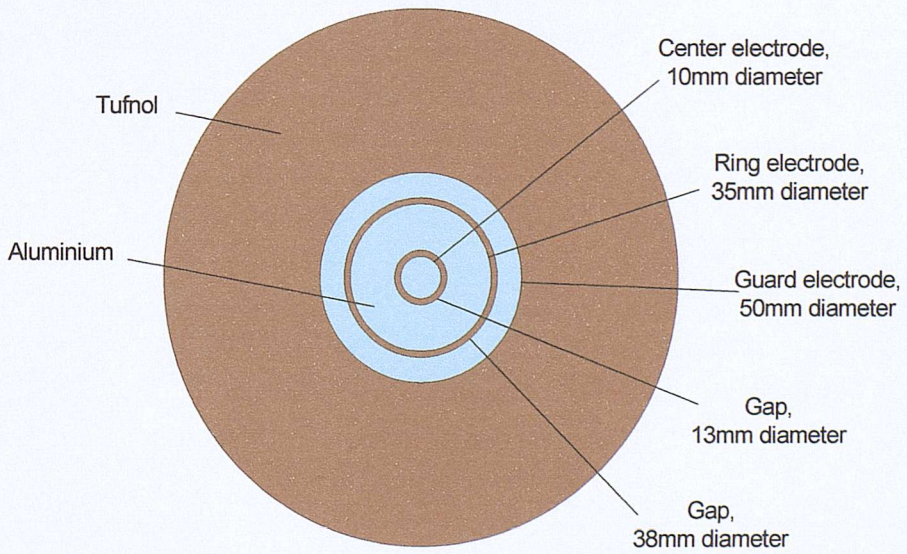

Figure 3.28. Dimensions of the centre, ring and guard electrodes (~50mm diameter) of the PEA system.

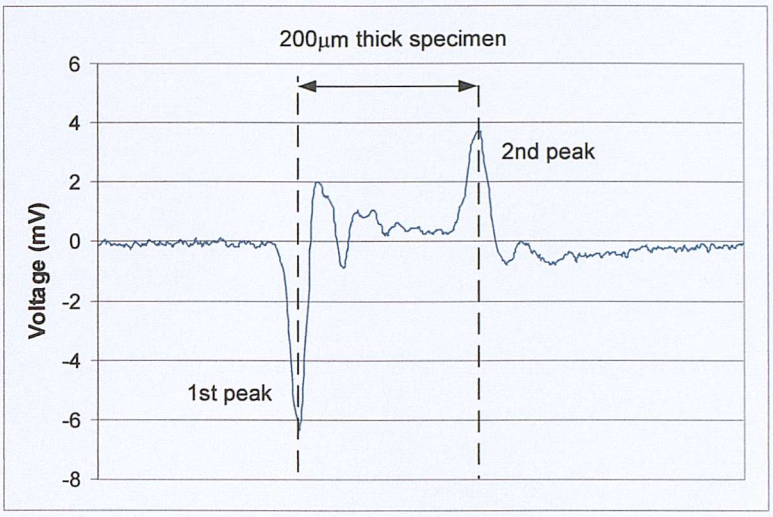

Figure 3.29. Output signal from the setup shown in figure 3.26 with a 50mm diameter electrode at 5kV.

Step 11

Further test to check the stability of the system was carried out by stressing the specimen at higher voltage for a period of time. As stressing time increased, the horizontal zero line of the signal was moving vigorously which then caused the result to be illegible. Further investigation showed that a gap had been formed between the tufnol plates at the top cell, which is supposed to maintain a constant pressure onto the top electrode. The nylon screws that were supposed to secure the tufnol plates in position, run out of the tread when too much pressure was applied, refer to figure 3.30. Once again a small refinement was made to the top cell construction so that a constant pressure can be sustained, the cross section view of our system is shown in figure 3.31.

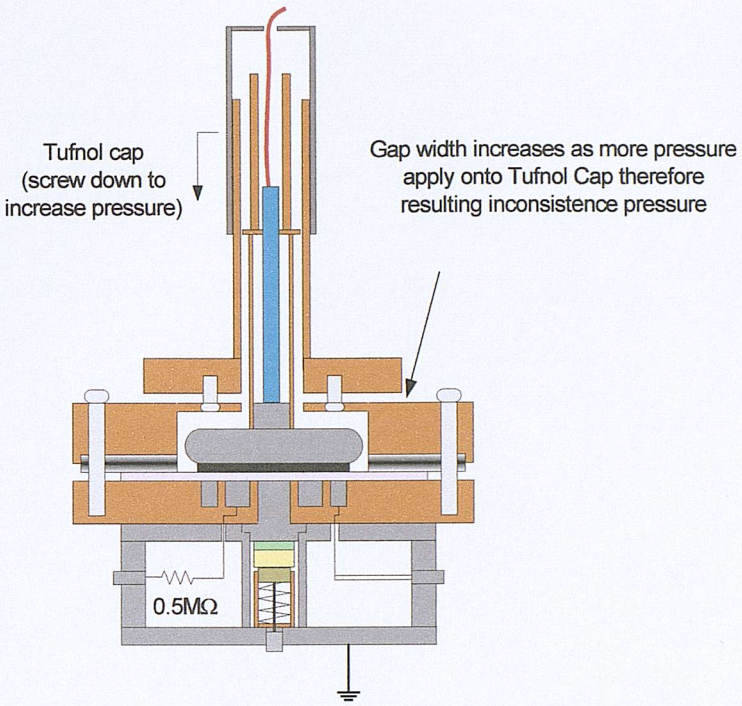

Figure 3.30. Cross section view of our PEA rig design with a gap formed between tufnol plates when too much pressure is applied.

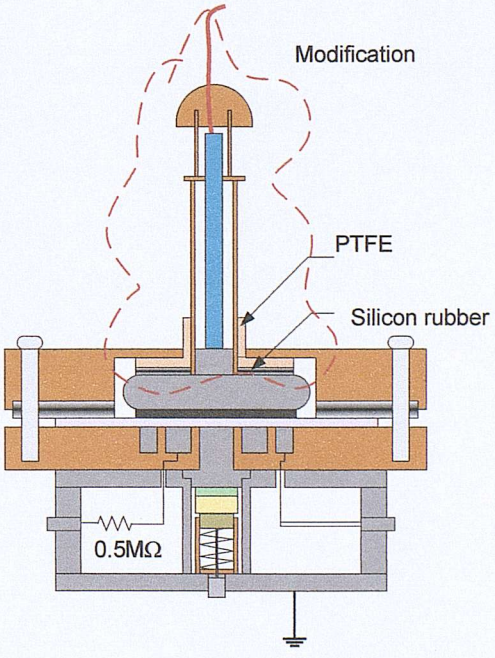

Figure 3.31. Cross section view of the PEA rig design for charge density measurement.

3.3.3 Trouble-shooting current measurement ability

With the system fully functioning, tests were carried out recording concurrent charge and current measurements. Unfortunately, when stressing voltage reached about 7kV, discharge behaviour occurs, it totally distorted the current readings. The following show one set of several similar test results being carried out. Figure 3.32 is the measured current under the following specification and conditions:

(a) Specimen type: Low-density polyethylene (LDPE),

(b) Specimen thickness: 200μm,

(c) Cathode (top electrode): Aluminium,
Anode (bottom electrode): Semiconducting material

(d) Specimen was stressed from 1-7kV at an interval of 1kV for a period of 45 minutes and at 8kV for 10 minutes.

(e) Room temperature at about 20°C

(f) Charge and current density profiles were recorded every 5 seconds throughout the stressing period.

Clearly the current spikes are due to discharge taken place in the system. The possible cause of the discharge is the surrounding of the top electrode. Glue like silicon rubber was used to fill up the space around the top electrode. Few runs of the test show no discharge behaviour even up to a voltage of 20kV. Figure 3.33 is the finalised PEA setup. The charge density output from the finalised PEA setup is similar to figure 3.29. Photos of the actual PEA setup can be viewed at Appendix A.

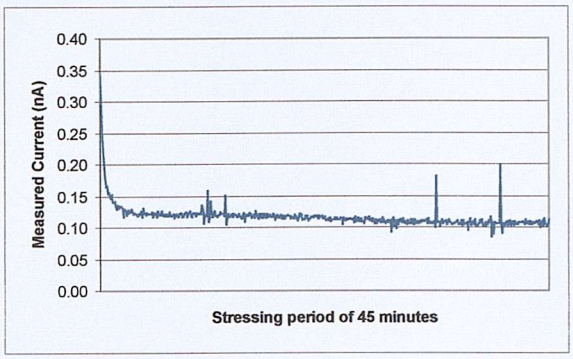

(a) at 1kV

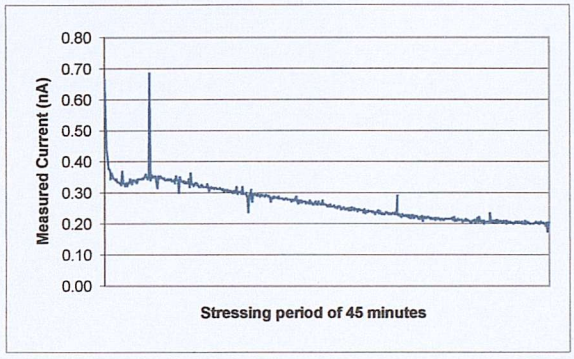

(b) at 2kV

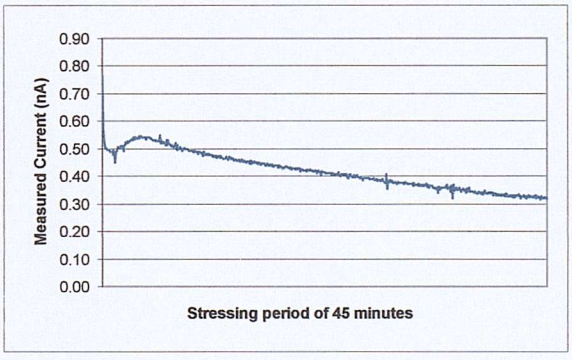

(c) at 3kV

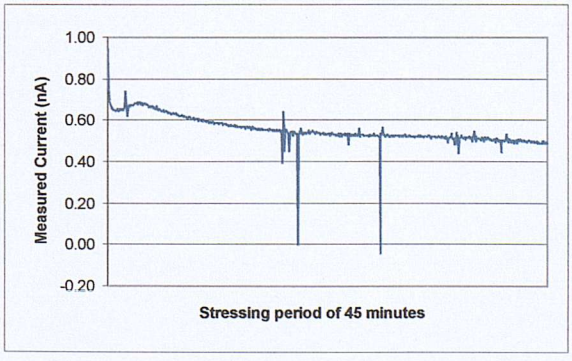

(d) at 4kV

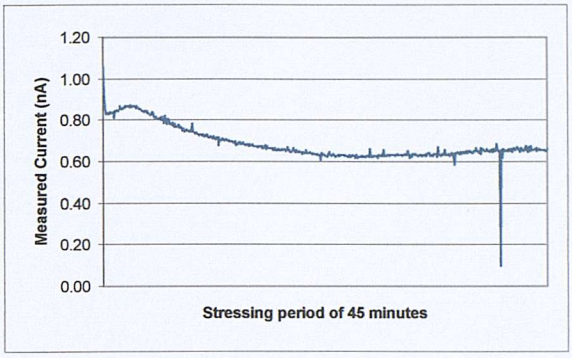

(e) at 5kV

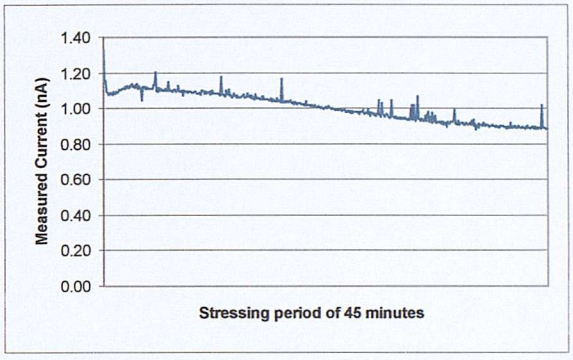

(f) at 6kV

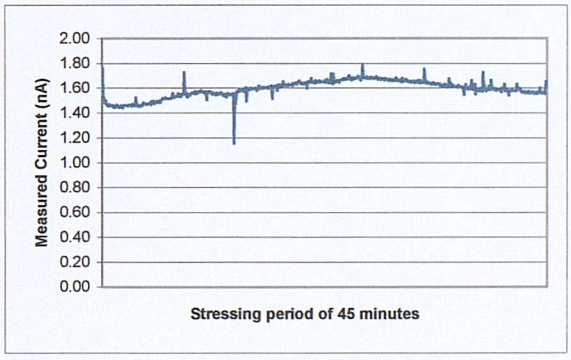

(g) at 7kV

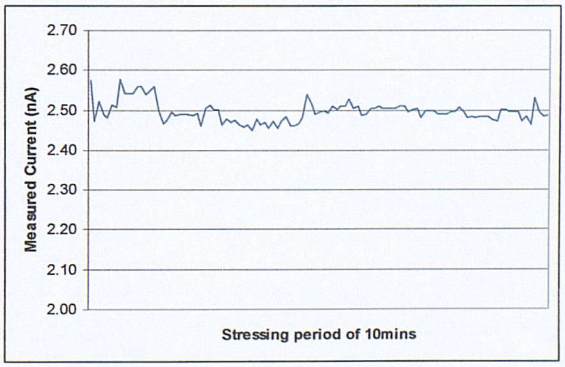

(h) at 8kV

Figure 3.32(a) – (h). Measured current from 1 to 8kV.

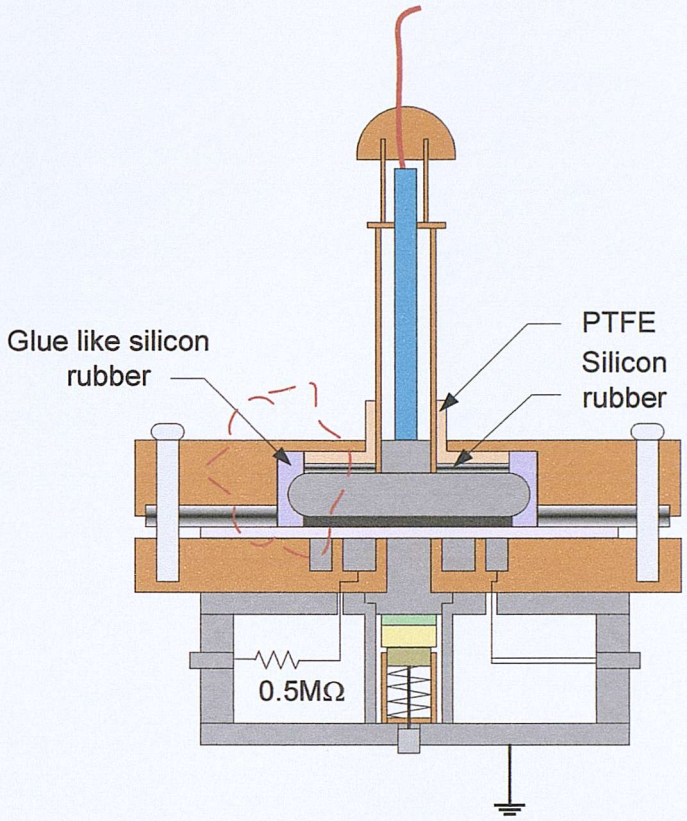

Figure 3.33. Finalised PEA setup.

3.4 Control of the experiments

Control of the PEA setup is just a click on the computer mouse. A computer equipped with a general-purpose interface board (GPIB) is the main control centre to most components except for the high voltage supply unit. Fully computer controlled abilities were achieved with the help of programs written using LabView software developed by National Instruments.

The process is started off by collecting a set of charge density data at lower voltage of a few kV for calibration. With a touch on the keyboard, a signal of 5V is sent from the RS232 port data pin of the CPU to a transistor for switching on the pulse generator, see figure 3.34.

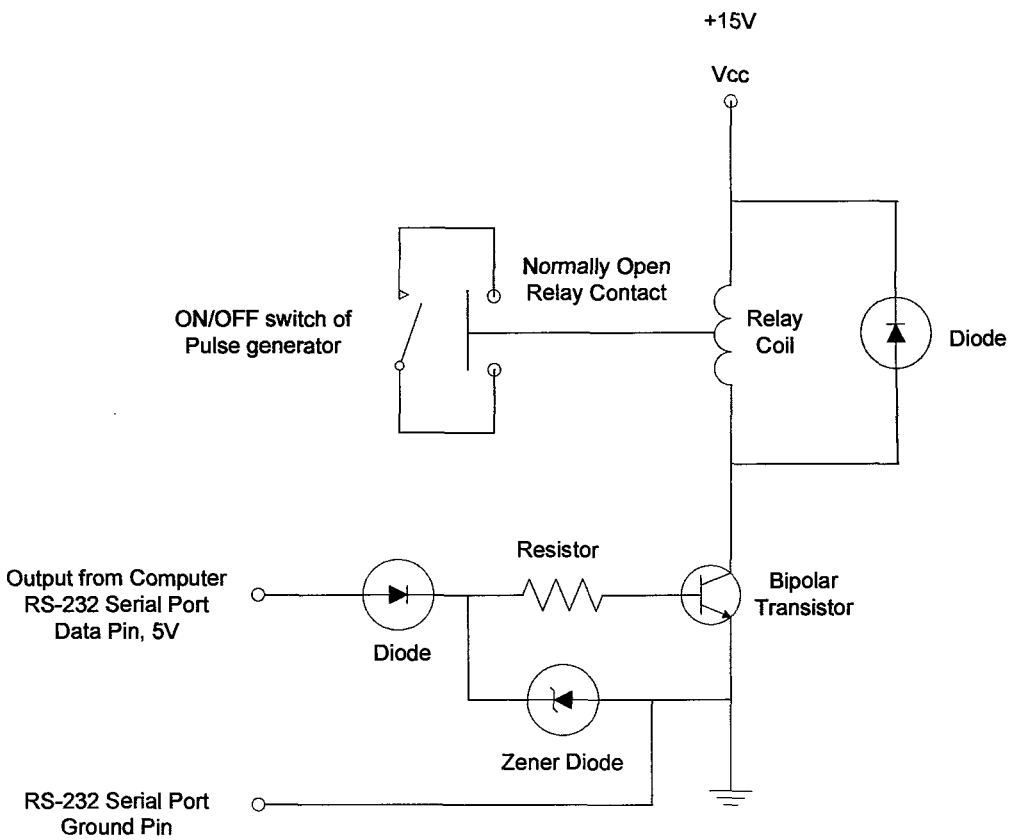

Figure 3.34. Schematic diagram of the switching circuit.

The pulse generator will then send a pulse of 600V amplitude (8ns pulse width) to the PEA system to excite the charge carrier; the movement of the carrier will be detected by the transducer, which translates the acoustic pressure wave to an

electrical signal. This signal is amplified by an amplifier (Mini-circuit ZFL-500LN) and read by the oscilloscope (Tektronix TDS 3052). Pulse generator will also send another pulse to trigger the oscilloscope to collect information and reflect it back to the computer that will process the raw signal and store the information in memory, see figure 3.35.

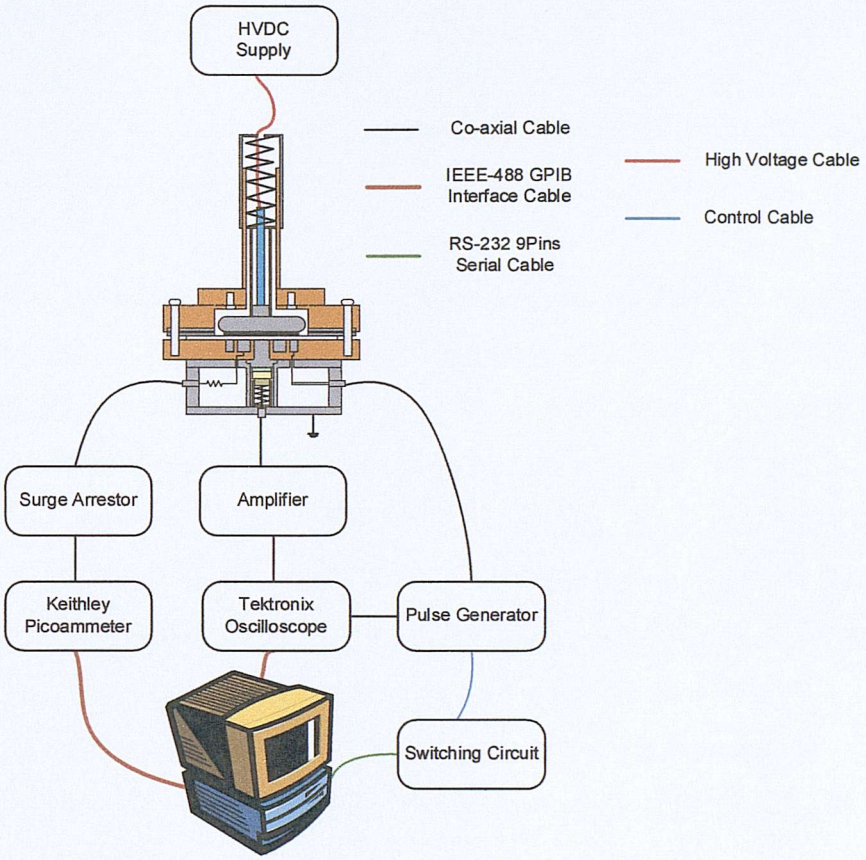

Figure 3.35. Control of the PEA system setup.

Next, higher stress (actual stressing) is applied onto the sample. A similar process will be repeated as has been described earlier but this time data will be collected continuously. Measurement time interval and number of measurements can be set to a desirable value for the computer to capture information from the oscilloscope. In addition current measurement is made by a Keithley 486 picoammeter, which is linked to the computer via IEEE-488 interface, concurrently with space charge measurement.

3.5 Signal processing for raw PEA signal

The collected signal from the oscilloscope contains space charge information that is obtained after perturbation by the specimen lossy and dispersive characteristic and several conversions, e.g. generation of acoustic pressure wave due to movement of space charge caused by electric pulse field, the electric output as the pressure wave exerts influence on the piezoelectric transducer, the output from the amplifier connected to the transducer and output from oscilloscope linked to the amplifier. Therefore, signal processing is necessary to remove these perturbations in order to acquire the real space charge information.

The measured resolution of this PEA system when only surface charges were induced on the electrodes at half-peak height is about 30μm. The spatial resolution of space charge distribution of a given system is defined theoretically as the product of the pulse width and the acoustic pressure wave velocity in the specimen. In this case, the pulse width is 8ns and the acoustic wave velocity in polyethylene is approximately 2200m/s, thus the best resolution achievable is estimated to be 18μm. This difference between the measured and theoretical value was probably caused by the application of the mathematical deconvolution technique (will be discussed in section 3.5.2), which utilizes a low pass filter to remove the high frequency noise introduced by round-up errors. The signal processing program is written in LabView software and can be viewed in Appendix B.

3.5.1 Offset and drift of the system

The signal process is started off with signal acquisition. A Tektronix digital Phosphor oscilloscope model TDS 3052 captures the signal with a sampling rate up to 0.5GHz. Figure 3.36 shows an example of a raw signal from the oscilloscope when no space charge exists, only surface charge is considered. The distance d (thickness of the sample) corresponds to the time between the wave due to the charge σ_1 and σ_2 arriving at the transducer are marked as point A and B.

Point A represents in time when the transducer begins to excite due to pressure wave corresponding to σ_1 and point B represents when transducer begins to excite due to pressure wave corresponding to σ_2.

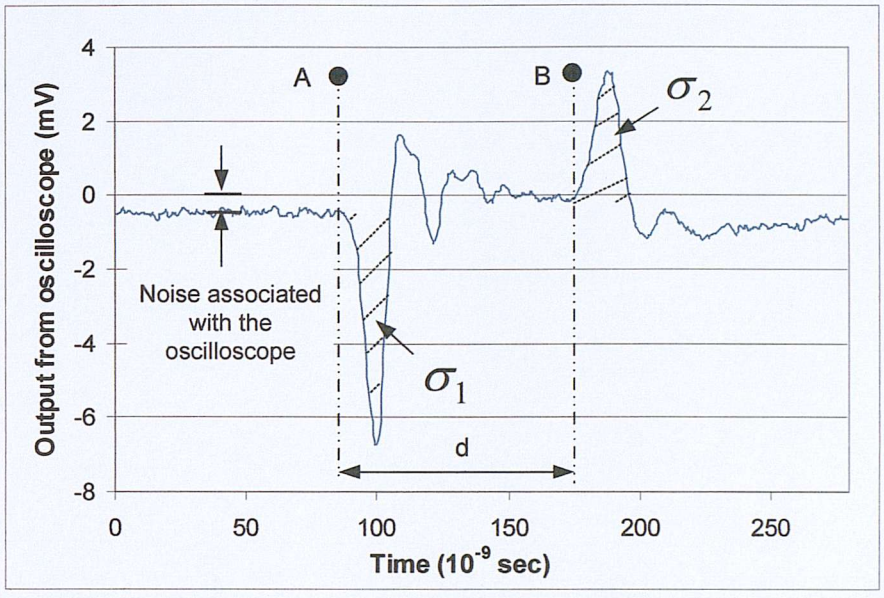

Figure 3.36. A typical signal output obtained with the PEA method.

The acquired signal is sometimes affected by a small offset (noise) associated with the oscilloscope. The offset is not a constant value but with a certain variance. The value of offset at each sampling point cannot be exactly predicted but can be minimised by considering its mean value. This is done by selecting the part of the signal before point A and the mean offset is calculated by:

$$Mean\ offset = \frac{\sum_{k=1}^{k=A} signalA(kT)}{A} \tag{3.3}$$

where A = number of points from time 0 to point A and

$signalA(kT)$ = output signal (volts) from oscilloscope.

Therefore signal after offset is:

$$signalAafteroffset(kT) = signalA(kT) - Mean\ offset \tag{3.4}$$

3.5.2 Deconvolution technique

The acoustic pressure wave signal *pw(t)* received at the transducer is converted into a electrical voltage signal, which is then fed to an amplifier, output is represented by *v(t)*. This conversion process can be interpreted in time domain by the block diagram in figure 3.37.

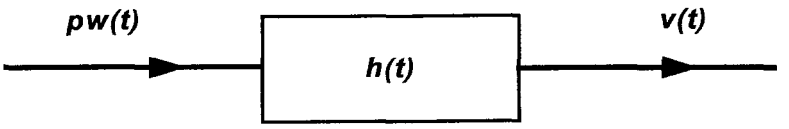

Figure 3.37. Conversion process of the PEA signal.

The mathematical description for the above process is given by

$$v(t) = h(t) * pw(t) \tag{3.5}$$

where *h(t)* is the unit impulse response of the overall PEA system which represents the effects of the piezoelectric transducer and the electrical amplification of the signal and "*" denotes the mathematical operator of the convolution process. In frequency domain, the relationship described by equation 3.5 between the acoustic pressure wave *PW(f)* and the electrical signal of the system *V(f)* can be expressed by using the transfer function of the whole system, *H(f)*,

$$V(f) = H(f) . PW(f) \tag{3.6}$$

If the transfer function of the system *H(f)* is known, the acoustic pressure wave in the frequency domain *PW(f)* can be determined. Consequently, by converting equation 3.6 back into time domain (applying inverse Fourier Transform), the acoustic pressure wave profile containing the information about space charge distribution can be obtained.

H(f) can be evaluated by application of a low electric stress to the specimen when no space charge is formed in the bulk. The thinness of the induced surface charge at both electrode interfaces are restricted by the finite width of the pulse

voltage and the limitation of the whole system's spatial resolution. However, it can assumed that the launched acoustic wave has a Gaussian distribution that is expressed by

$$pw_1(t) = Ae^{-\alpha(t-\tau)^2} \tag{3.7}$$

where A is the amplitude of the acoustic pressure wave and is a constant for a given specimen with a fixed thickness, DC stress and pulsed electric stress. α is a constant and is determined by the system's spatial resolution. In the frequency domain, $pw_1(t)$ is expressed by $PW_1(f)$. Correspondingly, its electrical output in frequency domain, $V_1(f)$ may also given by

$$V_1(f) = H(f) \cdot PW_1(f) \tag{3.8}$$

therefore the whole system transfer function $H(f)$ can be determined by the above equation. Thereafter, $PW(f)$ in equation 3.6 can be obtained.

To apply the deconvolution technique, $v_1(t)$ is selected which contains the impulse response of the whole system. Figure 3.38 (a) and (b) show the selection of $v_1(t)$ and $v(t)$ from the typical induced surface charge at the cathode and anode when there is no bulk charge present. As the first peak, which in this case is at the cathode, is not affected by the attenuation and dispersion factor, therefore being used as a reference signal to calculate the system transfer function.

(a)

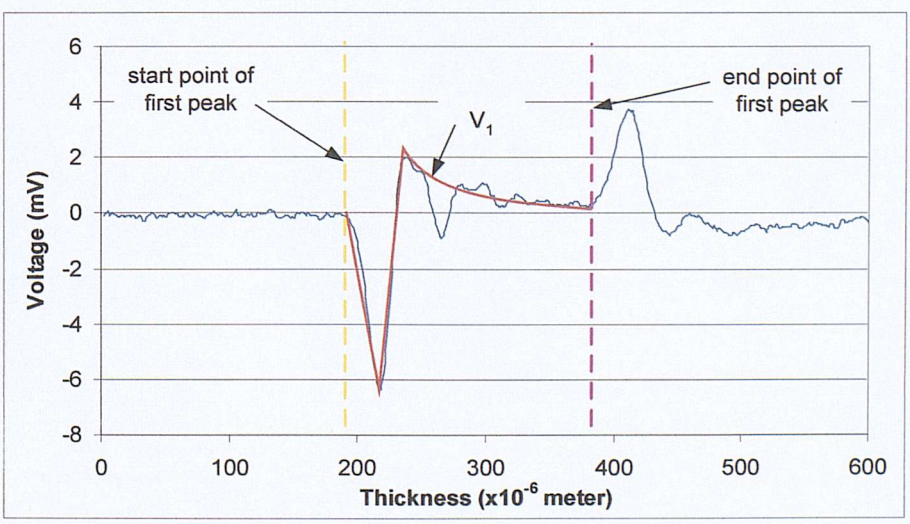

(b)

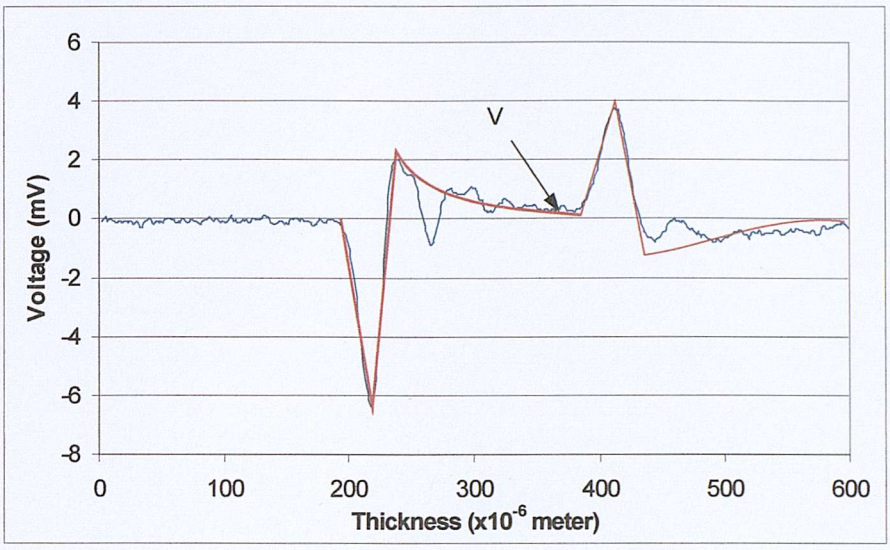

Figure 3.38(a) and (b). Selection of $v_1(t)$ and $v(t)$ from raw signal.

An artificial "unit impulse function" $PW_1(f)$ is generated by the software at the start point of the first peak to imitate pulse generated by the pulse generator. Thus, the transfer function of the system in frequency domain can be determined by

$$H(f) = \frac{V_1(f)}{PW_1(f)} \tag{3.9}$$

Similarly, applying Fast Fourier Transform to the whole output voltage signal $v(t)$, its frequency domain expression, $V(f)$ can be obtained. From equation 3.6, we then have

$$PW(f) = \frac{V(f)}{H(f)} \tag{3.10}$$

Therefore, acoustic pressure wave $pw(t)$ containing the space charge distribution can now be obtained by applying inverse Fast Fourier Transform to equation 3.10. Figure 3.39 shows the raw voltage signal in figure 3.38 after deconvolution.

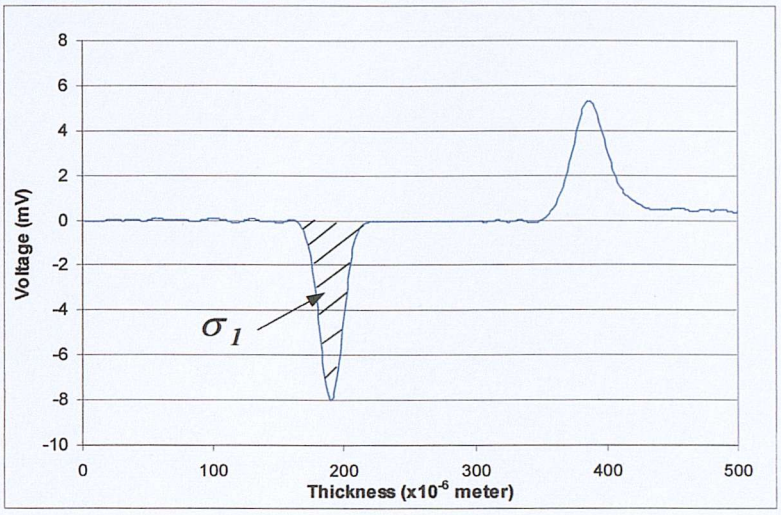

Figure 3.39. Signal after deconvolution.

3.5.3 Attenuation and dispersion factors

Until now, it had been assumed that the acoustic wave propagation is without attenuation and dispersion. However, in reality, the media is not perfect. Attenuation and dispersion of the acoustic wave during propagation needs to be considered in order to obtain the real space charge distribution. Imagine a plane harmonic wave propagates across a solid dielectric medium in the x-direction. It can be represented by the one-dimensional wave equation [64]

$$p(t,x) = p_o e^{jw(t-\frac{x}{v})} = p_o e^{j(wt-kx)} \tag{3.11}$$

where p_o is the amplitude of the plane harmonic wave at position x=0, w is the angular frequency, v is acoustic velocity and k is the wave number. In a lossy/dispersive medium, the real wave number k is replaced by its complex form

$$k = \beta - j\alpha \tag{3.12}$$

where α and β are defined as the attenuation and dispersion factors respectively. Applying Fast Fourier Transform after substituting equation 3.12 to 3.11, gives

$$P(f,x) = P(f,0) \cdot e^{-\alpha(f)x} \cdot e^{-j\beta(f)x} \tag{3.13}$$

The frequency spectra of acoustic pulses at $x = 0$ and $x = d$ is given as

$$P(f,0) = |P(f,0)| . e^{-j\phi(f,0)} \tag{3.14}$$

$$P(f,d) = |P(f,d)| . e^{-j\phi(f,d)} \tag{3.15}$$

where $|P(f, 0)|$ and $|P(f, d)|$ are the amplitude spectra and $\phi(f, 0)$ and $\phi(f, d)$ are phase spectra of the original acoustic wave at position x=0 and transmitted acoustic wave at position x=d. Substituting equation 3.14 and 3.15 into 3.13, the following equations are obtained

$$|P(f,d)| = |P(f,0)| . e^{-\alpha(f)d} \tag{3.16}$$

$$\phi(f,d) = \phi(f,0) + \beta(f).d \tag{3.17}$$

Solving equation 3.16 and 3.17 give

$$\alpha(f) = -\frac{1}{d} \times ln\left|\frac{P(f,d)}{P(f,0)}\right| \tag{3.18}$$

$$\beta(f) = \frac{1}{d} \times [\phi(f,d) - \phi(f,0)] \tag{3.19}$$

In order to apply these equations, the frequency spectrum of the input wave pressure $P(f, 0)$, and the output wave pressure $P(f, d)$ must be known. Deconvoluted signal has acoustic wave pressure profile which is linearly proportional to the voltage output from amplifier, therefore $P(f, 0)$ and $P(f,d)$ can be obtained by applying Fast Fourier Transform to the 1st and 2nd peak of the signal after deconvolution. Equation 3.13 can be expressed in the form of:

$$P(f,x) = P(f,0) \cdot [A(f)]^x \tag{3.20}$$

where $[A(f)]^x$ represents the effect of both attenuation and dispersion on the pressure wave for each frequency component f and at position x.

To recover the signal, simply use the counter effect of $A(f)$ to cancel out the attenuation and dispersion. We can recover the signal by applying a positive exponential effect to the signal which is exactly the same as the negative exponential effect that attenuates the signal, given by:

$$P(f)_{RECOVERED} = P(f,0)\cdot[A(f)]^{-x} \tag{3.21}$$

In order to use this equation numerically, equation 3.21 must be applied to each layer Δx of charge followed by a summation of all the values on each layer. The mathematical representation can be equated as:

$$P(f)_{RECOVERED} = \sum_{i=1}^{N} P(f,x_i)\cdot A(f)^{-x_i} \tag{3.22}$$

where $P(f, x_i)$ represents the frequency spectrum of the signal at the point x_i. Here x_i is the distance between the point 1 and i. The recovered signal is dependent on the value of N, i.e., the larger the value of N, the higher accuracy of the recovered signal. The recovered signal in figure 3.40 was achieved by applying inverse FFT to equation 3.22.

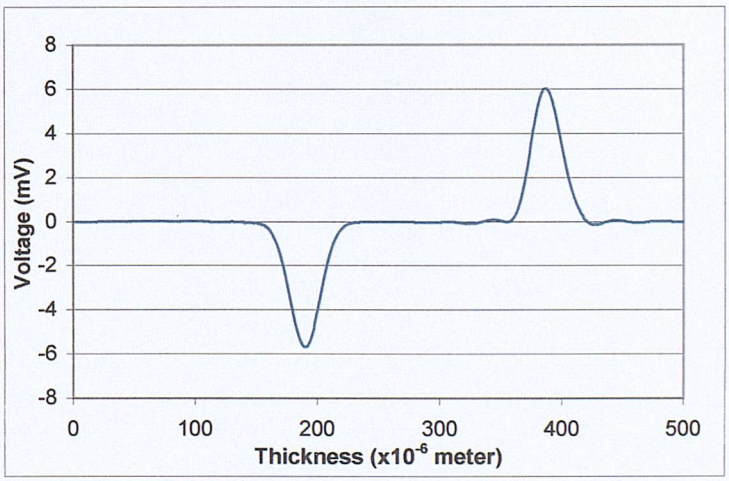

Figure 3.40. Signal after deconvolution and recovery.

3.5.4 Calibration of the recovered signal

Notice the recovered signal is still expressed in Volts, to scale voltage to charge density, calibration must be carried out. Using the deconvoluted signal (figure 3.39), the first peak is used to calculate the area of the surface charge σ_1 because this peak is not affected by attenuation and dispersion factors.

$$Area\ of\ \sigma_{1(calculated)} = \int_{x=end\ of\ 1st\ peak}^{x=start\ of\ 1st\ peak} (signal) \cdot dx \tag{3.23}$$

where x = acoustic velocity (m/sec) x sampling interval (sec).
The theoretical surface charge value can be obtained using this equation

$$\sigma_{1(theoretical)} = \varepsilon_o \cdot \varepsilon_r \cdot E_{DC} \tag{3.24}$$

where $E_{DC} = V_{DC}/d$, V_{DC} is the voltage applied to obtained signal in figure 3.39. Therefore ,

$$calibration\ factor = \frac{\sigma_{1(theoretical)}}{\sigma_{1(caluculated)}} \tag{3.25}$$

Thus calibration is attained by multiplying the recovered output $v(t)$ (figure 3.40) by the calibration factor. The calibrated signal is shown in figure 3.41.

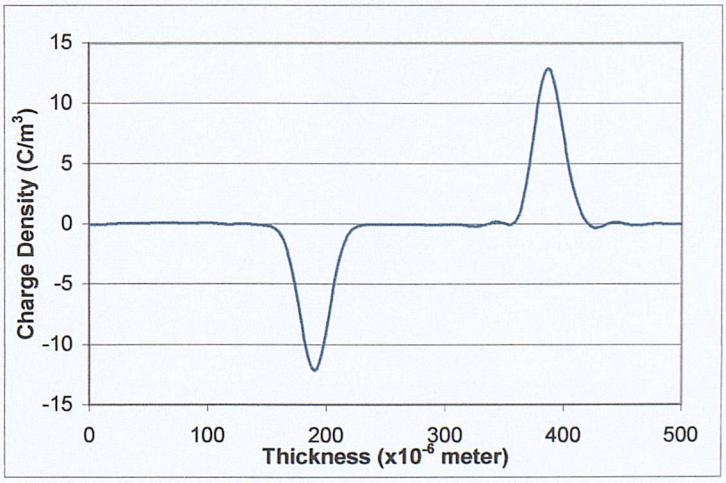

Figure 3.41. Signal after deconvolution, recovery and calibration.

3.6 Conclusions

The basic principals of non-destructive space charge measurement techniques such as PIPWP, LIPP and PEA had been reviewed. A new improved PEA system was built with abilities to measure both space charge and current simultaneously. A thorough description of the initial PEA system design, occurrence of unexpected complications and solutions to problems encountered was recorded. The collected signal straight from the oscilloscope contains distorted information caused by the perturbation of the specimen lossy and dispersive nature and conversion processes from acoustic pressure wave to electrical signal. For that reason, implementation of signal processing to the collected raw PEA signal is necessary. It includes deconvolution, attenuation-dispersion compensation and calibration.

Chapter 4

Relationship between Charge and Current Measurement

4.1 Introduction

Before non-destructive space charge detection techniques were widely used, charge trapping and transport characteristics of dielectrics were studied broadly by measuring the external current [65-67]. Since the significant development in non-destructive space charge measuring techniques, charge dynamics in dielectrics have been investigated extensively based on space charge profile. Space charge profile is in fact the measurement of the charge carriers' generation, accumulation and transportation processes, which are associated with the flow of current. Using the improved PEA setup, the flow of current through the insulation can be measured using a picoammeter. This supplementary parameter would give more insight about charge carrier conduction behaviour. By collecting space charge and current information simultaneously, it helps to reveal the relationship between these two parameters that will aid the interpretation of the physical processes.

Literature search revealed that not many researchers have carried out simultaneous space charge and current density measurements. Surprisingly even those who had performed such measurements did not conduct the test for a long stressing period and co-related any changes in external measured current trend to the space charge profile.

4.2 Elucidation of partial equivalent circuit of the PEA system with a specimen under test

Before considering the partial equivalent circuit of the PEA system with a specimen under test, figure 4.1 shows a simple perfect series capacitor-resistor circuit. According to the circuit theory, at any instant the voltage across resistor R is

$$V_R = V - V_C \tag{4.1}$$

where V_R, V_C and V represent voltage drop across the resistor, capacitor and the supply voltage. The current flowing through the circuit, which is also known as the charging current is

$$i = \frac{V - V_C}{R} \tag{4.2}$$

The current flow causes the capacitor C to be charged with the polarity illustrated in the figure. As the capacitor gets charged, the capacitor voltage is continuously increasing, the voltage across resistor R is continuously decreasing and therefore the charging current is continuously decreasing too. A typical graph of charging current versus time in figure 4.2 shows how the charging current changes with time. The charging current flow lasts only for a brief time and ceases just as soon as the plates are at the same potentials as the DC supply.

For the capacitor plate in figure 4.1 to have the same potential difference as the DC supply, electrons must be removed from the top plate (+) to make it positive, and the removed electrons must be delivered to the bottom plate (-) to make it negative. The electric stress across the dielectric causes a certain amount of distortion of the atoms to occur, as illustrated in figure 4.3. Figure 4.3(a) shows an atom in a field-free region and is neutral. If an electric field is applied, the symmetry will be

disturbed. The electron will be displaced in the opposite direction of the field and the nucleus may shift its position in the direction of the field. This is represented by figure 4.3(b) whereby a negative and positive charge separated by a distance dependent on the field strength. This is called an electrical dipole, and such dipoles are formed throughout the insulator, hence the name polarization is given. Polarization current decreases inversely as a function of time.

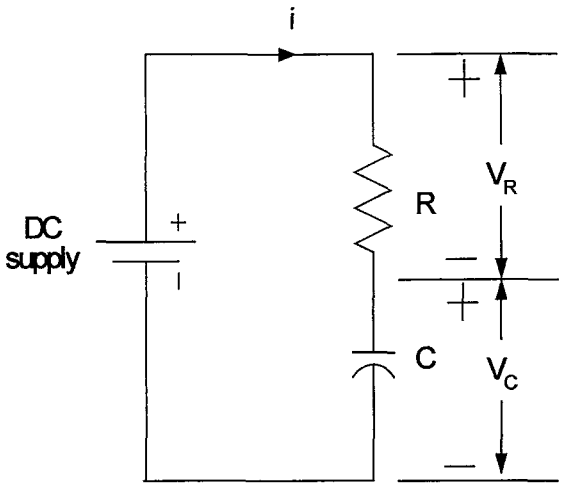

Figure 4.1. A perfect series capacitor-resistor circuit.

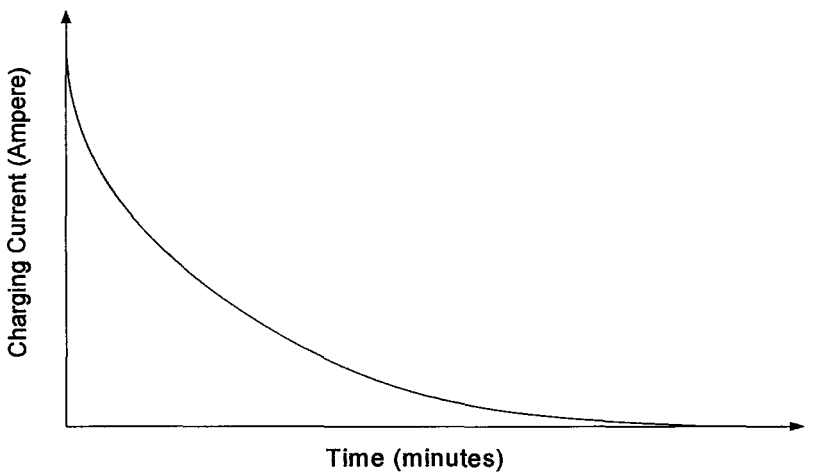

Figure 4.2. Graph of charging current versus time in a capacitor-resistor circuit.

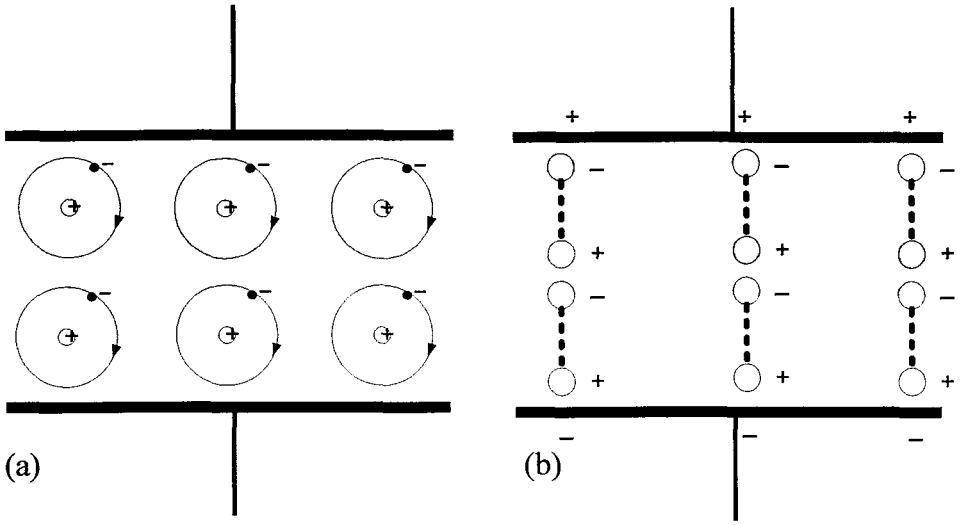

Figure 4.3. Electric stress occurs on the dielectric of charged capacitor. (a) Atoms in field-free region and (b) electrical dipoles created under an applied field.

The partial equivalent circuit of the specimen in the PEA system is shown in figure 4.4. This circuit resembles a typical parallel capacitor-resistor circuit. The 1MΩ resistor is the HV resistor used to isolate HV supply from the generator network and also to limit the current in case of specimen breakdown. The specimen under test behaves like a capacitor and this capacitor is not ideal at all, like all dielectrics they have some leakage current, therefore R_L represents the leakage resistance parallel to the capacitor. With the introduction of R_L current flowing through the circuit will never reach zero, which is exactly what happened in actual experimental situation.

In most cases, after the application of HVDC, the charging current decays with time until a "steady state" is achieved. In general, there are two processes resulting in decay of charging current, (a) just imagine that once charges have been injected into the bulk from the electrodes, it may be difficult for the charges to move further through the bulk due to the rate of carrier injection greater than rate of carrier transportation. Thus, space charge may be formed near the electrodes and throughout the bulk, this limits onward injection of the charge carriers from the electrode into the bulk and (b) polarization as described earlier, for these reasons the charging current decreases.

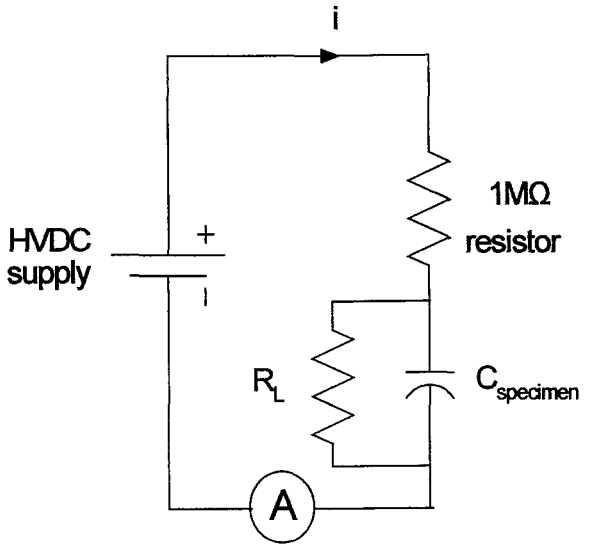

Figure 4.4. Partial equivalent circuit of the PEA system with a specimen under test.

Not only is the specimen far from ideal, the rate of charging depends very much on the type of specimen and electrode materials. The only possible reasoning if there is a rise in charging current rather than drop under a constant temperature environment is due to the increasing (compared to previous) amount of electrons injected into the bulk. This increased amount of electrons injected into the bulk from the cathode recorded by the ammeter is caused by the increasing amount of charges leaking out from the capacitor (specimen).

4.3 Charge carriers activity in energy band diagram

As mentioned in section 4.2, there is a restriction on injection of charge carriers into the bulk when charge carriers are accumulated near to the electrode, this can be better explained in terms of an energy band diagram in which there are traps. Taking electrons for example, figure 4.5 shows a series of probable electrons progression.

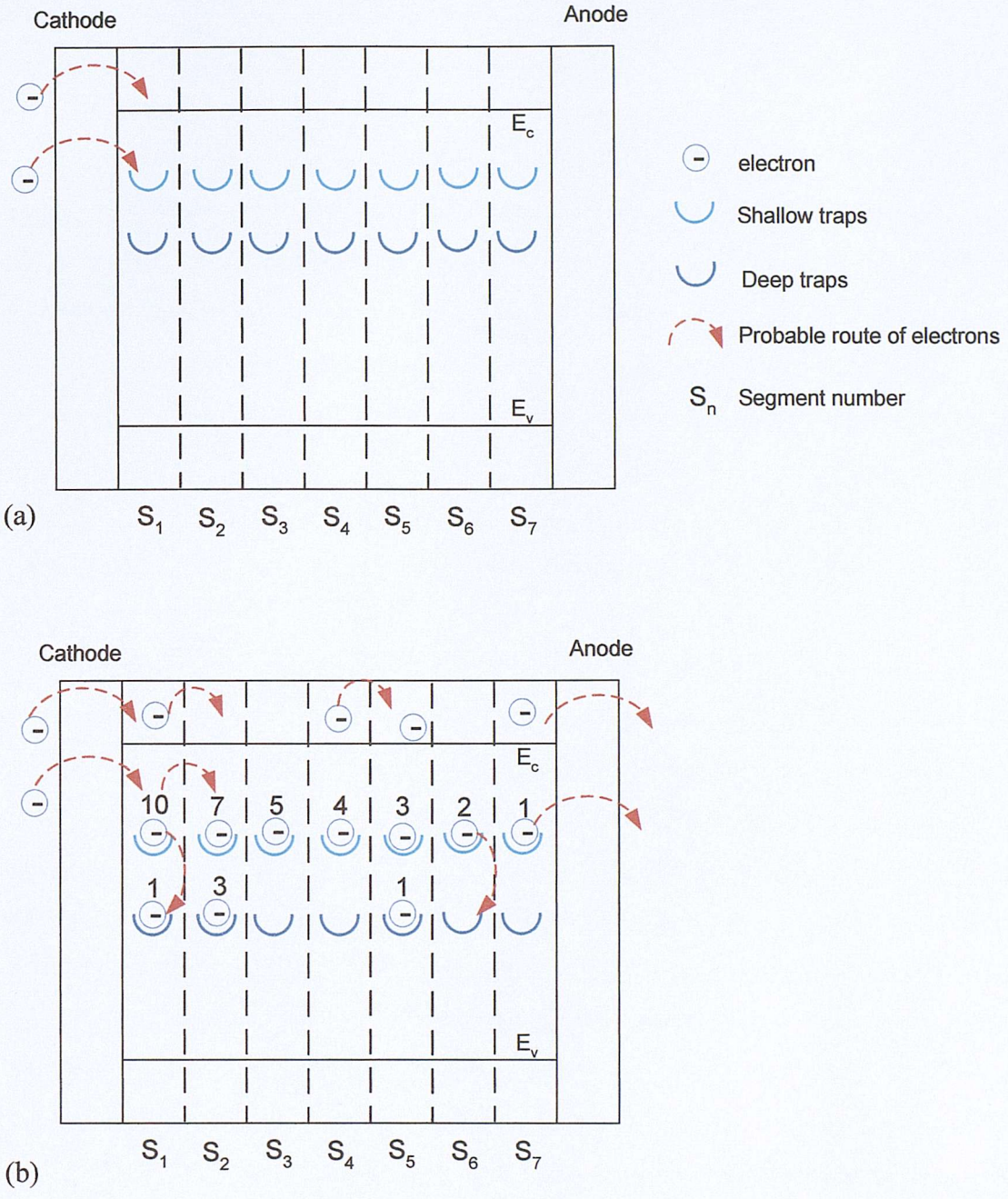

Figure 4.5. Probable electrons progression.

For illustration purpose, the specimen was sliced into equal segments. Figure 4.5(a) shows the probable route of injected electrons from the cathode if voltage is applied. Figure 4.5(b) is an example of injected electrons from the cathode after voltage was being applied and its probable subsequent movement. Electrons in the conduction band would have no problem travelling towards the anode. As for electrons in shallow traps, they might jump from one shallow trap to another or to a deeper trap. Electrons can be injected from the cathode into the bulk; it can also too

be extracted out from the anode which is equivalent to the injection of positive charge carriers [68].

At time when the transportation rate of the electrons is lower than the injection rate, more carriers will be accumulated near to the cathode, which will slow down further injection; therefore the measured current decreases. The possibility of measured current increases (under constant temperature condition) is after electrons in traps and conduction band nearer to the anode acquired sufficient energy to be extracted out from the anode. With more electrons being extracted at the anode, this will help the electrons near to the cathode to move further towards the anode, which therefore encourages progressively more electrons to be injected. The entire above-mentioned scenario refers to carriers injected from the electrode.

If impurities do exist in the specimen, another possible scenario is the ionisation process as a result of electric field assisted dissociation of chemical content. This is whereby electrons, positive and negative ions are formed. There are also probabilities of recombination between the electrons and negative ions with holes and/or positive ions; this process does not directly contribute to the increase in external current flow. The total number of carriers in a particular location is the sum of electrons (-), holes (+), positive and negative ions. In later chapters when attempts are made to explain the experimental results, positive charge carrier extraction (reducing amount of positive charge carriers) by the cathode refers to the electrons injected from the cathode where by it either neutralises or recombines with the holes and/or positive ions, whereas positive charge carrier injection from the anode signifies electrons getting out of the bulk by overcoming the interfacial barrier at the anode.

4.4 Illustration of charge carriers behaviour with experimental results

An experiment using the newly improved PEA system has been carried out to prove the above-mentioned charge carrier movement hypothesis. A 200μm thick undegassed XLPE specimen was subjected to a moderate stress at a constant

temperature, to ensure that some charge carriers had been injected into the bulk. Some time later, a higher electric stress was applied; this was done to allow more significant changes in carriers' transportation process. The corresponding charge and current density behaviour at the higher electric stress level is shown in figure 4.6.

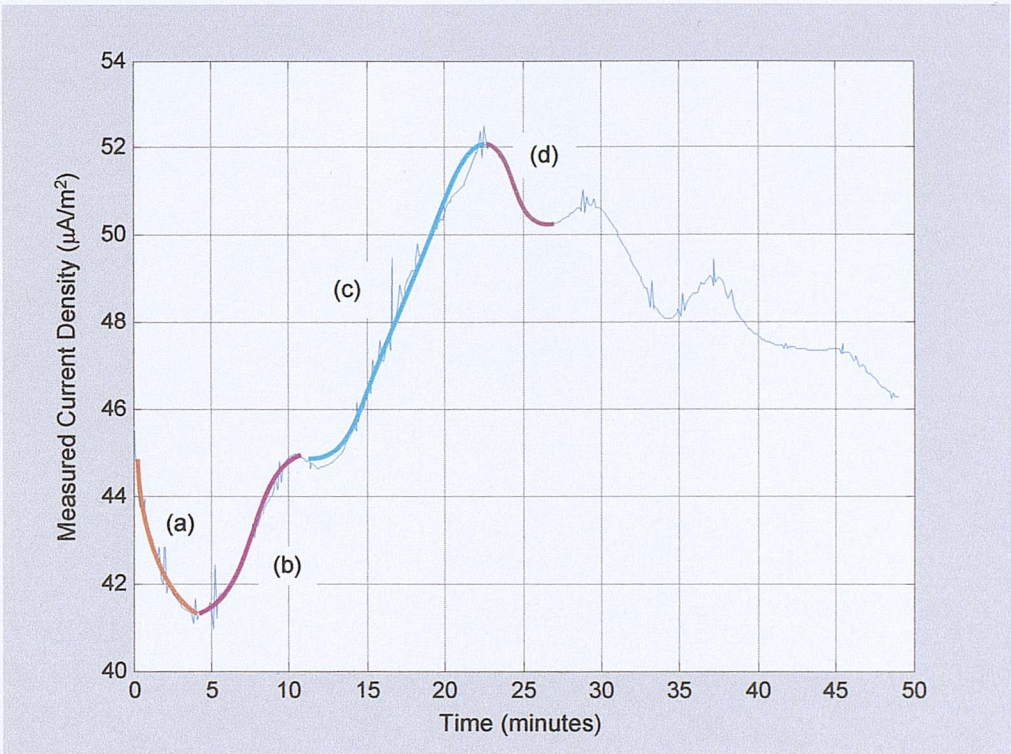

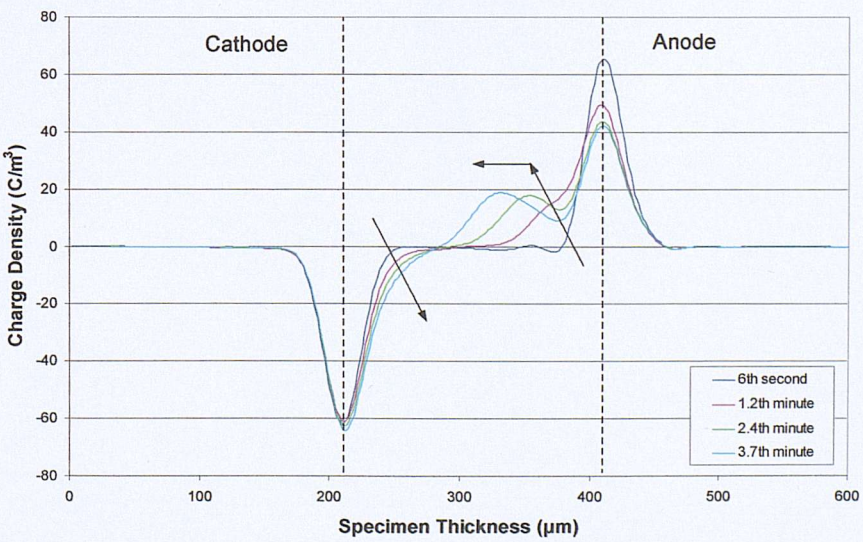

Space charge distribution of trend (a)

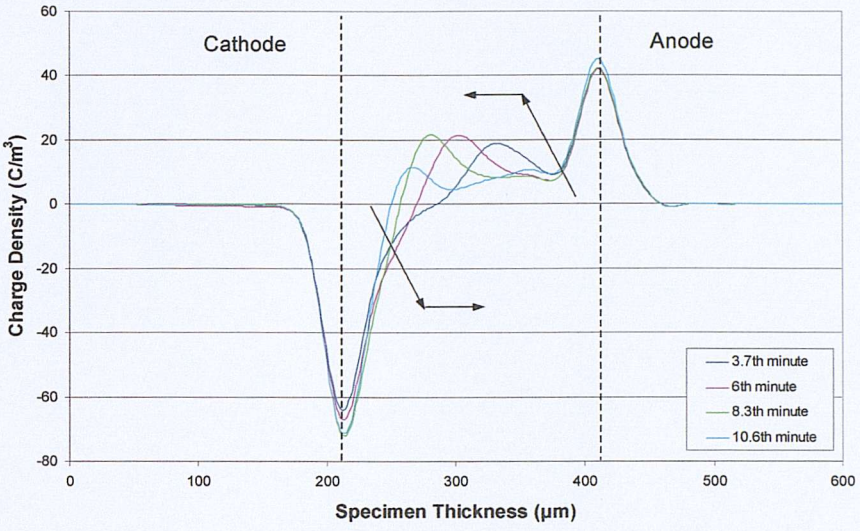

Space charge distribution of trend (b)

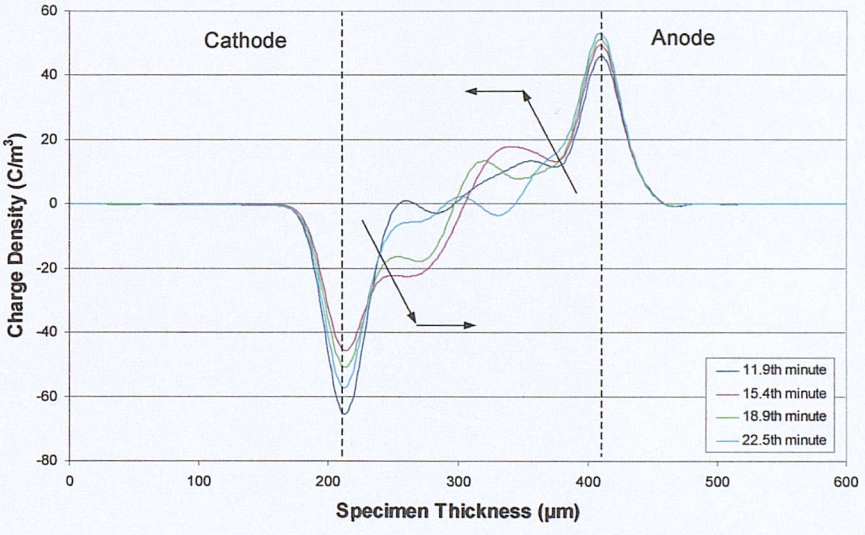

Space charge distribution of trend (c)

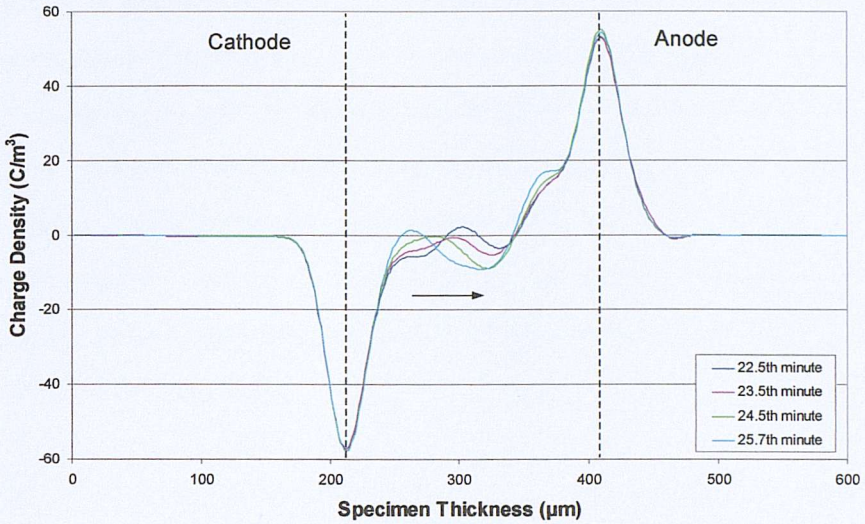

Space charge distribution of trend (d)

Figure 4.6. An example of corresponding current and charge density profiles of XLPE.

Parts of the measured current trend were picked to illustrate current-charge density connection. Trend (a) as labelled in the figure shows measured current reducing gradually, the charge density profile shows some of the injected negative charge carriers accumulated steadily near to the cathode, this hindered further subsequent negative charge carriers injection, which led to reducing amount of injected charge. At the same time, a portion of the negative charge carriers was also being extracted at the anode (larger quantity of positive charge carriers in bulk). Trend (b) shows the measured current increment, continuing from trend (a). Since more negative charge carriers were extracted at the anode, more negative charge carriers were able to move more freely towards the opposite electrode. As a result, increasing amount of negative charge carriers were easily being injected, this is more obvious after the 8.3^{th} minute, as the positive charge carriers near to the cathode collapses (extracted by the cathode) significantly.

In the case of trend (c), similar to trend (b) the external measured current escalated, the space charge profile showing a huge increase in injection of negative charge carrier starting from the 11.9^{th} minute. The injected negative charge carriers travel progressively towards the anode (reducing amount of negative charge carrier

near the cathode and positive charge carrier near to the anode) and were extracted ultimately which causes successively growth of the measured current. Trend (d) is another example similar to tend (a), it was obvious that no significant increase in the amount of negative charge carrier injected from the cathode because there was little continuous negative charge carriers extraction (the amount of positive charge carriers near the anode remains almost the same), with only the already injected and accumulated negative charge carriers near to the cathode trying to move closer towards the anode. All this evidence clearly supported the earlier deduction about the charge carrier behaviour.

The above experiment was performed to demonstrate the characteristic of charge carrier movement in relation to the external measured current changes. The external measured current includes a portion of constant leakage current (an imperfect capacitor, see figure 4.4) and a fraction of negative charges from the supply which are either injected into the bulk or surface charge on the cathode due to the injection of positive charges.

It is important to bear in mind that injection of the induced surface negative charges on the cathode into the bulk or negative injected bulk charges moving deeper towards the opposite electrode can affect the subsequent rate of electron injection (external measured current) from the supply. This is because as more negative carriers moving towards the anode there are also negative carriers being extracted by the anode, thus it allows higher rate of electron injection. The subsequent current measurement (picoammater current reading) reflects the amount of electron injection being injected from the supply towards the specimen at that moment of time; it does not include the existing surface charges on the cathode or the negative bulk charges. Therefore, sometimes when the space charge profile shows a growing quantity of electrons (decreasing amount of positive charge carriers) in the bulk, it is hard to deduce whether there is a new increase amount of electron injection from the supply into the bulk or injection of the induced surface charges on the cathode into the bulk, as both might occur concurrently. Therefore, measured current trend will help to verify the situation. The justification and reason for increment and decrement of the measured current will be discussed and analysed in chapter 8.

4.5 Importance of temperature on current measurement

The total current flowing in the external circuit is measured by the picoammeter. It can be expressed as

$$I_{ext}(t) = I_c(x,t) + I_d(x,t) + I_{diff}(x,t) \tag{4.3}$$

where I_{ext}, I_c, I_d and I_{diff} represent the external, the conduction, the displacement and diffusion currents respectively. Assuming diffusion current $I_{diff} << I_c$ and can be neglected [69, 70], therefore the conduction current is simply equal to

$$I_c(x,t) = I_{ext}(t) - I_d(x,t) \tag{4.4}$$

The displacement term can be expressed as

$$I_d(x,t) = S\varepsilon_o\varepsilon_r \frac{\partial E(x,t)}{\partial t} \tag{4.5}$$

where S is the area of the electrodes. In order to calculate the I_d, the variation of E versus t at each position x is calculated. In fact displacement current can also be disregarded because of the long time scales related to space charge build-up. Thus assumption can be made taking the external measured current to be the conduction current. The conduction current density equation is represented by

$$J = e\,n\,\mu\,E = \rho\,\mu\,E = \sigma\,E \tag{4.6}$$

where σ refer to conductivity of the material. The conductivity $\sigma(T)$ follows an Arrhenius relation

$$\sigma(T) = \sigma_o \exp\left(-\frac{E_a}{k_B T}\right) \tag{4.7}$$

where σ_o is a constant of the material, E_a is an activation energy and T is the temperature. The conduction current is temperature dependent therefore resulting in a conductivity change which is expected to affect space charge throughout the insulation bulk.

In order to emphasize the importance of temperature on the specimen under test, the following shows one example of the tests carried out with the following configuration under open room situation with no control over the surrounding temperature of the cell [71]. The testing conditions were as follow: -

(a)	Specimen type	: Low density polyethylene (LDPE)
(b)	Specimen thickness	: 200μm
(c)	Cathode	: Evaporated aluminium
	Anode	: Semicon
(d)	Applied voltage	: 20kV
(e)	Stressing period	: Continuously for 8 days

Figure 4.7 illustrates the current density profile over a period of 8 days and the space charge profiles at time corresponded to the peaks labelled on the measured current graph. Charge density profiles are selected at (1) lowest point before the peak, (2) at the peak and (3) lowest point after the peak. Huge spurious oscillations were observed in the measured current trend. When interrelating to space charge profiles, larger and steeper peak no. 2 did not reflect the anticipated enormous movement of charge carriers as compared to the peak 1 or 3 which is smaller and shallower.

Through more in depth examination, it has been realised that the oscillations were due to the fact that the temperature varied. The experiment was performed under open room situation where a slight change of temperature (few degree Celsius) during the day and night time can engender the fluctuation of the measured current. This can be visualized by the fact that changes from lower to higher temperature provides higher thermal excitation energy, which encourages movement of fast mobile charge carriers, the ammeter was able to capture this faster mobile charge progression. Incidentally, no conspicuous charge activity was observed using the PEA measurement system. It can be justified by the fact that conductivity (current) relies on two crucial factors, (a) the amount of mobile charge available for conduction and (b) its mobility. Since these two elements are temperature dependent, any increase of these two values (caused by higher temperature) will result in an

escalation of the external measured current. This insinuates the quantity of charge carriers detected by the PEA technique consist only a very small portion of fast mobile charge. This experiment was repeated under a temperature-controlled environment and the result is discussed in chapter 5.

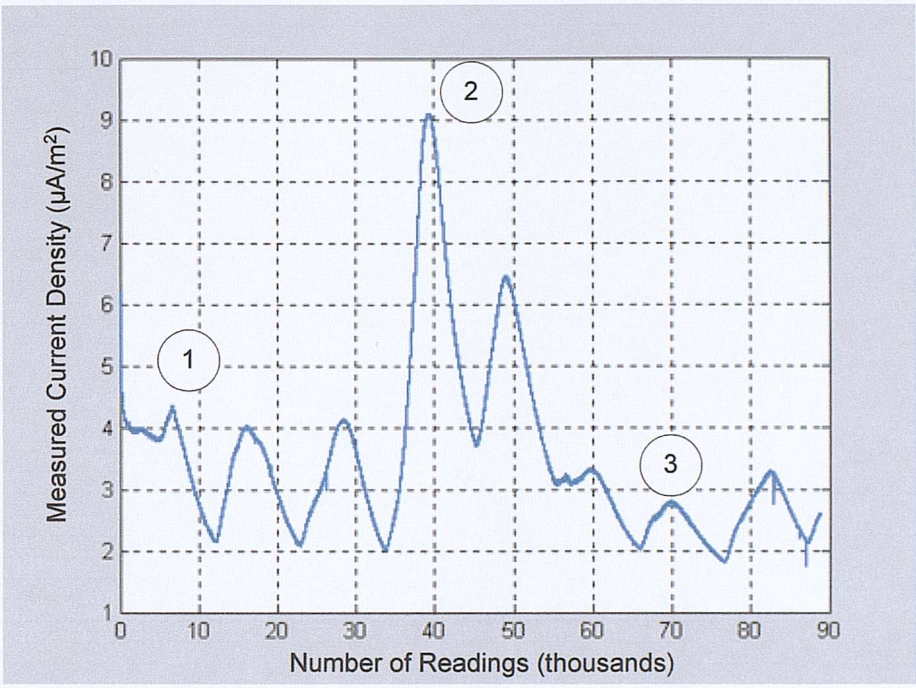

The first 5000 readings were based on every 5sec and thereafter every 8sec interval.

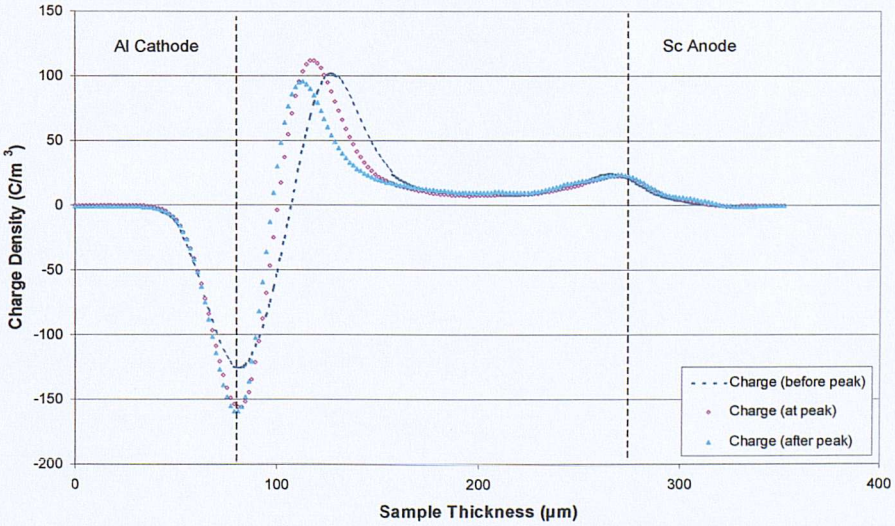

Space charge distribution of peak (1)

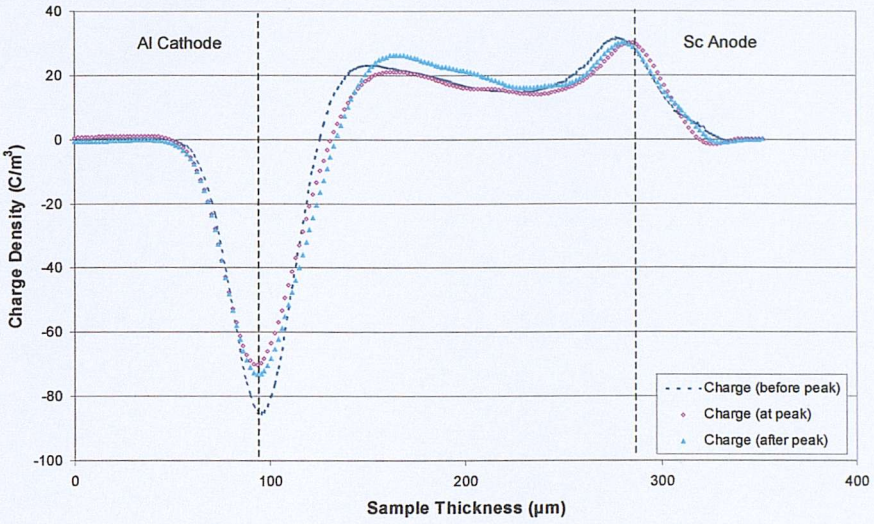

Space charge distribution of peak (2)

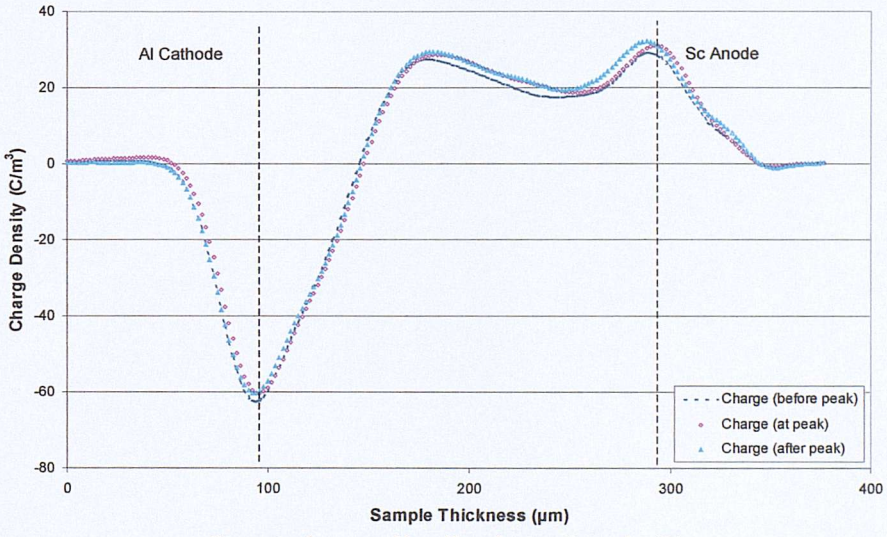

Space charge distribution of peak (3)

Figure 4.7. Corresponding current and charge density profiles of additive-free LDPE.

4.6 Conclusions

The charge carrier behaviour can be explained by the presence of electrons, holes, positive and negative ions depending on the type of specimens. The decaying of measured current (flow of electrons) before steady state is achieved include a proportion of constant leakage current and also a reducing portion of electrons from the supply either being injected into the bulk and/or surface charge on the cathode caused by injection of positive charge carriers. Whereas the increasing of the

measured current include the proportion of constant leakage current and also a escalating share of electrons from the supply being injected into the bulk although a small fraction of it might be the surface charge on the cathode due to injection of positive charge carriers.

The importance of temperature influence on current measurement was highlighted. The experimental result shows a slight change in few degrees Celsius will increase the mobility and amount of fast mobile charges; the changes can be captured very clearly by the picoammeter but are not so noticeable by the PEA system. This insinuates the charge profile captured by the PEA system consist of a very small amount of fast mobile charge.

Chapter 5

Charge Dynamics and Transport in Additive-free LDPE with Electrode and Temperature Effect

5.1 Introduction

It is known that low density polyethylene (LDPE) is used together with crosslinking agent to form crosslinked polyethylene (XLPE). Crosslinking reaction alters the chemical composite and structure of LDPE. It has been shown and recognised [40, 72, 73] that crosslinking by-products led to the formation of heterocharges in XLPE due to the dissociation of its chemical contents under the influence of the electric field. Before looking into the implication of crosslinking reaction, it is best to study the electrical conduction characteristic of LDPE under various testing conditions.

The nature of space charge, its density and distribution within the insulation depend on material structure, additives, crosslinking by-products, impurities and other defects. In the experiments reported here, the electrode material effect [74] and temperature [75] influence on charge dynamics in LDPE are investigated.

5.2 Electrode material effect on electrical conduction and space charge

Sample preparation and the electrode material can play a critical role in determining the charge carriers' behaviours. Formation of the electrode is of great importance. In laying down the conductive material, the surface should not be chemically changed and there should be no gaps between the electrode and sample. Vacuum deposition of metal such as silver, aluminium or gold is commonly employed. In this case, evaporated aluminium (Al), semicon (XLPE loaded with carbon black, Sc) and solid aluminium block were used to examine their individuality on space charge generation, transportation and accumulation processes in pace with external measured current behaviour.

5.2.1 Sample preparation

Commercially available additive-free LDPE of density 0.92g/cm^3 was used. It comes in a form of thin sheet that can be cut into required size. Dust can be removed by a gas jet directed at the specimen surface. Care must be taken to avoid scratches on the surface.

Three types of electrode material were used, namely (a) semicon press-moulded from granules into thin sheet was attached onto specimen, (b) aluminium was evaporated onto the specimen surface and (c) the solid aluminium block of the PEA rig's bottom cell. The purpose of having two different ways of preparing aluminium electrode (b) and (c), was to demonstrate the importance of contact surfaces. A thin layer of silicon oil was applied for all experiments on all contact surfaces to aid acoustic signal transmission.

5.2.2 Experimental protocols

Five sets of experiments were carried out in total. The electrode configurations used include (a) evaporated Al(-) with Sc(+), (b) Sc(-) with evaporated Al(+) and (c) solid aluminium block Al(-) with Sc(+). The signs (-) and (+) refer to the cathode and the

anode respectively. Measurements were taken at every 6 seconds intervals throughout the stressing period in an oven at a temperature of 30°C. Table 5.1 shows a summary of each experimental configuration.

Specimen	Electrode configuration	Applied voltage (kV)	Specimen thickness (μm)	Stressing period (days)
1	Evaporated Al(-) with Sc(+)	20	200	3
2	Evaporated Al(-) with Sc(+)	10	200	3
3	Sc(-) with evaporated Al(+)	20	200	3
4	Sc(-) with evaporated Al(+)	10	200	3
5	Solid Al block (-) with Sc(+)	20	195	2

Table 5.1. Summary of experimental configuration for electrode material effect.

5.2.3 Experimental results

Tests on specimen no. 1 to 4 were carried out to give an idea of electrode material effect when exposed to different polarities. Figure 5.1 represents the measured current and space charge density measurement for specimen no.1.

Right after the application of HVDC voltage, positive and negative carriers were injected into the bulk to form homocharges. The dominating positive charge packet was seen moving towards the cathode. The measured current density in figure 5.1(a) shows a decreasing trend until the ~74^{th} minutes, then it started to escalate for a period of about 46 minutes before returning to a declining signal until the end of the stressing period. Such a transient current peak can be imputed to transient space charge limited current (SCLC) peak (chapter 2.4.2, pp.30). Figure 5.1(b) shows the space charge profile corresponded to the time of the transient current peak. At the ~74^{th} minute, the accumulated dominating positive packet charge front (~150μm from the anode) was reducing gradually. The time at which the positive packet charge front diminishes to a stabilized state was at the ~120^{th} minute. This suggested that the transient current peak corresponded to the motion of the charge packet; this

is an analogy of direct effect of space charge dynamics on electrical conduction. Figure 5(c) presents the charge density profiles associated with the steep decrease of current between 30 to 190 minutes after the transient current peak. It clearly reveals that another positive charge packet accumulated at ~140μm from the anode and at the same time more negative charge carriers were trying to penetrate deeper into the bulk. Figure 5(d) manifests the charge density profile at time much later, from the 198th minute to the 4267th minute, the positive and negative charge carriers were moving deeper into the bulk towards the opposite electrode.

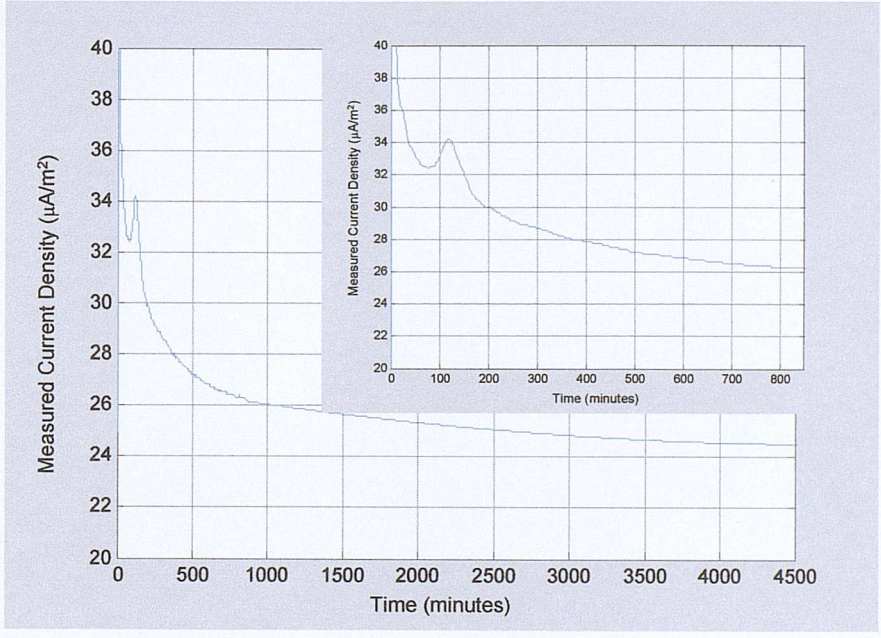

(a)

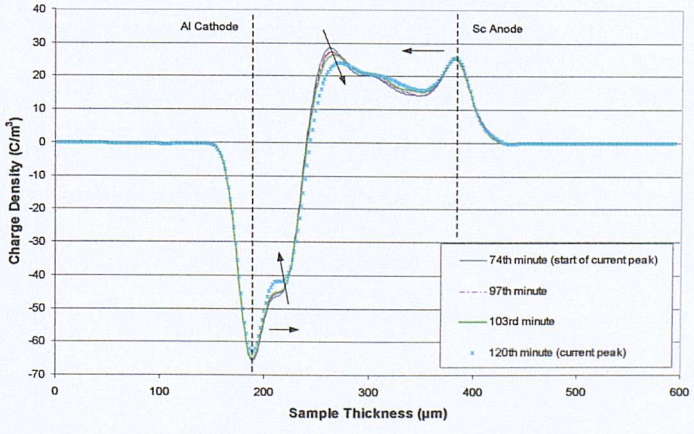

(b)

(c)

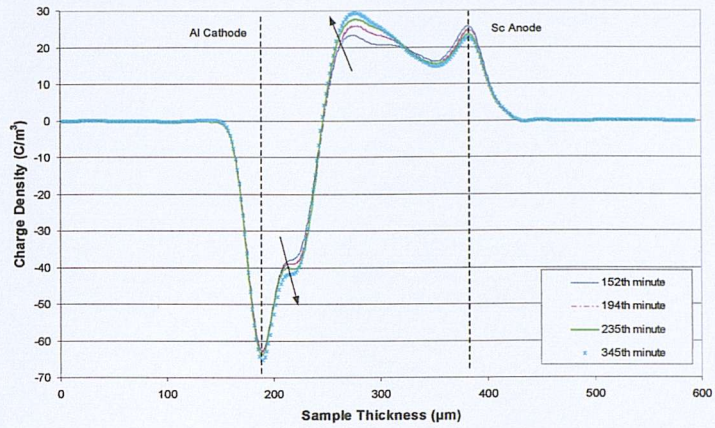

(d)

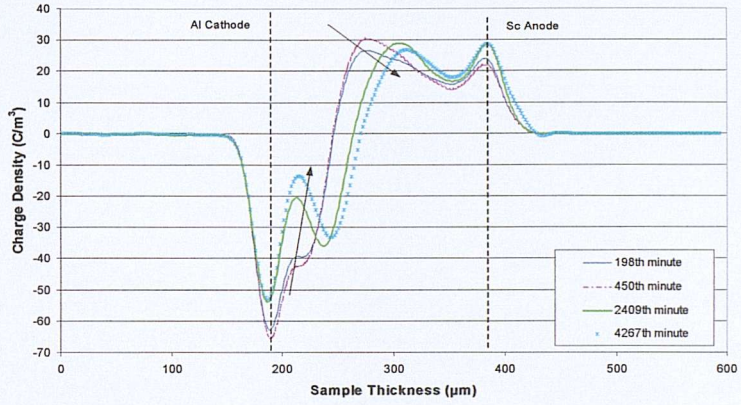

Figure 5.1. (a) The measured current density, (b) space charge density profile corresponded to the transient current peak, from the 74th to 120th minute, (c) space charge density profile from the 152nd to 345th minute and (d) space charge profile from the 198th to 4267th minute at 100kV/mm applied stress, using evaporated Al(-) with Sc(+).

Figure 5.2 represents the measured current and space charge density measurement for specimen no. 2. It uses the same electrode configuration as specimen no. 1 but at a lower applied electric stress of 50kV/mm. Figure 5.2(a) expresses a very small transient current peak at the ~680th minute and no other major current movement throughout the 3 days of stressing period. Figure 5.2(b) is the charge density distribution from the 10th to 3255th minute. It exhibited a similar behaviour to specimen no.1 where homocharges were injected from both electrodes and positive charge carriers were the dominant party.

(a)

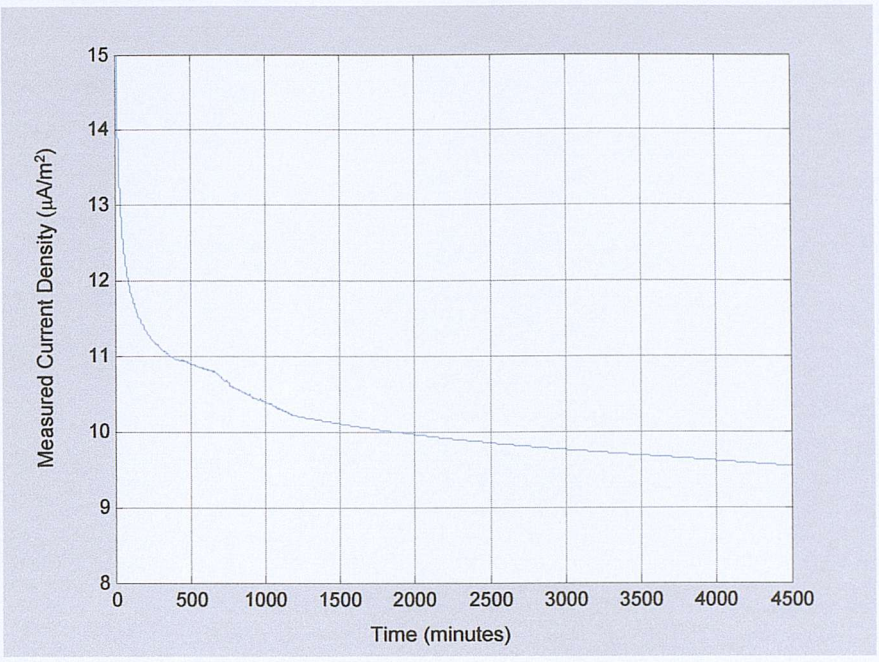

(b)

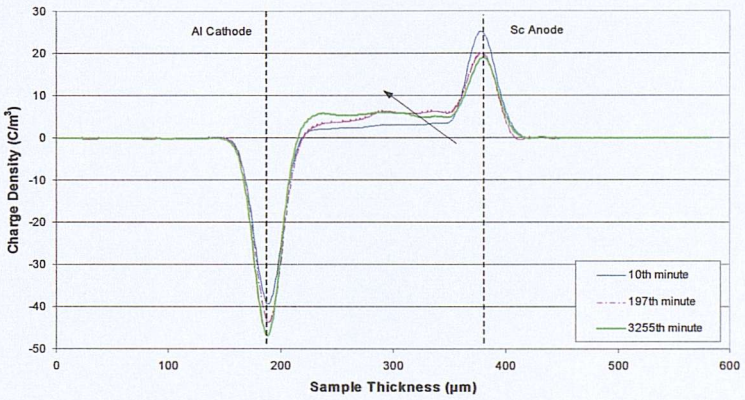

Figure 5.2. (a) The conduction current density and (b) space charge density distribution from the 10th to 3255th minute at 50kV/mm applied stress, using evaporated Al(-) with Sc(+).

Figure 5.3 represents the measured current and space charge density measurement for specimen no. 3. This test employed the same electrode material as in specimen no.1 with the opposite polarity. Current density graph is shown in figure 5.3(a). Small transient current peak occurred at the ~643rd minute which indicates an increasing positive charge extraction. Continuous increase in current was observed from the ~2000th minute towards the end of the stressing period. Soon after HVDC voltage was applied, positive and negative carriers were injected into the bulk to form homocharges. In this case, the dominating charge carrier was the negative

charge packet and it was moving towards the anode as time increased. Space charge distribution is shown in figure 5.3(b). Interestingly, the homocharges created became heterocharges after the ~2172nd minute; this is because the anode partially blocks the extraction of mobile charge injected from the cathode and vice versa. Notice the difference in space charge distribution between specimen no. 1 and 3 when the same electrode materials were utilised at different polarities. This implies that there is difference in charge injection efficiency.

(a)

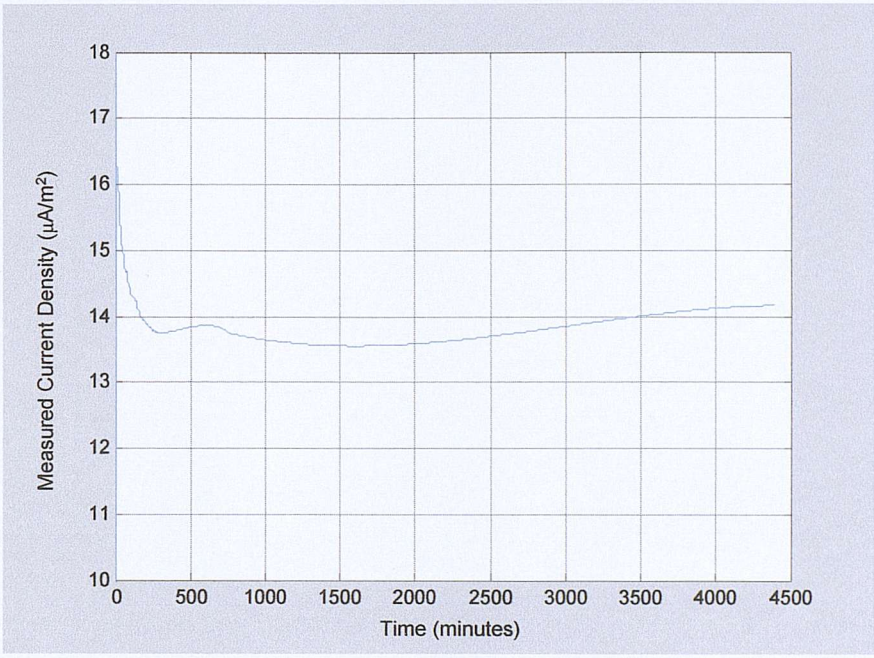

(b)

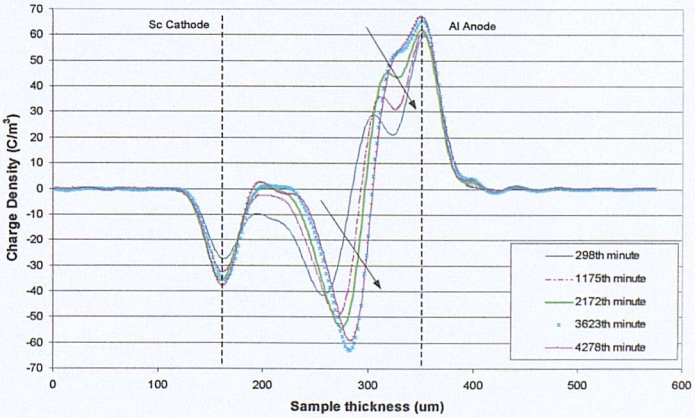

Figure 5.3. (a) The measured current density and (b) space charge density distribution from the 298th to 4278th minute at 100kV/mm applied stress, using Sc(-) with evaporated Al(+).

Figure 5.4 is the measured current and space charge density measurement for specimen no. 4. It used the same electrode configuration as specimen no. 3 but at a lower applied electric stress of 50kV/mm. A similar characteristic to figure 5.2 was captured, but this time, domineering injected negative charge packet was penetrated from the cathode to the anode. The charge density profile at the 1670th minute does not show much difference from the end of the stressing time at the 4320th minute.

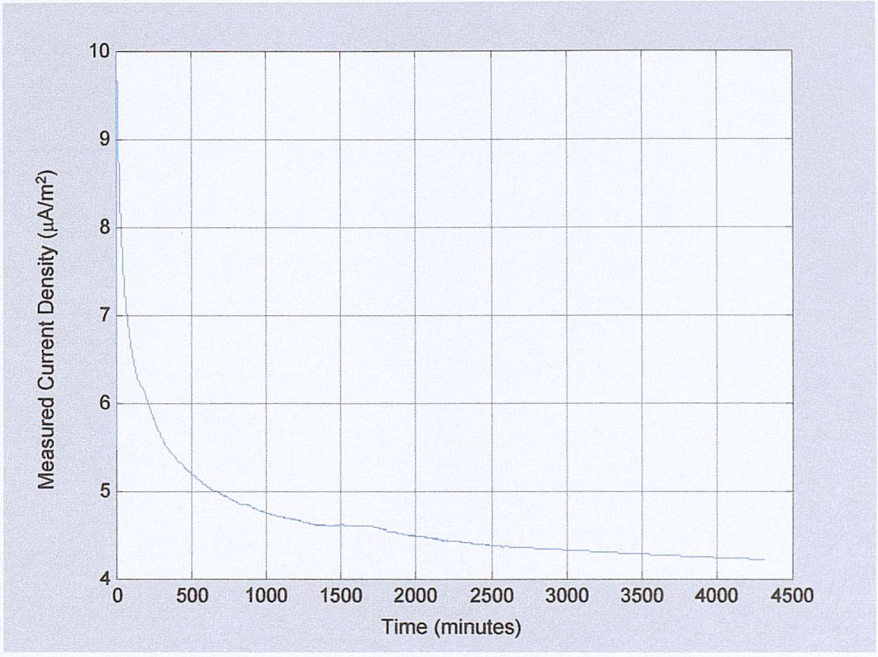

(a)

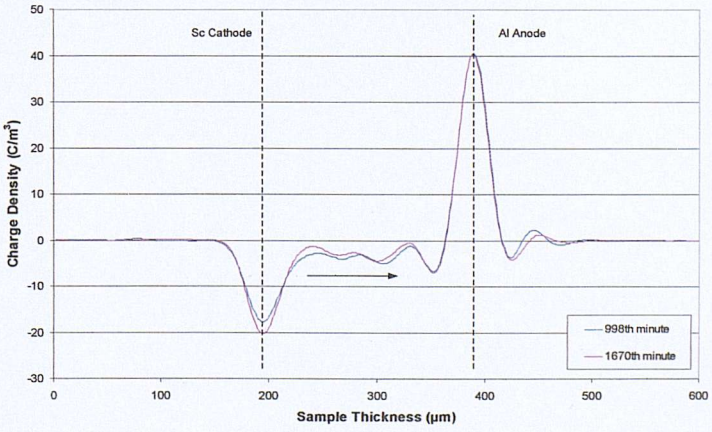

(b)

Figure 5.4. (a) The measured current density and (b) space charge density distribution from the 998th to 1670th minute at 50kV/mm applied stress, using Sc(-) with evaporated Al(+).

Figure 5.5 represents the measured current and space charge density measurement for specimen no. 5. It used the solid aluminium block of the PEA bottom cell (ground) as the cathode instead of evaporated aluminium onto the specimen. This experiment was performed to demonstrate the importance of contact surfaces.

Figure 5.5(a) is the current density graph. A transient current peak lasted for ~70 minutes started from the 60th minute. Space charge profile at time corresponded to the transient current peak is shown in figure 5.5(b). Positive and negative homocharges were injected into the bulk. Both cathode and anode can inject very well, large amount of the positive and negative carriers were accumulated at ~82μm from the cathode. At the 60th minute, the accumulated positive and negative charge packet started to trim down significantly for a period of ~70minutes. This denotes that large quantity of accumulated negative carriers were extracted constantly for that period of time which encouraged more negative carriers injection from the supply. Figure 5.5(c) presents the charge density profile from the 100th to 2880th minute, showing carriers almost stabilized after the 1960th minute with the measured current also practically stagnant.

(a)

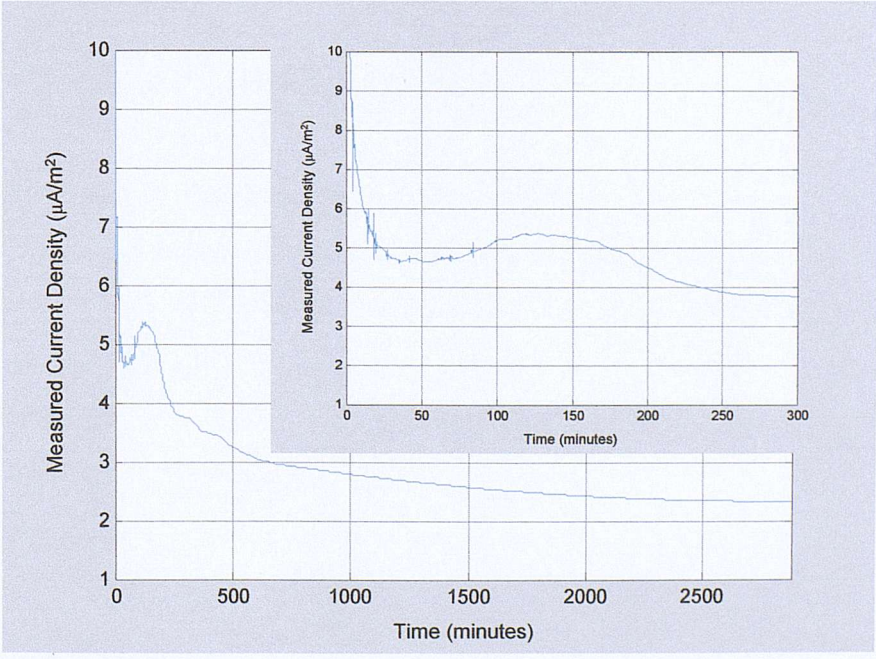

(b)

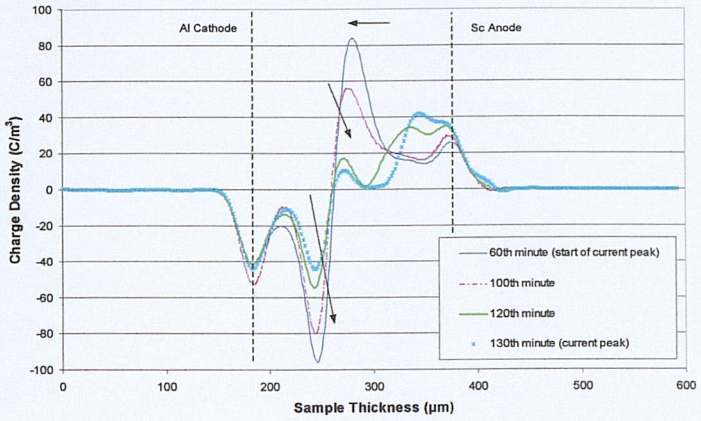

(c)

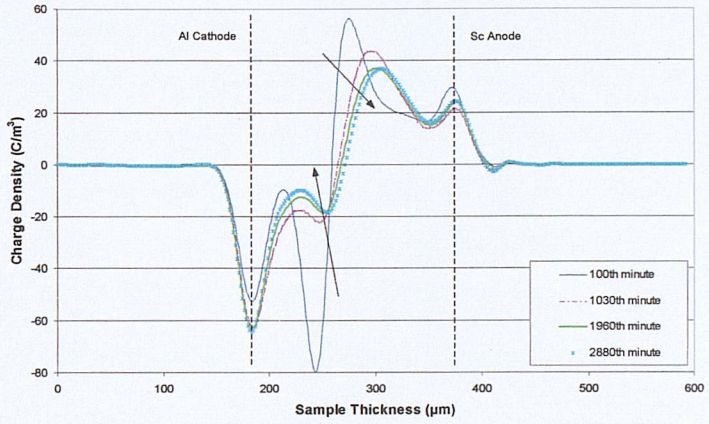

Figure 5.5. (a) The measured current density, (b) space charge density profile corresponded to the transient current peak, from the 60th to 130th minute and (c) space charge density profile from the 100th to 2880th minute at 100kV/mm applied stress, using solid Al block(-) block with Sc(+).

5.2.4 Analysis and discussion of the results

The results obtained clearly reveal that the efficiency of charge carrier injection is affected by the applied electric stress, electrode material and polarity. The material used for the experiments is additive-free LDPE; therefore the impurity effect should not be a major influence in the charge generation. In the absence of impurities dissociation in the bulk, charge distribution depends on the charge injection at both electrodes and mobility of charge carriers.

Here, the mechanism responsible for the efficiency of charge carrier injection seen earlier was credited to Schottky injection (chapter 2.4.1A, pp. 26); where the carriers were thermally excited over the interfacial potential barrier between the

electrode and specimen into the bulk with the help of the applied field lowering the barrier. With the same type of electrode material and specimen, the higher the applied electric field the easier the carriers are injected. This can be verified by comparing figures 5.1(d) to 5.2(b) and 5.3(b) to 5.4(b), where higher applied field of 100kV/mm presented with a larger quantity of accumulated charge carriers in the bulk and larger measured current too compared to the applied electric field at 50kV/mm. In addition, with the same level of the applied electric field used in the same type of specimen, the rate of injection depends on the type of electrode material. All materials have different work functions which will determine the interfacial potential barrier height upon bringing two materials in contact. The higher the barrier height the more difficult carriers were to be injected into the bulk. Again this can be confirmed by evaluating figures 5.1 to 5.4, a contrasting capacity of carriers being injected by the aluminium and semicon, obviously the amount of charge carriers injected by semicon were greater than aluminium irregardless of the polarity. This implied that the semicon-LDPE barrier height is lower than the aluminium-LDPE which therefore enhances more charge carriers.

However, with the same electrode material exposed to different polarity will also affect the interfacial barrier height. This is illustrated more evidently in specimen no. 1 and 3 (at 100kV/mm applied electric field) than specimen no. 2 and 4 (at 50kV/mm applied electric field). Figures 5.1 and 5.3 used the same electrode materials but at different polarity, although in both cases, the semicon electrode was able to inject more charge carriers than the evaporated aluminium electrode but in actual fact semicon cathode were able to inject more than semicon anode and aluminium anode had injected more than aluminium cathode [31]. This deduction was supported by calculating the amount of positive and negative charge carriers remaining in the bulk immediately after volts-off. This might be so because when Sc(-) with Al(+) electrode configuration was used, Sc(-) injected more charges as compared to Sc(+) and therefore this enhanced a higher local electric field in the bulk which encouraged more positive charge injection from Al(+). Similarly, when Sc(+) with Al(-) electrode configuration was employed, Sc(+) injected lesser charges as compared to Sc(-) and therefore it enhanced a lower local electric field in the bulk (as compared to Sc(-)) which encouraged lesser negative charge injection from Al(-). By

calculating the electric field distribution from the space charge profiles of figures 5.1 and 5.3, it has proven that the maximum enhance local electric field is ~160kV/mm for Sc(+) with Al(-) electrode configuration and ~180kV/mm for Sc(-) with Al(+) electrode configuration. Notice in figure 5.3(a) with Sc(-) with Al(+) configuration, current density graph shows the measured current kept increasing after the ~2000th minute, this inferred that there was increasing continuous injection of negative charge carriers till the end of the stressing period. The corresponding charge density distribution in figure 5.3(b) also supported this statement. In contrast to figure 5.1(a) current density graph displays a decaying measured current trend right after the 120th minute till the end of the stressing period. This led to the conclusion that conduction relies not only on the amount of electrons injected but also the ability of electrons extraction, only if more electrons can be extracted, more electrons can be injected.

Test on specimen no.5 demonstrates the importance of contact surfaces. This specimen has the same electrode configuration as specimen no. 1, Al(-) with Sc(+), the only difference was the way aluminium electrode at the cathode was prepared. For this instance, the PEA bottom cell solid aluminium block was treated as the cathode. Although, both were aluminium, but specimen no.5's solid aluminium block cathode can inject better than specimen no. 1's evaporated aluminium cathode, as illustrated in figure 5.5. The first instinct was that the evaporated aluminium(-)/LDPE interface should have a better intimate contact compared to aluminium block(-)/LDPE which logically meant that poorer contact will have weaker injection ability, but on the contrary there were more charge carriers accumulated in the bulk for the case of aluminium block electrode.

However a more likely cause could be the silicon oil that was applied to all surfaces to improve acoustic transmission. It has been reported [32], insulating silicon oil has a lower potential barrier height compared to aluminium, which supposed that silicon oil has a greater power of injecting than aluminium. Therefore, if the real contact was aluminium block/silicon oil(-)/LDPE instead of aluminium block(-)/LDPE, then silicon oil would have no problem transporting the charge carriers that were being injected by the aluminium block into the bulk of LDPE. This has been validated by relating the use of silicon oil for the tests on specimen no. 1 to

4. When evaporated aluminium was employed as an electrode, it gave a direct contact between aluminium and LDPE, even if silicon oil (lower potential barrier height, enhances easier charge carrier injection) was applied onto the evaporated aluminium surface, the evaporated aluminium (higher potential barrier height) which was in direct contact with the LDPE would have blocked and obstructed the carriers movement. And for the case of utilising semicon as electrode, the semicon was not in intimate contact with the LDPE, a layer of silicon oil was applied in between the semicon and LDPE. However, the potential barrier height of semicon is higher than silicon oil [32], which meant that semicon has a lesser aptitude of injecting. Consequently, the amount of charge carriers that could be injected into LDPE is limited by semicon electrode and silicon oil just acted like a middleman who delivered whatever was being injected by the semicon into the bulk of LDPE. In spite the presence of the silicon oil, all the earlier analysis still holds.

Literature search [76] revealed the existence of fast moving charge packet formation in XLPE insulation. These space charge packets formed periodically close to one electrode, migrate across the specimen and exit at the other with accompanying current oscillation. The formation of fast moving charge packet in XLPE will be investigated in chapter 6. Even though fast moving packet charge was not observed in LDPE, but in this study occasional current oscillation (transient current peak) was captured. The ascending and descending of the measured current was the result of the rate of carrier injection and extraction. The measured current are mainly caused by the movement of charge carriers which also known as conduction current. A small portion of it might be caused by dipole orientation but in the case of polyethylene [77], dipole polarisation is not the main contributor, as polarisation current will achieve steady state very quickly.

5.3 Temperature influence on electrical conduction and space charge

A slight change in operating temperature (few degrees Celsius) at a constant applied electric field would result a significant change in external measured current. This change reflects the amount of mobile charge carriers passing through the specimen

per unit time. Usually increase of the measured current and reduction in electrical breakdown strength occur with the escalation of temperature. Higher temperature is believed to encourage not only more mobile charge movement but also increase the probability of getting trapped charges detrapped, thereafter these charges might either recombine with charges of opposite sign or get extracted by the counter electrode.

Presently, there have been very few reports on the analysis of current behaviour with reference to space charge profile at high temperature. M. Nagao et al [78] detected the surface temperature of the sample during the application of DC voltage by means of a visual thermograph, from their observation; they concluded that Joule heating is the probable instigation of the increased current behaviour. Unfortunately, no simultaneous space charge profiles were available to support their argument. C. Zhang et al [79] also agreed that current causes Joule heating at 60°C, as a result, raises the temperature of the dielectric and vice versa. Their conclusion was supported by the space charge profiles showing the measured current increases with very little change in space charge. Both discoveries are found to be irrelevant to this study investigated.

5.3.1 Experimental protocols

Sample preparation procedure was the same as described in earlier section 5.2.1. Four sets of experiments were performed at various temperatures. Since the purpose was to determine the influence of temperature on electrical conduction and space charge, therefore only one electrode configuration was used, which was evaporated Al(-)/LDPE/Sc(+). Once the set temperature in the oven stabilized, the voltage was applied. Measurements were taken at every 6 seconds intervals throughout the stressing period. Table 5.2 summarizes the conditions of the specimens under test. Specimen no.4 at 65°C broke down after ~2880minutes (2days) of stressing.

Specimen	Electrode configuration	Temperature (°C)	Applied voltage (kV)	Specimen thickness (μm)	Stressing period (days)
1	Evaporated Al(-) with Sc(+)	30	20	200	3
2	Evaporated Al(-) with Sc(+)	45	20	200	3
3	Evaporated Al(-) with Sc(+)	55	20	200	3
4	Evaporated Al(-) with Sc(+)	65	20	200	2

Table 5.2. Summary of experimental configuration for temperature effect.

5.3.2 Experimental results

Figure 5.6(a) to (d) exhibits the measured currents throughout the stressing period for all specimens as stated in table 5.2. It unveils the pattern that the measured current escalates with temperature.

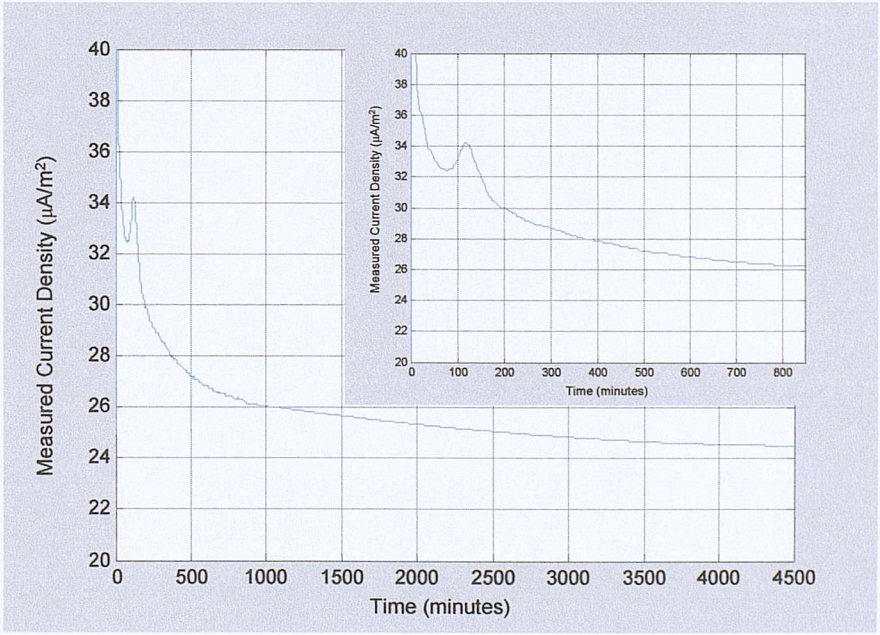

(a)

(b)

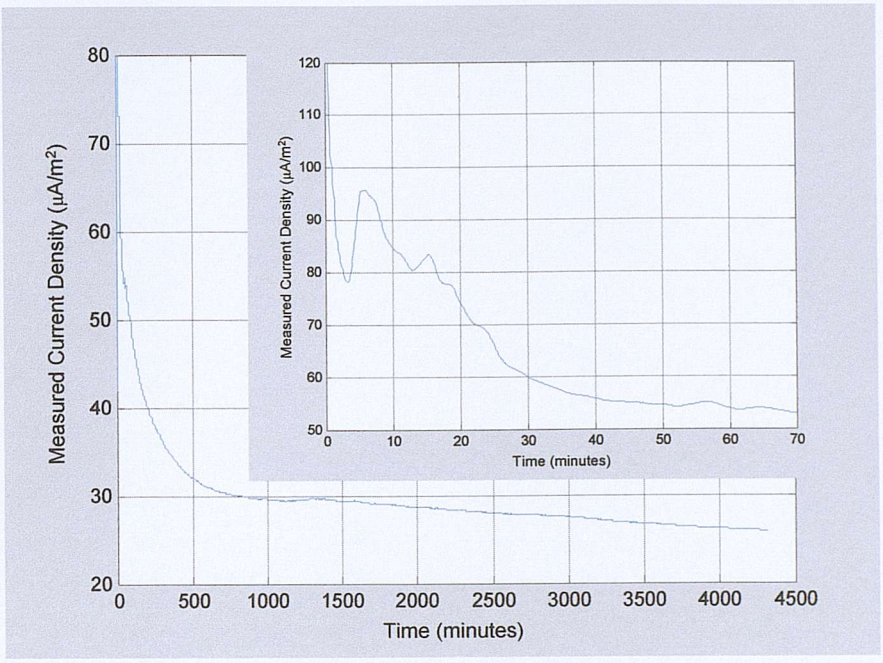
Measured Current Density (μA/m²)
Time (minutes)
Measured Current Density (μA/m²)
Time (minutes)

(c)

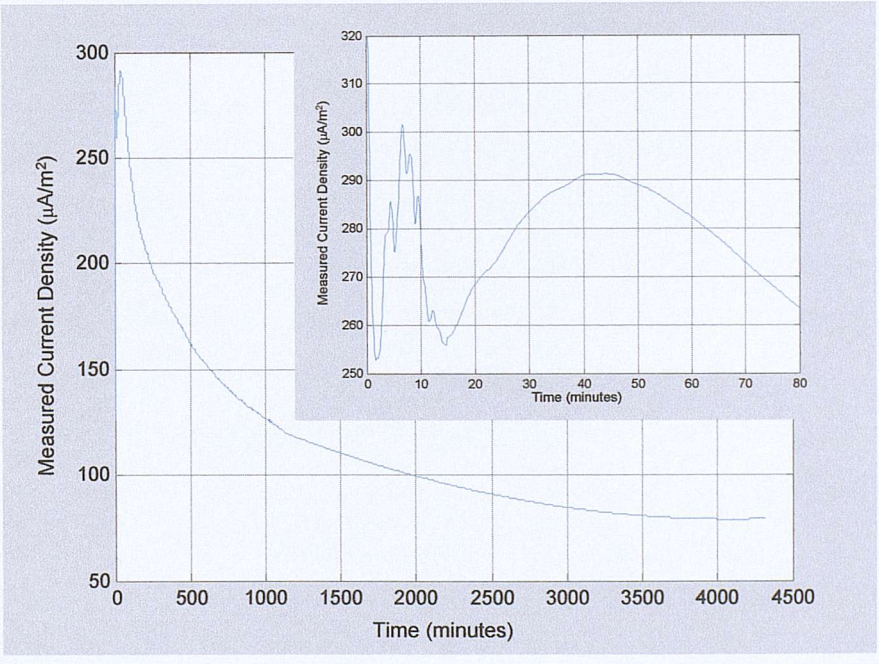
Measured Current Density (μA/m²)
Time (minutes)
Measured Current Density (μA/m²)
Time (minutes)

(d)

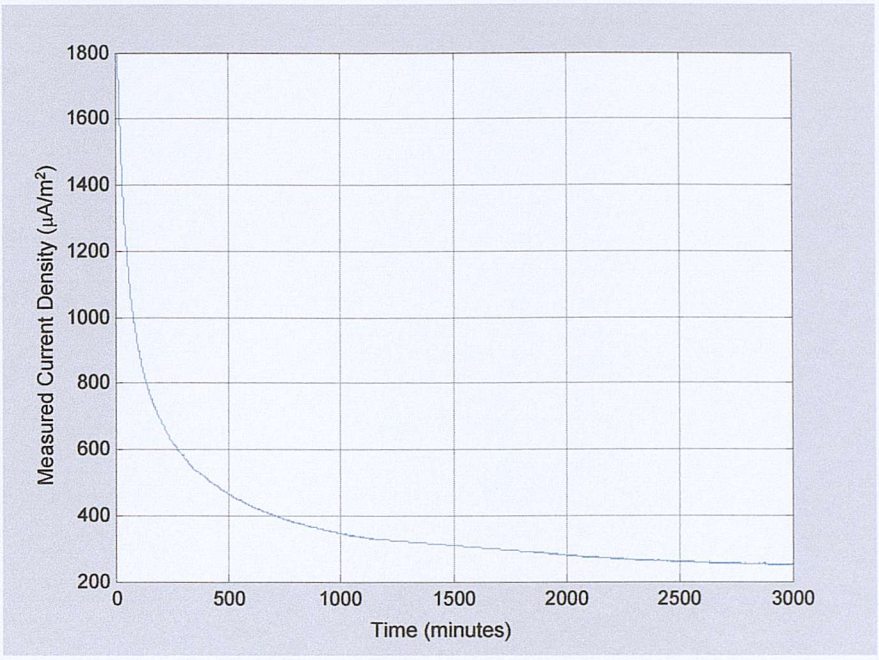

Figure 5.6. Measured current density at 100kV/mm applied field and temperature of (a) 30°C, (b) 45°C, (c) 55°C and (d) 65°C.

As expected, Sc electrode can inject charges more easily than Al, almost instantly after the voltage was applied, dominating positive charges from Sc(+) were advancing towards Al(-). Figure 5.7(a) to (c) demonstrates the charge density profiles corresponded to the time of the first transient current peak for specimen no. 1 to 3, where figure 5.7(d) manifests charge density profile with reference to the time for the second transient current peak for specimen no. 3. The following table 5.3 outlines the occurrence of the transient current peak at different temperatures.

Specimen	Measurement temperature (°C)	Time of occurrence starting from (minute)
1	30	74th
2	45	3^{rd} and 13^{th}
3	55	1.7^{th} and 15^{th}
4	65	Nil

Table 5.3. The time occurrence of transient current peaks.

(a)

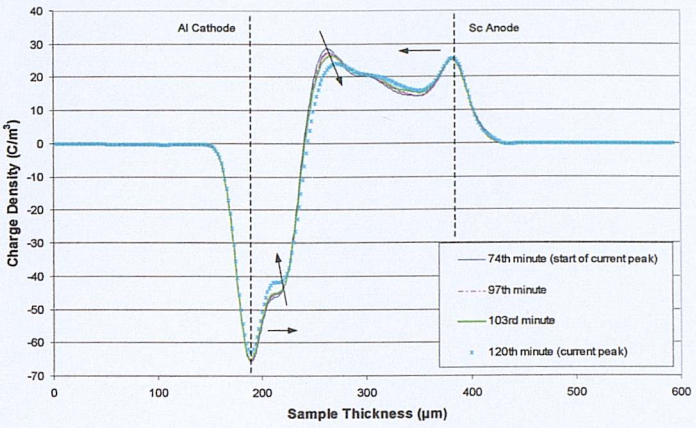
Al Cathode
Sc Anode
Charge Density (C/m³)
Sample Thickness (µm)
74th minute (start of current peak)
97th minute
103rd minute
120th minute (current peak)

(b)

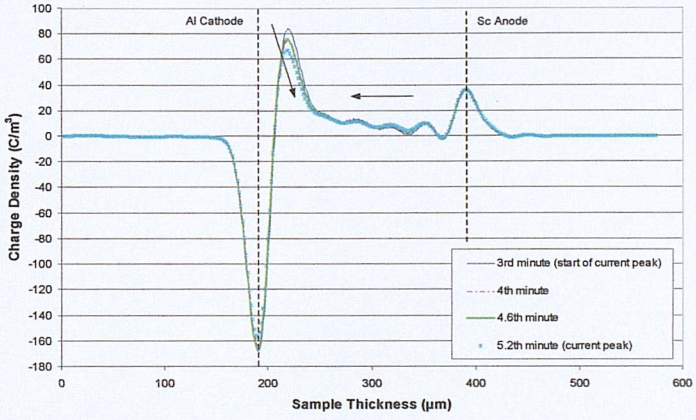
Al Cathode
Sc Anode
Charge Density (C/m³)
Sample Thickness (µm)
3rd minute (start of current peak)
4th minute
4.6th minute
5.2th minute (current peak)

(c)

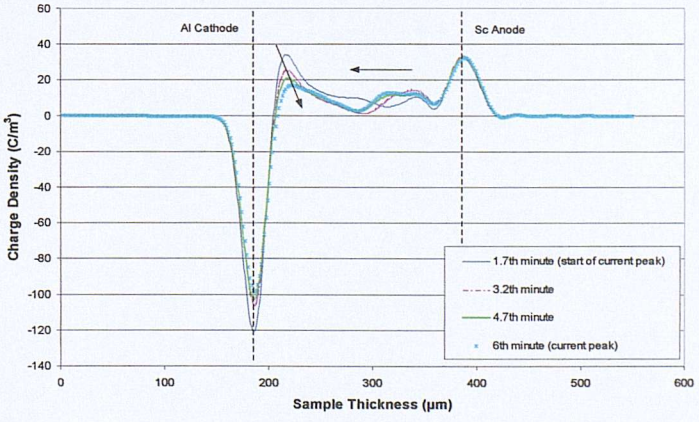
Al Cathode
Sc Anode
Charge Density (C/m³)
Sample Thickness (µm)
1.7th minute (start of current peak)
3.2th minute
4.7th minute
6th minute (current peak)

(d)

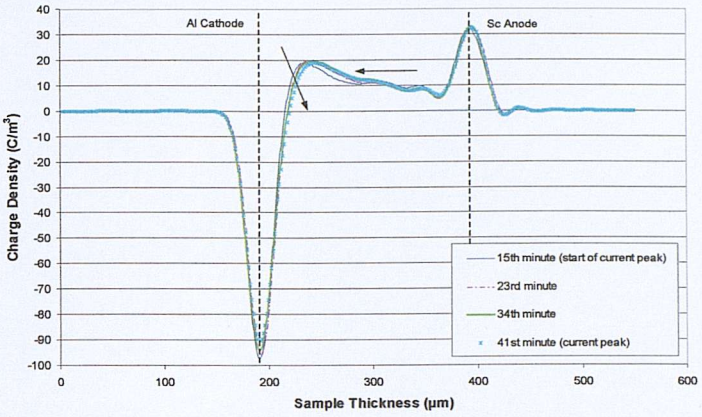

Figure 5.7. Charge density distribution corresponded to the transient current peak at 100kV/mm applied field and at temperature of (a) 30°C (from the 74th to 120th minute), (b) 45°C (from the 3rd to 5.2th minute), (c) 55°C (from the 1.7th to 6th minute) and (d) 55°C (from the 15th to 41st minute).

Figure 5.8 shows the charge density profiles at time much later after the transient current peak/s.

(a)

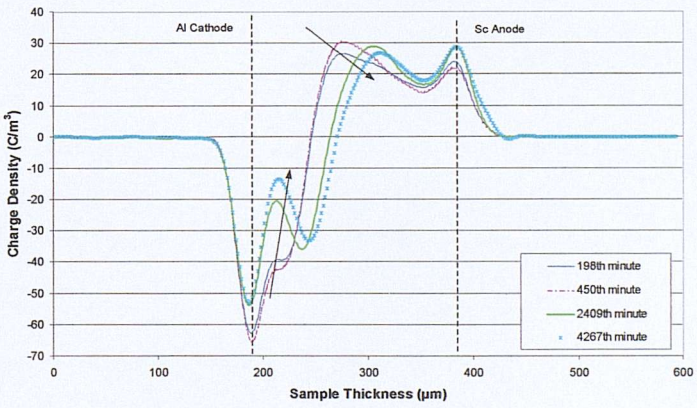

(b)

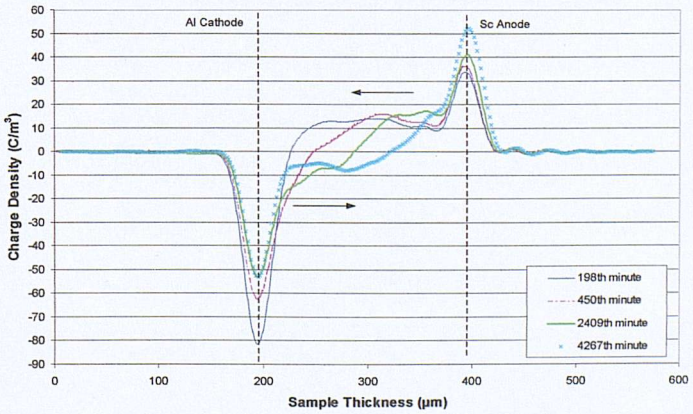

(c)

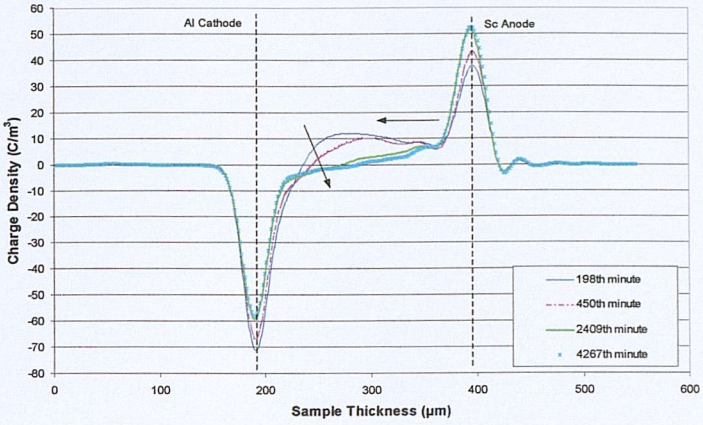

(d)

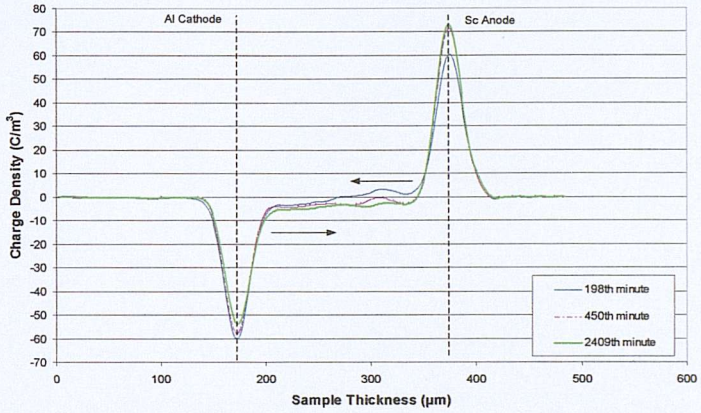

Figure 5.8. Charge density distribution at 100kV/mm applied field and at temperature of (a) 30°C, (b) 45°C, (c) 55°C from the 198th to 4267th minute and (d) 65°C from the 198th to 2409th minute.

5.3.3 Analysis and discussion of the results

The exploration of temperature influence on conduction characteristics divulges that the rise in temperature will not only increase the mobility of carriers and amount of carrier available for conduction (as can be seen from figure 5.6(a) to (d), the higher the temperature, the larger the current density magnitude) but also multiply the opportunity of getting trapped charges detrapped. Thus, they will continue to move towards the counter electrode, these charges will increase the probability of recombining with the opposite sign carriers or/and be extracted by the opposite electrode.

The increase of carrier mobility explains why at higher temperature, the time taken for the first transient current peak (increasing positive charge extraction) to occur is shortened. The first current peak at 30°C occurs at 74 minutes after the applied field. As the temperature goes higher, the time taken for the first current peak to happen is shorter and was followed by subsequence smaller peaks. At 65°C, no transient peak was observed, the possible reasoning might be (a) at such high temperature, the movement of charge extraction was too fast that it was missed out between measurement time, (b) neutralization took place in the bulk at the very instant of the applied electric stress, so when there is no increase amount of accumulated bulk charges being extracted, there will be no increase in charge injection and (c) due to the high mobility of charge carrier, the chances of carriers getting trapped become slimmer, therefore charge carriers available for getting detrapped and extracted by the anode reduces, this led to no increase amount of injected negative charges.

Examination from figure 5.6 showed the possible existence of transient current peak at various temperatures after ~1440minutes either did not take place or took place at a very small magnitude. The corresponding space charge profiles showed the charges of both signs on the electrodes tried to move through the bulk to the counter electrode. This implied that as time passed the occurrence of increasing positive charge extraction was (a) more difficult, (b) lower probability, (c) smaller increment and recombination is more likely to be the major activity.

At higher temperatures, the movement of all carriers intensified. This is supported by comparing the charge density profiles at various temperatures in figure 5.8. At lower temperature, larger amount of carriers were accumulated at the positive and negative carriers meeting point, at elevated temperature lesser charges were accumulated in the bulk. This is further substantiated by the volts-off charge density profiles. Table 5.4 below gives quantitatively the total absolute amount of charge carrier remained in the bulk immediately after volts-off.

Specimen	Measurement temperature (°C)	Total absolute amount of charge carriers (μC)
1	30	2.559
2	45	1.246
3	55	0.368
4	65	N. A.

Table 5.4. Total absolute amount of charge carriers after volts-off.

Figure 5.9 shows the plot of ln J vs (1/T) for LDPE specimens, where J is the 'steady state' measured current density and T is the temperature. Since the test on specimen no. 4 broke down after 2 days of stressing, therefore all the values of J used for plotting was at the ~2880th minute. The plot of ln J vs (1/T) shows a good straight line without taking the value at 30°C under consideration. The current density J obeys the Arrhenius relation (chapter 4.5, pp. 87), where the calculated value of E_a = 1.044eV (which is close to reported value [32] for evaporated aluminium contact). The current value at 30°C is so far off from the straight line plotted using current values at 45°C, 55°C and 65°C might be because the time needed to achieve steady state current is much longer at lower temperature.

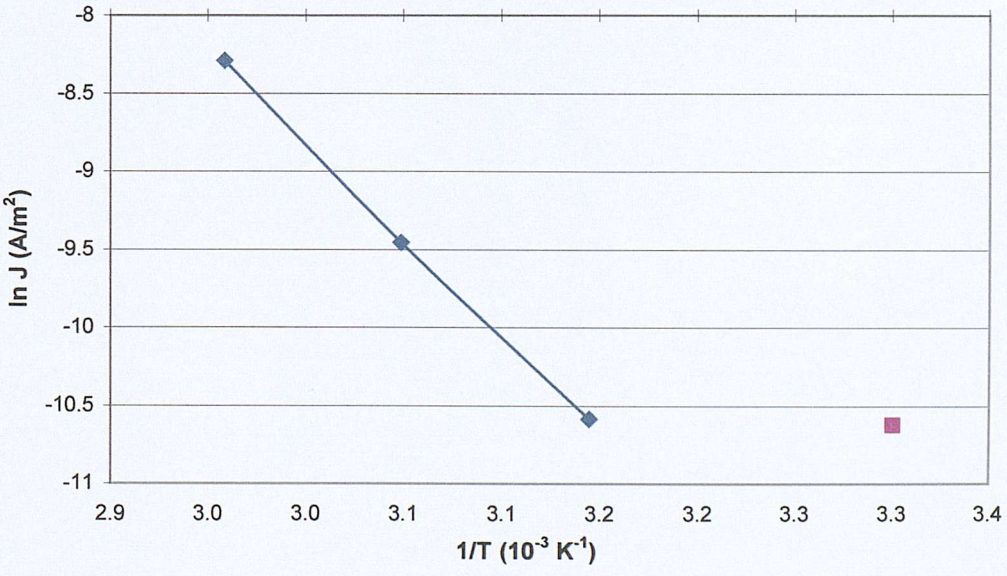

Figure 5.9. Measured current density in the LDPE specimens as a function of reciprocal temperature.

5.4 Conclusions

Due to the absence of impurities in LDPE, charge distribution depends only on the charge injection at both electrodes and mobility of charge carriers. Charge carrier injection and extraction rates are determined by the potential barrier height between electrode/specimen interfaces. The potential height barrier is strongly affected by electric stress, electrode material and polarity. Experiments carried out in section 5.2 show that a higher electric stress will help in lowering the barrier more which encourages more carrier injection. All materials have different work functions; therefore some might have the capability of injecting more than the others, for example Sc<Al. However, even with the same electrode material, it might favour positive charge injection more than negative charge injection or vice versa, for example Al(+)>Al(-) and Sc(-)>Sc(+). Contact surface is important, using evaporated Al or solid aluminium block with a layer of silicon oil shows a great deal of difference in conduction characteristics as the solid aluminium block with a layer of silicon oil enhanced more charge injection into the specimen compared to evaporated aluminium. The most probable reason is that the actual contact for the solid aluminium block is silicon oil/LDPE not aluminium /LDPE and silicon oil have a greater ability (lower potential barrier height compared to aluminium) of charge injection compared to evaporated Al/LDPE. Although fast moving charge packet was not found in LDPE but occasional current oscillation (transient current peak) was captured. This is caused by the aptitude of charge injection and extraction.

The impact of temperature on conduction behaviour is highlighted. Higher temperature increases the mobility and amount of carrier available for conduction, leading to larger conduction current. The increased mobility caused by higher temperature causes a shorter time for the occurrence of the first transient current peak. It also multiply the opportunity of getting trapped charges detrapped, thus, it increases the probability of recombination with opposite sign carriers and/ or extraction by the opposite electrode. This is verified by the larger amount of charges in the bulk whether volts-on or off at lower temperature compared to higher temperature. The plot of ln J vs (1/T) according to Arrhenius relation shows a good

straight line where the calculated value of the barrier height for aluminium contact is ~1.044eV.

Chapter 6

Charge Dynamics and Transport in XLPE with Electrode and Temperature Effect

6.1 Introduction

As the usage of crosslinked polyethylene (XLPE) in cable becomes more common, the study of space charge accumulation under an electric field becomes ever important. More extensive research of space charge behaviour under DC electric field was carried out compared to AC electric field as it is believed that space charge accumulation under DC electric field is much more significant. Space charge accumulation in fresh XLPE specimens has shown that heterocharges tend to accumulate at the electrodes [40, 72, 73]. These heterocharges have been assigned to bulk processes and are believed to be caused by ionisation of impurities.

Few have also witnessed the existence of charge packets at high DC fields. Charge packets were discovered in both XLPE and LDPE doped with impurities either in cable or thin planar films [39, 76, 80, 81]. It is believed that there are two sources of charge packet formation. In the first case [80], packet charge was formed

by injected charges and it moves across the bulk of the specimen. The other case in [40, 76] was that packet charge created by field assisted dissociation of impurities as an origin of carriers. In order to confirm the role and contribution of impurities, it was therefore decided to remove by-products by degassing. Space charge measurements on degassed XLPE specimens have reported fewer heterocharges and increase in the formation of homocharges [40, 82]. It has been explained in terms of charge injection and trapping near the injecting electrodes [40, 82, 83].

6.2 Crosslinking processes

The two main chemical methods of crosslinking low density polyethylene to produce XLPE are either (a) using a peroxide (frequently dicumyl peroxide, DCP) which decomposes to form free radicals, or (b) a silane-based grafting mechanism. In the former method the peroxide is incorporated into the polymer at elevated temperature and pressure, and decomposes to yield free radicals, which extract hydrogen atoms from PE chains. The resulting reactive sites then combine to form crosslinking. The crosslinking action results in the formation of residual by-products such as acetophenone, α-methylstyrene and cumyl-alcohol etc. The silane method [84] involves grafting a chemically multifunctional silane-based molecule onto the PE chains, using a method that also requires peroxide but at a much lower concentration than in the DCP method. After grafting, crosslinking is achieved through hydrolysis or condensation reactions.

6.3 Residual by-products and electrode material effect on electrical conduction and space charge

This section is to demonstrate (a) contribution of residual by-products caused by crosslinking reaction in fresh XLPE specimen and (b) the electrode material effect on both fresh (undegassed) and degassed XLPE specimen. Undegassed XLPE contains residual by-products caused by crosslinking action and these by-products were also identified to contribute to the formation of heterocharges caused by the dissociation of chemical species. It will be a help to understand how the presence of by-products

in undegassed XLPE could change the conduction behaviour and if the selected electrode materials would impinge on any of the known behaviour.

6.3.1 Sample preparation

The XLPE specimens used were press-moulded from granules. These granules were subjected to a temperature of 200°C; under such an environment DCP will be decomposed to create crosslinked structure. A high temperature [85] is necessary to ensure that the DCP content is totally decomposed. Freshly made specimens were used immediately for testing. Two different types of degassed specimens were prepared by placing freshly made specimens into a vacuum oven either at (a) ~60°C or (b) ~90°C for 24 hours. Figures 6.1 and 6.2 depict the infra-red spectra and weight change with time for fresh and degassed (at 90°C) XLPE specimens. Infra-red spectra did not show obvious difference between fresh and degassed specimen. But there is a weight reduction of ~0.51% after 24 hours of degassing at 90°C, further degassing up to 72 hours did not lower the weight. Therefore, all degassed specimens had undergone heat treatment for 24 hours.

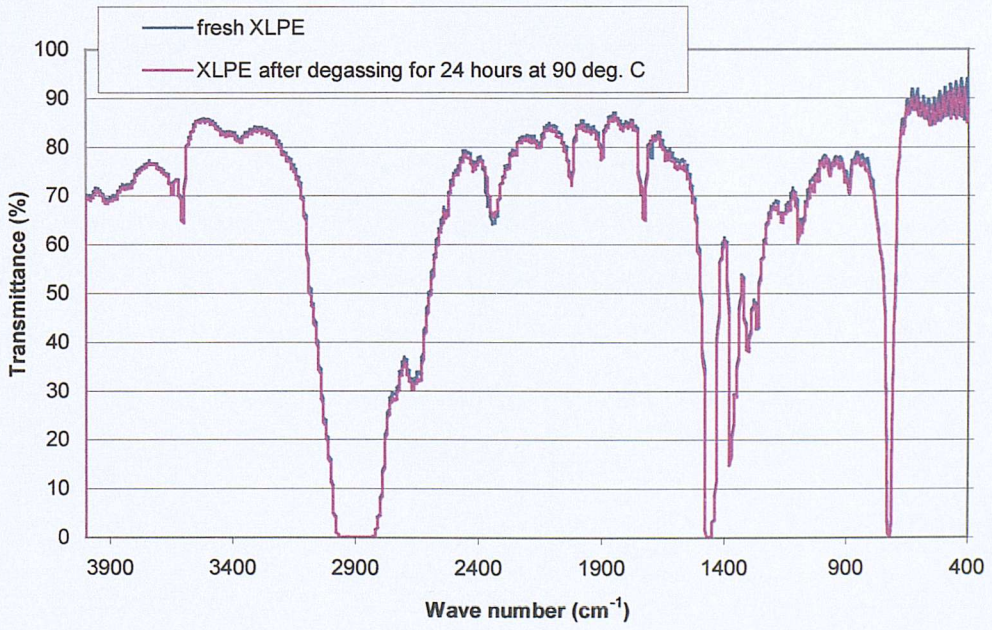

Figure 6.1. Infra-red absorption spectra of fresh and degassed XLPE specimens.

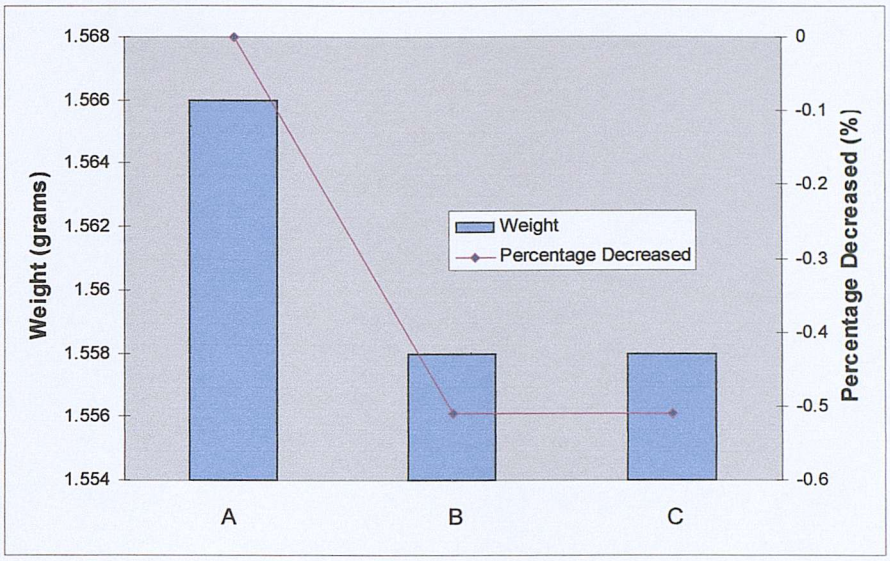

A - Fresh XLPE specimen
B - Fresh XLPE specimen after 24 hours of degassing at 90 deg. C
C - Fresh XLPE specimen after 72 hours of degassing at 90 deg. C

Figure 6.2. Weight changed in XLPE specimen before and after degassing process.

The electrode materials used were (a) semicon, (b) evaporated aluminium and (c) solid aluminium block of the PEA rig's bottom cell. The preparation and handling of the electrode materials were the same as described in section 5.2.1.

6.3.2 Experimental protocols

There were 5 sets of experiments being carried out. Two different electrode configurations were selected to carried out the tests, they were (a) evaporated Al(-) with Sc(+) and (b) solid aluminium block Al(-) with Sc(+). The signs (-) and (+) refer to the cathode and the anode respectively. Measurements were taken at every 6 seconds intervals throughout the stressing period at a temperature of 30°C. Table 6.1 shows a summary of each experimental configuration.

Specimen	Specimen type	Electrode configuration	Applied voltage (kV)	Specimen thickness (μm)	Stressing period (days)
1	Fresh XLPE	Solid Al block(-) with Sc(+)	20	195	2
2	Fresh XLPE	Evaporated Al(-) with Sc(+)	20	205	2
3	Degassed (at 60°C) XLPE	Evaporated Al(-) with Sc(+)	20	195	2
4	Degassed (at 90°C) XLPE	Solid Al block(-) with Sc(+)	20	195	2
5	Degassed (at 90°C) XLPE	Evaporated Al(-) with Sc(+)	20	200	2

Table 6.1. Summary of XLPE experimental configuration.

6.3.3 Experimental results

Figures 6.3 to 6.7 show the measured current density and correspondent space charge profiles at a time as stated in individual graph for specimen no. 1 to 5 as described in table 6.1. A few distinctive differences between these experimental results were spotted for the first 60 minutes. For fresh XLPE (specimen no.1) with solid Al(-) and Sc(+) electrode, (a) had the highest measured current compared to the rest, (b) huge transient current peaks, (c) carriers movement were the fastest and very blatant and (d) fast moving positive and negative charge packets travelling from one electrode to the opposite were identified. For fresh specimen no. 2 with evaporated Al(-) and Sc(+) electrode, although it was the same type of specimen as no. 1, it showed (a) much lower measured current compared to specimen no. 1 and (b) slower moving positive charge packet with no negative charge packets.

Specimens no. 4 and 5 are degassed specimens which have undergone heat treatment in a vacuum oven at 90°C for 24 hours. Degassed specimen no. 4 used solid Al(-) and Sc(+) electrode, where as specimen no. 5 employed evaporated Al(-) and Sc(+) electrode. Both the degassed specimens showed positive and negative charge packets but not as fast moving as in specimen no.1. Comparing fresh and degassed specimens no. 1 to 4 and no. 2 to 5, the most observable difference was that the faster carrier movement in fresh specimens than in degassed specimen in which the time taken for the appearance of the first transient current peak in fresh

specimens is shorter (compared between the same electrode configuration) than in degassed specimens.

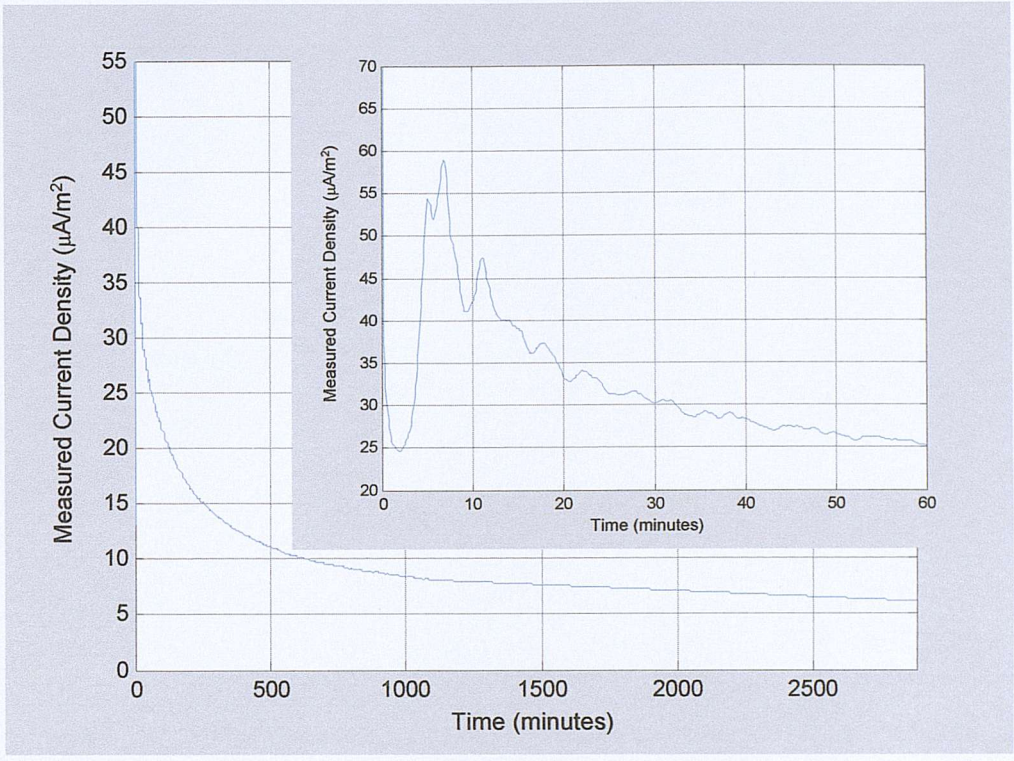

(a)

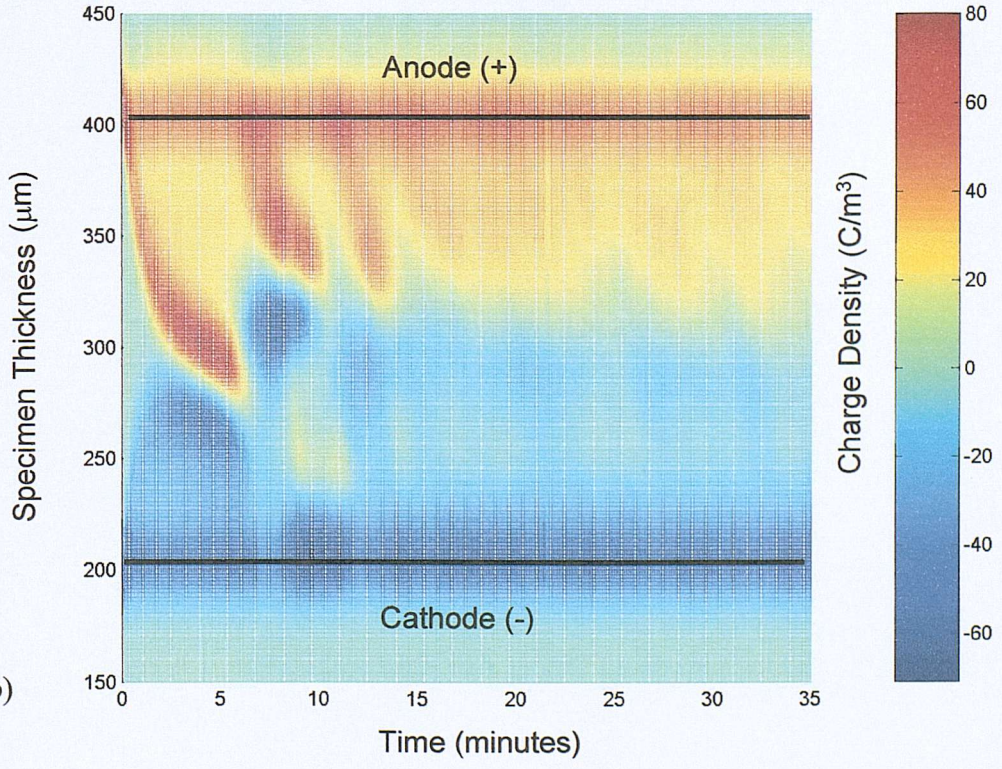

(b)

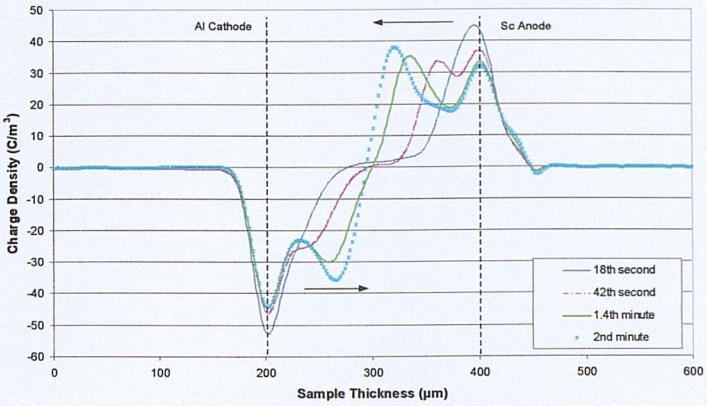

(c) Measured current dropped

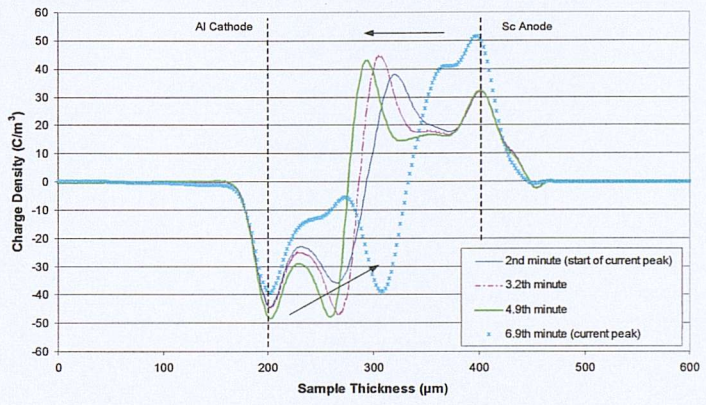

(d) Measured current increased

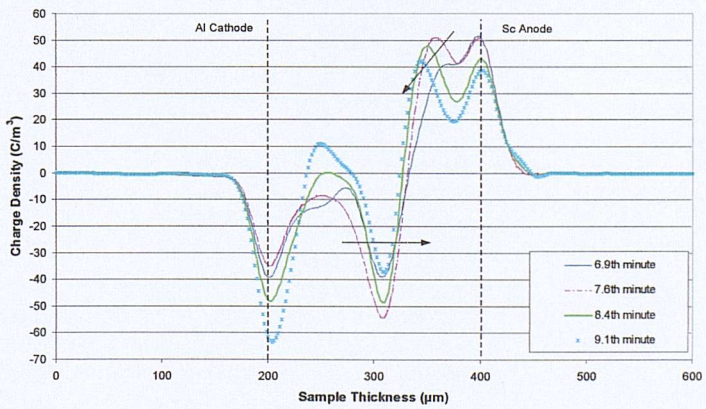

(e) Measured current dropped

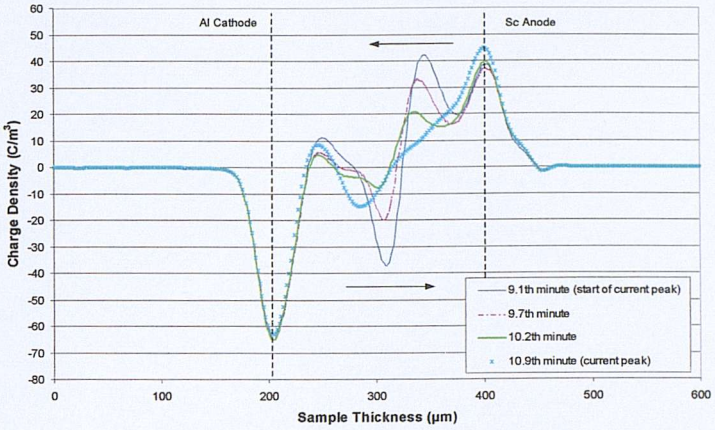

(f) Measured current increased

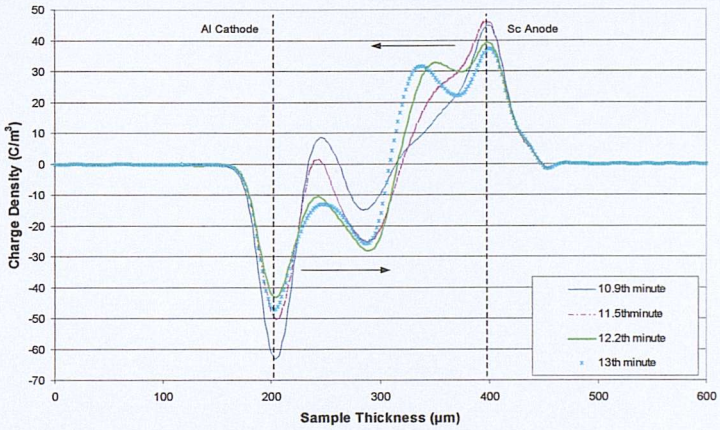

(g) Measured current dropped

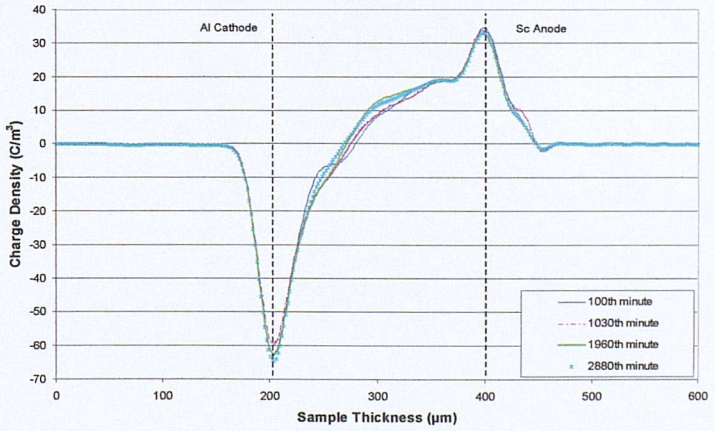

(h) Space charge density profile between the 100^{th} and 2880^{th} minute

Figure 6.3. (a) The measured current density, (b) space charge density colour contour graph for the first 35 minutes after applied voltage and (c)-(h) space charge density profile corresponded to measured current density as stated on each graph for fresh XLPE specimen no. 1 using solid Al block(-) with Sc(+).

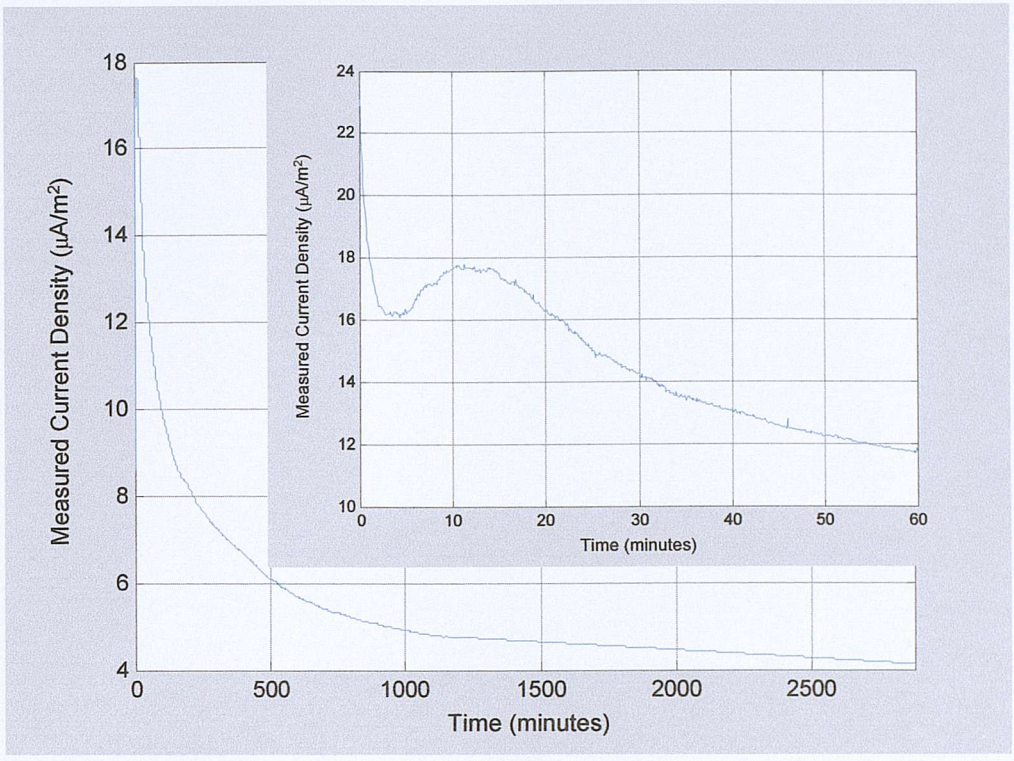
Measured Current Density (μA/m²)
Time (minutes)
Measured Current Density (μA/m²)
Time (minutes)

(a)

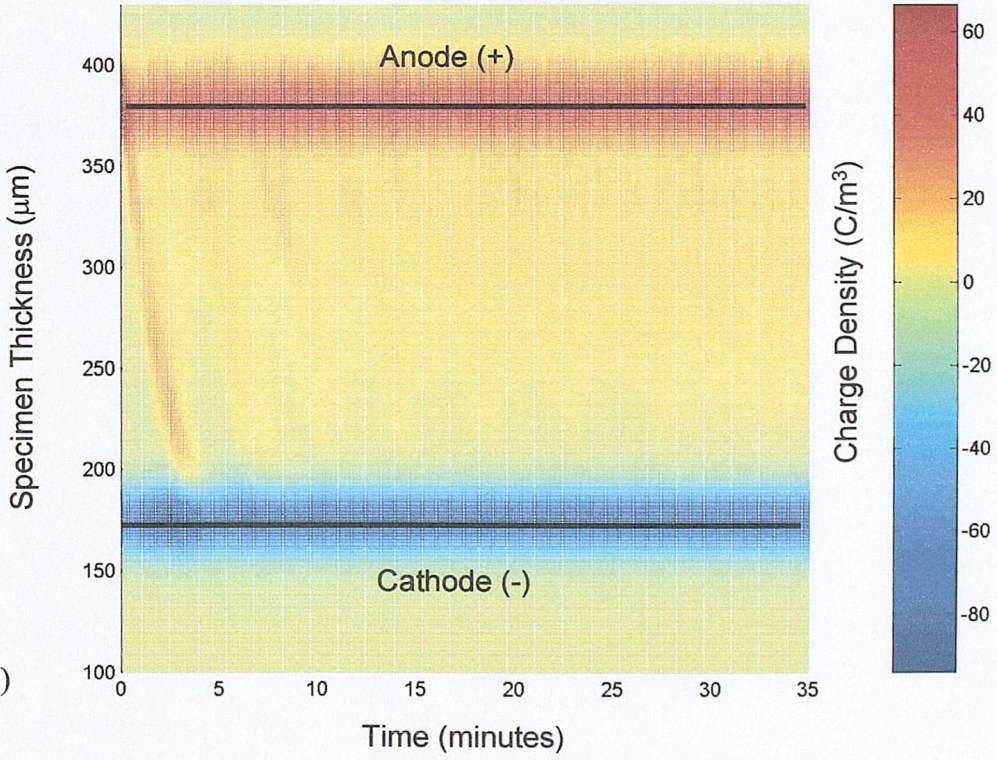
Anode (+)
Cathode (-)
Specimen Thickness (μm)
Time (minutes)
Charge Density (C/m³)

(b)

(c)

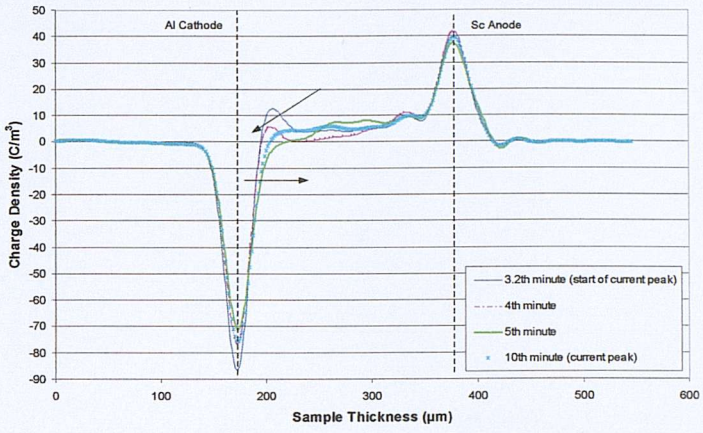

(d)

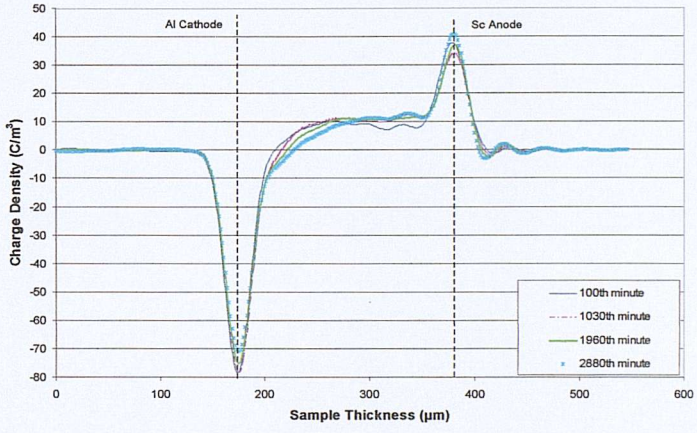

Figure 6.4. (a) The measured current density, (b) space charge density colour contour graph for the first 35 minutes after applied voltage, (c) space charge density profile corresponded to the transient current peak, from the 3.2th to 10th minute and (d) space charge density profile from the 100th to 2880th minute for fresh XLPE specimen no. 2 using evaporated Al(-) with Sc(+).

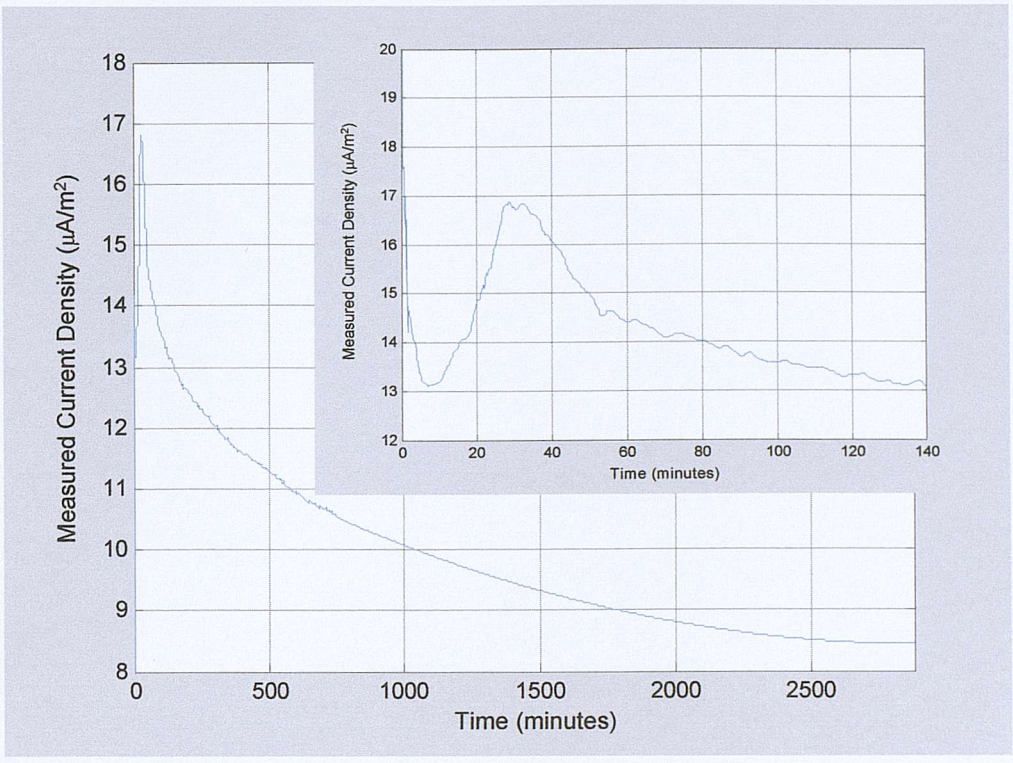
Measured Current Density (μA/m²)
Time (minutes)
18
17
16
15
14
13
12
11
10
9
8
0
500
1000
1500
2000
2500
20
19
18
17
16
15
14
13
12
0
20
40
60
80
100
120
140

(a)

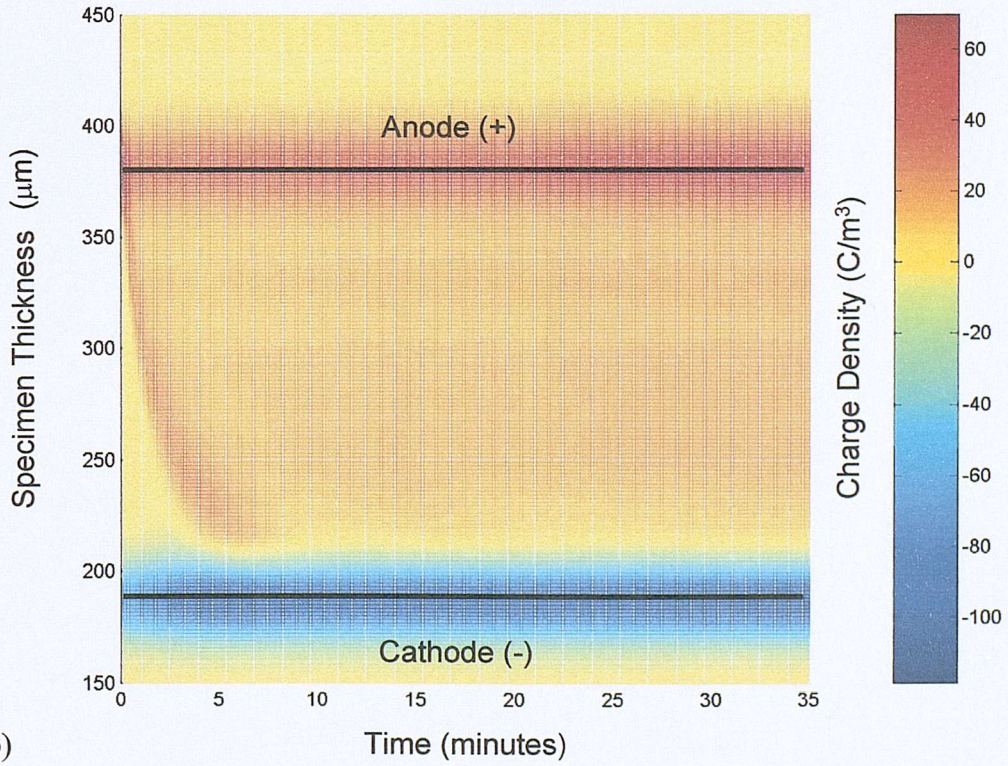
Specimen Thickness (μm)
Time (minutes)
Charge Density (C/m³)
Anode (+)
Cathode (-)
450
400
350
300
250
200
150
0
5
10
15
20
25
30
35
60
40
20
0
-20
-40
-60
-80
-100

(b)

(c)

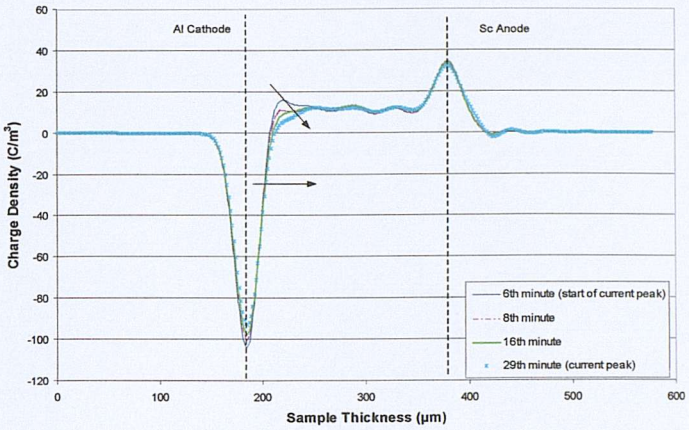

(d)

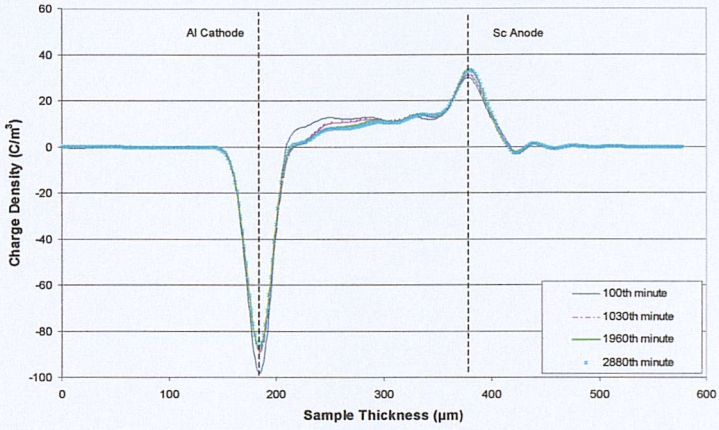

Figure 6.5. (a) The measured current density, (b) space charge density colour contour graph for the first 35 minutes after applied voltage, (c) space charge density profile corresponded to the transient current peak, from the 6th to 29th minute and (d) space charge density profile from the 100th to 2880th minute for degassed XLPE (degassed at 60°C) specimen no. 3 using evaporated Al(-) with Sc(+).

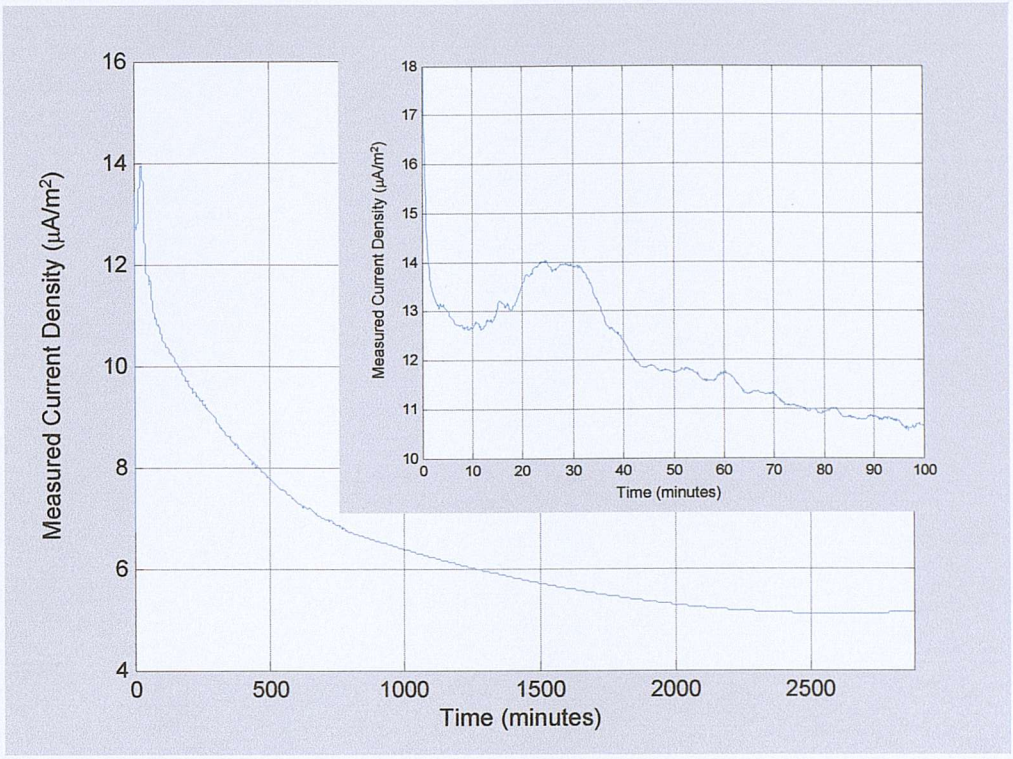
Measured Current Density (μA/m²)
Time (minutes)
Measured Current Density (μA/m²)
Time (minutes)

(a)

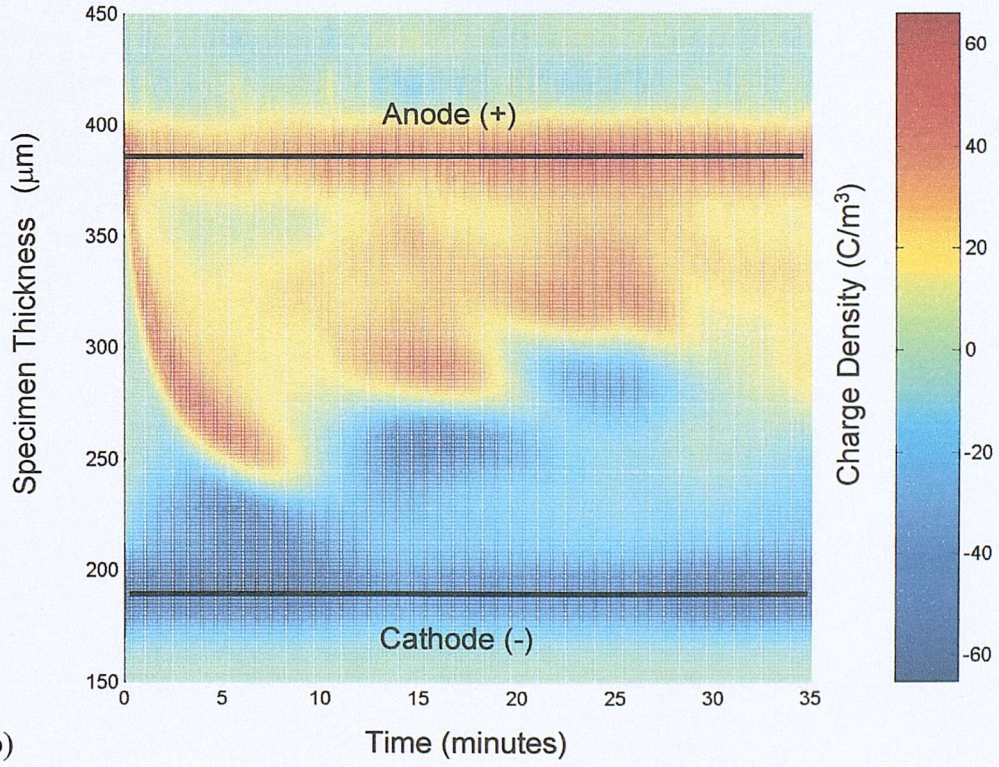
Anode (+)
Cathode (-)
Specimen Thickness (μm)
Time (minutes)
Charge Density (C/m³)

(b)

(c)

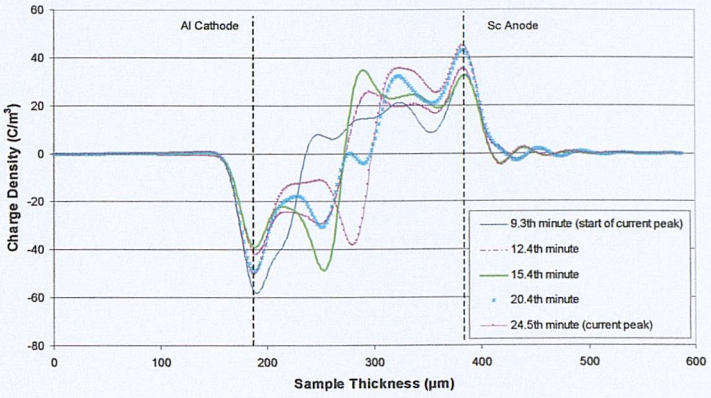

(d)

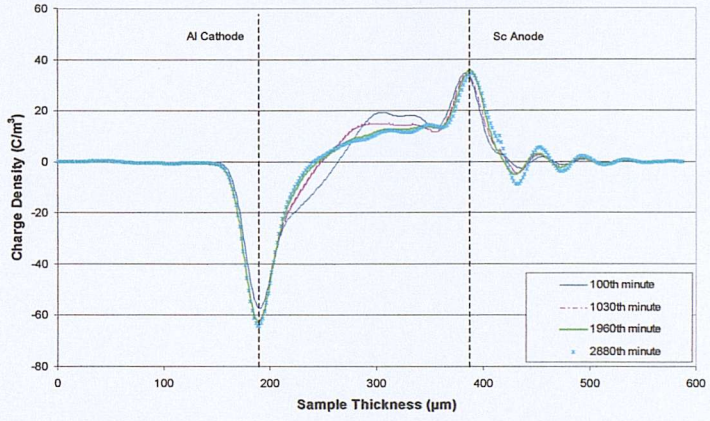

Figure 6.6. (a) The measured current density, (b) space charge density colour contour graph for the first 35 minutes after applied voltage, (c) space charge density profile corresponded to the transient current peak, from the 9.3th to 24.5th minute and (d) space charge density profile from the 100th to 2880th minute for degassed XLPE (degassed at 90°C) specimen no. 4 using solid Al block(-) with Sc(+).

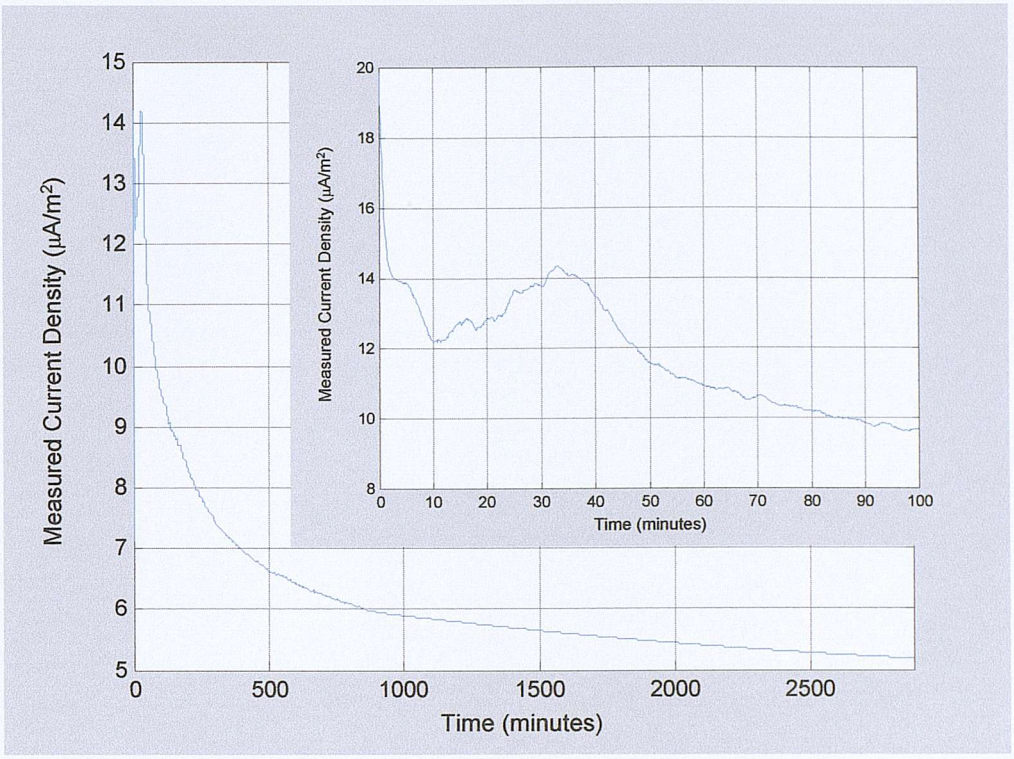
Measured Current Density (μA/m²)
Time (minutes)
Measured Current Density (μA/m²)
Time (minutes)

(a)

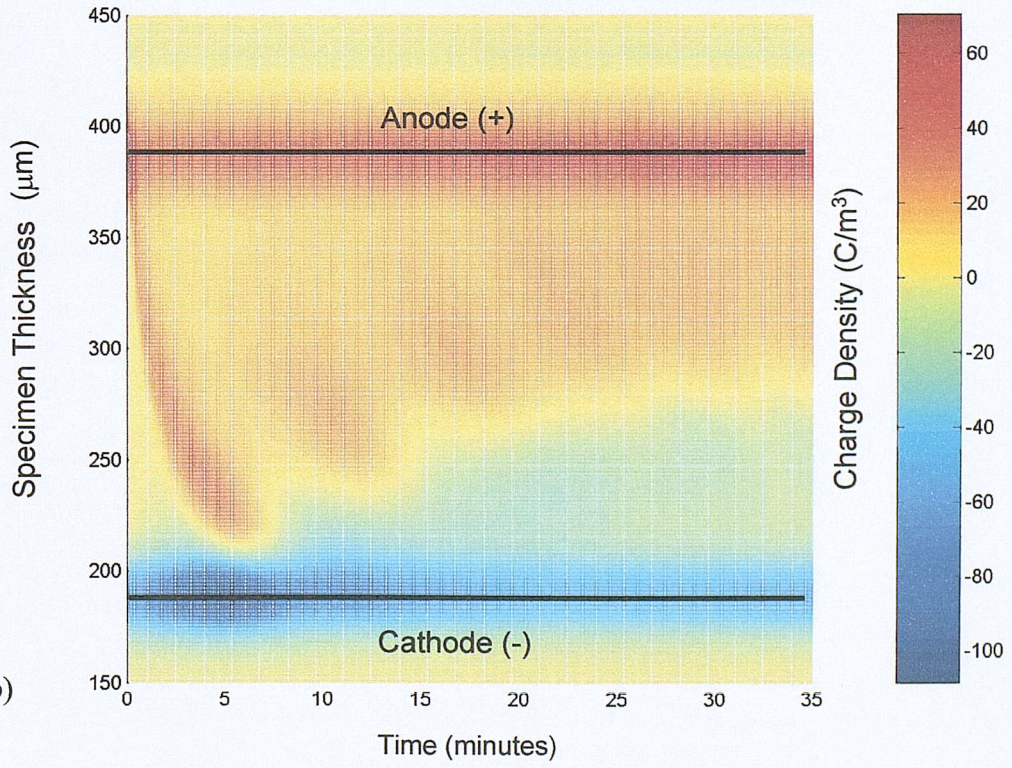
Specimen Thickness (μm)
Anode (+)
Cathode (-)
Time (minutes)
Charge Density (C/m³)

(b)

(c)

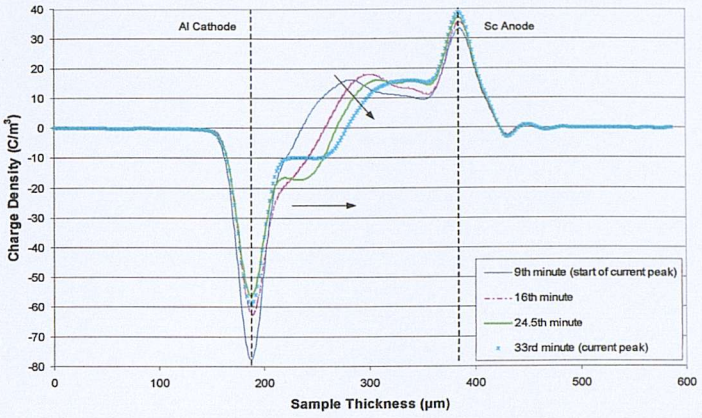

(d)

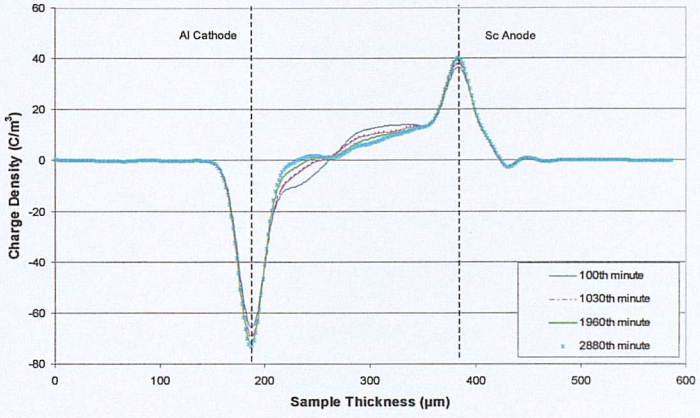

Figure 6.7. (a) The measured current density, (b) space charge density colour contour graph for the first 35 minutes after applied voltage, (c) space charge density profile corresponded to the transient current peak, from the 9th to 33rd minute and (d) space charge density profile from the 100th to 2880th minute for degassed XLPE (degassed at 90°C) specimen no. 4 using evaporated Al(-) with Sc(+).

6.3.4 Analysis and discussion of the results

A. Electrode effect

In order to show electrode effect on the conduction behaviour, we compared fresh specimens no. 1 (figure 6.3) with 2 (figure 6.4) and degassed specimens no. 4 with 5 (figures 6.6 and 6.7). Specimen no.1 and 2 are fresh XLPE having solid and evaporated aluminium as the cathode respectively. Figure 6.3(b) shows the dynamic space charge density colour contour graph of specimen 1 for the first 35 minutes after applying voltage, very fast moving positive and negative packet charge

travelling from one electrode to the other were captured one after another, it was more apparent for the first 20 minutes. Figure 6.3(c) to (g) show the charge density distribution for the first 13 minutes at an interval as stated in the graphs. Each of these charge density distribution graphs corresponded to the increase and decrease of the measured current development (transient current peaks). The charge packet behaviour becomes less prominent with time and so does the oscillatory current.

Figure 6.4(b) shows the dynamic space charge density colour contour graph of specimen 2 for the first 35 minutes after applying voltage. Due to the fact that evaporated aluminium at the cathode has a higher potential barrier height compared to solid Al/silicon oil(-), positive charge carrier was the dominant party throughout the stressing period and only a very infinitesimal amount of negative carrier near to the cathode was observed. After voltage was applied, a large positive charge packet was seen moving towards the cathode, at ~3 minutes later, this positive charge packet started to diminish, at the same time the measured current increased for about 7 minutes. There were subsequent smaller magnitude of overlapping positive charge packets; these packets did not cause perceptible increase in the measured current.

Although specimens no. 1 and 2 were the same type of fresh XLPE but under the influence of the electrode materials (as explained in chapter 5 the actual contact for solid aluminium block electrode is with a layer of silicon oil in between the specimen/solid aluminium and evaporated aluminium is in direct contact with the specimen), it displayed entirely different characteristics. Specimen no. 2 using evaporated aluminium cathode did not show continual fast moving charge packet that corresponds to the oscillatory current as in specimen no. 1. This implies that the occurrences of fast moving packet charge depend on not only the applied electric field as reported in [76], it also depends on the choosen electrode material.

The reported transit time for each charge packet from one electrode to the other varies. At an applied field of 120kV/mm, H. Kon et al [76] witnessed moving negative charge packets in oxidized XLPE doped with antioxidant (using gold electrodes on both sides of the specimens), where the transit time was about 6 to 7 minutes and it lasted for about 90 minutes. A. See et al [81] perceived moving

positive charge packets (at 120kV/mm applied field) in specimen peeled from actual XLPE cable (specimen not coated with electrode, using solid aluminium block as the cathode and evaporated aluminium coated on the semicon as the anode) taking about 2.5 hours to cross from the anode to the cathode, persisted for 48 hours. In our case, at an electric field of ~102.5kV/mm with solid aluminium block/silicon oil/XLPE at the cathode and semcon/silicon oil/XLPE at the anode, both positive and negative charge packets moving towards the counter electrode but positive was the more prominent one. The transit time for the charge packet was ~6 minutes, it was more obvious for the first 20 minutes and it decays gradually with time but can be vaguely seen up to ~60minutes. The different transit time and behaviour in these three cases inferred that formation of packet charge behaviour might also depend on the content of XLPE and the way XLPE specimen was prepared.

Degassed specimens no. 4 and 5 utilised solid and evaporated aluminium as the cathode respectively. Figure 6.6(b) shows the space charge colour contour graph (the first 35 minutes) of specimen no. 4, it exhibits positive and negative charge packets, the speed of these charge packets was not as fast as those in fresh specimen no.1. There are clearly 3 growing and fading charge packets, the speed of these charge packets is slow, before one packet reaches the counter electrode another one is formed (overlapping of charge packet) therefore we cannot see solitary positive or negative charge packets reaching the opposite electrode. Every one of the successive positive and negative breeding charge packet lessen some time after they met up with each other. This might be the reason for the slow continuous increase of measured current for the period of about 15 minutes instead of the abrupt current trend as in specimen no. 1. Figure 6.7(b) is the space charge contour graph of specimen no. 5, for the fact that evaporated aluminium electrode hinders carrier injection (compared to solid Al/silicon oil electrode), the positive charge packet dominated the whole time but gradual increasing observable small quantity of negative carriers was seen from the ~9^{th} minute. And there are several large overlapping positive and small negative charge packets within the first 35 minutes. The similarity between specimens no. 4 and 5 is the consecutive overlapping positive and negative charge packet formation and both charge packets lessen some time after they met. Specimen

no. 5 too exhibited continuous slow increase measured current instead of abrupt current trend.

There are a few obvious doubts that can be questioned, like why (a) the charge carrier's movement were much slower in degassed specimens than in fresh specimens and (b) evaporated aluminium cathode used in degassed specimen (degassed at 90°C) can inject more charge than when used in fresh specimen, this will be discussed in the next section dealing with the contribution of by-products.

B. By-products effect

The residual by-products like acetophenone, α-methylstyrene and cumyl-alcohol in undegassed XLPE do play a part in the conduction process. Degassed (heat treatment) process was performed to eliminate the content of these by-products in XLPE insulation. The presence of by-products causes heterochanges at lower field (~10 to 40kV/mm) [86] due to dissociation of impurities (creation of electrons, positive and negative ions), whereby the electrons and negative ions attracted towards the anode and positive ions towards the cathode. At higher field, charge injection from the electrode has a greater effect and the injected homocharges overlapped the existence of heterocharges near to the electrode.

A comparison between fresh and degassed specimens no. 1 with 4 and 2 with 5 for the first 35 minutes will demonstrate the role of the by-products. Fresh specimen no. 1 shows distinct fast moving positive and negative packet charge reaching the cathode and the anode respectively. The electrons and dissociated negative ions together with electrons injected from the cathode moved towards the anode, at the same time, the dissociated positive ions and holes injected from the anode travelled towards the cathode. This creates an image as if all the positive and negative charge were injected from the electrodes and were moving speedily from one electrode to the other, but in fact the creation of dissociated species had played a part in making the carriers looking as though they were moving faster. The presence of by-products increases the conductivity (at least for the first hundred minute) that led to the higher measured current density and the time for the appearance of the first

transient current peak also shortens. C. Shinoda et al [87] had made a similar conclusion based on their experimental results. In their work, the increase in residual by-product content led to the higher peak current and the time to first transient current peak also decreased.

The collapse of each positive charge packet at the cathode was caused by the extra injection of electrons which increases the measured current. The transit time of each packet depends on the rate of dissociation and the amount of dissociation species available. Notice that the packet charge decays with time suggesting that the availability of dissociable species reduced with time too.

Degassed specimen no. 4 shows a slower moving negative and positive charge packet, both positive and negative show successive overlapping charge packets and they diminished some time after meeting with each other. Degassed specimen no. 4 has undergone heat treatment and it is believed to have majority of by-products removed. Therefore the positive and negative charge packet contained mostly injected charges from the electrodes, and these slower moving charges needed more time to get across the bulk and therefore cause the overlapping of successive charge packets.

Fresh specimen no. 2 on the other hand only shows large positive charge packet due to the fact that aluminium electrode hinders charge injection which in this case is electron injection. By-products' dissociation still exists but because of evaporated Al(-), the limited amount of injected electrons were overshadowed by the injected holes from the Sc(+) anode and dissociated positive ions which have travelled near to the cathode, that is why very few electrons were seen near to the cathode throughout the stressing period. Also the domineering positive charge carriers had overshadowed the dissociated electrons and negative ions. In contrast, degassed specimen no. 5 had impurities removed; therefore positive charge carriers containing mostly holes injected from the anode were present. The dominating injected positive charge moved slower which gave time for the limited amount of injected electrons to be visible near to the cathode. This resulted in a longer time taken for the slower moving injected charges to get extracted. The first occurrence of

increase in the measured current for fresh specimen no.2 was at the ~3.2th minute and degassed XLPE at the ~9th minute.

To further support the fact that impurities had been removed from heat treatment, another experiment was carried out at a different degassing temperature. Specimen no. 3 (using evaporated Al(-) with Sc(+)) had undergone heat treatment at 60°C instead of 90°C as in specimen no. 4 and 5. The result shows a similar behaviour to fresh specimen no. 2. Very little negative charge carriers accumulated near to the cathode throughout the stressing period. It is believed that there is still a substantial amount of impurities present (less than for the fresh specimen no. 2 but more than degassed specimen no. 5) and the impurities were participating in the conduction process, where the dissociable positive ions and holes injected from the anode travelled near to the cathode and gradually overshadowed the limited amount of electrons injected from evaporated Al(-). This proved that degassing procedure did help to remove impurities content from fresh XLPE and the selected degassing temperature has an important part in deciding the amount of impurities being removed.

6.4 Temperature influence on electrical conduction and space charge

6.4.1 Experimental protocols and the results

Sample preparation procedure was the same as described in earlier section 5.2.1. Fresh and degassed XLPE specimens were stressed at an applied voltage of 20kV at 55°C. The purpose was to determine the influence of temperature on electrical conduction and space charge therefore the following four tests have the same testing configuration as in section 6.3.2 specimen no. 1, 2, 3 and 5. Measurements were taken at every 6 seconds intervals throughout the stressing period. Table 6.2 shows a summary of each experimental configuration.

Specimen	Specimen type	Electrode configuration	Temp. (°C)	Specimen thickness (μm)	Stressing period (days)
1	Fresh XLPE	Solid Al(-) block with Sc(+)	55	195	2
2	Fresh XLPE	Evaporated Al(-) with Sc(+)	55	196	2
3	Degassed (at 60°C) XLPE	Evaporated Al(-) with Sc(+)	55	210	2
4	Degassed (at 90°C) XLPE	Evaporated Al(-) with Sc(+)	55	200	2

Table 6.2. Summary of XLPE experimental configuration for demonstrating temperature effect.

Figure 6.8 shows the measured current graphs for all the specimens at the condition as stated in table 6.2. The measured current for all specimens is very much higher than at 30°C. All specimens show transient current peak behaviour, the corresponded space charge profiles to the transient current peaks will not be shown as they display a similar characteristic to those at 30°C where there is a reduction of positive charge carriers. Figure 6.9 shows that space charge profiles for all specimens at much later time from the 100th to 2880th minute.

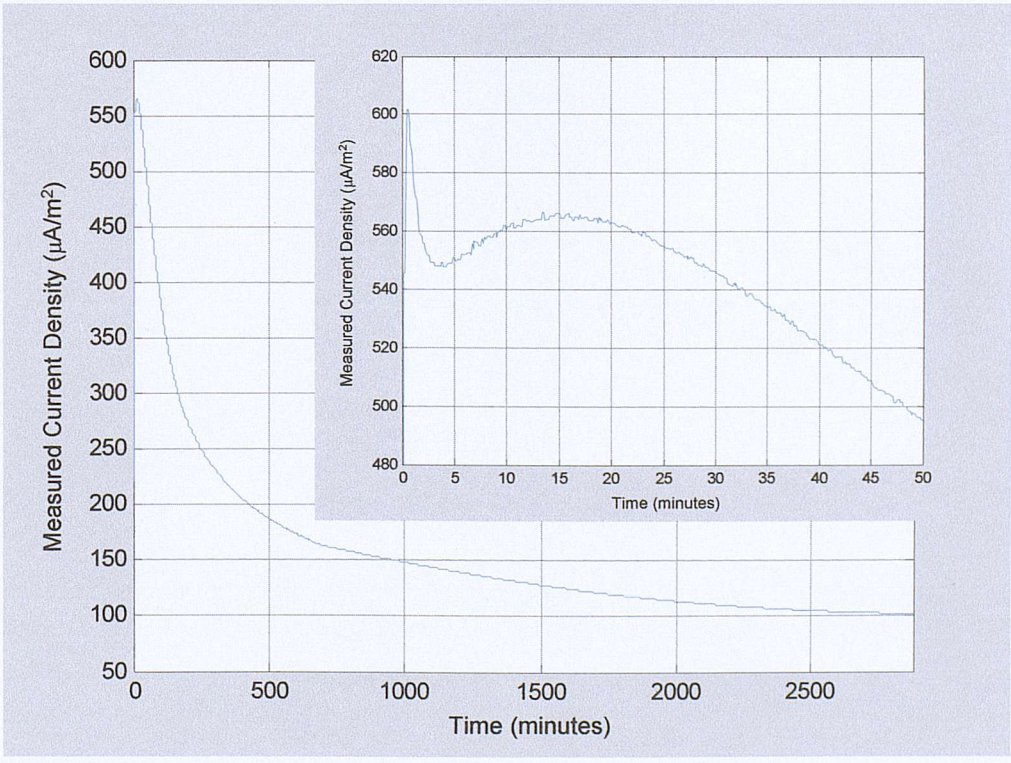

(a) Fresh XLPE specimen no. 1

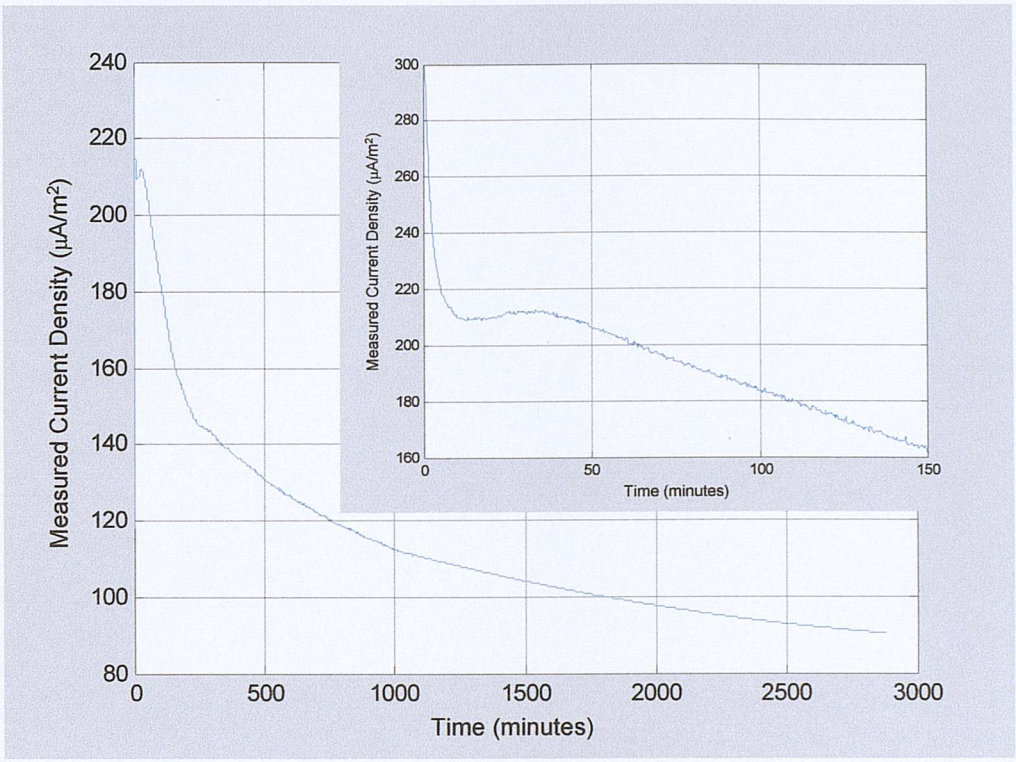

(b) Fresh XLPE specimen no. 2

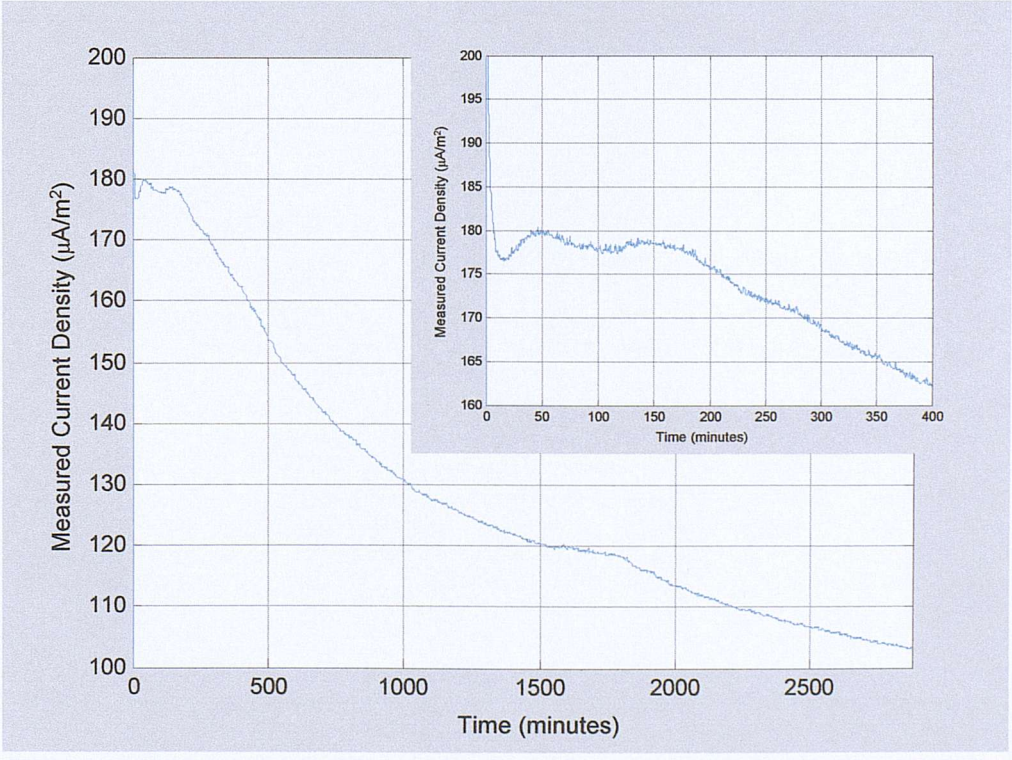

(c) Degassed XLPE specimen no. 3

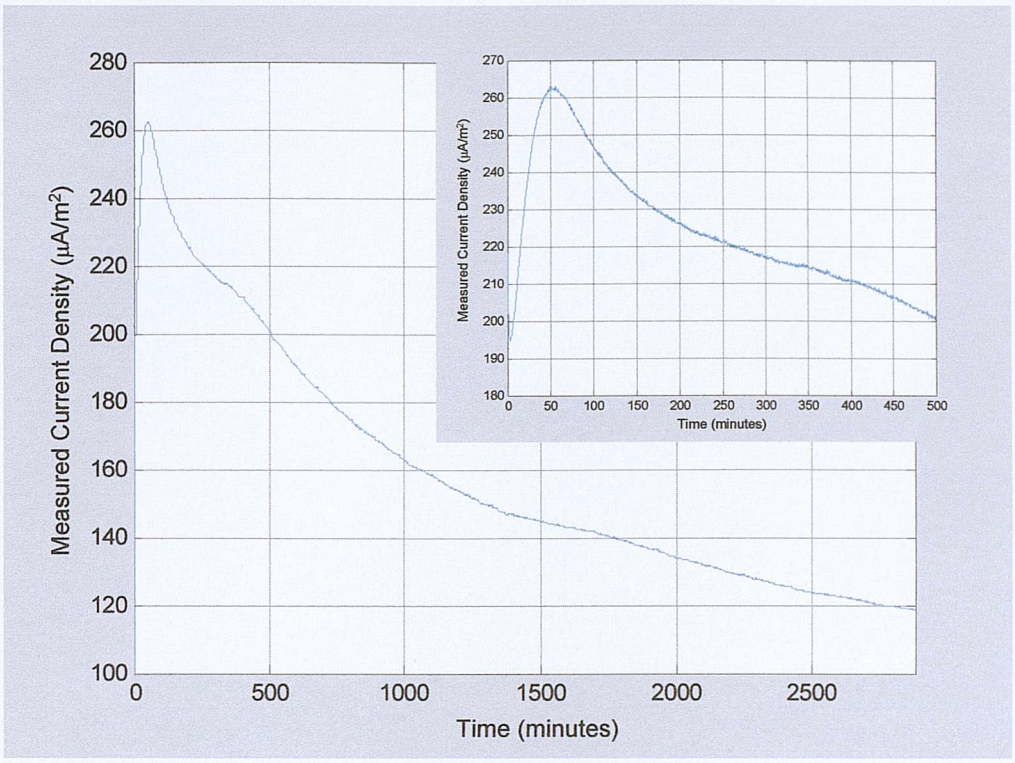

(d) Degassed XLPE specimen no. 4

Figure 6.8 (a) to (d). Measured current density of XLPE specimens at a temperature of 55°C with experimental configuration as stated in table 6.2.

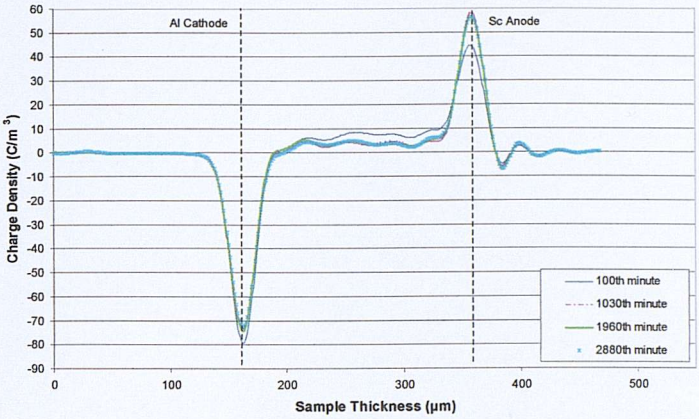

(a) Fresh XLPE specimen no. 1

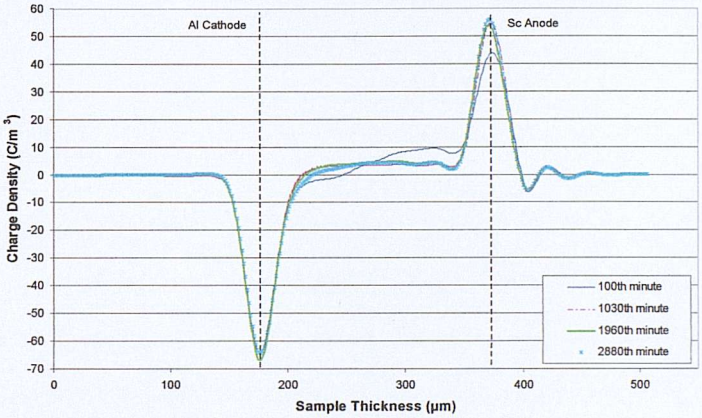

(b) Fresh XLPE specimen no. 2

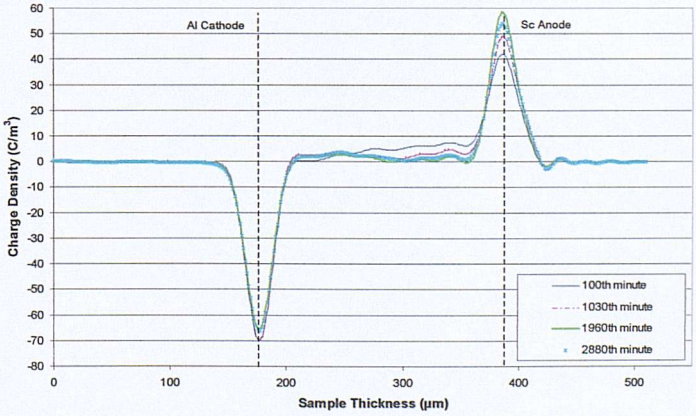

(c) Degassed XLPE specimen no. 3

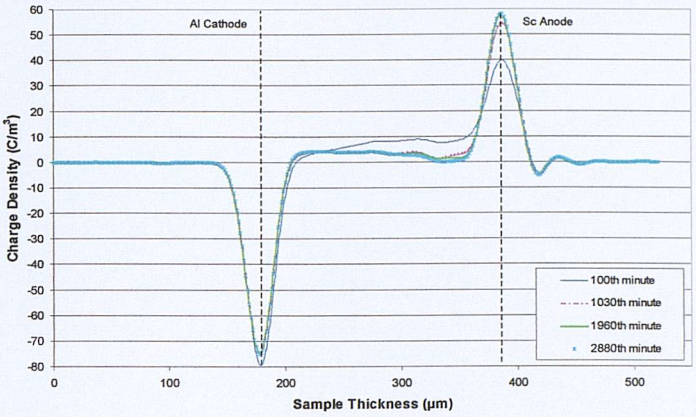

(d) Degassed XLPE specimen no. 4

Figure 6.9 (a) to (d). Space charge density of XLPE specimens at a temperature of 55°C with experimental configuration as stated in table 6.2 from the 100th to 2880th minute.

6.4.2 Analysis and discussion of the results

The main contribution of higher temperature in section 6.4.1 is to increase the conductivity. No consecutive fast moving charge packet was observed in fresh specimen no.1 using solid Al(-), the most likely reason was that at such high temperature, the carrier mobility increases and fast consecutive charge packets were missed out between measurement interval. Notice that there is a very sharp peak at the very beginning after the voltage was applied; it only lasted for about 12 seconds. This might be one of the fast moving packet charges that it managed to capture.

The transient current peak for fresh specimen no. 1 also shows the highest magnitude among the rest irrespective of temperature at 30°C or 55°C compared to other specimens at the same temperature. Degassed specimens no. 3 and 4 that contained more injected charge carriers moved slower as compared to fresh specimens no. 1 and 2 whose carriers looked to be moving faster due to the presence of by-products. It can be verified by the fact that the transient current peak duration for degassed specimens lasted longer. Similar to section 5.3.2, at higher temperatures, the movement of all carriers intensified. At lower temperature, larger amount of carriers were accumulated at the positive and negative carrier meeting

point (section 6.3.3), at elevated temperature fewer charges were accumulated in the bulk.

In the case of tests carried out on LDPE specimens at higher temperature (section 5.3.3), the time taken for the occurrence of the first transient current peak decreased as temperature escalated, it can be explained that higher temperature had increased the mobility of the carriers. Here with XLPE specimens, tests carried out at higher temperature (55°C) did not shorten the time taken for the first transient current peak (comparing it to the same type of experiment configuration at 30°C). The most probable reason might be the presence of impurities and at high temperature resulted in enormous increase in carrier mobility, the carriers might be moving so fast that current peaks might have been missed out in between measurement interval.

6.5 Conclusions

XLPE is manufactured either by using a peroxide with LDPE or a silane-based grafting mechanism. The consequence of crosslinking LDPE with a peroxide created residual by-products. These by-products caused the formation of heterocharges through field-assisted dissociation of impurities and also increased the conductivity. Consecutive fast moving packet charge behaviour was observed in fresh XLPE using solid aluminium as the cathode. The fast packet charge behaviour depends not only on the applied electric field but also the electrode material. The use of solid aluminium as the cathode exhibited fast moving packets charge but not for evaporated aluminium. The by-products in fresh XLPE specimen can be removed through degassing process whereby freshly made specimens are placed in a vacuum oven at 90°C for 24 hours. Once the by-products were removed, the conductivity decreased which led to the decrement in the measured current. In addition, the absence of fast packet charge in degassed specimen using solid aluminium at the cathode proven that the by-products had been removed through the high temperature degassing procedure.

The fast moving charge packets behaviour in fresh XLPE (at 30°C) using solid aluminium as the cathode when exposed to higher temperature increases the

measured current but was unable to capture an expected shorter transit time of consecutive charge packets. It is believed that there was presence of fast charge packet but was missed out between measurement interval time. The overall influence of higher measurement temperature increases the mobility and amount of carrier available for conduction, leading to a larger conduction current. Unlike the tests on LDPE specimens, the time taken for the occurrence of the first transient current peak shortened as the measurement temperature escalated. With XLPE specimens, all the tests carried out at higher temperature (55°C) did not shorten the time taken for the first transient current peak (comparing it to the same type of experimental configuration at 30°C). The most probable reason might be the presence of impurities and at high temperature resulted in enormous increase in carrier mobility, the carriers might be moving so fast that current peaks might have been missed out in between measurement interval.

Chapter 7

Charge Dynamics and Transport in Chemically-soaked Additive-free LDPE

7.1 Introduction

XLPE insulation is commonly used in AC power cables and is hopefully to bring its advantages to DC cables. However, for dc transmission, XLPE cables are still under extensive study due to severe concern about space charge since it is more significant under DC stresses than under AC stresses. In the manufacturing process of XLPE cables, dicumyl peroxide (DCP) is widely used as a crosslinking agent. Several curing decomposition products are generated during this cross linking process using DCP. Variable amount of acetophenone, α-methylstyrene and cumyl-alcohol, methane and water are produced in addition to the crosslinks. Curing decomposition products of low molecular weight such as methane and water are so volatile that they are lost from the insulation rather soon. High boiling point substances such as acetophenone, α-methylstyrene and cumyl-alcohol can remain in the insulation for a long period of time.

It has been reported that space charge is highly affected by the presence of by-products in insulation. Even the existence of fast moving charge packet in XLPE has also been accredited to them. In this chapter, three different by-products namely acetophenone, α-methylstyrene and cumyl-alcohol were impregnated into additive-free LDPE to investigate their individual influence on conduction current and space charge evolution under high DC electric field.

7.2 Electrical conduction and space charge in chemically-soaked additive-free LDPE

Many researches had been carried out to examine the effect of acetophenone, α-methylstyrene and cumyl-alcohol [88-92] on charge distribution in LDPE. However, the validity of some of the conclusions is debatable. Most experiments performed by others were stressed for a short time, without considering diffusion rate and concentration of the chemicals. Here, chemical-soaked specimens were aged continuously for 2 days. The diffusion and absorption rate of chemicals were monitored by weighing and performing FT-IR spectroscopy.

7.2.1 Sample preparation

The same type of commercially available additive-free LDPE of density 0.92g/cm^3 was used as in chapter 5. Sample preparation procedure was the same as described in earlier section 5.2.1. Then the cleansed specimens were immersed into acetophenone or α-methylstyrene at room temperature or cumyl-alcohol at 80°C for 2 hours. Higher soaking temperature for cumyl-alcohol is necessary due to its higher melting point (23°C). The soaking period was decided based on the fact that the rate of weight increased almost saturated in ~2 hours time. Figures 7.1 and 7.2 depict the infra-red spectra and weight change with time in specimens soaked in acetophenone, α-methylstyrene and cumyl-alcohol. The band between 1630 to 1780 cm^{-1} is characterized by the stretching of the C=O (carbonyl) groups and from 2500 to 3550 cm^{-1} results from stretching of O-H (hydroxyl) groups. Specimen soaked in

acetophenone and α-methylstyrene show the greatest change in the carbonyl groups and specimen soaked in cumyl-alcohol exhibits largest response in hydroxyl groups.

The specimen soaked in α-methylstyrene shows the most weight gained after 2 hours of soaking, followed by cumyl-alcohol and acetophenone. On the other hand, the rate of the chemical diffusion was also very high, take α-methylstyrene soaked specimen for example, the initial weight gained was ~9.77%, in less than an hour it dropped to ~1.54%. The weight gain dropped tremendously as time passed and in 48 hours all specimens return to the initial weight. Fascinatingly, the infra-red spectra portrayed a similar characteristic, the changes at various frequencies range were almost totally reversible in 48 hours after removal from soaking.

(a)

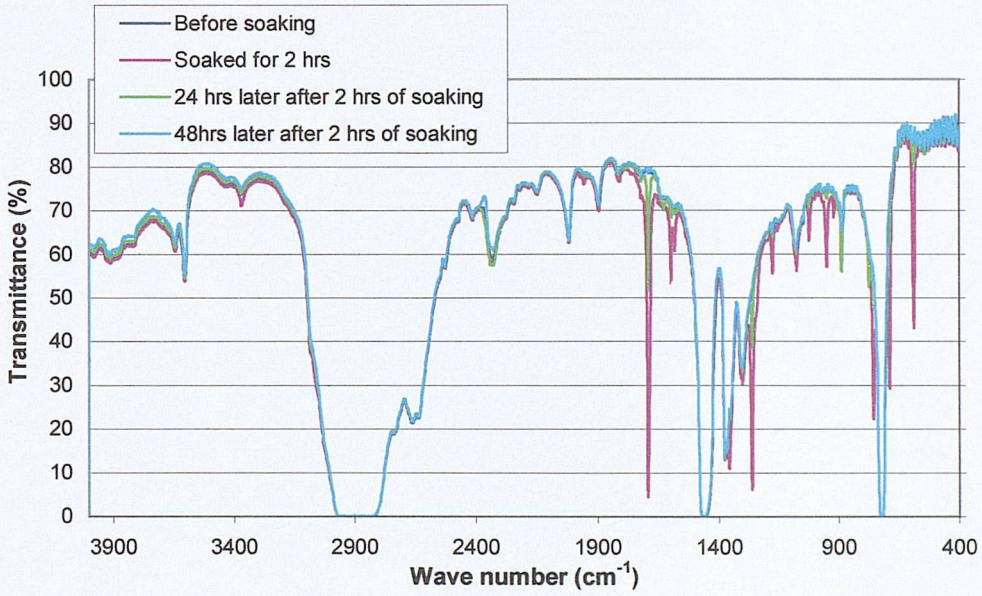

(b)

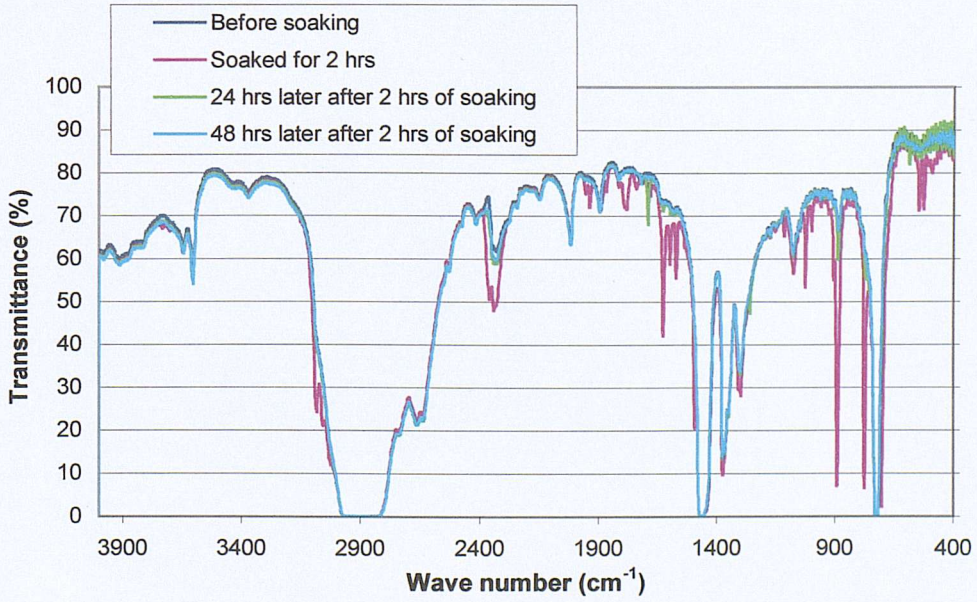

(c)

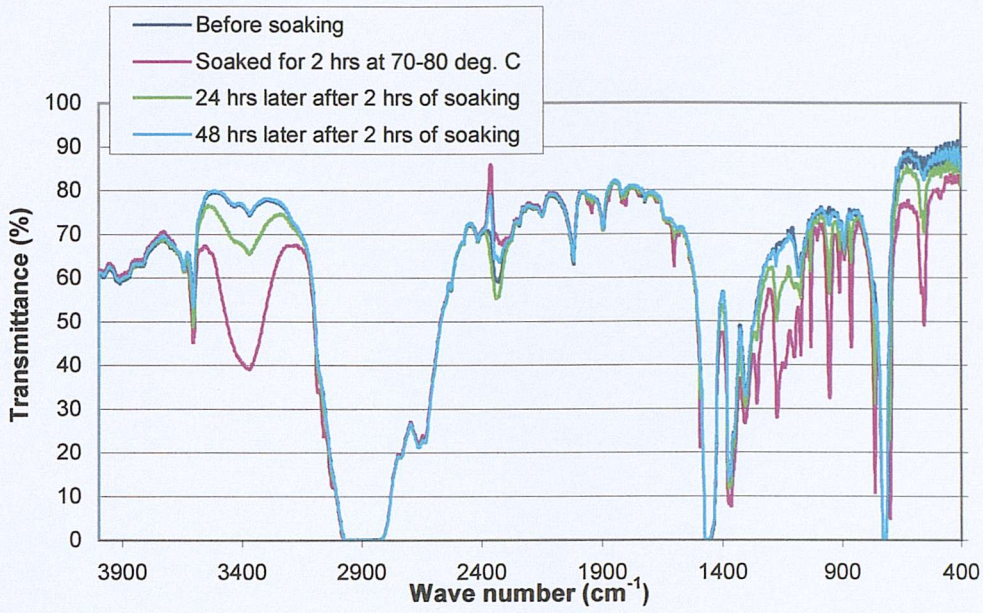

Figure 7.1. Infra-red absorption spectra of LDPE specimen soaked in (a) acetophenone, (b) α-methylstyrene and (c) cumyl-alcohol.

(a)

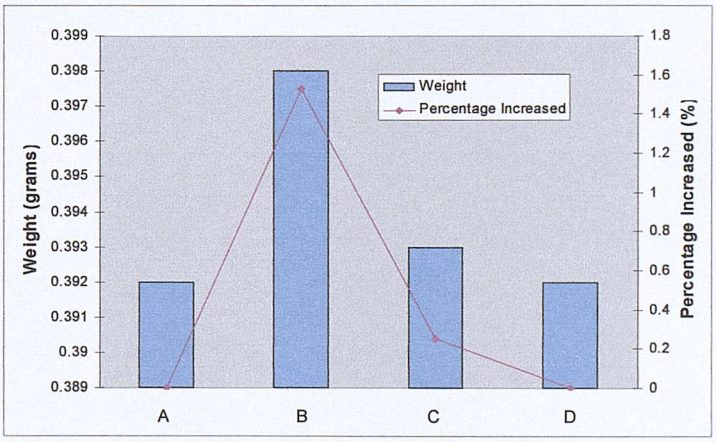

A - Before soaking
B - After soaking for 2 hours
C - 24 hours after 2 hours of soaking
D - 48 hours after 2 hours of soaking

(b)

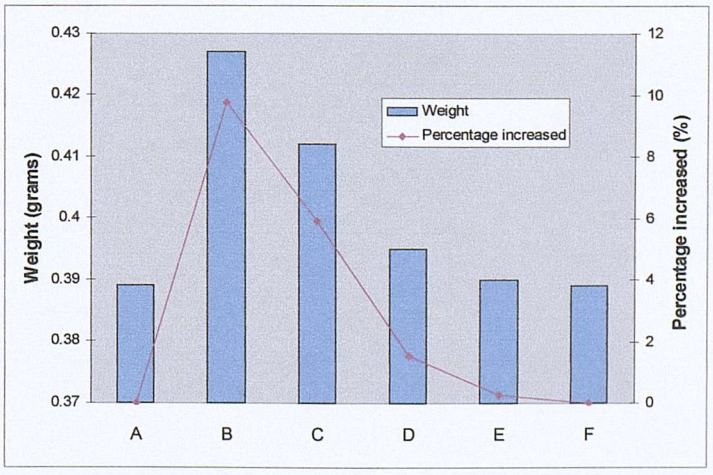

A - Before soaking
B - After soaking for 2 hours
C - 5 minutes after 2 hours of soaking
D - 30 minutes after 2 hours of soaking
E - 24 hours after 2 hours of soaking
F - 48 hours after 2 hours of soaking

(c)

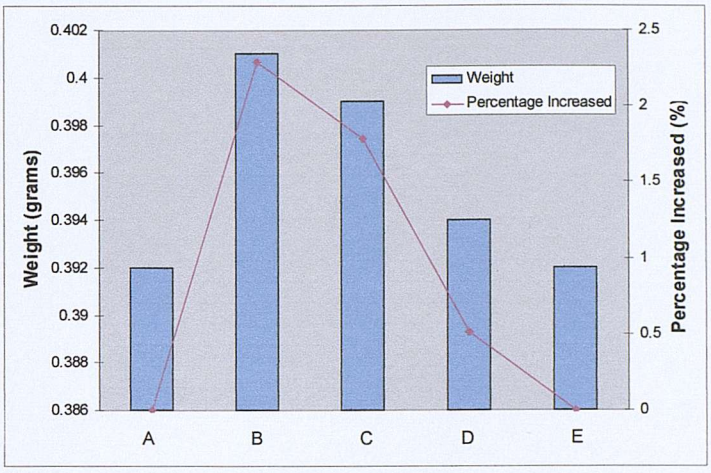

A - Before soaking
B - After soaking for 2 hours
C - 30 minutes after 2 hours of soaking
D - 24 hours after 2 hours of soaking
E - 48 hours after 2 hours of soaking

Figure 7.2. Weight changed in LDPE specimen soaked with (a) acetophenone, (b) α-methylstyrene and (c) cumyl-alcohol.

7.2.2 Experimental protocols

Four sets of experiments were carried out in total. Since the purpose was to determine the influence of various chemicals on electrical conduction and space charge especially on the formation of fast moving packet charge, therefore the same electrode configuration as for fast-moving packet-charge capture was used, which is solid Al(-)block/LDPE/Sc(+). Measurements were taken every 6 second intervals throughout the stressing period in an oven at a temperature of 30°C. Table 7.1 shows a summary of each experimental configuration.

Specimen	Chemical used	Applied voltage (kV)	Specimen thickness (μm)	Stressing period (days)
1	None	20	195	2
2	Acetophenone	20	195	2
3	α-methylstyrene	20	195	2
4	Cumyl-alcohol	20	195	2

Table 7.1. Summary of experimental configuration.

7.2.3 Experimental results

Figures 7.3 to 7.6 show the measured current and charge density profile for specimen no.1 to 4. Figure 7.7 shows the combined graph of the measured current for all specimens, for the first 200 minutes. Notice that the current density of acetophenone is larger than α-methylstyrene initially but after 100minutes, current density of α-methylstyrene was greater than acetophenone. Table 7.2 displays the value of conductivity (σ) calculated using the measured current density at the 200th minute and at the end of 2 days. It clearly shows that every chemical-soaked specimen has a higher conductivity than the non-soaked one either at the 200th minute or at the end of 2 days.

All current density measurements show a transient current peak but occurred at very different time and the duration last varies. Table 7.3 summaries the time and duration of the occurrence of transient current peak.

Specimen	Chemical used	Conductivity (1/Ωm) at the 200th minute	Conductivity (1/Ωm) at the end of 2 days
1	None	4.870e-13	4.253e-13
2	Acetophenone	6.783e-13	5.950e-13
3	α-methylstyrene	1.218e-12	1.058e-12
4	Cumyl-alcohol	1.730e-12	1.0633e-12

Table 7.2. The values of conductivity calculated from the measured current at the 200th minute and at the end of 2 days.

Specimen	Chemical used	Time of occurrence	Duration
1	None	60th minute	~70 minutes
2	Acetophenone	6.3th minute	~7 minutes
3	α-methylstyrene	48th second	~150 seconds
4	Cumyl-alcohol	24th second	~42 seconds

Table 7.3. Summary of time and duration of occurrence of the transient current peak.

(a)

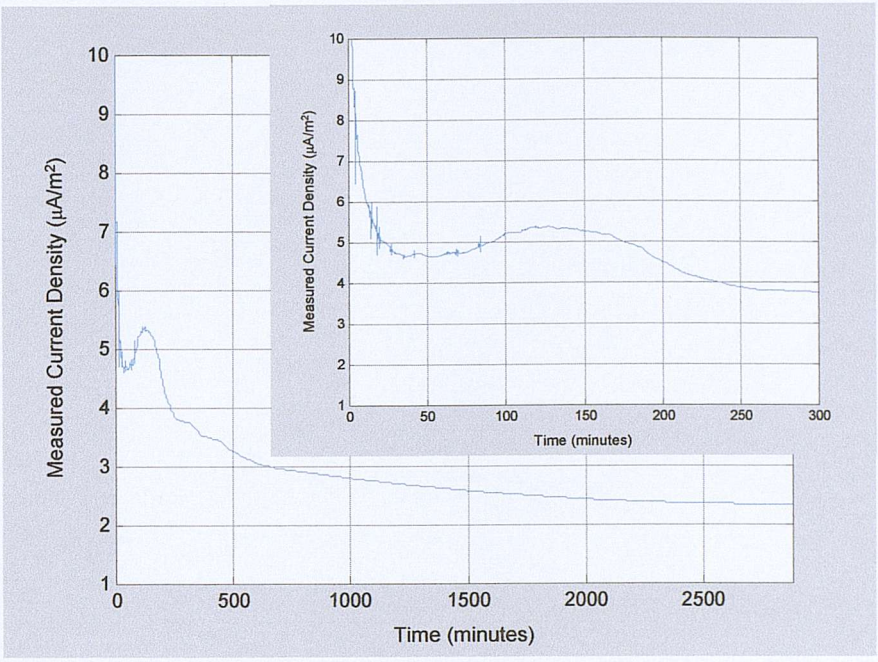

(b)

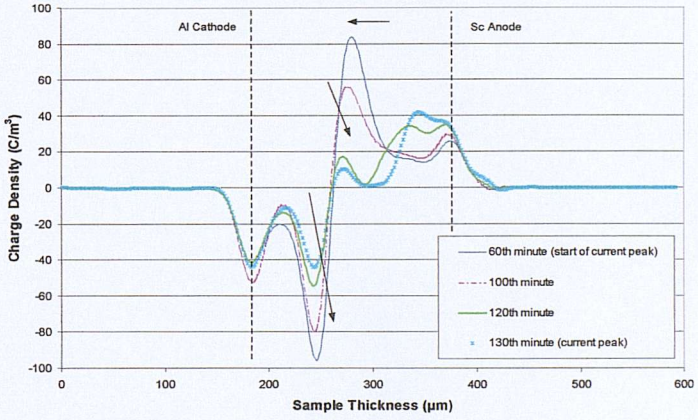

(c)

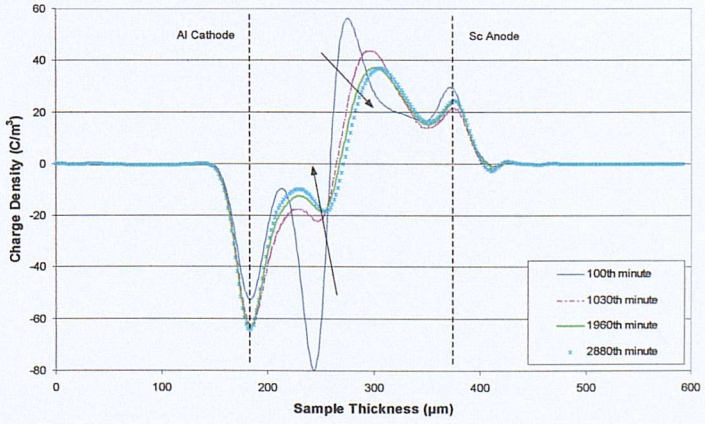

Figure 7.3. (a) The measured current density, (b) space charge density profile corresponded to the transient current peak, from the 60th to 130th minute and (c) space charge density profile between the 100th and 2880th minute for non-soaked specimen no.1.

(a)

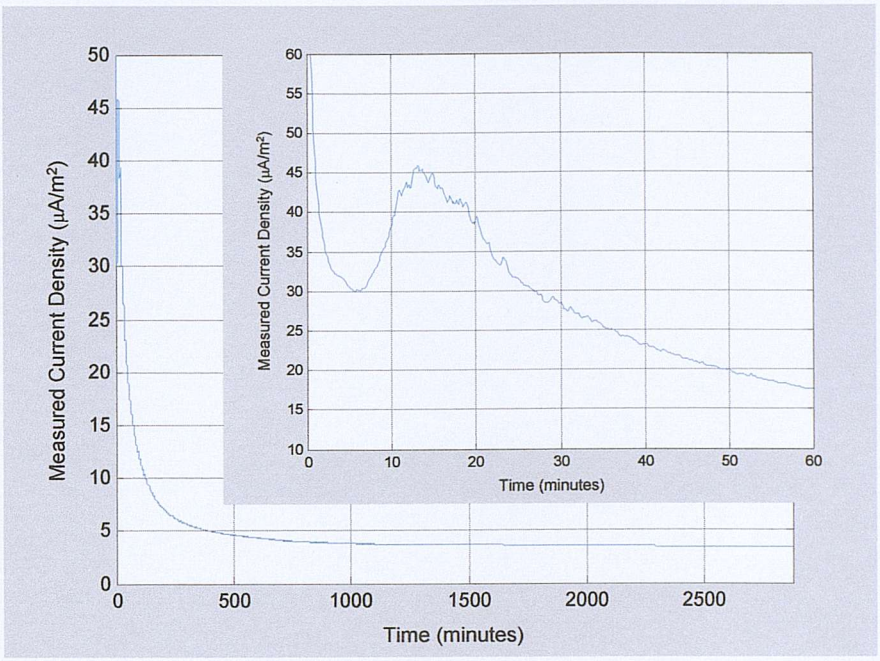

(b)

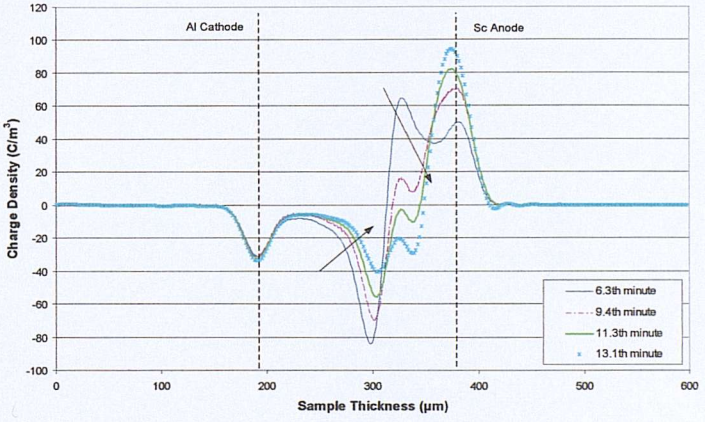

(c)

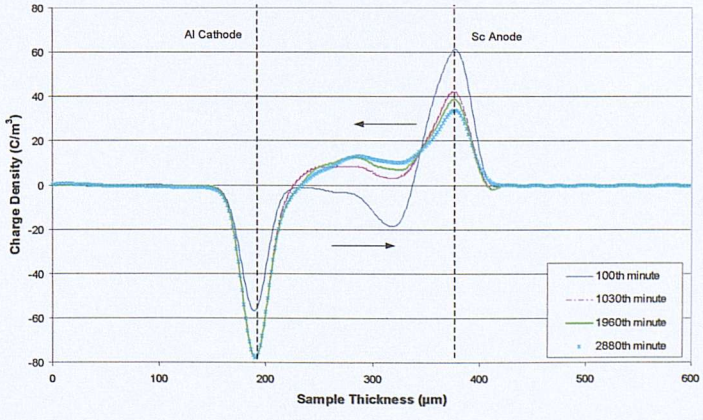

Figure 7.4 (a) The measured current density, (b) space charge density profile corresponded to the transient current peak, from the 6.3th to 13.1th minute and (c) space charge density profile between the 100th and 2880th minute for acetophenone-soaked specimen no.2.

(a)

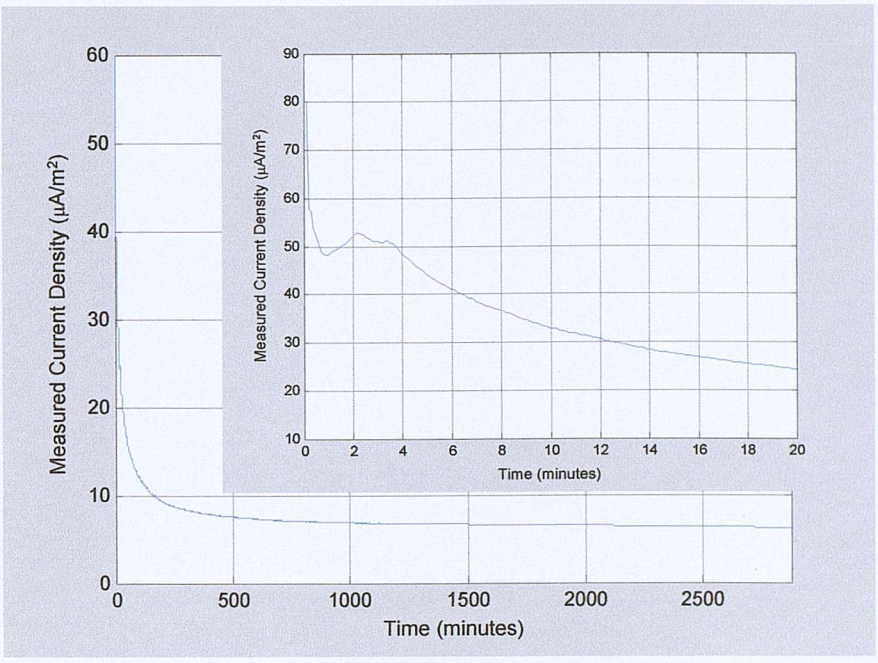

(b)

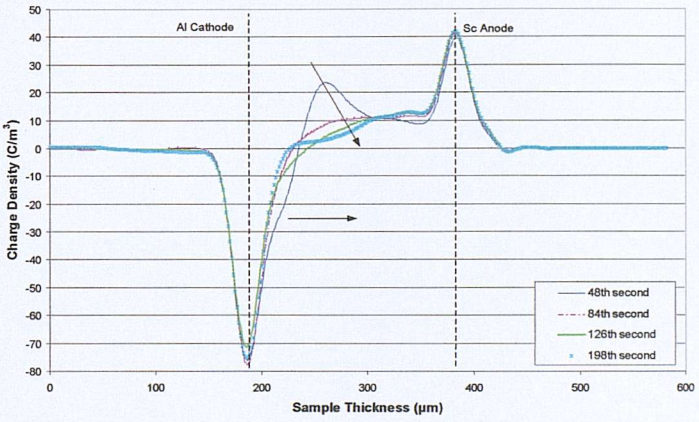

(c)

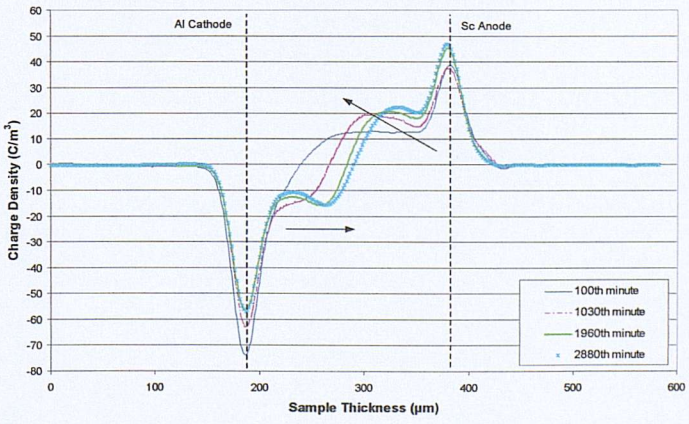

Figure 7.5 (a) The measured current density, (b) space charge density profile corresponded to the transient current peak, from the 48th to 198th second and (c) space charge density profile between the 100th and 2880th minute for α-methylstyrene-soaked specimen no.3.

(a)

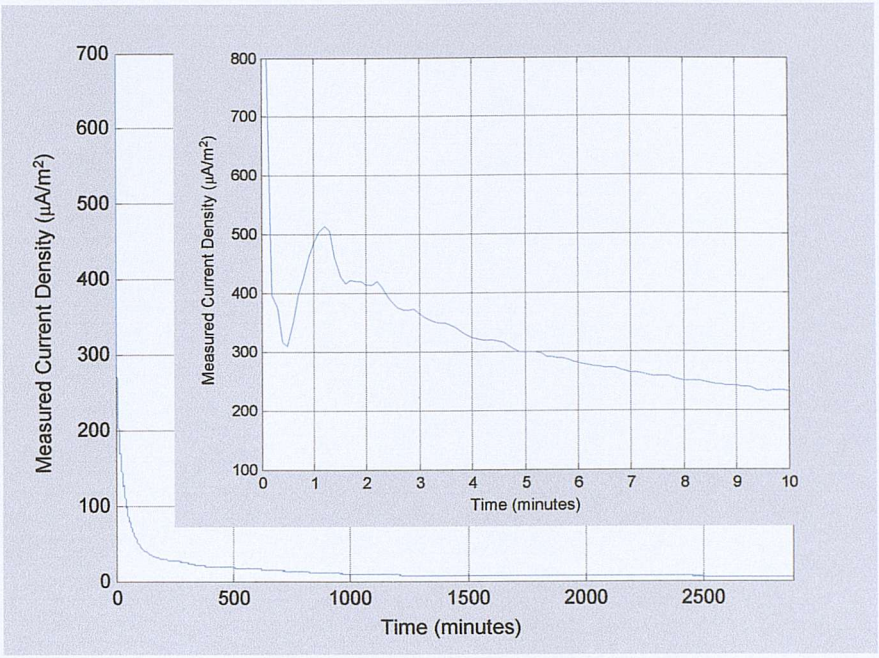

(b)

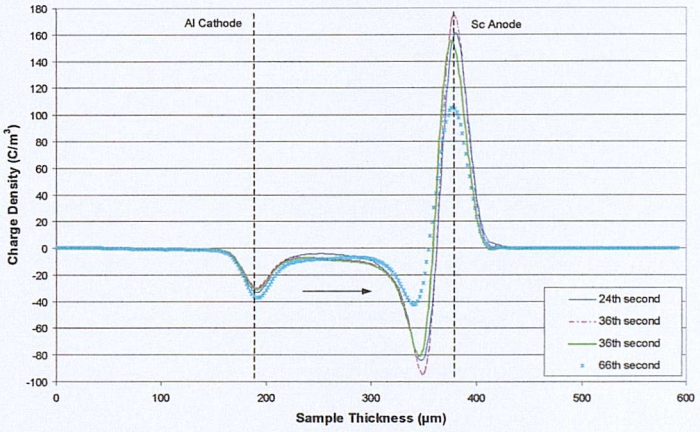

(c)

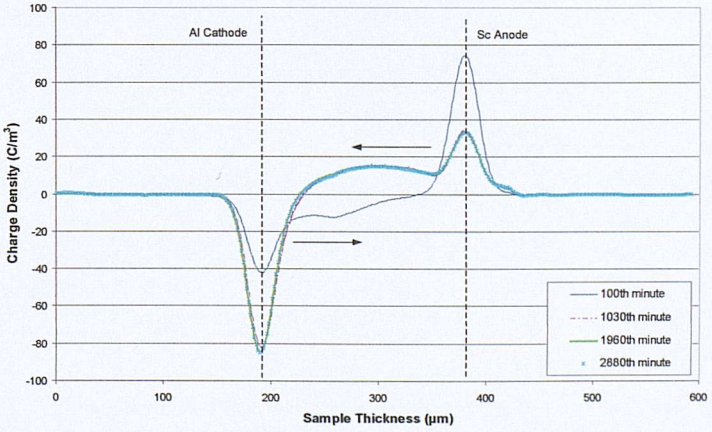

Figure 7.6 (a) The measured current density, (b) space charge density profile corresponded to the transient current peak, from the 24th to 66th second and (c) space charge density profile between the 100th and 2880th minute for cumyl-alcohol-soaked specimen no.4.

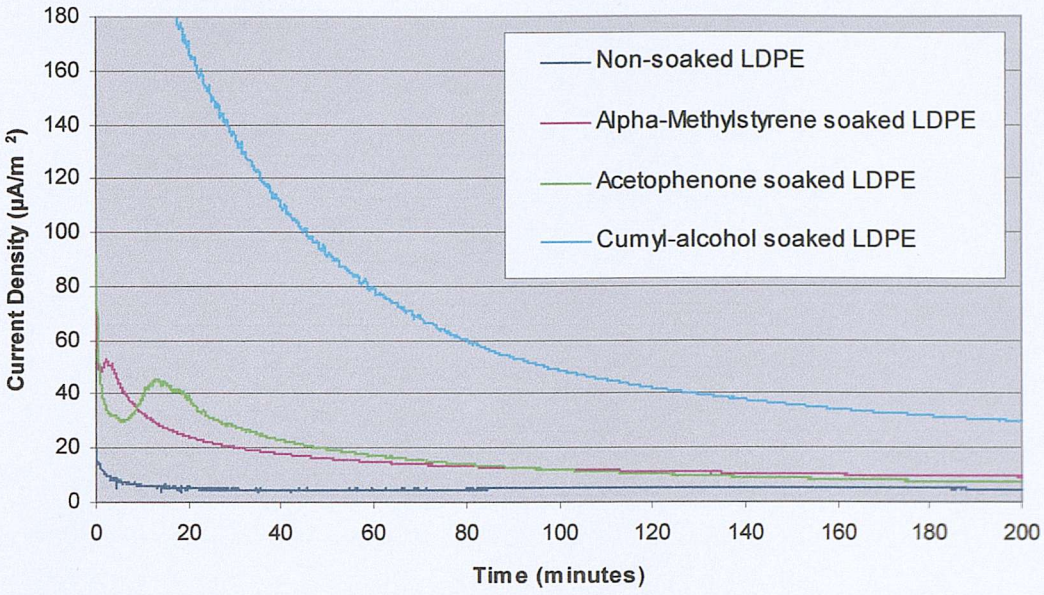

Figure 7.7. Measured current density for non-soaked and chemical-soaked specimens for the first 200 minutes of stressing.

7.2.4 Analysis and discussion of the results

From the weight changed and FT-IR spectra graphs, it was known that the chemicals diffused away quite speedily, with weight gained and chemical content alteration reversed back to the almost original state in one-day time. Therefore, the greatest chemicals effect on the charge density behaviour might be in the early stages. This was verified by calculating the conductivities as shown in table 7.2. Specimen soaked in cumyl-alcohol has the highest conductivity followed by specimen soaked in α-methylstyrene, acetophenone and non-soaked specimen presents with the lowest conductivity at the 200th minute. But at the end of 2 days of stressing the conductivities dropped drastically, with cumyl-alcohol and α-methylstyrene having almost the same conductivity. Therefore, attention was placed on the first 100 minutes of stressing.

The FT-IR spectra of specimen soaked in acetophenone and α-methylstyrene show the greatest change in the carbonyl groups and specimen soaked in cumyl-alcohol exhibits greatly in hydroxyl groups. It has been documented [93] that chemical containing carbonyl functions constitute of deeper electron traps where

chemical originating from hydroxyl present shallower electron traps. M. Meunier et al [93] had reported that the electron trap depth for acetophenone, α-methylstyrene and cumyl-alcohol molecule is 0.9eV, 1.53eV and 0.28eV respectively. The electron trap depth can be used to understand the difference in conductivity for each chemical-soaked specimen. Cumyl-alcohol introduced shallower electron traps (0.28eV) which helped charge carriers to move faster (mobility increased, therefore conductivity increased) as compared to acetophenone and α-methylstyrene. Acetophenone and α-methylstyrene introduced deeper electrons traps which carriers needed a long time (mobility decreased, therefore conductivity decreased) to move from one trap to the other compared to cumyl-alcohol. The presence of these by-products has undoubtedly increased the conductivity of the material. It can also be substantiated by the fact that a shorter time was taken for the first transient current peak to appear on each chemical-soaked specimen. Although the measured current for the chemical-soaked specimens were enormous (at least for the first 100 minutes) compared to the fresh XLPE, this is because the initial weight gain (~1.6% to 10%) from soaking specimen in each individual chemical was much greater compared to impurities content in fresh XLPE specimen. The actual removal amount of residual by-products from fresh XLPE is only ~0.51%.

By the ~1000th minute, space charge profile of all chemical-soaked specimens have stabilised, the stabilised profile were very different from its beginning (few hundred minutes) profile. All the stabilised space charge profiles including the non-soaked specimen look almost alike with more positive carriers than the negative. The calculated amount of the positive bulk charges is greater than negative (after 2 days) immediately after volts-off for all specimens. The look alike space charge profiles after the ~1000th minutes for all specimens validated that the chemical content in the soaked-specimens have diffused away greatly.

N. Hirai et al [88] concluded from their experimental results that with the presence of acetophenone and α-methylstyrene carrier transport becomes accelerated and with cumyl-alcohol carriers are trapped. In our case a different observation was made from space charge profiles that corresponded to the transient current peaks, the largest amount of charges remained in the bulk for the longest time were in the order

of non-soaked specimen followed by specimen soaked in acetophenone, α-methylstyrene and cumyl-alcohol. Furthermore, the calculated absolute amount of charges remained in the bulk (after 2 days) immediately after volts-off have also proved that non-soaked specimen have the largest amount of charge followed by specimen soaked in acetophenone, α-methylstyrene and cumyl-alcohol.

Comparing the non-soaked specimen to the acetophenone-soaked specimen, both of them have similar charge profile pattern before the occurrence of transient current peak. However, the non-soaked specimen has taken ~60 minutes to accumulate the amount of charge and the increased measured current started at the ~60^{th} minute. On the other hand, the acetophenone-soaked specimen just took ~6.3 minutes to build up a similar charge profile and the measured current increases starting at the ~6.3^{th} minute. This revealed that acetophenone reduces the injection barrier and enhanced charge injection for both negative and positive charges. References [89-92] have also reported a similar experience. α-methylstyrene lowered the injection barrier at the anode and favoured more positive charge injection whereas cumyl-alcohol strongly supported negative charge injection.

All chemical-soaked specimens did not exhibit consecutive charge packet behaviour as in fresh XLPE specimen, this might be attributed also to the fact that the by-products in fresh XLPE are a combination of these chemicals and not individually. Since the removal of by-products in fresh XLPE and chemical-soaked specimens did not show consecutive fast charge packets behaviour, therefore the combination of crosslinking by-products together with the crosslinked polymer morphology might be responsible for the consecutive fast charge packets behaviour. There is also another possibility that the presence of antioxidants in fresh XLPE which is not found in chemical-soaked specimens is accountable for the consecutive fast charge packets behaviour.

7.3 Conclusions

The presence of by-products like of acetophenone, α-methylstyrene and cumyl-alcohol plays a part in the conduction process whereby it increases the conductivity

of the material. All chemical-soaked specimens have higher measured current than the non-soaked one. Experimental results show that acetophenone reduces the injection barrier and enhances charge injection of both signs. α-methylstyrene lowers the injection barrier at the anode and favoured more positive charge injection whereas cumyl-alcohol strongly supports negative charge injection. The most likely factors responsible for fast packet charge behaviours might be (a)the combination of impurities together with the crosslinked polymer morphology and/or (b)the presence of antioxidants in fresh XLPE which is not found in chemical-soaked specimens.

Chapter 8

Comparison and Discussion of All Experimental Results

8.1 Comparison and Discussion

Analysis of chapter 5 to 7 experimental results shows one important fact. The transient current peaks behaviour is not exclusive to fresh XLPE material; it can also surface in LDPE and degassed XLPE. Transient current peak is part of a conduction process characteristic whereby it will arise under the circumstance if the rate of electron injection from the supply is greater than the previous time. The increase of electron injection will occur when there is sufficient increase in amount of electrons extraction at the anode, in other words it all depends on the rate of extraction and injection. Therefore the time taken for the first transient current peak to appear can be used to judge and compare the initial mobility of the carriers.

Temperature, electrode materials and impurities are the three factors that had been proven to affect the time required for the first transient current peak to occur. Whether the transient current peak occurs consecutively for a short period of time or

several times but lasts for a longer period of time depends on the rate of carrier injection and extraction which of course depends on (a) the interfacial potential barrier height between electrode and specimen and (b) content of impurity.

Researchers who had carried out only current measurement on dielectrics to study the conduction characteristics and observed a current peak usually ascribe it to transient SCLC peak theory. Also researchers who had carried out both current and charge measurement and spotted a current peak credited it either to transient SCLC peak theory claiming a current peak occurs when the injected charge front reaches the counter electrode [36] or by the increase in number of residual by-products drift carriers [87]. Scrutinizing all experimental results redefines the understanding and explanation for transient current peaks phenomenon.

Here, it had been proven successfully that simultaneous space charge and current measurement is achievable. Simultaneous charge and current measurement is important as external current detection gives extra information about the total charge carrier behaviour as PEA technique is only able to measure the net amount of positive and negative charges presence in the bulk of the specimen.

The electrode configuration plays a critical role in charge carrier behaviour. This can be demonstrated by the formation of consecutive charge packet accompanied by corresponding transient current peaks in fresh XLPE specimen (chapter 6). Fresh XLPE specimens with solid aluminium cathode exhibited recurring transient current peaks, whereas when a solid aluminium cathode was used, only one current peak was observed.

The measured current is affected by the mobility of carriers. LDPE specimens soaked in different chemicals show a different mobility for each type of carrier. Therefore, if modelling of carrier behaviour in fresh XLPE is to be carried out, different mobility must be considered for each type of impurity present instead of using just one constant mobility.

Tests on both LDPE and XLPE using evaporated or solid aluminium as the cathode and semicon as the anode show no transient current peak re-occurring as time increase to 24 hours. This might be due to the restricted amount of injected electrons near to the cathode got deeply trapped with time, therefore less charge carriers were extracted at the anode, leading to less chances of increased electron injection. As for test on LDPE using semicon as the cathode and evaporated aluminium as the anode (chapter 5, figure 5.3), electrons were easily injected from Sc(-) compared to holes from Al(+). There were large amount of electrons being injected and it takes a longer time for the electrons to move towards the anode. It took more than 200 minutes before the occurrence of the first transient current peak and the 2^{nd} subsequent current peak lasted for a long period of time. The generous electrons injection and more electrons gradually reached the anode and got extracted, attracting more electrons from the supply which therefore caused the measured current to increase. The 2^{nd} current peak lasted for such a long time is believed due to the strong injecting ability at the cathode, which keeps pushing the injected electrons towards the anode.

General observation when there is an increase in the measured current includes (a) there is an increasing amount of positive charge carriers in the bulk some time before the increment occurs and (b) the increment occurs with the decreasing amount of positive charge carriers in the bulk.

The applied stress causes charge carriers to be injected into the bulk and creation of electrons, positive and negative ions if impurities are present. Space charge distribution in the bulk alters the local electric field (section 2.3.3) inside the specimen where it is being enhanced and reduced at different locations. The electric field distribution in the bulk affects subsequent charge carrier transportation. It is believed that a threshold field is required for initiation of a higher injection current. And this threshold field needed varies with the location in the bulk.

Attempts were made to investigate the threshold field on all experimental results. Investigation shows no conclusive value as the threshold field value for initiation of higher injection current varies with time. Nevertheless, a few general

trends were observed such as (a) the value of the threshold field depends on the distance away from the cathode. The nearer the enhance field is from the cathode; the lower the field is needed to initiate the increment. The further away the enhance field is from the cathode; the higher the field is needed to initiate the increment and (b) the threshold field required for subsequent transient current peak, if any, is much lower than the first.

8.2 Conclusions

Transient current peaks can occur in any dielectrics under the applied voltage condition, it is part of a conduction process characteristic whereby it will arise under the circumstance if the rate of electron injection from the supply is greater than the time before. The misconception that most researchers have is that carrier movement within the bulk caused the transient current peak. Scrutinizing all experimental results redefine the understanding and explanation for transient current peaks phenomenon. Carrier movement such as injection of the induced negative surface charges on the cathode into the bulk or negative bulk charges moving deeper towards the opposite electrode do not contribute to the succeeding current measurement.

General observation when there is an increased in the measured current include (a) there is an increasing amount of positive charge carriers in the bulk some time before increment occurs and (b) the increment occurs with the decreasing amount of positive charge carriers in the bulk. Attempts were made to investigate the threshold field on all experimental results. Investigation shows no conclusive value as the threshold field value for initiation of higher injection current varies with time. Nevertheless, a few general trends were observed such as (a) the value of the threshold field depends on the distance away from the cathode. The nearer the enhanced field is from the cathode; the lower the field is needed to initiate the increment. The further away the enhanced field is from the cathode; the higher the field is needed to initiate the increment and (b) the threshold field required for subsequent transient current peak, if any, is much lower than the first.

Chapter 9

Conclusions and Further Work

9.1 Conclusions

This thesis presented here reports on (1) the designing, building, testing, trouble-shooting of the improved Pulsed Electro-acoustic system which is capable of measuring charge and current simultaneously and (2) using the system to establish a relationship between charge and current measurement through experimenting on polyethylene cable insulation. Long before non-destructive space charge detection techniques were commonly used, conduction characteristics of cable insulation were studied broadly by measuring the external current. The combination of measuring current and charge concurrently helps to establish a link between these two parameters which will aid the interpretation of the experimental results.

The construction of this PEA system has to include many detail considerations. It includes (a) taking into account the width of the pulse injected into the specimen; this will affect the resolution of the signal (the width of the first and second peak), (b) constant evenly applied pressure must be asserted onto the specimen to ensure no gap between contact surfaces which will cause the distortion

of collected signal, (c) the thickness of the transducer employed, a thicker transducer will give a larger signal magnitude but this will sacrifice the resolution of the signal. If a thinner transducer is used, a better resolution is achievable with the sacrifice on the signal magnitude. In our case, a thicker transducer caused oscillations in the signal output. Therefore a compromise has to be made between these two, (d) if separate bottom electrode are to be constructed so as to enable current and charge detection, a small disturbance is unavoidably present in the signal output and (e) if the size of the top electrode is too large, it might lead to oscillation which results in deformed signal output.

The fully computerised rig (except the high voltage supply unit) is made possible by programs written in LabView enironment. It enables raw signals to be collected, processed and stored in the computer at a short continuous time interval as desired.

For the experiment aspects, at the initial stage additive-free low density polyethylene (LDPE) specimens were employed to investigate the electrode effect. LDPE is the basic element of crosslinked polyethylene (XLPE) cable insulation. All materials have different work function where this will determine the interfacial potential barrier height upon bringing two materials in contact, in this case were the electrode material and LDPE specimen. The higher the barrier height the more difficult carriers are going to be injected into the bulk. The mechanism responsible for the efficiency of charge carrier injection seen earlier was credited to Schottky injection where the carriers were thermally excited over the interfacial potential barrier into the bulk with the help of the applied field lowering the barrier.

Impact of temperature on conduction behaviour is also highlighted using LDPE. The higher temperature increases the mobility and amount of carrier available for conduction, leading to a larger conduction current. It also multiplies the opportunity of getting trapped charges detrapped, thus it increases the probability of recombining with opposite sign carriers and/ or extracted by the opposite electrode. This is verified by the larger amount of charges in the bulk whether volts-on or off at lower temperature compared to higher temperature. If constant measurement

temperature is not maintained, a slight change in few degrees Celsius will increase the mobility and amount of fast mobile charges, this changes was clearly captured by the picoammeter but not so noticeable by the PEA system. This insinuates the charge profile captured by the PEA system consist of a very small amount of fast mobile charge.

The next stage of tests was carried out using XLPE specimens exploring the residual by-products (created through the crosslinking process) and electrode effect. There are two kinds of XLPE specimens being used, namely freshly (undegassed) press moulded XLPE and degassed XLPE where it had undergone heat treatment in an vacuum oven to have its by-products removed. Test on fresh XLPE specimen using the rig bottom electrode with a layer of silicon oil as the cathode and semicon with a layer of silicon oil as the anode exhibited consecutive fast moving charge packets moving from one electrode to another. This is due to the dissociation of residual by-products (creation of electrons, positive and negative ions) and injected positive and negative charges from the electrodes whereby the dissociated electrons and negative ions together with electrons injected from the cathode moved towards the anode, at the same time, the positive ions and holes injected from the anode travelled towards the cathode. The charge packet movement corresponded with the oscillations in the measured current. The same kind of specimen tested using evaporated aluminium as cathode did not show similar behaviour, this verified the fact the electrode did influence the conduction characteristics. The fast packet charge behaviour depends not only on the applied electric field but also the electrode material.

A comparison between fresh and degassed XLPE specimen (both using the rig bottom electrode with a layer of silicon oil as the cathode and semicon with a layer of silicon oil as the anode) shows that the degassed XLPE specimen did not display with consecutive fast moving charge packets as the fresh XLPE specimen did. This implies that the heat treatment process did remove some of the impurities which were present in the specimen originally. The presence of by-products has also increased the conductivity that led to a higher measured current. Higher temperature testing condition on these fresh and degassed XLPE specimens displayed a similar

characteristic to those LDPE specimens where the movement of carriers intensified with lesser charges accumulated in the bulk.

The final stage of tests involved chemical-soaked LDPE specimens. The chemicals used were those found in fresh XLPE specimens, namely acetophenone, α-methylstyrene and cumyl-alcohol. The aim of these tests was to validate the contribution of these chemicals as compared to those in XLPE. Each LDPE specimen was impregnated into the chemical individually. It was found that these chemicals have undoubtedly increased the conductivity of the material. All chemical-soaked specimens did not exhibit consecutive fast moving charge packet behaviour as in fresh XLPE specimen, this might attribute to the fact that the by-products in fresh XLPE are a combination of these chemicals and not individually. Since the removal of by-products in fresh XLPE and chemical-soaked specimens did not present with consecutive fast charge packets behaviour, therefore the combination of crosslinking by-products together with the crosslinked polymer morphology might be responsible for the consecutive fast charge packets behaviour. There is also another possibility that the presence of antioxidants in fresh XLPE which is not found in chemical-soaked specimens is accountable for the consecutive fast charge packets behaviour.

From all the experimental results, it helps to establish a relationship between the charge and current measurement and re-defines the explanation for the transient current peak phenomenon. There are electrons continuously being pumped either onto the surface of the specimen and/or into the bulk from the supply when voltage are applied, this current include (a) current due to the leakage resistance parallel to the specimen, (b) electrons induced on the surface of the cathode due to the movement and injection of positive charge carriers and/or (c) electrons injected into the bulk. Transient current peak is part of a conduction process characteristic whereby it will arise under the circumstance if the rate of electron injection from the supply is greater than the time before. Carrier movement such as injection of the induced negative surface charges on the cathode into the bulk or negative bulk charges moving deeper towards the opposite electrode do not contribute to the succeeding current measurement. However, such carrier movement does help to encourage and attract more carriers from the supply subsequently.

General features when there is an increase in the measured current include (a) there is an increasing amount of positive charge carriers in the bulk some time before the increment occurs and (b) the increment occurs with the decreasing amount of positive charge carriers in the bulk.

No conclusive threshold field value for initiation of higher injection current was found as it varies with time. However, general trends were observed such as (a) the value of the threshold field depends on the distance away from the cathode. The nearer the enhanced field is from the cathode; the lower the field is needed to initiate the increment. The further away the enhanced field is from the cathode; the higher the field is needed to initiate the increment and (b) the threshold field required for subsequent transient current peak, if any, is much lower than the first.

9.2 Further Work

Enormous amount of experimental work on space charge measurement on cable insulation has been carried out by researchers all over the world. In the recent years only little modelling work [83, 94-97] was performed to verify theories governing the carrier behaviour and all these modelling work do not universally feasible on all the actual physical range of parameters. I have tried using the model proposed by N. Zebouchi et al [95], where it involves the carriers hopping theory and trapping coefficient, the model generate illogical results if a certain particular parameter is changed. A conversation discussion with Professor C. Laurent from Université Paul Sabatier, one of the co-authors of [97] also shares and confirmed the same standpoint with his proposed model. More in depth study and research into modelling work to substantiate the experiments is favourable.

Appendix A

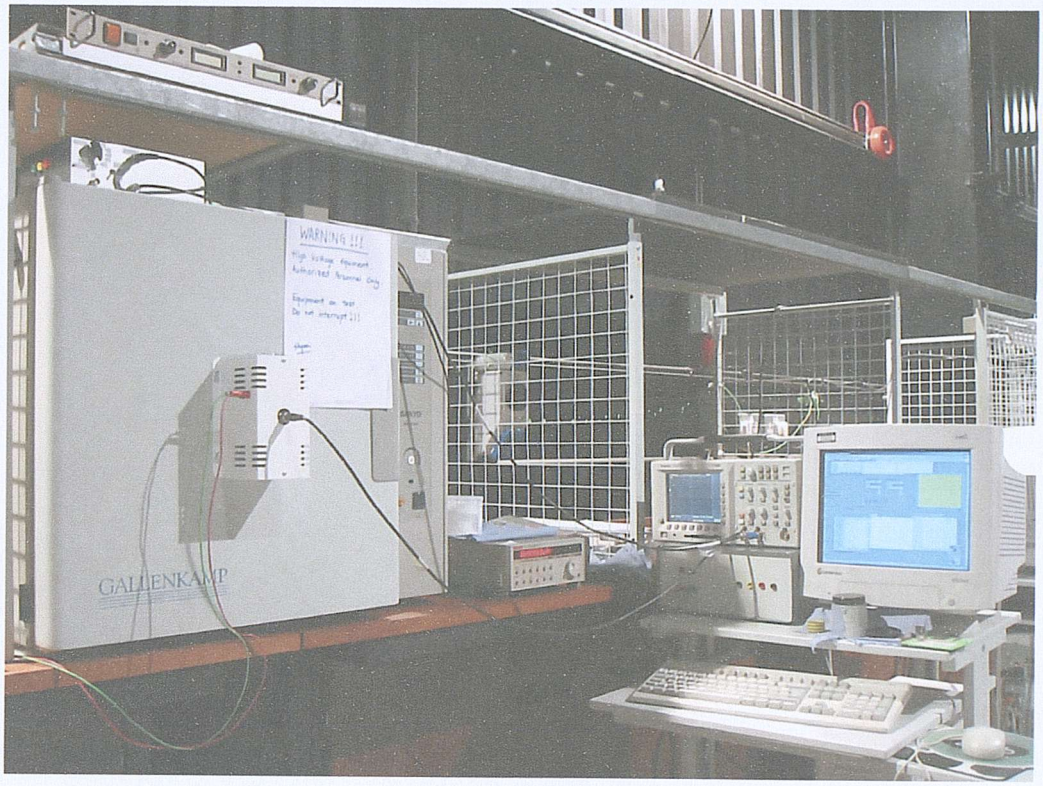

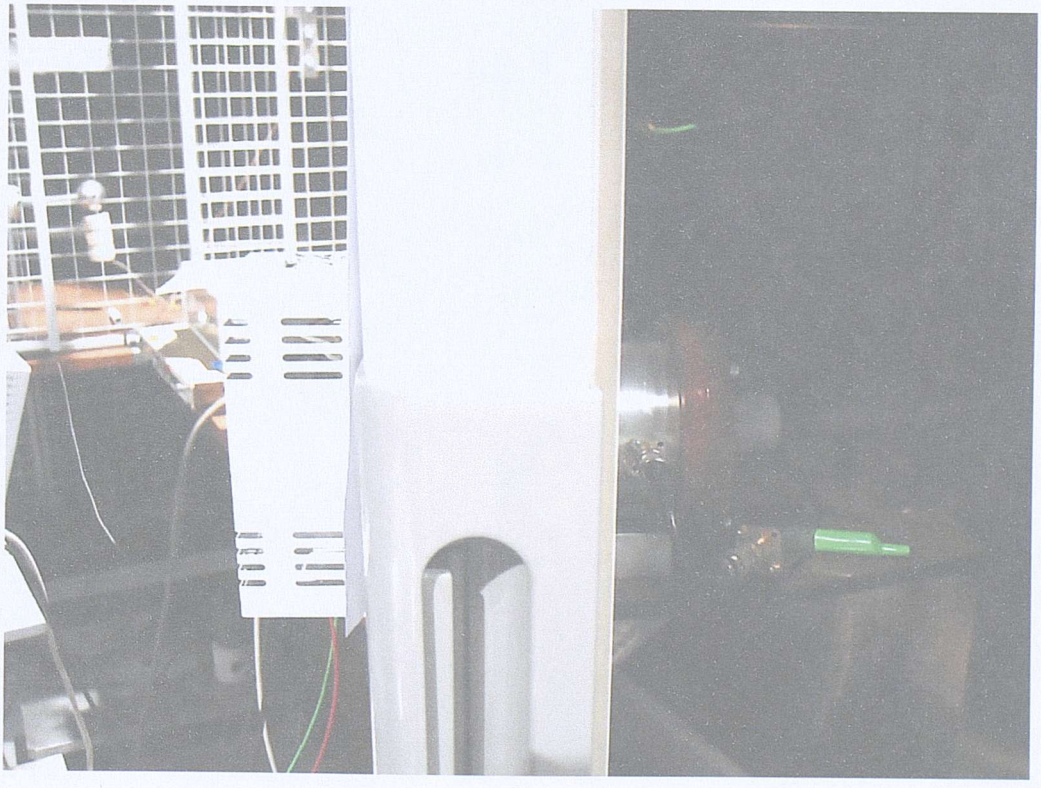

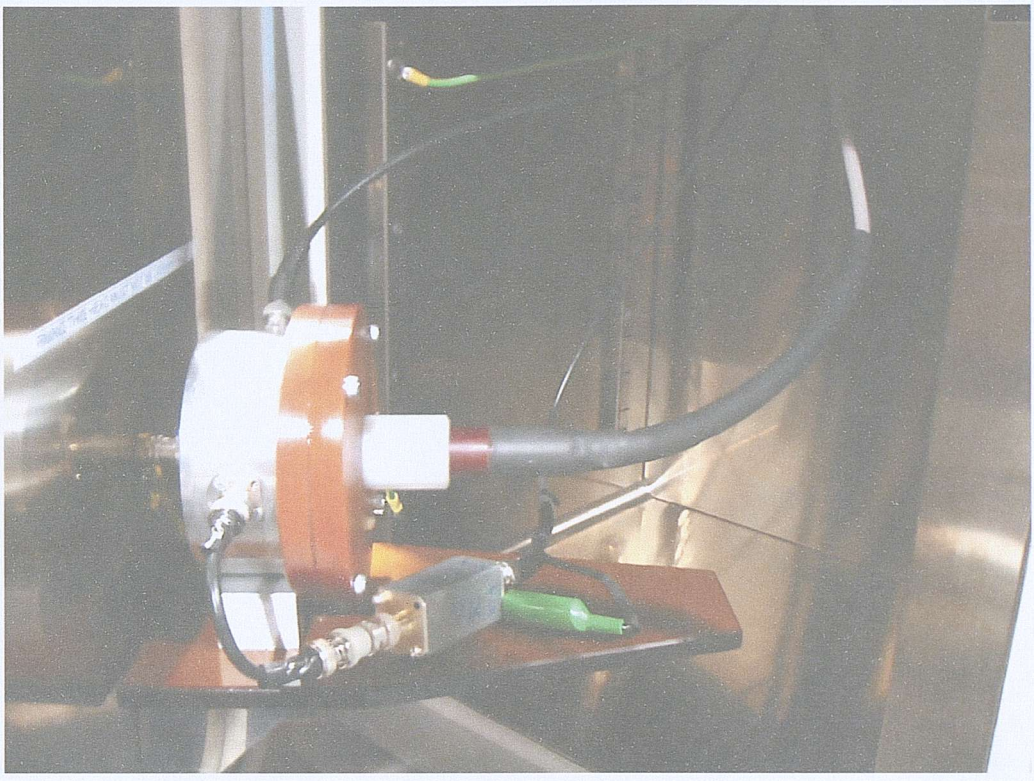

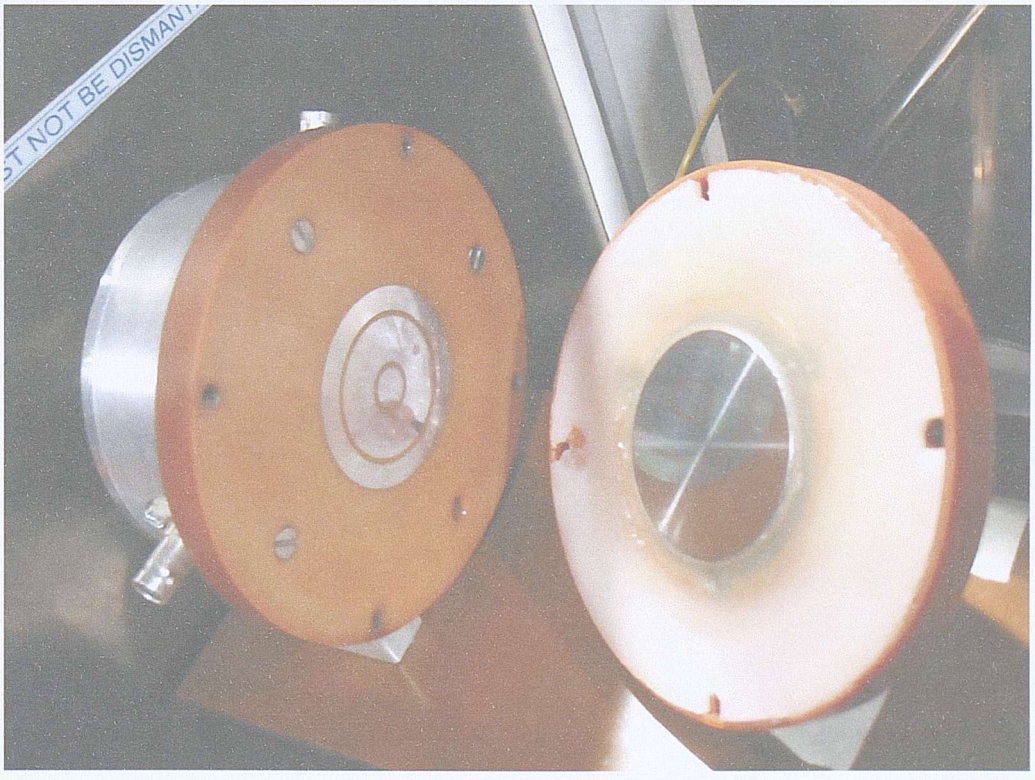
ST NOT BE DISMANT

Appendix B

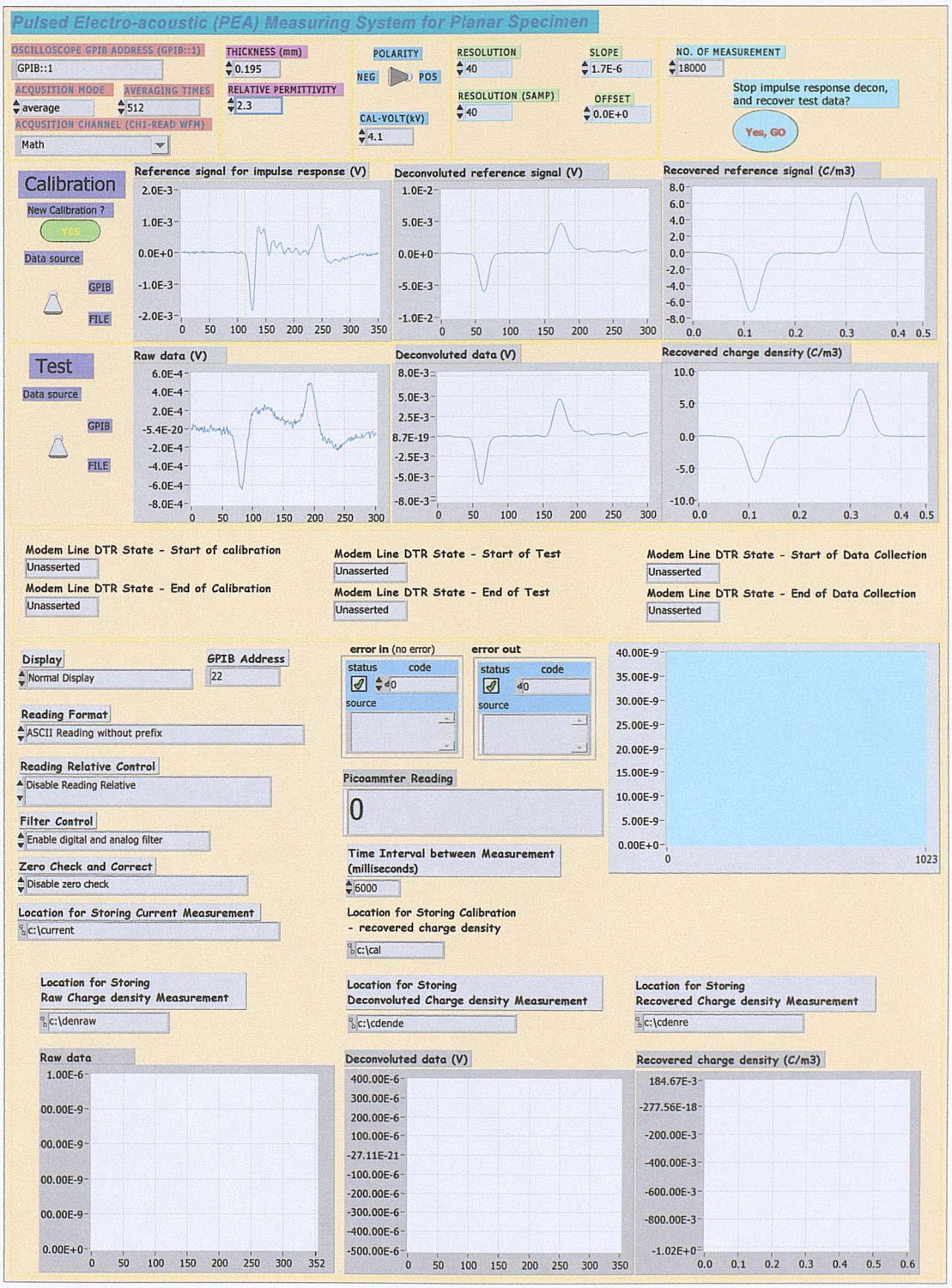
Pulsed Electro-acoustic (PEA) Measuring System for Planar Specimen
OSCILLOSCOPE GPIB ADDRESS (GPIB::1)
GPIB::1
ACQUISITION MODE
average
AVERAGING TIMES
512
ACQUISITION CHANNEL (CH1-READ WFM)
Math
THICKNESS (mm)
0.195
RELATIVE PERMITTIVITY
2.3
POLARITY
NEG
POS
CAL-VOLT(kV)
4.1
RESOLUTION
40
RESOLUTION (SAMP)
40
SLOPE
1.7E-6
OFFSET
0.0E+0
NO. OF MEASUREMENT
18000
Stop impulse response decon, and recover test data?
Yes, GO
Calibration
New Calibration ?
YES
Data source
GPIB
FILE
Reference signal for impulse response (V)
Deconvoluted reference signal (V)
Recovered reference signal (C/m3)
Test
Data source
GPIB
FILE
Raw data (V)
Deconvoluted data (V)
Recovered charge density (C/m3)
Modem Line DTR State - Start of calibration
Unasserted
Modem Line DTR State - End of Calibration
Unasserted
Modem Line DTR State - Start of Test
Unasserted
Modem Line DTR State - End of Test
Unasserted
Modem Line DTR State - Start of Data Collection
Unasserted
Modem Line DTR State - End of Data Collection
Unasserted
Display
Normal Display
GPIB Address
22
Reading Format
ASCII Reading without prefix
Reading Relative Control
Disable Reading Relative
Filter Control
Enable digital and analog filter
Zero Check and Correct
Disable zero check
Location for Storing Current Measurement
c:\current
error in (no error)
status
code
source
error out
status
code
source
Picoammter Reading
0
Time Interval between Measurement (milliseconds)
6000
Location for Storing Calibration - recovered charge density
c:\cal
Location for Storing Raw Charge density Measurement
c:\denraw
Location for Storing Deconvoluted Charge density Measurement
c:\cdende
Location for Storing Recovered Charge density Measurement
c:\cdenre
Raw data
Deconvoluted data (V)
Recovered charge density (C/m3)

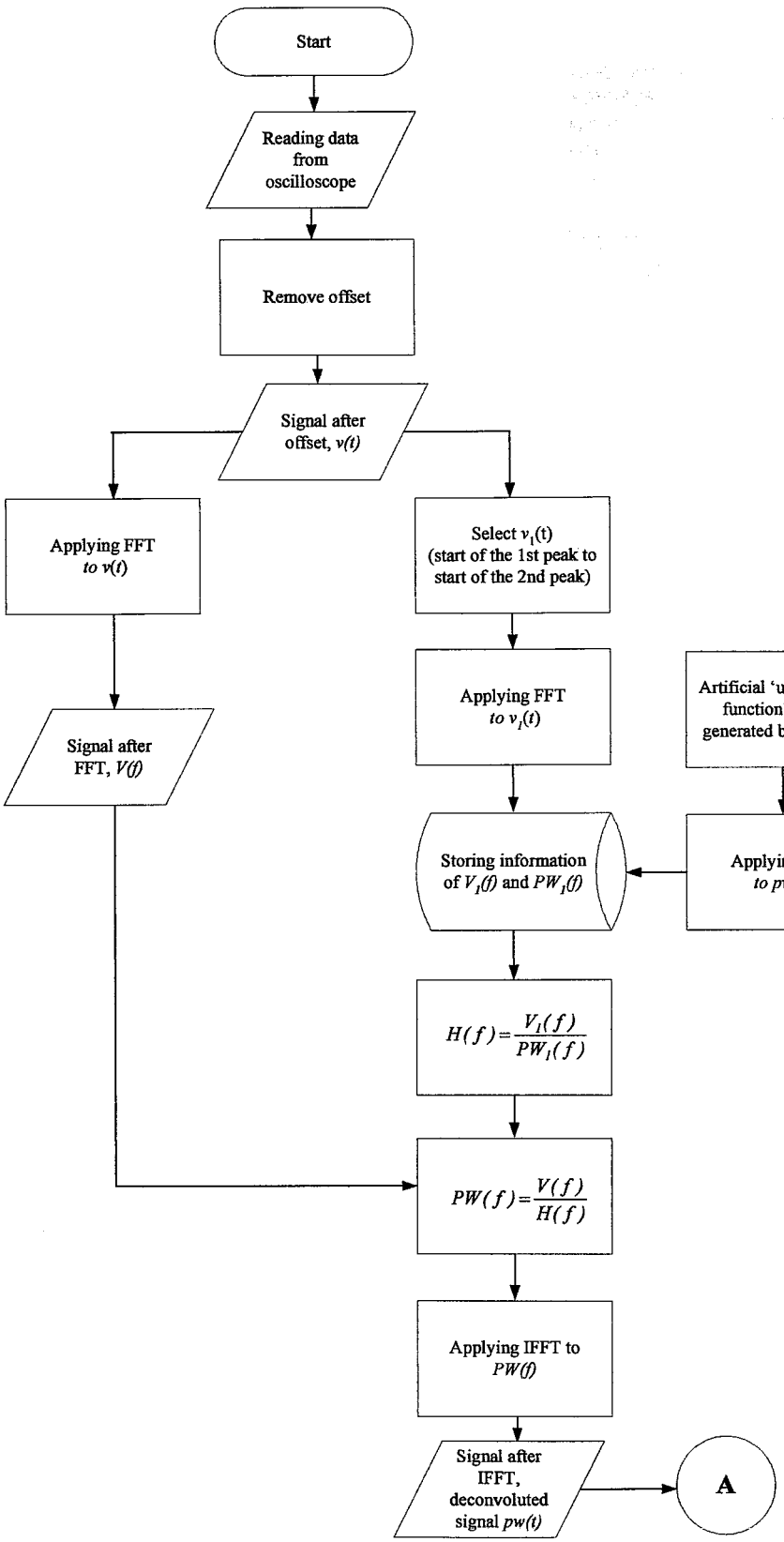

Flowchart showing deconvolution process

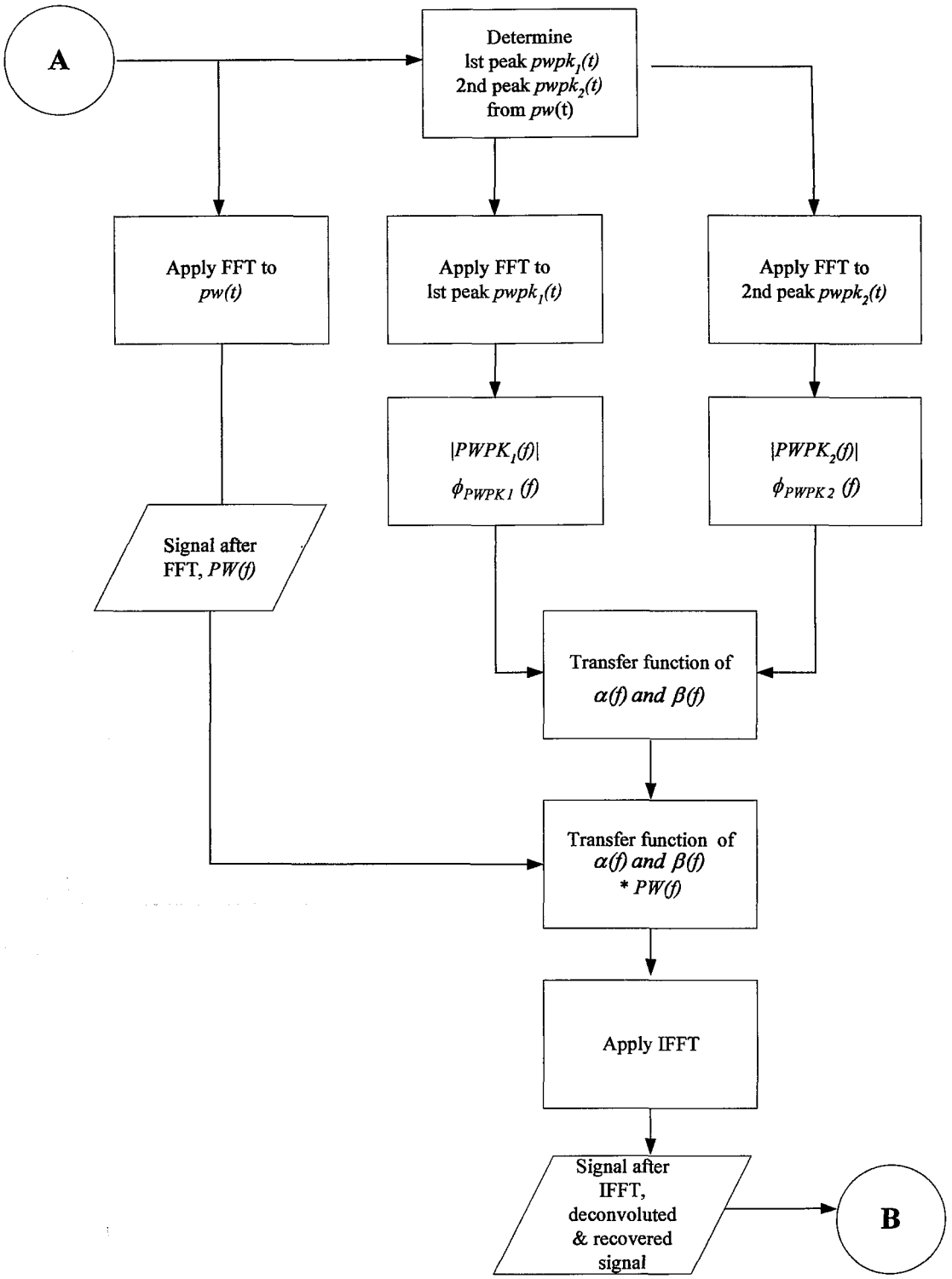

Flowchart showing attenuation and dispersion compensation process

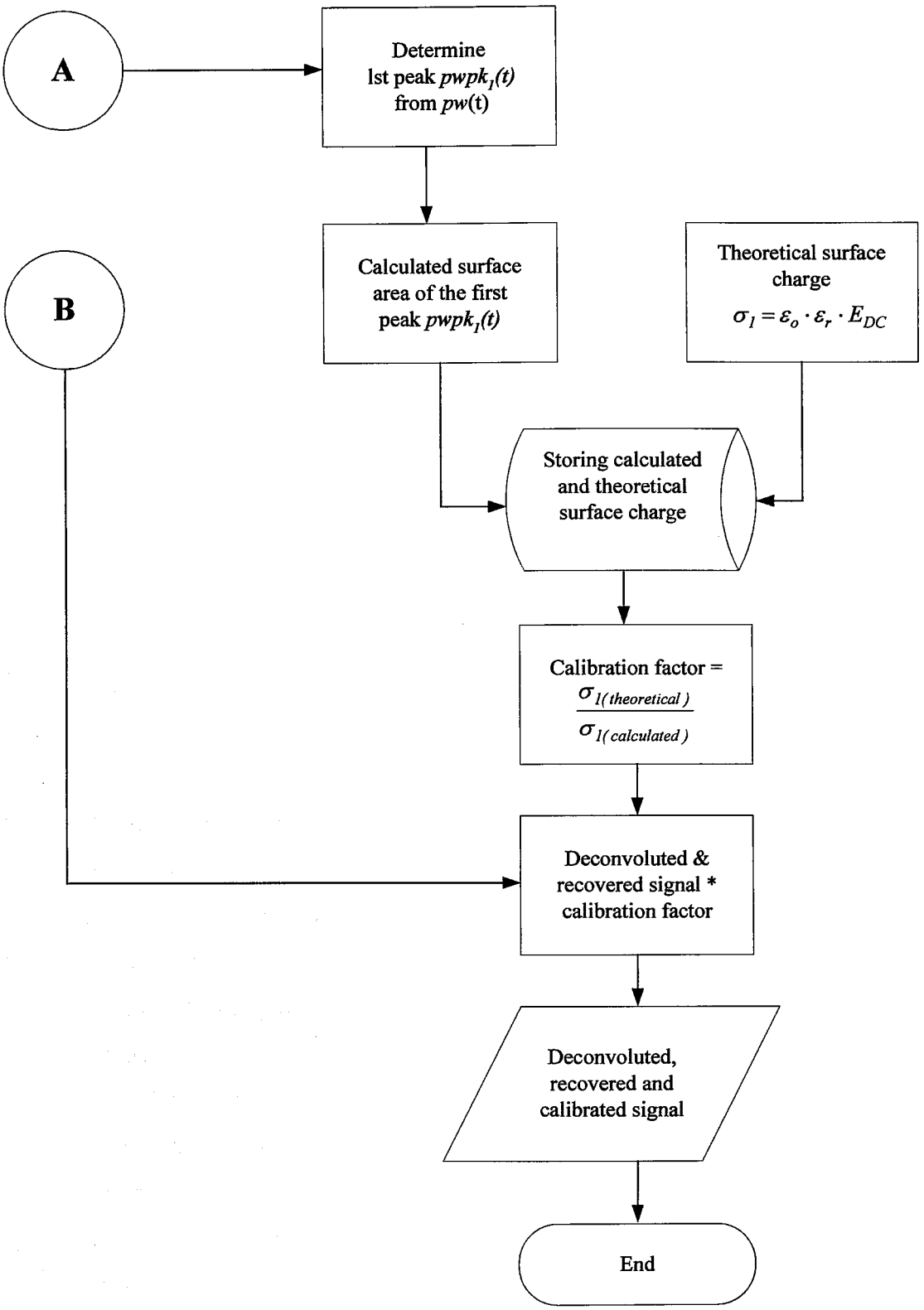

Flowchart showing calibration process

References

1. R. M. Black, "The History of Electric Wires and Cables", Chapter 3, pp. 37-47, Peter Peregrinus Ltd, ISBN 0-86341-001-4, 1983.
2. R. M. Black, "The History of Electric Wires and Cables", Chapter 9, pp. 120-130, Peter Peregrinus Ltd, ISBN 0-86341-001-4, 1983.
3. R. M. Black, "The History of Electric Wires and Cables", Chapter 5, pp. 68-84, Peter Peregrinus Ltd, ISBN 0-86341-001-4, 1983.
4. C. C. Barnes, "Electric Cables", Chapter 5, pp. 47-67, Sir Isaac Pitman & Sons Ltd., London, 1964.
5. L. A. Dissado, G. Mazzanti and G. C. Montanari, "Role of Trapped Space Charges in the Electrical Ageing of Insulating Materials", IEEE Transactions on Dielectrics and Electrical Insulation, vol. 4, no. 5, pp. 496-506, October 1997.
6. M. S. Khalil, "International Research and Development Trends and Problems of HVDC cables with Polymeric Insulation", IEEE Electrical Insulation Magazine, vol. 13, no. 6, pp. 35-47, Nov/Dec 1997.
7. M. Ieda and Y. Suzuoki, "Space Charge and Solid Insulating Materials: In Pursuit of Space Charge Control Molecular Design", IEEE Electrical Insulation Magazine, vol. 13, no. 6, pp. 10-17, Nov/Dec 1997.
8. T. Mizutani, H. Semi and K. Kaneko, "Space Charge Behavior in Low-Density Polyethylene", IEEE Transactions on Dielectrics and Electrical Insulation, vol. 7, no. 4, pp. 503-507, August 2000.
9. D. K. Das-Gupta, "Electrical Properties of Surfaces of Polymeric Insulator", IEEE Transactions on Electrical Insulation, vol. 27, no. 5, pp. 909-923, October 1992.
10. K. S. Suh, J. H. Koo, S. H. Lee, J. K. Park and T. Tanaka, "Effects of Sample Preparation Conditions and Short Chains on Space Charge Formation in LDPE", IEEE Transactions on Dielectrics and Electrical Insulation, vol. 3, no. 2, pp. 153-160, April 1996.
11. K. C. Kao and C. Hwang, "Electrical Transport in Solids", Pergamon Press, ISBN 0-08-023973-0, 1991.

12. J. M. Alison, "A High Field Pulsed Electro-Acoustic Apparatus for Space Charge and External Circuit Current Measurement within Solid Insulators", Measurement Science and Technology, vol. 9, no. 10, pp. 1737-1750, October 1998.

13. T. L. Hanley, R. P. Burford, R. J. Fleming and K. W. Barber, "A General Review of Polymeric Insulation for Use in HVDC Cables", IEEE Electrical Insulation Magazine, vol. 19, no. 1, pp. 13-24, Jan/Feb 2003.

14. E. F. Peschke and R. V. Olshausen, "Cable Systems for High and Extra-HighVoltage", Chapter 4, pp. 119, Publicis MCD Verlag, ISBN 3-89578-118-5, 1999.

15. D. McAllister, "Electric Cables Handbook", Chapter 1, pp. 51, Granada, 1983.

16. C. C. Barnes, "Electric Cables", Chapter 5, pp. 68-77, Sir Isaac Pitman & Sons Ltd., London, 1964.

17. S. G. Swingler, "Factors Controlling the Electric Strength of Extruded Polyethylene Cable - A Review", Central Electricity Research Laboratories, Lab.note No. RD/L/210 4N81, pp.1-16, August, 1981.

18. A. Barlow, "The Chemistry of Polyethylene Insulation", IEEE Electrical Insulation Magazine, vol. 17, no. 1, pp. 8-19, Jan/Feb 1991.

19. G. Mazzanti and G. C. Montanari, "A Comparison between XLPE and EPR as Insulating Materials for HV Cables", IEEE Transactions on Power Delivery, vol. 12, no. 1, pp. 15-28, January 1997.

20. G. C. Montanari and G. Pattini, "Electrical Aging of EPR Cables", Material Engineering, pp. 605-613, vol. 1, no. 2, 1989.

21. M. Brown, "Performance of Ethylene-Propylene Rubber Insulation in Medium and High Voltage Power Cable", IEEE Transactions on Power Apparatus and Systems, vol. PAS-102, no. 2, pp. 373-381, February 1983.

22. Z. Lin, Y. Zou and C. Tang, "The Research on Cross-linked Polyethylene for Electric Cable", Proceedings 2nd International Conference on Properties and Applications of Dielectric Materials, vol. 1, pp. 372-374, September 1988.

23. J. Muccigrosso and P. J. Philips, "The Morphology of Cross-linked Polyethylene Insulation", IEEE Transactions on Electrical Insulation, vol. 13, no. 3, pp. 172-178, June 1978.

24. F. Precopio, "The Invention of Chemically Crosslinked Polyethylene", IEEE Electrical Insulation Magazine, vol. 15, no. 1, pp. 23-25, Jan/Feb 1999.
25. T. J. Lewis, "Charge Transport in Polymers", IEEE Proc. Electrical Insulation and Dielectrics Phenomenon, pp. 533-561, 1976.
26. L. A. Dissado and J. C. Fothergill, "Elecical Degradation and Breakdown in Polymers", Peter Peregrinus Ltd, ISBN 0-86341-196-7, 1992.
27. J. G. Simmons, "DC Conduction in Thin Films", Mills & Boon Limited, London, ISBN 0.263.51786.1, 1971.
28. B. Sanden, E. Ildstad and R. Hegerberg, "Space Charge Accumulation and Conduction Current in XLPE Insulation", 7th International Conference on Dielectric Materials Measurements & Applications, pp. 368-373, September 1996.
29. R. J. Fleming, M. Henriksen and J. T. Holboll, "The Influence of Electrodes and Conditioning on Space Charge Accumulation in XLPE", IEEE Transactions on Dielectrics and Electrical Insulation, vol. 7, no. 4, pp. 561-571, August 2000.
30. M. Henriksen, J. T. Holboll and R. J. Fleming, "The Influence of Pre-conditioning on Space Charge Formation in LDPE", Space Charge in Solid Dielectrics, pp. 235-243, April 1997.
31. G. Chen, T. Y. G. Tay, A. E. Davies, Y. Tanaka and T. Takada, "Electrodes and Charge Injection in Low-density Polyethylene Using the Pulsed Electroacoustic Technique", IEEE Transactions on Dielectrics and Electrical Insulation, vol. 8, no. 6, pp. 867-873, December 2001.
32. K. S. Suh, C. R. Lee, J. S. Noh, J. Tanaka and D. H. Damon, "Electrical Conduction in Polyethylene with Semiconductive Electrodes", IEEE Transactions on Dielectrics and Electrical Insulation, vol. 1, no. 2, pp. 224-230, April 1994.
33. T. Mizutani, K. Shinmura, K. Kaneko, T. Mori, M. Ishioka and T. Nagata, "Space Charge behavior near LDPE/LDPE Interface", 2000 Conference on Electrical Insulation and Dielectric Phenomena (CEIDP), pp. 800-803, 2000.
34. F. Chapeau, C. Alquié and J. Lewiner, "The Pressure Wave Propagation Method for the Analysis of Insulating Materials: Application to LDPE Used

in HV Cables", IEEE Transactions on Electrical Insulation, vol. 21, no. 3, pp. 405-410, June 1986.

35. T. Ditchi, C. Alquié, J. Lewiner, E. Favrie and R. Jocteur, "Electrical Properties of Electrode/Polyethylene/Electrode Structure", IEEE Transactions on Electrical Insulation, vol. 24, no. 3, pp. 403-408, June 1989.
36. T. Mizutani, "Space Charge Measurement Techniques and Space Charge in Polyethylene", IEEE Transactions on Dielectrics and Electrical Insulation, vol. 1, pp. 923-933, 1994.
37. C. Zhang and T. Mizutani, "Space Charge Bahaviour of LDPE with a Blocking Electrode", 2002 Conference on Electrical Insulation and Dielectric Phenomena (CEIDP), pp.614-617, 2002.
38. Y. Murakami, S. Mitsumoto, M. Fukuma, N. Hozumi and M. Nagao, "Space Charge Formation and Breakdown in Polyethylene Influenced by the Interface with Semiconducting Electrodes", Electrical Engineering in Japan, vol. 138, no. 3, pp. 19-25, 2002.
39. N. Hozumi, T. Takeda and H. Suzuki, "Space Charge Behavior in XLPE Cable Insulation under 0.2-1.2MV/cm dc Fields", IEEE Transactions on Dielectrics and Electrical Insulation, vol. 5, pp. 82-90, February 1998.
40. K. S. Suh, J. H. Sun and S. N. Jin, "Effects of Constituents of XLPE on the Formation of Space Charge", IEEE Transactions on Dielectrics and Electrical Insulation, vol. 1, no. 6, pp. 1077-1083, December 1994.
41. T. Mizutani, K. Shinmura, Y. Taniguchi and K. Kaneko, "Effects of Anti-Oxidants on Space Charge in Low-Density Polyethylene", 2001 IEEE 7th International Conference on Solid Dielectrics, pp. 228-231, June 2001.
42. S. Fujita, Y. Kamei and K. Tanaka, "Effect of Water Absorption in Polyimide on Electrical Properties", 2001 IEEE 7th International Conference on Solid Dielectrics, pp. 183-186, June 2001.
43. M. Ieda, T. Mizutani and Y. Suzuoki, "TSC and TL studies of Carrier Trapping in Insulating Polymers", Memoirs of Faculty of Engineering, Nagoya University, vol. 32, no. 2, pp. 173-219, 1980.
44. M. Ieda, "Electrical Conduction and Carrier Traps in Polymeric Materials", IEEE Transactions on Electrical Insulation, vol. 19, no. 3, pp. 162-178, June 1984.

45. G. A. Cartwright, "The Measurement of Space Charge and its Effect on the Breakdown Strength of Solid Polymeric Insulation", PhD Thesis, University of Southampton, 1994.

46. W. Schottky, "Uber den einfluß von strukturwirkungen, bedonder der thomsonschen bildkraft, auf die elecktronenemission der metalle", Z. Phys, vol. 15, pp. 872-878, 1914.

47. R. H. Fowler and L. Nordheim, "Electron Emission in Intense Electric Fields", Proceeding Royal Society A, vol. 119, pp. 173-181, 1929.

48. N. F. Mott and R. W. Gurney, "Electronic Processes in Ionic Crystals", pp. 172, Oxford University Press, 1940.

49. A. Many and G. Rakavy, "Theory of Transient Space-Charge-Limited Currents in Solids in the Presence of Trapping", Physical Review, vol. 126, no. 6, pp. 1980 -1988, 1962.

50. J. G. Simmons, "Poole-Frenkel Effeect and Schottky Effect in Metal-Insulator-Metal Systems", Physical review, vol. 155, no. 3, pp. 657-660, 1967.

51. H. J. White, "Conduction Process in Polymers", Engineering Dielectrics, vol. IIA, pp. 286-290, 1992.

52. Y. Zhang, J. Lewiner and C. Alquié, "Evidence of Strong Correlation between Space Charge Buildup and breakdown in Cable Insulation", IEEE Transactions on Dielectrics and Electrical Insulation, vol. 3, no. 6, pp. 778-783, December 1996.

53. Y. Li and T. Takada, "Progress in Space Charge Measurement of Solid Insulating material in Japan", IEEE Electrical Insulation Magazine, vol. 10, no. 5, pp. 16-28, Sep/Oct 1994.

54. N. H. Ahmed and N. N. Srinivas, "Review of Space Charge Measurement in Dielectrics", IEEE Transactions on Dielectrics and Electrical Insulation, vol. 4, no. 5, pp. 644-656, October 1997.

55. T. Takada, "Acoustic and Optical Methods for Measuring Electric Charge Distributions in Dielectrics", IEEE Transactions on Dielectrics and Electrical Insulation, vol. 6, no. 5, pp. 519-547, October 1999.

56. Y. Zhang, J. Li, Z. Peng, X. Qin and Z. Xia, "Research of Space Charge in Solid Dielectrics in China", IEEE Electrical Insulation Magazine, vol. 17, no. 5, pp. 25-30, Sep/Oct 2001.

57. C. Alquié, G. Dreyfus and J. Lewiner, "Stress Wave Probing of Electric Distributions in Dielectrics", Phy. Rev. Lett., vol. 47, pp. 1483-1487, 1981.

58. G. M. Sessler, J. E. West, R. Gerhard-Multhaupt and H. V. Seggern, "Nondestructive Laser Method for Measuring Charge Profiles in Irradiated Polymer Films", IEEE Transactions on Nuclear Science, vol. 29, no. 6, pp. 1644-1649, December 1982.

59. W. Eisenmenger and M. Haardt, "Observation of Charge Compensated Polarization Zones in Polyvinylendenfluoride (PVDF) Films by Piezoelectric Acoustic Step-wave Response", Solid State Communications, vol. 41, no. 2, pp. 917-920, March 1982.

60. F. Chapeau, C. Alquié, J. Lewiner, H. Auclair, Y. Pelet and R. Jocteur, "The Pressure Wave Propagation Method for the Analysis of Insulating Materials: Application to LDPE used in HV Cables", IEEE Transactions on Electrical Insulation, vol. 21, no. 3, pp. 405-410, June 1986.

61. Y. Li, M. Yasuda and T. Takada, "Pulsed Electroacoustic Method for Measurement of Charge Accumulation in Solid Dielectrics", IEEE Transactions on Dielectrics and Electrical Insulation, vol. 1, no. 2, pp. 188-195, April 1994.

62. T. Maeno, T. Futami, H. Kushibe and T. Takada, "Measurement of Spatial Charge Distribution in Thick Dielectrics Using the Pulsed Electro-Acoustic Method", IEEE Transactions on Electrical Insulation, vol. 23, no. 3, pp. 433-439, June 1988.

63. Y. Li, "Space Charge measurement in Lossy Solid Dielectric Materials by Pulsed Electroacoustic Method", PhD Thesis, Musashi Institute of Technology, Japan, March 1994.

64. W. Sachse and Y. Pao, "On the Determination of Phase and Group Velocities of Dispersive Waves in Solids", Journal of Applied Physics, vol. 49, no. 8, pp. 4320 - 4327, August 1978.

65. T. Mizutani and M. Ieda, "Carrier Transport in High-Density Polyethylene", Journal of Physics D: Applied Physics, no. 12, pp. 291 - 296, 1979.

66. T. Mizutani, T. Tsukahara and M. Ieda, "The Effects of Oxidation on the Electrical Conduction of Polyethylene", Journal of Physics D: Applied Physics, no. 13, pp. 1673 - 1679, 1980.

67. G. Chen, H. M. Banford, R. A. Fouracre and D. J. Tedford, "Electrical Conduction in Low-Density Polyethylene", 1989 Conference on Conduction and Breakdown in Solid Dielectrics (ICSD), pp. 277 - 281, July 1989.

68. T. J. Lewis, "The Micro-Physics of Charge in Solid Dielectrics", Space Charge in Solid Dielectrics, pp. 1-17, April 1997.

69. P. Morin, C. Alquié and J. Lewiner, "Study of the Electrode-insulator Interfaces by Simultaneous Measurement of External Current and of Space Charge Distributions", 1995 JICABLE, pp. 189-194, 1995.

70. P. Morin, J. Lewiner, C. Alquié and T. Ditchi, "Study of Space Charge Dynamics in Solid Dielectrics by Simultaneous Measurement of External Current and of Space Charge Distributions", Space Charge in Solid Dielectrics, pp. 43-57, April 1997.

71. W. S. Lau, G. Chen and A. E. Davies, "Concurrent Space Charge and Current Density Measurements in Additive-free LDPE", 2002 Conference on Electrical Insulation and Dielectric Phenomena (CEIDP), pp. 640-643, October 2002.

72. Y. Tanaka, T. Takada, C. Shinoda and T. Hashizume, "Temperature Dependence of Space Charge Distribution in XLPE Cable", 1994 Conference on Electrical Insulation and Dielectric Phenomena (CEIDP), pp. 334-339, 1994.

73. X. Wang, D. Tu, Y. Tanaka, T. Muronaka, T. Takada, C. Shinoda and T. Hashizume, "Space Charge in XLPE Power Cable under DC Electrical Stress and Heat Treatment", IEEE Transactions on Dielectrics and Electrical Insulation, vol. 2, no. 3, pp. 467-474, June 1995.

74. W. S. Lau and G. Chen, "Simultaneous Space Charge and Current Assessment in additive-free LDPE under HVDC Condition", ICEMP and ACEID China, April 2003.

75. W. S. Lau and G. Chen, "The influence of temperature on electrical conduction and space charge in LDPE", 2003 JICABLE, pp. 485-490, 2003.

76. H. Kon, Y. Suzuoki, T. Mizutani, M. Ieda and N. Yoshifuji, "Packet-like Space Charges and Conduction Current in Polyethylene Cable Insulation", IEEE Transactions on Dielectrics and Electrical Insulation, vol. 3, no. 3, pp. 380-385, June 1996.

77. Y. Suzuoki, H. Muto, T. Mizutani and M. leda, "Effects of Space Charge on Electrical Conduction in High Density Polyethylene", Journal of Physics D: Applied Physics, no. 18, pp. 2293-2302, 1985.

78. M. Nagao, T. Kimura, Y. Mizuno, M. Kosaki and M. leda, "Detection of Joule Heating before Dielectric breakdown in Polyethylene Films", IEEE Transactions on Electrical Insulation, vol. 25, no. 4, pp. 715-722, August 1990.

79. C. Zhang, T. Mizutani and K. Kaneko, "Temperature Increase and Charging Current in Polyethylene Film During Application of High Voltage", Applied Physics Letters, vol. 79, no. 23, pp. 3839-3841, December 2001.

80. N. Hozumi, H. Suzuki, T. Okamoto, K. Watanabe and A. Watanabe, "Direct Observation of Time-dependent Space Charge Profiles in XLPE Cable under High Electric Fields", IEEE Transactions on Dielectrics and Electrical Insulation, vol. 1, no. 6, pp. 1068-1076, December 1994.

81. A. See, L. A. Dissado and J. C. Fothergill, "Electric Field Criteria for Charge Packet Formation and Movement in XLPE", IEEE Transactions on Dielectrics and Electrical Insulation, vol. 8, no. 6, pp. 859-866, December 2001.

82. Y. Li and Y. Takada, "Experimental observation of Charge Transport and Injection in XLPE at Polarity Reversal", Journal of Physics D: Applied Physics, no. 25, pp. 704-716, 1992.

83. J. M. Alison and R. M. Hill, "A Model for Bipolar Charge Transport, Trapping and Recombination in Degassed Crosslinked Polyethylene", Journal of Physics D: Applied Physics, no. 27, pp. 1291-1299, 1994.

84. A. D. Nichols, "The Manufacture and Application of Cables by the Monosil Process", 1990 Conference on Electricity Supply Engineers Association of New Zealand, Wellington, vol. 60, pp. 110-116, 1990.

85. Y. Sekii, T. Ohbayashi, T. Uchimura, T. Hukuyama and T. Maeno, "A Study on the Space Charge Formation in XLPE", 2001 Conference on Electrical Insulation and Dielectric Phenomena (CEIDP), pp. 469 - 472, October 2001.

86. Y. F. F. Ho, G. Chen, A. E. Davies, S. G. Swingler, S. J. Sutton and R. N. Hampton, "Effect of Semiconducting Screen on the Space Charge Dynamic in XLPE and Polyolefin Insulation under DC and 50Hz AC Electric Stresses Conditions", IEEE Transactions on Dielectrics and Electrical Insulation, vol. 10, no. 3, pp. 393 -403, June 2003.

87. C. Shinoda, T. Hashizume, T. Tani, Y. Tanaka and T. Takada, "A Consideration of Mechanism of DC Leakage Current Peak in XLPE Cables", 1997 International Conference on Properties and Application of Dielectric Materials (CPADM), pp. 402-405, 1997.

88. N. Hirai, R. Minami, T. Tanaka, Y. Ohki, M. Okashita and T. Maeno, "Chemical Group in Crosslinking Byproducts Responsible for Charge Trapping in Polyethylene", 2002 Conference on Electrical Insulation and Dielectric Phenomena (CEIDP), pp. 626-630, October 2002.

89. F. Aida, G. Tanimoto, M. Aihara and E. Hosokawa, "Influence of Curing By-products on Dielectric Loss in XLPE Insulation", 1990 Conference on Electrical Insulation and Dielectric Phenomena (CEIDP), pp. 465-473, October 1990.

90. T. Tsurimoto, S. Mitsumoto, M. Nagao and M. Kosaki, "Effect of Acetophenone on Electric Conduction in LDPE Film", 1995 International Symposium on Electrical Insulating Materials, pp. 267-270, September 1995.

91. S. Mitsumoto, M. Nagao and M. Kosaki, "Effects of Acetophenone on High-field Electrical Properties in Polyethylene", 1996 Conference on Electrical Insulation and Dielectric Phenomena (CEIDP), pp. 157-160, October 1996.

92. T. Doi, Y. Tanaka and T. Takada, "Measurement of Space Charge Distribution in Acetophenone Coated Low-density Polyethylene", 1997 Conference on Electrical Insulation and Dielectric Phenomena (CEIDP), pp. 32-35, October 1997.

93. M. Meunier, N. Quirke and A. Aslanides, "Molecular Modeling of Electron Traps in Polymer Insulators: Chemical Defects and Impurities", Journal of Chemical Physics, vol. 115, no. 6, pp. 2876 - 2881, August 2001.

94. M. Fukuma, M. Nagao and M. kosaki, "Computer analysis on Transient Space Charge Distribution in Polymer", 1984 International Conference on Properties and Applications of Dielectric Materials (CPADM), pp. 24-27, July 1984.

95. N. Zebouchi, M. Se-Ongoua, D. Malec and T. G. Hoang, "Modeling of Transient Space Charge Distribution in Polymer", Journal of Electrostatics, no. 40&41, pp. 495-501, 1997.

96. K. Kaneko, T. Mizutani and Y. Suzuoki, "Computer Simulation on Formation of Space Charge Packets in XLPE Films", IEEE Transactions on Dielectrics and Electrical Insulation, vol. 6, no. 2, pp. 152 -158, April 1999.

97. S. LeRoy, G. Teyssedre, C. Laurent and P. Segur, "Numerical Modeling of Space Charge and Electroluminescence in Polyethylene under DC Field", 2002 Conference on Electrical Insulation and Dielectric Phenomena (CEIDP), pp. 172 -175, October 2002.